Air-Data Estimation For Air-Breathing Hypersonic Vehicles

by
Bryan Heejin Kang

B.S., University of Southern California (1987)
S.M., Massachusetts Institute of Technology (1989)

Submitted to the Department of
Aeronautics & Astronautics
in Partial Fulfillment of the Requirements
for the Degree of

DOCTOR OF PHILOSOPHY
at the
MASSACHUSETTS INSTITUTE OF TECHNOLOGY
October 1995

Signature of Author _____
Department of Aeronautics and Astronautics
October 23, 1995

Certified by _____
Professor Wallace E. Vander Velde
Thesis Supervisor and Committee Chairman

Certified by _____
Dr. Philip D. Hattis
CSDL Technical Supervisor and Committee member

Certified by _____
Professor Robert J. Hansman Jr.
Thesis Committee Member

Certified by _____
Professor Manuel Martinez-Sanchez
Thesis Committee Member

Accepted by _____
Professor Harold Y. Wachman
Chairman, Department Graduate Committee

Air-Data Estimation For Air-Breathing Hypersonic Vehicles

by

Bryan Heejin Kang

Submitted to the Department of Aeronautics and Astronautics
on October 23, 1995 in partial fulfillment of the requirements for
the degree of Doctor of Philosophy

Abstract

Air-data sensing and estimation methodologies for generic air-breathing hypersonic vehicles (AHSVs) are developed and the resulting estimation strategies are demonstrated with an example vehicle configuration. The methodologies cover the steps from problem formulation and modeling through the resulting nonlinear estimator design. The core emphasis of the AHSV air-data estimation strategy is to improve the accuracy of the angle of attack estimate to a degree necessitated by the stringent operational requirements of the air-breathing propulsion and flight stabilization systems.

A requirement set for air-data estimation accuracy is provided. The air-data sensor selection and placement issues are discussed, and a most likely scenario of sensor usage is covered. Based on a Draper Laboratory developed AHSV simulation code, a parameterized vehicle model is formed along with sensor and environment models that are later incorporated into the estimation algorithms.

The resulting estimation problem involves solutions to time-dependent nonlinear estimation equations. Because the solutions to the nonlinear estimation problem(Zakai equation) is infinite dimensional, a finite approximation is needed. A statistical analysis based on a simulation of the vehicle dynamics and observation show that the diffusion (propagation) process does not significantly alter the basic characteristics of the initial Gaussian conditional density of state variables. Similarly, the nonlinearities within the observation do not distort the initial density shapes for large hypersonic flight spans covering a Mach 10 to 15 range. The results provide the basis for applicability of an Extended Kalman Filter (EKF) and substantiate the application requirements from necessary assumptions and finite approximations.

The EKF for the AHSV air-data system is implemented and statistical analysis (Monte-Carlo simulation) is used to provide the estimator performance. In conjunction with the estimator design, the sensor precision requirements are approached from the context of the estimation problem. By starting from the covariance equations of an EKF, a sensor precision requirement criteria is developed.

Through numerical example study and design, the AHSV air-data estimation methodologies described above are demonstrated systematically. The numerical results provided some insight into the achievable performance of the estimator design. Finally, the demonstrated methodologies lay out the design guidelines for future AHSV air-data estimator design and analysis when higher fidelity models are available.

Thesis Committee:

Dr. Wallace E. Vander Velde,	Professor of Aeronautics & Astronautics
Dr. Philip D. Hattis,	Technical Staff, C.S. Draper Laboratory, Inc.
Dr. John R. Hansman,	Professor of Aeronautics & Astronautics
Dr. Manuel Martinez-Sanchez,	Professor of Aeronautics & Astronautics

Acknowledgments

Recollections of my graduate school years conjure up the fact that the most important academic achievements of mine came from interactions with numerous people at both MIT and Charles Stark Draper Laboratory. Countless discussions and advises from people surrounded me provided an environment where I can truly explore the extremes of imagination while realizing limitations in theory and practice of engineering. This thesis would not be possible without the contributions from those people.

This research was made possible through financial support of the Charles Stark Draper Laboratory. The laboratory provided opportunity to pursue a graduate education at MIT and provided the environment full of technical expertise. Such a combination I will not find anywhere.

I am very grateful to all members of my doctoral committee. Special thanks go to my research supervisor, Phil Hattis. He provided unlimited moral and technical support. Without his help this thesis work would not have been possible. Professor Vander Velde always provided insightful and positive suggestions whenever I reached an obstacle. He has special ability to explain complex things in very simple and logical terms. I truly thank him for his guidance. I give special thanks to Professor Martinez-Sanchez for his technical advises in the subject of hypersonic propulsion and vehicle modeling. He also provided insightful comments throughout the thesis work. I give special thanks to Professor Hansman. As a masters thesis adviser to a doctoral thesis committee member, he provided initial inception of the hypersonic air-data sensing problem and he guided me through to the end of my doctoral program. He always tried to provide a focus in my thesis work.

I would also like to thank many of Draper faculties and Draper fellow students for their advises and assistance. I give special thanks to Brent Appleby, Greg Chamitoff and Rami Mangoubi for their friendship, technical supports and unlimited hours of valuable discussions. Greg developed a smart way of controlling the AHSVs. His vehicle and control system design codes and his thesis provided a solid background for the vehicle design, analysis and simulation efforts in my thesis. He also provided detailed and accurate insights on the AHSV systems. Brent and Rami never turned me down when I had questions or needed to discuss various ideas. Rami always motivated me to look into new theoretical foundlings and helped me to understand difficult mathematical equations. I would also like to thank Dino DeAngelus for his friendship and partnership while participating in the Browning Random Talk seminar series. I would like to thank other Draper faculties including; Milt Adams, Neil Adams, Harvey Malchow, Bob Roberson, Jim Negro, John Dowdle, John Deyst (now he is a Professor at MIT).

Special thanks go to my parent for their love. Without their patience, support and encouragements, none of this work would have been possible. I also like to thank my newly wed wife, Hyun Jung for her love and care. I would like to thank my sisters, Jane, Susan, Christen and Laura. My brother in law, Andy also deserves special thanks for his moral and financial support throughout my school years.

I would also like to thank my friends: i) All 101 members; Ben, Seung Jin, Frank, Albert, Song Keun, Ha Yong and Henry ii) My old friends; James, Mike, Andy, Joseph and Ken iii) All the KGSA members including CQC, Young Chang, BHSohn, Jae Sang, Seung Hun and Byong Won.

This thesis was prepared at The Charles Stark Draper Laboratory, Inc., under I.R.&D. Projects 300 and 527.

Publication of this thesis does not constitute approval by Draper or the sponsoring agency of the findings or conclusions contained herein. It is published for the exchange and stimulation of ideas.

I hereby assign my copyright of this thesis to The Charles Stark Draper Laboratory, Inc., Cambridge, Massachusetts.

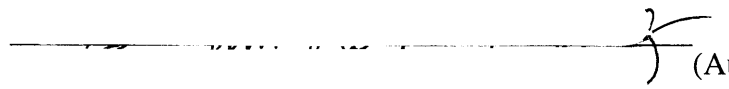

(Author's signature)

Permission is hereby granted by The Charles Stark Draper Laboratory, Inc., to the Massachusetts Institute of Technology to reproduce any or all of this thesis.

Table of Contents

List of Figures

List of Tables

List of Symbols And Acronyms

ADS	Air-Data System
AHSV	Air-Breathing Hypersonic Vehicle
A_e	Elevon area
A_p	Projected area
a_g	Slope of gradient layer
a_x	Acceleration in x-direction
a_y	Acceleration in y-direction
a_z	Acceleration in z-direction
α	Angle of attack
α_d	Design or desired angle of attack
b	Vehicle wing span
β	Angle of side slip
CARS	Coherent Anti-stoke Raman Scattering
CFD	Computational Fluid Dynamics
C_{BE}	Coordinate transform matrix from earth to body coordinate
C_{BW}	Coordinate transform matrix from wind to body coordinate
C_{WE}	Coordinate transform matrix from earth to wind coordinate
C_D	Aerodynamic drag coefficient
C_{Do}	Aerodynamic drag coefficient at zero angle of attack
C_L	Aerodynamic lift coefficient
C_{Lo}	Aerodynamic lift coefficient at zero angle of attack
C_{ma}	Aerodynamic moment coefficient
C_{mp}	Propulsion moment coefficient
C_{Tn}	Thrust coefficient, normal to the velocity vector
C_{Tv}	Thrust coefficient, tangential component, parallel to the velocity axis

$C_{X\delta_e}$	Normalized control force along the velocity axis due to the elevon
$C_{Z\delta_e}$	Normalized control force normal to the velocity vector due to the elevon
$C_{m\delta_e}$	Normalized control torque in the pitch axis due to the elevon
$C_{X\delta_T}$	Normalized control force along the velocity axis due to throttle variation
$C_{Z\delta_T}$	Normalized control force along the normal axis due to throttle variation
$C_{m\delta_T}$	Normalized control torque along the pitch axis due to throttle variation
$C_{X\delta_v}$	Normalized control force along the velocity axis due to thrust vectoring
$C_{Z\delta_v}$	Normalized control force along the normal axis due to thrust vectoring
$C_{m\delta_v}$	Normalized control torque along the pitch axis due to thrust vectoring
c	Mean chord length for wing
DOF	Degrees Of Freedom
Δt	Pulse duration
δ_e	Elevon control input
δ_T	Throttle control input
δ_v	Thrust vector control input
EKF	Extended Kalman Filter
F_x	Forces in x - Direction
F_y	Forces in y - Direction
F_z	Forces in z - Direction
f(•)	Function of •
ϕ	Roll angle
GPS	Global Positioning System
g, g(•)	Gravity constant, or gravity function (function of altitude)
Γ	Flight path angle
γ	Specific heat ratio
HI-FADS	Subsonic High Angle-of-Attack Flush Air-Data Sensing System
HOT	Higher Order Terms
HTOL	Horizontal Take-Off and Landing
Hyflite	Hypersonic Flight Test Experiment
H_e	Free stream enthalpy
H_g	Gyro angular momentum
H_o	Total enthalpy
H_s	Step function
h	Altitude
h_k	Planck's constant
h_p	Pressure altitude

h_r	Reference altitude for the environment model
η_c	Collection optic efficiency
η_d	Detector quantum efficiency
IMU	Inertial Measurement Unit
I	Vehicle moment of inertia matrix (it's components I_{xx}, I_{xy}, etc.)
I_{ga}	Moment of inertia - gimbal axis
I_o	Source laser power
I_r	Rayleigh scattered power
KBF	Kalman-Bucy Filter
K_G	Gravity coefficient
k	Spring constant of the torsion bar
k_d	Viscous damping
LDV	Laser Doppler Velocimetry
LEO	Low Earth Orbit
LHP	Left Half Plane
LTI	Linear Time Invariant
LVLH	Local-Vertical-Local-Horizon
L_s	Length of sample volume
MIMO	Multi-Input-Multi-Output
MIT	Massachusetts Institute of Technology
M	Mach number
M_a	Flight Mach number
M_d	Design or desired flight Mach number
M_x	Moment on roll axis
M_y	Moment on pitch axis
M_z	Moment on yaw axis
M_∞	Free stream Mach number
m	Vehicle total mass
m_E	Earth mass
NASA	National Aeronautics and Space Administration
NASP	National Aero-Space Plane
N_i	Number density of species i
n_p	Number of pulses during the measurement interval
ν	Radiation frequency
ν_d	Doppler shift frequency
ν_o	Laser frequency

P_i	Pressure at ith pressure port
P_r	Reference pressure for the environment model
P_t	Total pressure
P_∞	Static pressure
p	Roll rate
Q	Dynamic Pressure
Q_i	Rayleigh cross-section of species i
q	Pitch rate
θ	Pitch angle
θ_g	Gyro gimbal angle
RHP	Right Half Plane
R	Distance from center of the Earth, altitude plus earth radius
R_e	Reynolds number
R_g	Universal gas constant
R_p	Ratio of static pressure over total pressure
r	Yaw rate
ρ_e	Engine inlet density
ρ_r	Reference density for the environment model
ρ_∞	Free stream air density
SEADS	Shuttle Entry Air-Data System
SISO	Single-Input-Single-Output
SSTO	Single Stage To Orbit
S	Reference area, typically wing surface area
T	Temperature
T_e	Engine inlet temperature
Tr	Reference temperature for the environment model
T_t	Total temperature
T_∞	Free stream air temperature
t	Time
u	X-direction velocity of vehicle c.g.
V_a	Relative air velocity
V_e	Engine inlet velocity
V_s	Speed of sound
v	Y-direction velocity of vehicle c.g.
W_x	Wind velocity in x-direction

W_y	Wind velocity in y-direction
W_z	Wind velocity in z-direction
$\mathbf{w}$	Z-direction velocity of vehicle c.g.
Ω_c	Solid angle of collection optics
ω_E	Earth rotation rate
ω_i	Gyro rate input
ψ	Yaw angle, Heading angle

Chapter 1

Introduction

1.1 Motivation

1.1.1 Historical Context

Until the fall of the Berlin wall, the main driving force behind the aerospace technology was the arms race of cold war. In the current era, characterized by the end of cold war and the beginning of an international economic race, aero-space programs can not follow the military oriented path of the past but rather should be stimulated by socioeconomic criteria. Technology developments in aero-space programs must emphasize international competitiveness in primary industries while also stimulating development of other engineering fields.

In recent years, enthusiasm for hypersonic flight research has been renewed by the promise of a fully reusable, horizontal take-off, single stage to orbit flight vehicle with air-breathing engines. The current state-of-the-art launch vehicles such as the Space Shuttle and expendable rockets have demonstrated their capabilities in the past; however, the existing vehicles are far short of an ideal launch system. Existing launch vehicles suffer from shortcomings in efficiency, reliability, and complexity. Projected air-

breathing hypersonic vehicles (AHSVs), such as was envisioned with the X-30 or National Aero-Space Plane (NASP) program, would potentially be very efficient [Peg1].

A unique feature of this class of vehicles is the usage of air-breathing engines as the main propulsion system during most of the ascent trajectory. Since typical launch vehicles may allocate up to 90% of the vehicle weight to fuel and oxidizer, using atmospheric oxygen significantly reduces vehicle weight when compared to the rocket propulsion system with similar payload capability. For example, about 1/3 of the Space Shuttle mass, excluding the solid rocket boosters, are liquid oxygen [Lew1]. In the extreme case, liquid oxygen contained within the first three stages of the Apollo Saturn V launch vehicle contributed about 72% of its total weight [Lew1]. Full reusability and single-stage-to-orbit (SSTO) capability provides simplicity in operation and potentially cost effectiveness. Horizontal-take-off capability will eliminate complicated and costly launch facilities.

The inherent advantages of AHSVs make them quite attractive. The projected increase in demand for future spacecraft launches will justify the development of the AHSV technology; consequently, the AHSV concept qualifies as a future aero-space program justification criterion. Moreover, the derived new technology will be multi-faceted, since every aspect of building this class of vehicle would require innovation. High temperature materials, propulsion, system integration, control, sensors and estimation techniques are a few areas which can gain in their respective state-of-the-art by pursuing this program. Lessons learned from this vehicle development will greatly influence many industries.

1.1.2 AHSV Mission Requirements and Challenges

The anticipated result of the NASP research vehicle development program would have been an AHSV that would deliver a significant amount of payload to low earth orbit (LEO) via use of air-breathing engines [Peg1]. A future vehicle in the NASP class is expected to take off horizontally on conventional runway without complex launch facilities. The vehicle will have a single stage configuration that eliminates stage separation issues and insures full reusability. With a single stage configuration, the vehicle will cruise through the atmosphere following a narrow air-breathing corridor. The employed air-breathing engines will operate in both ramjet and Scramjet modes.

Hydrogen fuel will be burned with atmospheric oxygen ingested into the propulsion system. The total expected hypersonic flight time would be about 2000 seconds, longer than any existing launch systems [Hat1]. Once the vehicle gains speed to near orbital velocity, it will be inserted into low earth orbit with the assist of small rockets. Reentry will be performed using high drag maneuver similar to the Space Shuttle Orbiter following a trajectory much higher than the air-breathing ascent corridor at hypersonic speeds.

Operational requirements of an air-breathing hypersonic vehicle differ in many ways from conventional spacecraft and aircraft, mainly due to its unique propulsion system. Design of an air-breathing hypersonic vehicle will be dominated by considerations regarding air-breathing engine performance and stability, because the engine performance and stability will dictate the mission success. With likely slender lifting-body configurations, AHSVs will have propulsion, aerodynamics, and flight dynamics that are highly integrated and interactive [Sch2, Sch3, Peg1]. The vehicle lower surface would act as inlet and nozzle while providing lift. The flight control, guidance, engine control and vehicle cooling are heavily coupled to the propulsion system design; consequently, the major tasks of these subsystems would be to contribute to the proper combustion conditions. Propulsion, aerodynamics, and thermal constraints will be the main emphasis in the vehicle configuration design procedure. Moreover, the air-breathing engines of hypersonic vehicles will introduce restrictions on the flight trajectory envelope, vehicular motion and atmospheric conditions [Kan2].

Developing an efficient air-breathing propulsion system which can operate over a wide range of flight Mach numbers is a difficult task. Even though development of ramjet technology started as early as the 1950's, ramjet technology can only be used below about Mach 7 [Nas1]. The major difficulties in implementing conventional (subsonic combustion) ramjet technology are in the thermal limitations in combustor materials, inlet normal shock stability, combustor flame stability and the inherent problem of poor efficiency at low supersonic speeds and at Mach numbers greater than 7 [Pet1]. The worst propulsion failure is called engine unstart that can occur if the normal shock position can not be properly controlled inside the compression inlet [Leh1, Sha2].

The technology of supersonic combustion ramjets which are called Scramjets promises good efficiency at higher Mach numbers [Kop1]. However, Scramjet technology is not yet mature enough to be implemented in an operational design. Many

problems associated with Scramjet technology are due to a still deficient understanding of supersonic combustion. Supersonic combustion chemical kinetics must be well modeled and managed to obtain stable and efficient combustion. Just injecting hydrogen fuel and promoting combustion in supersonic flow presents a substantial challenge [Kop1, Wal1]. Inlet and nozzle design and the associated Aero-thermodynamics also must be fully understood and accommodated. Because of the high dynamic pressure, high Mach number flight conditions expected during Scramjet operation, materials capable of withstanding high thermal stresses are needed (greater than 3000°F) [Kan2].

Both a theoretical understanding and experimental investigations of the aerodynamics and Aero-thermodynamics associated with hypersonic flight are needed. An understanding of the aerodynamic phenomena is required to determine vehicle dynamic variables such as stability derivatives, lift and drag coefficients. The vehicle control effectiveness can also be determined by investigating these aerodynamic problems [Cha2]. The aero-thermodynamics must be studied to determine the cooling requirements of the propulsion system and vehicle structure. The vehicle will have a hot structure configuration with long heat soak duration; therefore, an active cooling strategy must be developed [Peg1, Wal1, Lew1].

Similarly, AHSV structural designs are also a challenge. Slender and shell structure lifting-body AHSVs are difficult to design and analyze due to their extreme temperature variation and heat loads. Furthermore, high temperature materials are difficult to find and then manufacture into vehicle components [Wal1], and their strength and stiffness are difficult to estimate at extreme temperature. Even when such vehicle can be manufactured, it will be difficult to estimate the amplitude and frequencies of the vehicle vibration and bending modes. The resulting structural design may cause interaction problems with the control systems, propulsion, sensors and estimators.

Overall AHSV design is a difficult task since the interactions between subsystems are severe when compared to the conventional vehicles. Thus an AHSV must be designed as an integrated system instead of separate subsystems. For example, the flight controller can not be designed with conventional methodology based on just vehicle geometric and mass properties with experimentally derived stability derivatives. Given that the vehicle motion is heavily coupled to the air-breathing engines, and the engine control capability can be limited by actuator placement, complexity, bandwidth, and weight, the flight controller may be required to supplement the engine controller by

flying within specified attitude and maneuver ranges as a function of Mach number [Kan2]. Similarly the structural dynamics will be strongly interactive with the flight controller and propulsion systems; therefore, structural dynamics should also be addressed in the flight controller design process [Sch1]. Due to the wide operating envelope of AHSVs, the flight control system includes highly nonlinear, time varying, and often unstable plants [Cha2].

Often the problem of state measurement and the associated data processing system is ignored as a serious problem during early flight vehicle development; however, for the AHSV, it is a very important problem to consider from design conception [Kan2]. The measurement and data processing system is the nervous system of the vehicle where the information is sensed, processed, and exchanged between the important functional subsystems. As part of integrated vehicle design methodology, the design of the measurement and data processing system must also be treated in integrated form. The design of sensors that can operate in such an extreme temperature environment is difficult. The hypersonic flow effects prohibit any sensors that intrude into the flow [Neu1]. Also, accuracy and bandwidth requirements on sensors are stringent [Kan2]. Even if sensors can be designed and properly placed on the vehicle, it will still be challenging to manage and process thousands of measurements [Neu1]. Furthermore, some measurements must be processed in real time thereby introducing constraints on data processing time.

Development of AHSV sensing and estimation capability can be categorized into several major tasks. The first task involves the control of information traffic; that is to define the transaction rules for the sensed and processed information. In other words, the task defines what parameters are needed by each subsystem, defines what measurements are available, and defines how sensed or processed information should interface between each subsystem. Also the transfer rate should be determined. The second task is to analyze the measurement process. In addition, the sensor noise and disturbance noise of measurement processes must be characterized. A third task is to provide algorithms that supply information in a compact and efficient form and provide an estimate of important variables. In order to solve such an involved problem, it is necessary to understand the overall system functionality as well as applicable requirements.

The performance and stability of air-breathing engines are highly dependent on the air data parameters which are the quantified description of air flow around the

vehicle. In other words, the performance and stability of the air-breathing engines can be characterized only if the nominal and perturbations of the vehicle attitude in the wind frame are specified. Past investigations of the sensitivity of ramjet and Scramjet performance with respect to air data parameters indicated that the operation of the air-breathing engines outside the design envelope severely degrades the propulsion efficiency and could lead to combustion instability [Kan2,Hat1]. For example, if angle of attack is off one degree from the design value then about 5% of total fuel will be wasted[Hat1]. The past and current rocket based hypersonic flight vehicles, such as X-15 and Space Shuttle, do not require the measurement of air data for the propulsion performance and safety. However, for the air-breathing hypersonic vehicles, the measurement and control of the air data parameters will play as important a role in their operational success as inertial platforms have for rocket propelled vehicles.

Other important physical variables are the parameters associated with flight environment. Describing the atmosphere around the flight trajectory, they are difficult to measure and are poorly known a priori. The variables such as free stream temperature, pressure, density, and wind vector distributions are required to operate the engine and flight control. For example, free stream static pressure and total pressure measurements along with free stream density are needed to fully characterize the true operating conditions of the engines. These operating conditions and the flow angle parameters are needed to adjust the fuel injection and other engine control variables. Therefore, along with engine parameters and air-data states, free stream atmospheric variables must be measured and processed. The data processing of atmospheric variables will involve estimation based on a combination of sensor measurements and the a priori data base.

The propulsion related parameters must also be measured and processed. The engine parameters, such as inlet thermodynamic states, mass flow rate and fuel flow are required to properly control the engine through throttle setting as well as inlet and nozzle geometry. Since the vehicle attitude regulation is also used as a method of engine control, those variables are needed by the flight controller to assist proper combustion. The applicable sensors are difficult to find since the sensors have to operate in an extreme temperature environment.

The interactions among subsystems described above calls for a system integration approach to measurement system design. With a full understanding of each subsystem, the inertial, air-data, propulsion, and environment sensing problem should be laid out

altogether and solved in an integrated manner. To demonstrate appropriate information processing methodologies and to obtain particular solutions would be significant, and enabling contributions to the development of AHSVs.

1.2 Research Objectives

The global objective of this research is to formulate and to demonstrate an air-data estimation strategy for Air-breathing Hypersonic Vehicles (AHSVs). In particular, the estimation efforts are focused on improving the air-data estimate accuracy, since there are stringent observation requirements which can not be addressed directly with accurate sensor readings. Even when applying all previously available knowledge of AHSVs, alternative estimation methodologies are needed, must be explored, and then evaluated on a realistic AHSV hypersonic flight digital simulation. The specific thesis research objectives are:

- To define AHSV measurement requirements by analyzing each subsystem such as engine control, flight control, guidance, and the vehicle cooling. In addition, analyze how required information is to be used by each subsystem. The accuracy requirements should be updated from previous work.[Kan2]

- To formulate the air-data estimation problem based on the accuracy requirements and available sensor technologies.

- To select and design applicable estimation strategies. The data processing schemes emphasize estimation of air-data states, propulsion parameters, and environment parameters. On the basis of fundamental nonlinear filtering theory and numerical analysis of a particular AHSV configuration, a particular solution of the air-data estimator should be designed and analyzed.

- To verify the estimator performance by obtaining a demonstrated solution to the estimation problem and performing statistical analysis. A computer simulation that has implemented the estimator concept should verify its performance.

- To assess the air-data sensor precision requirements in the context of air-data estimation. Relate the sensor issues such as applicability of currently available air-data sensor technologies and sensor precision requirements based on a demonstrated estimator solution and estimation constraints.

1.3 Contributions

- The development of a systematic approach to air-data estimator design methodologies that is applicable to any class of generic Air-Breathing Hypersonic Vehicles(AHSVs). This covers AHSVs with dynamic models that have nonlinearities within the vehicle flight dynamics, propulsion system, and measurement processes (observation equations).

- The treatment of coupled estimator and flight control problem that arise from the AHSV characteristics. Nonlinearities within the AHSV dynamics and observations result in solutions to the air-data estimation problem being dependent on control history. A flight controller is designed in the process of obtaining a particular solution.

- The assessment of air-data sensor precision requirements based on a demonstrated solution to the air-data estimation problem as well as a new method which is derived from the Extended Kalman Filter formulation to form inequality constraints with the state estimation error covariance and sensor noise covariance.

- A demonstrated solution to the AHSV air-data estimation problem. This includes:
  - Graphical solutions to the Fokker-Planck equation of the AHSV dynamics. That is based on a set of flight simulation runs with a statistical analysis.
  - The Extended Kalman Filter design and its performance estimate based up on a Monte-Carlo simulation.
  - An estimate of the air-data sensor precision requirements derived by using an iteration algorithm containing the covariance inequality constraints.

1.4 Organization of Thesis

Chapter 2 describes the research approach of this thesis. First part describes a global view of the thesis problem. Problem of the AHSV air-data estimation and constraints of the air-data sensing issues are qualitatively discussed to motivate the unique characteristics that are associated with this problem. Interactions between the air-breathing engines with other flight subsystems (most importantly with the vehicle attitude) are emphasized as the main motivation for the development of an accurate estimation strategy. Second part of this chapter presents brief solution strategies for the AHSV air-data estimation problem. The research tasks are presented in a systematic order and provide a general overview of the AHSV air-data estimation methodology.

Chapter 3 presents some introductory materials on the AHSV missions and configurations. Typical flight envelop and trajectory of the AHSV are presented with explanation of the air-breathing engine constraints. The most likely configuration of the AHSV is synthesized and discussed. The final AHSV design, that is being used within this thesis work, is configured based on the Chamitoff's AHSV design tools [Cha2]. Also this chapter discusses the status of the AHSV research. The last part of this chapter discusses the interactions between the air-breathing propulsion and other sub-elements of AHSVs such as structure and flight dynamics. The impact of these unique AHSV characteristics on the air-data instrumentation is discussed.

Chapter 4 discusses the AHSV air-data instrumentation issues. This chapter begins with the historical overview of hypersonic instrumentation. The air-data sensors from previous research and operational vehicles such as the X-15 and the Space Shuttle are discussed along with some other previously proposed conceptual sensor designs. This historical review of the potential sensor technologies provides the foundation for the AHSV instrumentation. The second part of this chapter presents the projected accuracy requirements of the air-data states. The accuracy requirements are derived in two perspectives, constraints from the air-breathing propulsion and the vehicle acceleration limits. The accuracy requirements are gathered and concluded from various sources such as [Kan2, Hon1, Hat1] and several Space Shuttle documents. Also, the sensor selection issues are discussed. On the basis of functional characteristics of each applicable sensor candidate, sensor selection criteria are formed with the considerations from operational regimes, accuracy, and operation environment. The last part of this chapter discusses the sensor placement issues. The sensor installation criteria are motivated by the functional

characteristics of each sensor technology, shock structure and thermo/aerodynamics of the vehicle forebody, and the thermal loads.

Chapter 5 derives the necessary models for the AHSV dynamics, sensors, and simple environment models in the context of the AHSV air-data estimation. Two different models are presented to cover different flight regimes. First model contains wind effects and this model can be used to describe the vehicle motion during ramjet assisted flight (Mach 3 to 6). This model is derived and specialized to longitudinal motion from the 6 degree of freedom derivation of [Fro1]. Second model is based on the LVLH formulation of [Cha2] and the equations are manipulated to treat angle of attack as one of the state variables. The inertial and air-data sensors are modeled such that the models are readily implementable for the estimation. The sensor models are simplified from the references [Pru1, Hil3, Mil1,Mil2, Mil3]. A simple environment model is presented.

Chapter 6 is a large chapter that discusses the air-data estimation methodologies. This chapter begins with the theoretical background necessary to understand and to derive the properties of the AHSV air-data estimation algorithm. The fundamentals of the estimation theory are briefly stated and the Extended Kalman Filter is derived from the fundamental equations as a special case.

The second part presents the estimation problem formulation. The equations from the models of vehicle dynamics and sensors are specialized to form a set of equations that represent the air-data estimation problem. The next section explains the AHSV air-data estimation strategy. The estimator design procedure is discussed from the problem formulation to the final performance verification stage. Control system design process is presented. The control system design has been motivated by the estimator's dependence on control history. Therefore a functional control system is designed and the performances are shown.

The next section presents a method of visualizing propagation of the state conditional densities. In order to guess at an appropriate approximation of the state conditional densities, the state conditional densities are visualized by multiple simulations and statistical analysis. The histograms of the propagation and update processes are plotted and presented. The results concluded that the Extended Kalman Filter should be a good approximation for this problem.

The last section demonstrates the Extended Kalman Filter development. The EKF design procedure is explained. A Statistical analysis (Monte-Carlo Simulation) is implemented and the necessary considerations are explained. The results from the statistical analysis are presented. The Gaussian assumption on probability density function of the estimation error is substantiated by the statistical analysis.

Chapter 7 provides a method to estimate the sensor precision requirements bounded by the estimator performance specifications. This chapter begins with the motivation for this analysis. An inequality constraint is derived from the EKF formulation. Later in this chapter, the solution strategy is demonstrated for several operational points and different sensor combinations.

Chapter 8 summarizes the thesis and discusses the conclusions. Also some recommendations for future research efforts are included.

Chapter 2

Research Approach

2.1 Problem Definition

The objective of this research is to understand and to develop the AHSV instrumentation and air-data estimation system. In particular, the research efforts have been focused on to the design and analysis methodologies of the AHSV air-data estimator with large emphasis on the air-data estimate accuracy improvement. The most important air-data state variables are the variables that depict air-relative attitude of the vehicle such as angle of attack. Throughout this thesis, several smaller pieces of problem are defined such that these problem definitions, solution strategies, and example demonstrations combined to layout the back bone of the design and analysis methodologies for the AHSV air-data system.

The measurement and data processing system is the nervous system of the vehicle where the information is sensed, processed, and exchanged between the important functional subsystems such as propulsion, thermal management, guidance and flight control. The instrumentation and information processing problem is critical to efficient and stable operation of AHSVs. For example, the engine control requires information on inlet, combustor, and nozzle flow parameters as well as vehicle motion (direct interdependence between propulsion and vehicle motion, Chapter 3) in order to execute

the feedback control law. Since the vehicle flight dynamics are highly nonlinear, unstable, and time varying, active control of vehicle motion is inevitable for both flight control and propulsion. Therefore, an accurate estimate of important states and parameters is absolutely necessary.

The AHSV state information can be obtained either by direct measurements and/or by processed measurements that are derived by numerical techniques such as nonlinear state estimation. Similarly instrumentation and information processing systems are needed by flight control, guidance, the structure thermal management, and various hypersonic experiments. In particular, the information on air-data states and propulsion parameters are considered as the most critical variables for the estimation.

The interaction among functional subsystems of AHSVs complicates the estimation problem formulation. The variables for the vehicle flight dynamics have direct inter-dependence with the propulsion state variables. In order to achieve greater estimation accuracies, it is desirable to treat all air-data sensitive elements of the AHSV. As a result, the problem formulation requires augmentation of all the interacting elements of interdependent functional blocks. The required information can be acquired through various sensors located around the vehicle combined with a priori knowledge or data about the systems prior to flight. It is a challenging task to provide methods to distribute and integrate these numerous information sources so as to insure a proper and efficient operation of the vehicle propulsion systems.

A part of this thesis research effort involves understanding of how each functional subsystem behaves during the hypersonic flight. For each subsystem, it is necessary to define what are the important states and how they affect the overall flight performance and stability. If these states require monitoring or control, then the accuracy and bandwidth requirements on these states must be defined. Also, design of sensors that can operate in the applicable extreme temperature environment is difficult. Therefore another part of this research involves selection of applicable sensors, and sensor placement. The measurement requirements and sensor issues lay out a foundation for the AHSV air-data estimation problem.

Once the air-data estimation problem is defined, another challenge is to find an appropriate estimation strategy. The problem is to determine what type of signal processing and/or estimation strategy would be most applicable for that particular

assignment. Because the AHSV problems contain nonlinear elements, the selection of an appropriate estimation algorithm is not trivial. Since a model based estimation strategy is considered to be the most appropriate strategy, the required models should be formed. The modeling problem is also a challenging problem since all the elements of hypersonic flight and air-breathing propulsion should be addressed without complicating the representing models. The measurement processes (including sensors) are needed to be modeled. After an estimation strategy is established, next issue is to develop algorithms which provide a compact and efficient source of processed information derived from measured data set. The algorithms and the selected set of sensors must provide estimates of important variables within the required accuracy and bandwidth.

Once the air-data estimator is developed, some measure of its expected performance is needed. Since the problem involves stochastic response of the nonlinear dynamics, a statistical analysis is needed for the system performance verification. The algorithm implementation issues and the system practicality should be addressed. Due to the unique nature and complexity of the AHSV information processing system, demonstration of the information processing methodology and obtaining particular solutions would be a significant contribution to the development of AHSV technology.

The last problem of this thesis is the assessment of the air-data sensor precision requirements. For this given air-data estimation problem, the problem of finding an upper bound of the sensor performance requirements can be defined This problem would be a significant interest to the hypersonic air-data sensor designers. The AHSV air-data sensors are still under development. Most of the proposed sensor technologies are either laboratory techniques or conceptual stage. By obtaining a method to bound an upper bound of the sensor performance and providing a demonstrated solution, the results may be used as an accuracy goal for the future sensor development.

2.2 Solution Strategy

In an attempt to solve the problem defined in section 2.1, a solution strategy is laid out and will be discussed in this section. The solution strategy for the AHSV instrumentation and air-data estimation can be briefly summarized as follows. The first phase of this research is in understanding of the AHSV system. The instrumentation and information processing requirements of each functional block are defined. Once the requirements are defined, the engineering analysis that is based on physically available hardware provides the basis for the problem formulation in the context of the air-data estimation. The second phase involves the air-data estimation problem formulation and the system modeling. Once the important states and parameters are selected, models of the interacting functional elements are created. These models include sensors, vehicle dynamics, and the environment. The third phase involves formulation of estimation algorithms. On the basis of the problem formulation and the related system models, a simulation based analysis is performed to provide a clue to the estimator design solution. The last phase addresses the performance verification and the numerical implementation issues along with some recommendations for the sensor precision requirements.

Phase I: By investigating the detailed characteristics of AHSV subsystems such as vehicle configurations, guidance and control requirements, detailed propulsion characteristics, and flight dynamics, the measurement and information flow requirements are defined. There are several previous investigations on flight dynamics and control, trajectory optimization, and propulsion in both theoretical and experimental forms. On the basis of these studies as applied to the selected vehicle configurations, the AHSV measurement requirements are defined with emphasis on air-data states. A candidate set of inertial, air-data, and propulsion sensor technologies that can span the AHSV flight envelope is selected on the basis of functional requirements and first principles of sensor operation. These sensors may utilize mechanical, pressure, and advanced optical measurement techniques. With the list of applicable sensors, the AHSV operational requirements, and the information flow structure, the basis for the problem formulation is formed.

Phase II: The model based estimation approach is the most applicable for AHSV air-data state estimation. The AHSV flight dynamics contain full of air-data information. The force components are direct function of thermo/aerodynamic parameters, angle of attack and velocity. Therefore, the model of AHSV dynamics can

boost the information on the air-data states assuming that a sufficiently accurate model can be obtained. Once the model based estimation strategies are considered, the models for vehicle dynamics, propulsion, environment, and sensors are formulated. The vehicle and propulsion models are developed based on the NASA Langley [Sha1] and Draper Lab data bases [Cha2]. The sensor model formulations are based on the first principles of operation and/or previous implementation results. Also the corresponding sensor noises and disturbances will be modeled and characterized. The review of existing data and conceptual preparation on wind information, and some of the propulsion coefficients lead to the necessary models.

The environment model, by definition the free stream parameters such as pressure, temperature, density, and wind velocity vector field, are incorporated within the vehicle flight dynamics. The propulsion and aero-thermodynamics describing the AHSV dynamics contain the parameters that are depend on the environment model parameters. Therefore, the models are needed to be updated by measurements and processed in order to implement the estimation strategy. This information should also be distributed for the engine and flight controller.

Once the measurement and data processing requirements are established, the estimation problem is formulated. A first task is to define the states to be estimated. With laid out models for sensors, sensor noises, vehicle dynamics, and environment, a model based estimator block diagram is constructed. Part of the problem is in dynamic state estimation form, while other parts are in the form of static filtering. Due to the vehicle dynamics and sensor characteristics the problem involves treating nonlinear, time varying, unstable, and nonlinear observation processes.

Phase III: In order to solve the estimation problem defined in phase II, nonlinear filtering theory is reviewed and applicable filtering strategies are composed. In order to acquire an approximate solution for the AHSV air-data estimator, it is desirable to know the characteristics of the state conditional densities. A visualization tool based on a statistical analysis is recommended. Initially the Extended Kalman filter (EKF) is considered since it is the easiest to implement. However, the implementation of EKF requires certain assumptions on its state conditional densities and the AHSV air-data estimation problem should be analyzed to verify its applicability. The visualization tool would provide some evidences for the applicability of EKF. If EKF fails as the solution

to the estimation problem, the estimator design can be approached in more fundamental methods.

The problem posed by the AHSV air-data estimation requires a control system design. When looking into the evolution of the state conditional densities for the AHSV air-data estimation problem, the governing equation depends on specific control history, measurement, initial conditions, and operation boundary conditions. Consequently, the solutions will depend on a specific controller design.

Throughout the estimator design phase, a statistical analysis tool such as the Monte-Carlo simulation may be used to characterize the problem. Because of the fact that the estimation problem is a nonlinear problem, an achieved solution will depend on a specific design and operating condition. The obtained results will be used to reassess the air-data sensor precision requirements.

Phase IV: Once a reasonable estimation strategy is selected and an appropriate estimator is designed, full scale simulation is needed to be performed with both the plant, which consists of high fidelity models of vehicle dynamics, sensors, and disturbances, and the estimator, which is designed based on simpler models with uncertainties in model coefficients. Through Monte-Carlo analysis, the performance of the designed estimator can be estimated. Engineering analysis is then used to address issues regarding numerical implementation, and estimator characteristics.

With the estimation results, the issue of air-data sensor precision requirements can be addressed. Also, if possible, an upper bound of the sensor precision requirements should be derived. With these results, some recommendations for the sensor accuracy requirements can be made.

Chapter 3

AHSV System Overview

3.1 Air-Breathing Hypersonic Flight

3.1.1 Air-Breathing Corridor and Flight Trajectory

The air-breathing ascent trajectory is determined by air-breathing combustion requirements and thermal load considerations in addition to guidance requirements. For a given speed, air-breathing engines require bounded ranges of atmospheric pressure, density and temperature for proper combustion, thus the requirements set a particular Mach number - altitude envelope called the air-breathing corridor. More detailed trajectory optimization results based on these requirements can be found in [Hat2]. The trajectory restrictions, along with maneuver restrictions and bounds of allowable environmental conditions, set part of the requirements for sensor selection and operation. Thus these bounds or results can be used to obtain the particular operating conditions for AHSVs. Therefore, the results will be applied as nominal conditions throughout the thesis analysis. Since more detailed work can be found in [Hat3, Kan2, Lew1], the requirements are briefly stated, then more importantly, the resulting operating conditions will be used to provide nominal conditions for the models within the estimators during numerical simulations.

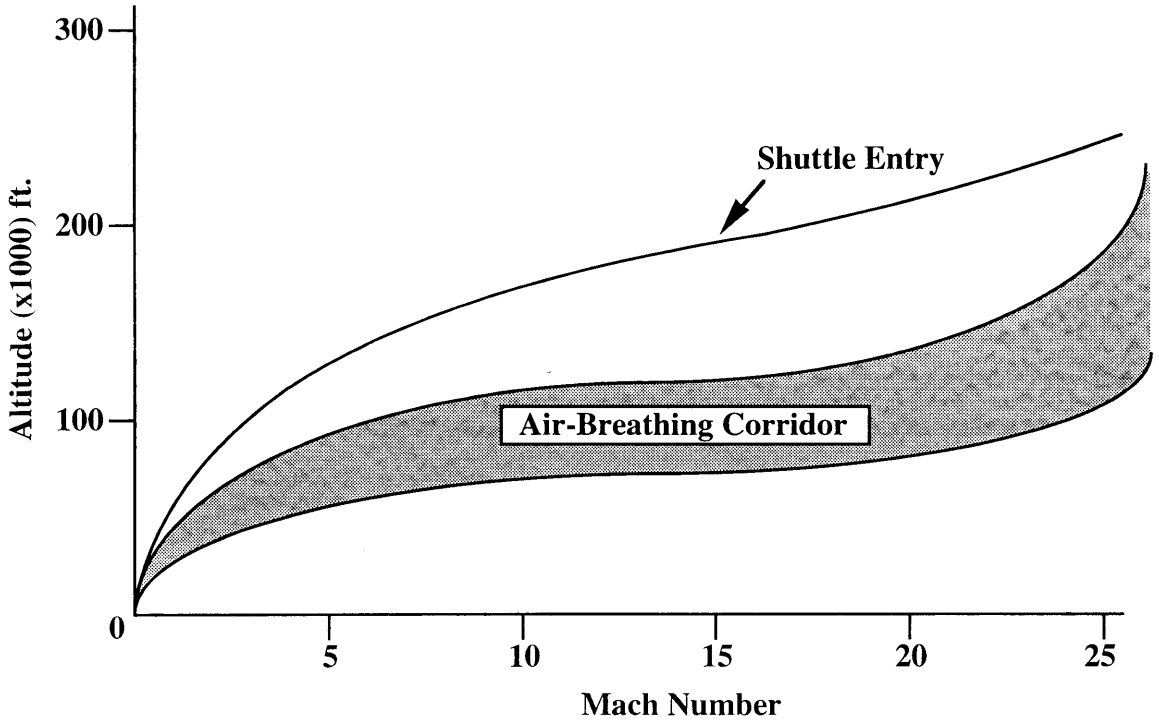

Figure 3-1 NASP Trajectory Corridor

The combustion requirements can be briefly summarized as follows. The combustor inlet temperature must be low enough to permit addition of heat to the flow with an increase in enthalpy. At sufficiently high temperature, added fuel will dissociate, and the dissociation will absorb energy and result in a net loss of heat from the flow. On the other hand, the combustor inlet temperature must be high enough to create spontaneous combustion [Lew1]. Combustor inlet pressure must be as high as the structure can withstand to maximize combustion efficiency; however, if inlet temperature is low, then the inlet pressure must be kept below the cutoff pressure where secondary reactions start [Lew1]. Therefore, inlet pressure and temperature should be controlled within a narrow range. Detailed numerical data on combustion requirements can be found in [Lew1, Cha2, Kan2]. Typical dynamic pressure bounds of 500 to 2000psf are expected during most of the hypersonic flight phase and up to a 3000°F peak temperature is expected on the vehicle structure. The constraints defined by combustion and structural loads will dictate a flight envelope similar to the air-breathing corridor shown

in Figure 3-1. Most of the hypersonic flight will occur within the 100k to 200k ft altitude range. Total air-breathing flight time will be about 2000 seconds [Hat1].

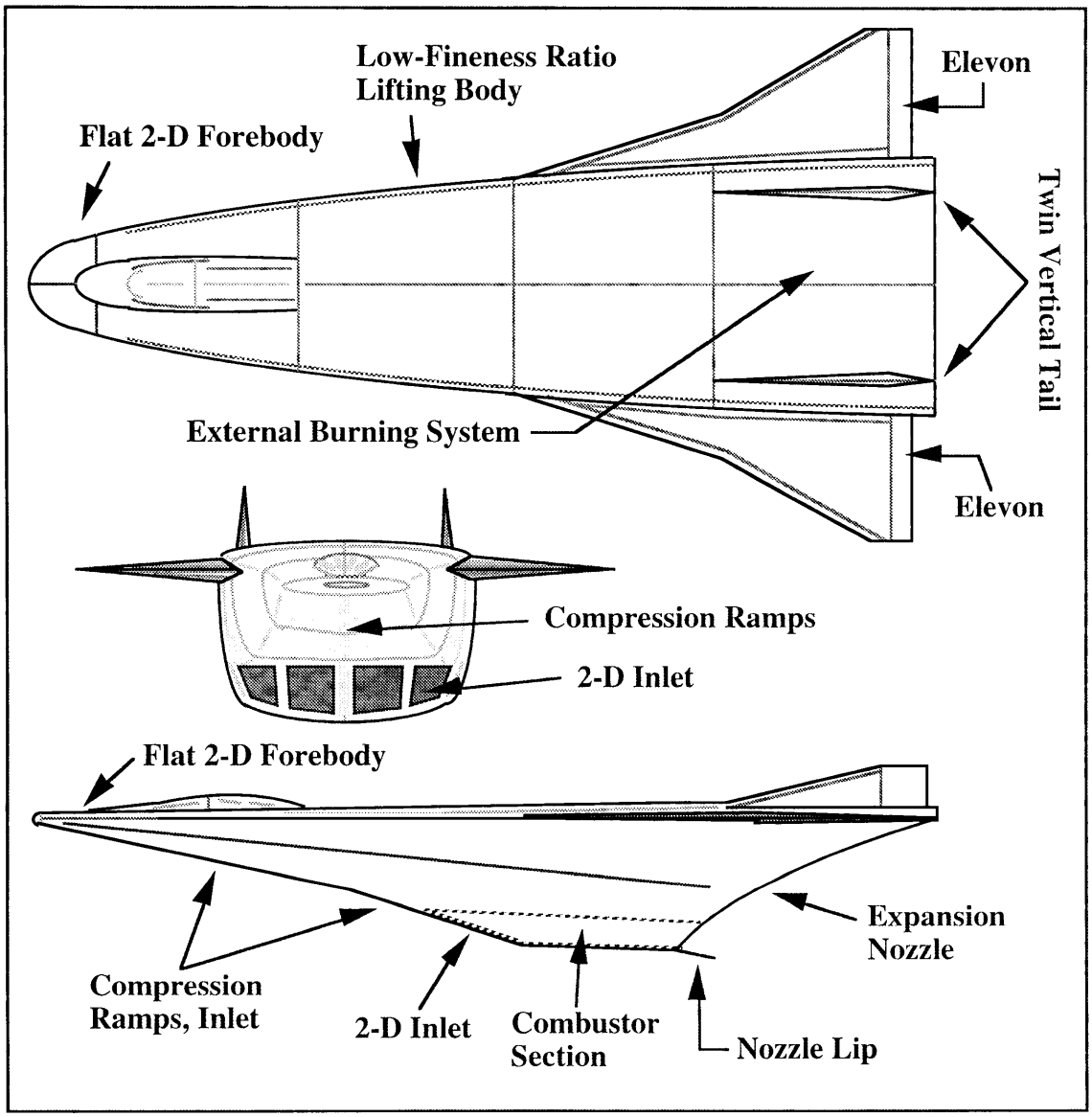

Figure 3-2 AHSV Configurations

3.1.2 AHSV Configuration

The proposed AHSV will have low fineness ratio lifting body configuration as shown in Figure 3-2 [Wal1, Sch1]. A total vehicle length and weight of 150 ft and 250,000 LB are expected [Sch1]. The vehicle will have flat 2-D forebody which acts as a

series of inlet compression ramps. The free stream atmosphere will be compressed through oblique shock waves formed by the inlet ramps and the compressed air will feed into the combustor located under the vehicle. A stepped inlet - combustor boundary will minimize the interactions between the inlet and the combustor. Either liquid or slush hydrogen fuel will be drawn from the fuel tank, heated to a gaseous form, while cooling the air frame, and then injected into the combustor [Wal1]. If the flow inside the combustor is decelerated to subsonic speed by forming a normal shock wave, then the engine will be operating in ramjet mode. Otherwise, the engine will be operating in Scramjet mode where combustion occurs in supersonic flow. The energized gases will expand over the aft-body, which will function as part of the nozzle. Because the vehicle's underside functions as part of the air-breathing engine, aerodynamics and vehicle motion will be highly coupled to the performance and stability of combustion. Some literature suggests that an external burning system would also be employed to augment the main propulsion system during the low supersonic flight regime. The controllable aerodynamic surfaces are elevons, twin vertical tails, and nozzle lip. Part of the under surfaces such as inlet ramps, nozzle surface, and nozzle lip may be actively moved to control the combustion process and thrust vectoring. The AHSV configuration is not yet fixed and there is still on-going research to improve the overall performance in both the supersonic and hypersonic flight phases [Wal1].

3.2 Status of AHSV Technology

Hypersonic flight vehicle programs started as early as the 1950's. During the 50's and 60's, an enormous amount of hypersonic research was pursued under several programs such as ballistic missiles, the X-15 and X-20. Most significant work was in ramjet propelled intercontinental missiles, X-series vehicles, and space plane concepts [Nas1, Neu1]. The ideas of single-stage-to-orbit, horizontal take-off, and Scramjet air-breathing propulsion were introduced around this era. Unfortunately, these programs all died before the 70's except for limited research on 3-D Scramjet designs and the associated vehicle configuration studies within NASA's Langley research center. Around 1984, DARPA started a classified hypersonic research program called Copper Canyon. In early 1986, President Reagan announced in his State of the Union address that hypersonic research would be pursued under the NASP program. He approved a program aimed at making a decision to build a NASP prototype by 1990, with first flight planned

by 1993, and achievement of orbit by 1995. Right after the President's approval, several airframe and engine contractors were selected and the NASP Joint Program Office was formed with NASA, the Air Force, the Navy, DARPA, and SDIO as participating agencies. However, the NASP program suffered from severe budget restrictions which delayed technology maturation necessary to build a first prototype. When the contractors were down selected and teamed, the National Program Office began operations in mid 1990 on an interim basis [Wal1]. By mid 1993, the NASP program was redefined and redirected to accomplishment of the Hypersonic Flight Test Experiment (Hyflite) due to shrinking budgets and concerns regarding the status of several technologies needed to construct a flight test demonstrator, X-30 [Avi1]. The program now was aimed at accomplishing several rocket launched unmanned hypersonic flight experiments to study boundary layer transition, Scramjet performance, and vehicle stability and control but has since been canceled.

Since the 50's, ramjet technology has been demonstrated for applications in long range ballistic missiles [Nas1]. Limited Scramjet performance has been demonstrated and a broad data base developed up to Mach 7. SR-71 inlet control and Concord two dimensional variable ramp inlets represent bases for the supersonic cruise inlet design. Limited research has been done on Scramjet inlet design. Performance potential has been demonstrated for fixed geometry supersonic inlets for the Mach 3 to 10. A several-stepped combustor upper surface is considered for minimizing inlet combustor interactions. Complex Computational Fluid Dynamics (CFD) codes are available to simulate flow around the high Mach vehicles including after body flows. Much work was done toward development of a slush hydrogen fuel system. The most significant advancement toward the completion of the AHSV technology was in the area of materials and structures[Wal1]. Due to the emphasis carried on to the development of high temperature materials from early stage of the NASP program, a large portion of the funding was diverted into the development of exotic materials such as carbon-carbon, metal matrix composite, silicon-carbide, etc., along with extensive efforts from the contractors. The moving elevon components and several leading edges were prototyped and developed to demonstrate the manufacturing capability. Also these parts were put on to arc-jet heater for the testing of thermal integrity[Wal1].

In the technical area of instrumentation and control for the NASP, or AHSVs in general, fewer efforts were put on by the contractors, mainly due to lack of significant funding from the program. Most of the instrumentation and control research were done

by the Universities or Internal Research and Development (IR&D) programs of aerospace related companies. The research efforts on optimizing the AHSV design configurations were carried out since early eighties by Hattis with emphasis on control and guidance issues[Hat5, Hat6]. In the area of AHSV flight control and guidance, significant efforts and results were accomplished by Chamitoff [Cha2], McRuer [McR1], and Schmidt [Sch1]. McRuer provided insight into the behavior of AHSV dynamics through analysis. Schmidt analyzed the dynamics via a linearization approach, and developed the controller based on the linear theory [Sch1, Sch3, Sch4]. Chamitoff advanced the AHSV study and development in two interesting areas [Cha2]. First, he developed a complex computer based model of the vehicle which is the most realistic vehicle model known up to date (unclassified), and developed a control methodology based on the A-star search which takes account of full integrity of the nonlinear model.

The AHSV instrumentation issues were investigated by two contractors, McDonnell-Douglas and Honeywell. The McDonnell-Douglas researchers investigated the feasibility of the SEADS system on the AHSVs. The Honeywell researchers performed a survey of applicable sensing technologies [Hon1]. Miles, working in conjunction with the sub-contractors, analyzed the feasibility of laser based optical sensors on the AHSVs [Mil1]. Most of the previous work on instrumentation was no more than the feasibility study of old/new sensing technologies on the AHSV platform. None of the previous work addresses the problem of the estimation of air-data states in conjunction with the sensor development. Therefore, it was highly desirable to envision and establish the estimation problem for the AHSVs as part of the AHSV development. Since 1990, Kang and Hattis pursued the development of estimation strategies for the AHSVs, and part of the results are contained in this thesis.

3.3 System Interactions

Even from the beginning of manned flight, the superb engineers and pilots of that time, the Wright brothers, experienced the dilemma of solving a problem which involved closed loop interactions.

It is hard to find even a point from which to start, for nothing about a propeller, or the medium in which it acts, stands still for a moment. The

thrust depends upon the speed and the angle at which the blade strikes the air; the angle at which the blade strikes the air depends upon the speed at which the propeller is turning, the speed the machine is traveling forward, and the speed at which the air is slipping backward; the slip of the air backward depends upon the thrust exerted by the propeller and the amount of air acted upon. When any of these changes, it changes all the rest, as they are all interdependent upon another. But these are only a few of the factors that must be considered...

Orville Wright
Spring of 1903 [And1]

Now, there exists a closed form solution for the propeller design problem of the Wright brothers. Similar to the Wright brothers' dilemma, AHSV design requires investigation of a system which has highly interactive elements. For example, there are strong interactions between vehicle motion and propulsion, between structural deformation and propulsion, and between propulsion and aerodynamics. Even though this research is focused in instrumentation and data processing, it is extremely important to understand the nature of the AHSV system because it provides sensing requirements and forms the basis for the problem formulation. The next few subsections are devoted to discussion of important interactions associated with flight of AHSVs.

3.3.1 Attitude - Propulsion Interactions

In general, the vehicle motion and propulsion have strongly coupled interactions. Most importantly the engine performance is interdependent on angle of attack, angle of side slip and flight Mach number. Since the vehicle forebody functions as the compression inlet, if angle of attack or side slip angle changes then the propulsion efficiency changes [Nas1, Lew1, Kan2, Cha2]. If this inlet conditions change, then the thermo/aerodynamics of the flow inside combustor change. Consequently, the thrust magnitude, flow expansion in nozzle, and thrust direction change when combustor states change. These changes in thrust then influence the attitude dynamics.

The flight trajectory dependent parameters such as altitude and flight Mach number dictate the engine design and, if possible, the vehicle inlet and nozzle geometry.

Because the vehicle geometry can not vary dramatically, one has to design for a particular nominal design [Cha2]. These nominal conditions for the engine operation will set the degree of interaction among attitude and propulsion which change along the flight trajectory. The functional dependence of these parameters is discussed in Chapter 5, vehicle modeling.

3.3.2 Aerodynamics - Propulsion Interactions

Because the vehicle under surface is the air-breathing engine and the vehicle is configured as a lifting-body, aerodynamics and propulsion are strongly interdependent. The under-surface pressure distributions, which include inlet and nozzle surface pressure, dictate the propulsion conditions as well as lift, drag, and moments. For example, if the thrust is changed by adding more fuel and increased mass flow, then the pressure distribution along the inlet and nozzle changes and alter the total lift and drag of the vehicle. Such problems could be most severe at the nozzle because the flow expansion and attachment at the nozzle are a complex function of the flow exiting the combustor and the vehicle external atmospheric conditions. The inlet pressure and nozzle flow condition will dictate the net pitching moment applied to the vehicle. The vehicle attitude and aero/thermodynamics of flow within the inlet, combustor, and nozzle will set conditions for the boundary layer transition point and thickness [Lew1]. Conversely, if particular lift and drag values are needed to follow a particular guidance trajectory, the desired angle of attack not only changes lift and drag but changes net thrust and pitching moment.

3.3.3 Structure - Dynamics - Propulsion Interactions

Structural interaction with vehicle dynamics and propulsion is considered critical in the performance and stability of AHSVs. These interactions are highly convoluted in the sense that a phenomenon can not be analyzed without considering structure, dynamics, and propulsion issues together. The structural interactions can occur in both static bending as well as forced and free vibration. The static deflections of AHSVs are caused by non-uniform pressure distributions along the body surfaces as well as thermal deflections. For example, the SR-71 has significant in-flight aerodynamic and thermal distortions as shown in Figure 3-3 [Neu1]. Similarly for the hot structure of AHSVs,

static deflections can alter the geometry of inlet and nozzle and create significant alteration in combustion conditions. Moreover, if the geometry and combustion condition change, the vehicle dynamics change as well.

AHSV structural vibration can be caused by the vehicle's inherent flexibility which is forced by either aerodynamics, vehicle motion, or propulsion disturbances. The thermal effect can also cause the vibration frequency and damping to change. If the energy associated with these bending modes is small and the frequencies are well above vehicle rigid body modes, then the vibrational modes can be ignored. Otherwise, the structural vibration can interfere with vehicle dynamics. The worst scenario is when bending modes modulate the angle of attack and consequently results in thrust modulation. If the vehicle thrust is modulated with bending frequency, it is possible to excite the bending modes further and/or affect the vehicle flight dynamics. These phenomena are closely interactive and create serious flight control, engine control, and instrumentation problems.

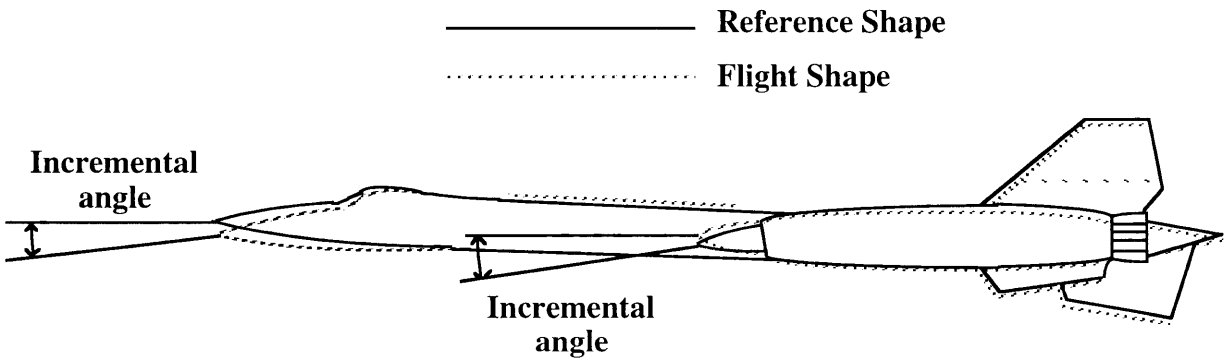

In-Flight Aerodynamics and Thermal Distortion of the YF-12 Aeroplane
Figure 3-3

3.3.4 Instrumentation & Estimation Problems From Interactions

The overall configurations and interactions described above pose serious problems for systems engineers. For the air-data instrumentation, there are problems of sensor placement and alignment. The structural motion, either dynamic or thermal bending related, can contribute to the errors in the sensor alignment. The instrumentation problem includes the uncolocated sensor-actuator problem for the case of measuring angle of attack with the sensors installed at the nose while the vehicle is vibrating at low

frequency structural modes. For the problem of designing control and estimation algorithms for AHSVs, the interactions of the vehicle dynamics and propulsion cause the plant (models) dynamics for the control and estimation to be a highly nonlinear, time varying, and unstable plant. Moreover, the complexity or dimension of the problem increases if rigid body dynamics, structural dynamics, aerodynamics, and propulsion have to be treated simultaneously. In order to control vehicle motion, the interactions from propulsion and aerodynamics must be properly treated.

Chapter 4

AHSV AIR-DATA INSTRUMENTATION

4.1 History of Hypersonic Instrumentation

Only a few hypersonic flight vehicles, from which to draw hypersonic instrumentation technology, currently exist. Among these, the X-15 and the Space Shuttle Orbiter are the most significant. Although these vehicles do not employ air-breathing engines and have different flight trajectories, their instrumentation techniques and requirements can provide insight into the AHSV technology requirements. The instrumentation techniques of these vehicles represent the state of the art in flight-proven technology. [Kan2, Neu1] provide detailed descriptions of the available hypersonic air-data sensing technology, listing their requirements and performances. Also, the references [Kan2, Hat4, Hon1] describe the applicable air-breathing hypersonic air-data sensing techniques and requirements. Therefore, the sensing techniques are only briefly summarized here.

X-15: The X-15 was a rocket-propelled hypersonic research aircraft. It had typical missions of rocket powered boost from 40kft to about 200kft with a ballistic coast to a maximum height of 350kft while traveling at flight Mach numbers up to 7.

Reentry occurred at a high angle of attack to dissipate energy while maintaining the skin temperature below the 1200°F. The hypersonic flight segment typically lasted 10 to 15 minutes [Web1].

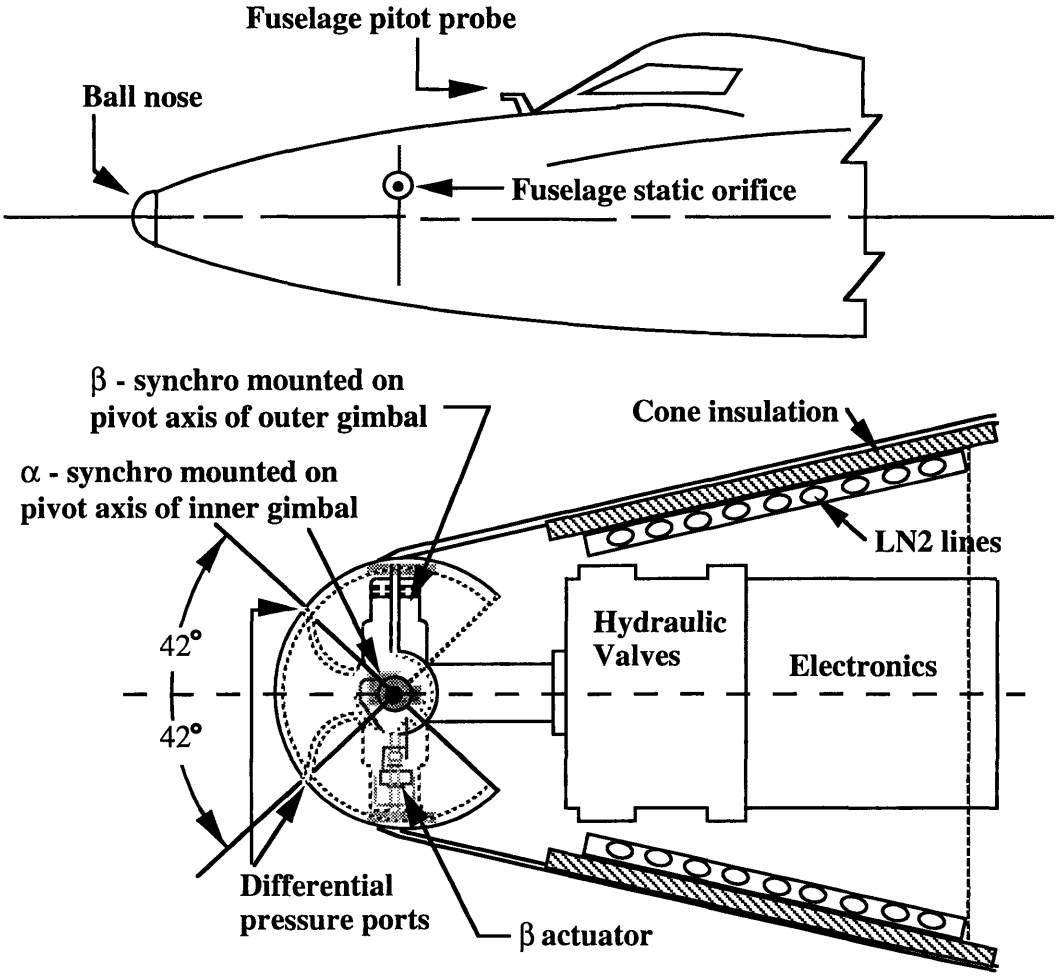

Figure 4-1 Schematic Drawing of the X-15 Ball Nose Sensor

For flight Mach numbers less than 3, the X-15 used a conventional Pitot static nose boom with angle of attack and angle of side slip flow vanes. Such a method would not withstand high thermal loads at higher Mach numbers, so a ball nose sensor was implemented [Web1, Wol1]. As shown in Figure 4-1, the sphere was housed in the end of the conic nose. It was rotated by a hydraulic actuator to face the stream-wise direction by nulling the differential pressure between vertical and lateral pressure sensor pairs. The alignment angles of the sphere with respect to the aircraft reference axis indicated the angles of attack and of side slip.

The rear portion of the sphere contained the mechanical and electrical components. These components, along with the sphere, were cooled by vaporized liquid nitrogen. Thus, the X-15 structure and associated components behind stagnation points were capable of withstanding temperature of up to approximately 1200°F (922°K). The static pressure sensor was flush mounted on the side of the conic nose. Besides air-data sensors, the X-15 had the capability to accommodate up to 1000 sensors, including those for measuring skin temperature, pressure, structural strain, etc. [Neu1]. The tabulated sensing requirements and sensor performance are listed in [Kan2].

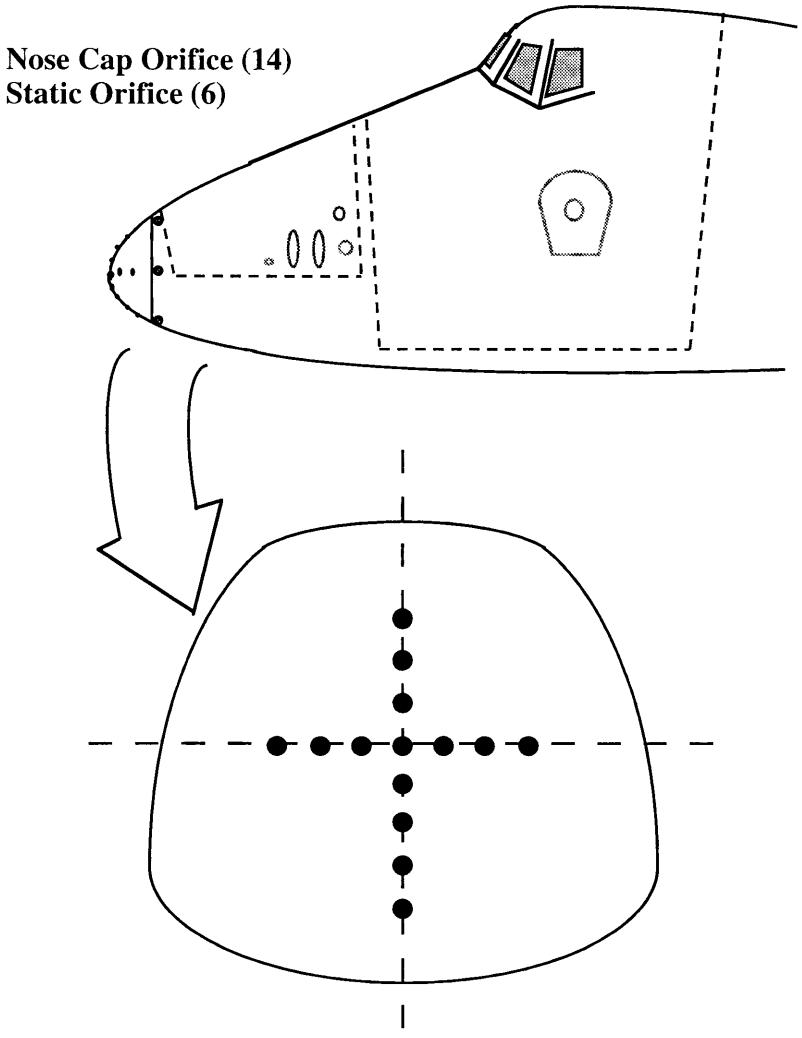

Figure 4-2 SEADS Orifice Configuration

Space Shuttle: The reentry part of Space Shuttle flight envelope, as shown in Figure 3-1, has a much higher flight altitude for a given flight Mach number than that

AHSV would experience during its air-breathing ascent. The AHSV reentry trajectory would be similar that of the Space Shuttle. Therefore, the Shuttle entry flight environment can be used as the reference for AHSV's. The main purpose of the reentry flight maneuver is to decrease flight kinetic energy by using high angle of attack (higher than what an AHSV would experience during its ascent), high drag maneuvers. By gliding through a high altitude envelope, the thermal load on the structure is dissipated by radiation cooling, without significant convection, while obtaining sufficient deceleration. The flight envelope spans the Mach numbers from 27 to touch down, the angle of attack from -5° to 45°, and the peak stagnation temperature up to about 2000°F to 2300°F (1366°K to 1532°K) [Hil3].

The Shuttle Entry Air Data System (SEADS), designed for hypersonic flight experimentation, is currently mounted on the Shuttle Columbia since the STS 61-C mission and is used to collect atmospheric research data during entry operations [Hat4]. As shown in Figure 4-2, the SEADS employs a cruciform array of 14 flush mounted pressure transducers on the nose cap as well as 6 static orifices located aft of the nose cap. The SEADS uses dual pressure transducers in each of 14 pressure ports to collect data below 1 psia and below 20 psia respectively, with resulting measurement error discontinuities at transition from one set of transducers to the other [Hat4].

The nose cap heating rates can reach 50 W/cm^2 [Hat4]. The nose of the Shuttle Orbiter functions as both a Pitot-static probe and a flow direction sensor by implementing numerical pressure sensor data processing techniques [Hil2, Pru1]. A computational technique, which includes calibration parameters derived from wind tunnel data, is used to extract air-data parameters from the pressure field measurements without a rotating ball nose. A rotating ball like the one used on the X-15 would have an operational Mach limit too low for the Shuttle. The tabulated sensing requirements and realized sensor performances were detailed in [Kan2].

Besides the X-15 and the Shuttle sensors, several other AHSV applicable sensor technologies exist. Several temperature and strain measurement techniques applicable to both hot and cold structure hypersonic vehicles, were developed for the X-15, the SR-71, the Shuttle, and the X-20A programs [Neu1]. However, the sensing techniques for other necessary measurements such as heat flux, skin friction, and boundary layer transitions only have limited performance [Neu1]. A UV based sensor was proposed for the X-20A in the early 60's. The UV densitometer was based on crossing a transmitter UV beam with a receiver beam. The scattered UV beam is sensed and processed [Neu1]. Similarly,

AVCO proposed an electron beam device for ballistic vehicles in the late 60's. The electron beam exits the vehicle surface and interacts with the flow around the surface. Then the scattered UV light is picked up by photo multipliers. The exit angle of the electron beam is controlled by a magnet located near the exit window [Neu1].

There are other more recent reports on laboratory tested optical air-data sensors with AHSV applicability based on Rayleigh scattering, Raman spectroscopy, laser Doppler shift, and laser induced florescence [Mil1, Mil2, Mil3, Mil4]. These sensors show certain advantages due to their non-intrusive sensing methods although there exist several shortcomings such as unproved resolution, unknown sensor-environment interactions, and altitude limitations for some classes of sensors. A detailed description of these optical sensors can be found in Chapter 5, the Sensor Modeling section.

4.2 Accuracy Requirements For State Parameters

The required measurement accuracies of air-data state and propulsion related parameters are derived from the unique functional requirements within the context of the operational AHSV state estimation problem[Kan2, Hat2]. Air-breathing hypersonic vehicles have highly coupled propulsion, aerodynamics, and flight dynamics, and each of these sub-systems dictates accessibility requirements of relevant physical variables. These requirements provide the foundation for the estimation and control problems of AHSVs.

The performance uncertainties and operational requirements of the AHSVs are defined based on the analysis of operational AHSV flight dynamics and propulsion. The parameters needed for feedback control and estimation systems are selected on the basis of need for propulsion efficiency and stability. Thus, the key questions include the following: what parameters are needed to provide feedback to the controller?, what accuracy is required for particular piece of state information, and how fast should the information be updated?

Accuracy requirements for AHSV air-data states were derived in [Kan2, Hat2, Hat3] from trajectory optimization and performance sensitivity studies including consideration of both engine sensitivity analysis and vehicle configuration. The requirements impose implicit accuracy demands on the vehicle models, the atmosphere

models, and the associated parameters. These specifications, in turn, ensure proper operation of the AHSV. For example, the AHSV configuration chosen for the Mach 10 to 15 flight exhibit extreme sensitivity respect to angle of attack as shown in Figure 4-3. For one degree angle of attack perturbation around the nominal equilibrium condition, the normal component of the vehicle acceleration can vary from 5 to 10 m/s^2 (half to one g). The sensitivity increases as the flight Mach number increases. If the angle of attack feedback is needed by the flight controller, the maximum allowable angle of attack perturbation should be much better than about one degree. For one degree angle of attack regulation, the 0.1 degree angle of attack measurement accuracy requirement is not an unrealistic figure.

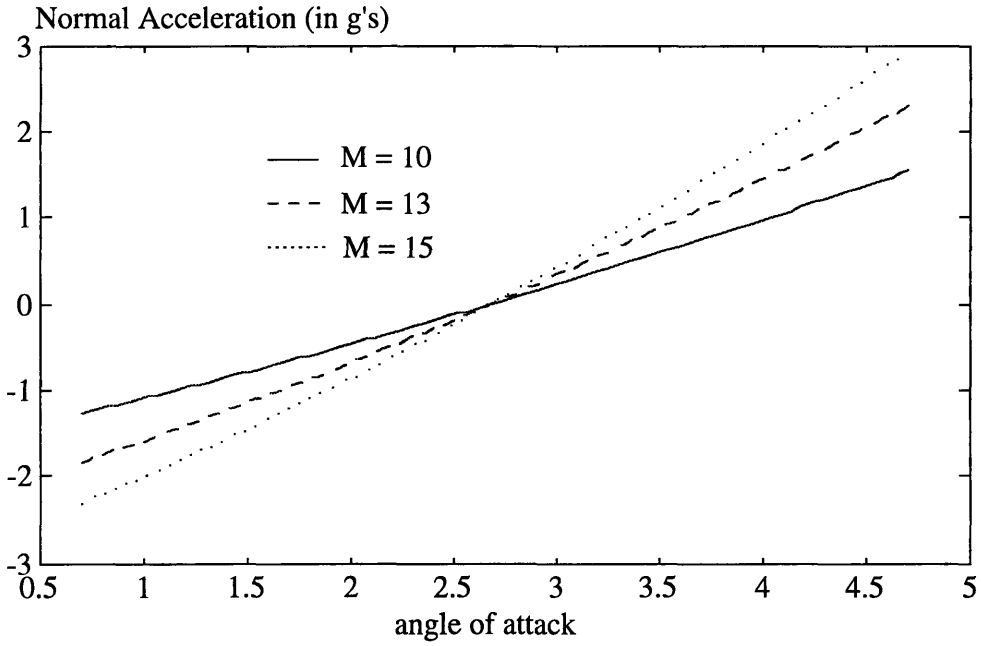

Figure 4-3 Normal Acceleration Vs Angle of Attack & Mach numbers

A brief summary of the requirements is in Table 4-1 below [Kan2, Hat3]. Due to the stringent accuracy requirements, precise modeling of the flight environment and the vehicle dynamics is imperative to the estimator design. The most stringent requirements are imposed on the flow direction parameters such as angle of attack and side slip angle. According to [Hat2], about extra 5% fuel consumption will occur if angle of attack is changed by one degree from the design value. However, 0.1 degree accuracy requirements in angle of attack and side slip measurements are difficult to meet with the currently available air-data sensors. An engine sensitivity analysis [Hat2] notes that the free stream conditions such as temperature, density and pressure will dictate the air-breathing engine's performance.

Table 4-1 Air-Data Requirements

	States	Required Accuracy	Measurement Range
α	angle of attack	0.1 deg.	-5° - +30°
β	side slip angle	0.1 deg.	$\pm$ 5°
Q	dynamic pressure	5%	0 - 2000 psf
ρ_∞	free stream density	0.5%	0 - 0.0025 slug/cu-ft
T_∞	free stream temperature	0.5%	360° - 560° R
V_a	air relative velocity	0.5%	0 - 28,000 fps
ρ_e	engine inlet density	0.5%	0 - 0.0025 slug/cu ft
T_e	engine inlet temperature	0.5%	360° - 3500° R
V_e	engine inlet velocity	0.5%	0 - 3000 fps

4.3 Sensor Selection

The feasible inertial and air-data sensors for the AHSV application are selected based on their operational range, accuracy and the expected operational environment. A variety of air data measurement technologies exists in flight-proven, wind tunnel demonstrated, or conceptual forms. However, each measurement technique has specific envelope limitations, and none of these techniques individually meets the AHSV accuracy requirements. Furthermore, each technology has its unique disturbance susceptibilities and has different sources of measurement uncertainties. From the list of existing or conceptual hypersonic sensors, several workable concepts are selected so that, in the aggregate, they constitute a satisfactory sensor package. This section presents the selected sensor technologies along with a brief explanation of the selection criteria and justifications. More detailed information on the sensor mechanization and expected performance can be found in Chapter 5, the modeling section.

Inertial sensors: The AHSV inertial sensors would be similar to any other aircraft or spacecraft inertial sensors. Because of its close functional resemblance to the

Space Shuttle, the proposed AHSV avionics system is assumed to include the inertial sensors functionally similar to those on the Space Shuttle with the addition of Global Positioning System(GPS) receivers. An Inertial Measurement Unit(IMU) would include integrating rate gyros and accelerometers. They would provide both rotational and translational positions, velocity and acceleration data. Since the GPS can provide very accurate inertial position and translational velocity, it will be used to correct translational bias drifts. Interferometric GPS can be used to correct attitude drift and bias.

Air Data sensors: Although the inertial measurements can be used to provide computed air data parameters [Hon1], direct air data measurements are necessary; because, the atmospheric variations and disturbances contribute to greater air data uncertainties than the required accuracy. Both pressure and optical based air-data state measurement sensors were considered for the AHSV applications. The available pressure based sensor technologies include Pitot probes and arrayed, flush mounted pressure port sensors like the Shuttle Entry Air Data System (SEADS). The optical sensor technologies include Rayleigh scattering sensors, Laser Doppler Velocimetry (LDV) based on Mie scattering, Raman spectroscopy and Raman Doppler Velocimetry based on Coherent Anti-Stokes Raman Scattering (CARS), and Laser Induced Fluorescence (LIF).

Pitot probes cannot be operated above Mach 3 and may only be used for takeoff and landing phases because of the intrusive nature of the probe in the heavy thermal load hypersonic flow environment. Therefore, the Pitot probe technology is excluded from the candidate sensor array. The flush mounted pressure sensor class includes SEADS and engine inlet sensors. The SEADS has demonstrated its performance from reentry to landing. The flush-mounted pressure transducers are located aft of the vehicle nose shock wave. Therefore, they require a blunt nose shape for maximum sensitivity and very accurate vehicle/flow interaction models for maximum accuracy. Furthermore, the flush mounted sensing technologies such as SEADS are most accurate when used with post-flight calibration [Hil2]. The post flight calibration refines the numerical model of the hypersonic flow around the nose to achieve improvement in accuracy. Although the SEADS technology has not proven to independently achieve the required AHSV accuracy [Kan2], it is selected because of its wide operational Mach number envelope.

The flush-mounted pressure sensor technology is also considered for the engine inlet. The flush mounted pressure transducers would be placed under the first and second ramp of the engine inlet (vehicle under-surface) to measure engine inlet flow states. These

propulsion sensors can determine free stream air-data states with proper modeling of the overall inlet aerodynamics. The sensing strategy is similar to the SEADS, requiring extensive modeling of the vehicle/flow interactions (i.e. aerodynamics and aero-thermodynamics). Flush mounted engine inlet pressure sensor technology is also included in the AHSV candidate sensor set because it can operate over a wide range of Mach numbers.

Laser Doppler Velocimetry (LDV) and Raman scattering techniques are not selected because: i) their operating range is limited to low supersonic speeds; ii) they provide only a limited number of air data parameters; and iii) they have poor accuracy. The accuracy of the LDV depends on the atmospheric particle abundance, particle size uniformity, scattering properties, and interaction of the particles with flow disturbances. Though the laser velocimetry techniques have proven their capability in supersonic flight vehicles, they have significant altitude limitations. At high altitude, where most of AHSV hypersonic flight would occur, the concentration of appropriately sized particles is very low and these sensing techniques will be useless [Hat4]. Also, the coherent Raman spectrometer technique is ruled out because of its poor accuracy. Furthermore, its accuracy decreases in hot regions away from surfaces.

The Rayleigh scattering and Laser induced fluorescence (LIF) techniques are selected for the AHSV sensor set as the most promising optical sensor technology. The LIF technique has been successfully applied to hypersonic flow measurements in a variety of ground-based test facilities [Mil3, Mil4]. The LIF technique uses oxygen molecules as a tagging and tracing agent. Therefore, it has a wide operation envelope. The laboratory results suggest that the technique can provide adequate measurement accuracy. However, the measurement technique has several problems related to the flow and tracing agent interactions, and which need to be resolved prior to flight application. The Rayleigh scattered signal is stronger than that of Raman scattering methods, but it is weaker than that of LIF. If a pulsed laser beam is used with well-designed molecular filters, the Rayleigh scattering measurement accuracy can be improved to an acceptable level for AHSV applications. For all of the optical sensing techniques, the accuracy of flow angle measurements, such as angle of attack and side slip angle, depends on the alignment errors, the angular resolution of the optical devices, and disturbances in the tracing agents.

To summarize, the selected sensor technologies include SEADS-like flush mounted pressure sensing system, flush mounted inlet sensors, IMU and GPS inertial sensors,

Rayleigh scattering sensors, and LIF sensors. The individual sensor operation envelopes vs. flight speed are shown in Figure 4-4. The corresponding altitude envelope can be found in Figure 3-1.

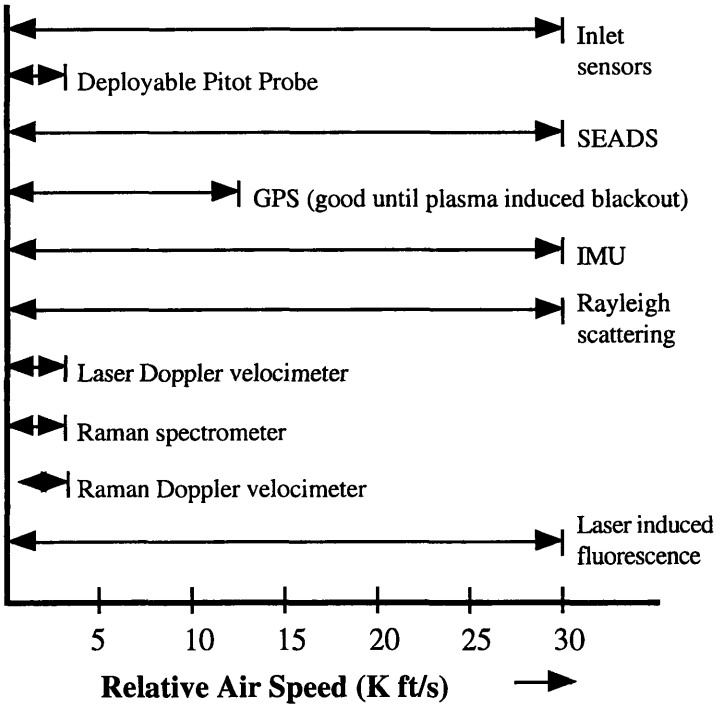

Figure 4-4 Useful Sensor Range[Hat4]

4.4 Air-Data Sensor Placement

The selected air-data sensor placement strategy is considered for a typical AHSV configuration as described in Chapter 3. The inertial sensor placement is assumed to be similar to that in the Space Shuttle and further discussion is omitted. The placement of sensors involves trade-off between maximizing sensitivity and minimizing disturbance effects while remaining within constraints imposed by thermal loads on the transducers. The hypersonic environment and the flow field around the forebody can not be determined precisely with the currently available data. Therefore, the exact location of the transducers is to be determined after extensive testing or analysis of the flow/vehicle interactions along with thermal and bending loads imposed on the structure.

In order to implement the SEADS like pressure based sensors, the curvature and the pressure distribution of the nose must be obtained by extensive wind tunnel and/or in-flight testing. The maximum sensitivity occurs at the blunt tip of the nose, but the thermal loads are also maximized at that location. Furthermore, at the tip of the nose, the flow deformation due to the vehicle body displacement is at a minimum. Active cooling is necessary to implement the flush mounted transducers. The static pressure sensors are placed on both sides of the vehicle where the surface is normal to the velocity axis, assuming a zero side slip condition. Example locations of the flush mounted air-data sensors are shown in Figure 4-5.

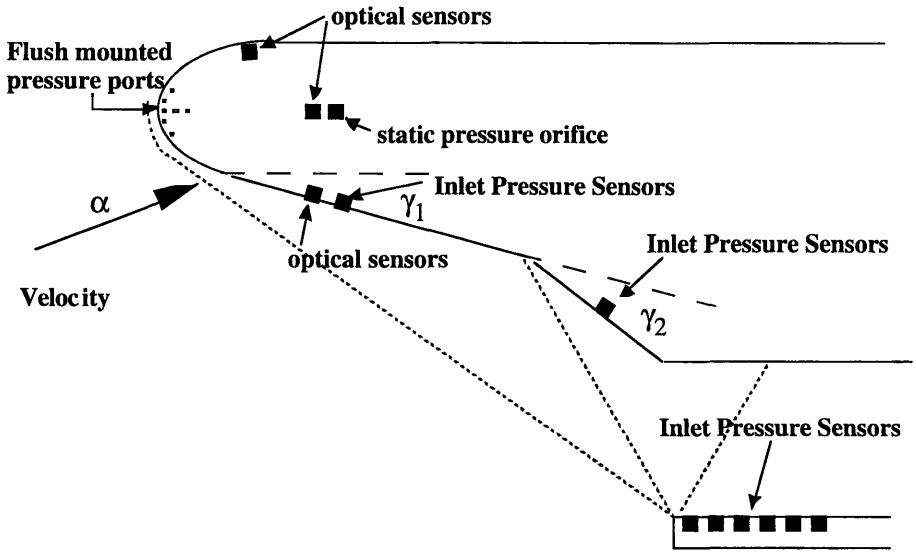

Figure 4-5 Air-Data Sensor Placement

The Rayleigh scattering and LIF optical sensors require precise component alignment, because the flow angle measurement accuracy depends directly on the alignment error. The density and temperature measurements do not require stringent sensor alignment, but a focusing capability of the optical devices is needed to pin-point the sample volume at the desired locations. To resolve the three velocity vector components with maximum sensitivity, three sensor optics are needed in nearly orthogonal axes. Two optical module configurations, each with three pairs of laser sheets/spots that are projected into the flow with single receiver optics, have been considered by a contractor interested in the LIF technology[Hon1]. The sensor location is decided by optical window accessibility. The optical windows should allow sampling of all three components of the velocity vector. The expected thermal loads on the optical window must also be considered. Also, the thermal deformation of the vehicle structure should be considered since the deflection can

alter the alignment angle with respect to the body axis (as discussed in Chapter 2). Window contamination, active cooling, and sensor system volume can also affect sensor location. Optical sensors can be placed under the first and second inlet ramps to measure inlet flow velocity and density. The sensors may also be placed to measure the boundary layer thickness and the mass flow rate by scanning through the inlet area.

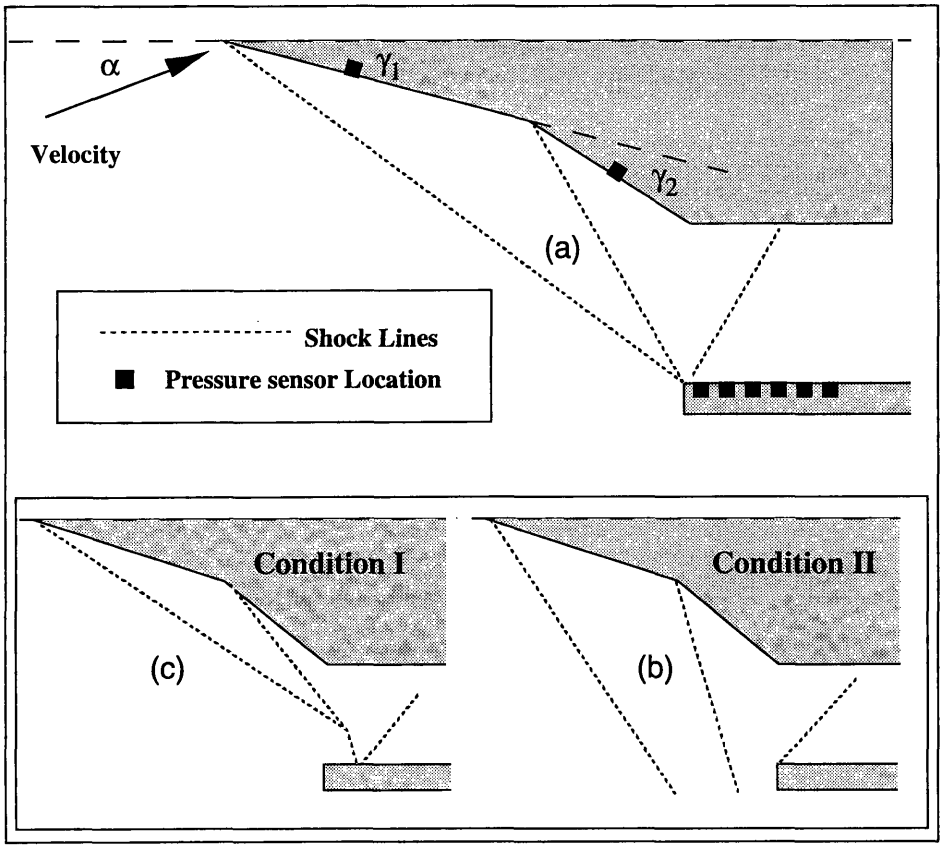

Figure 4-6 Inlet operating Conditions

Engine inlet pressure measurements have been considered to improve the estimate of the angle of attack and flight Mach number as well as to obtain the propulsion state. An analysis was carried out to determine the effectiveness of the sensing method and to locate the sensor installation points. The motivation for this approach was based on the fact that the oblique shock angle of a wedge has nearly a one-to-one ratio with respect to the vehicle nose wedge angle. Since the apparent wedge angle is the ramp angle plus the angle of attack, the shock angle will have a direct functional relationship with the angle attack and the free stream Mach number. Moreover, there is a distinct pressure jump across a shock wave. Small changes in the shock angle will cause large variations in the shock attachment location because the vehicle has a slender forebody. The shock-boundary layer interaction

creates pressure and geometric distortion around the impingement area. However, these effects may be ignored since the movement of the shock impingement location is in the order of couple meters for a degree of the angle of attack variation while the distortion is predicted to be in the order of few centimeters (interpreted from supersonic case) [Ada1].

As shown in Figure 4-6, there are three different inlet conditions. The optimal engine operation occurs at the critical condition where the oblique shocks impinge on the lower cowl lip (engine under surface). For the inlet condition shown in Figure 4-6 (a), there are sharp pressure jump at the shock impingement location. Another problem with this inlet condition is an extremely high heat flux at the shock impingement area (perhaps an order of magnitude higher than at any non-impingement locations). A second operating condition is when the shocks move outside of the engine, as shown in Figure 4-6 (b). For this particular condition, the inlet capture area has been greatly reduced, and there are no distinct pressure jumps within the engine since both shocks exist outside. The third operating condition is when shocks crawl inside of the combustor as shown in Figure 4-6 (c). In this case, the two oblique shocks merge and the shock impingement location will have a distinct pressure jump location.

Based on 1-D analysis, the inlet section has been modeled as a simple two ramp wedges. Ignoring viscous effects, a simple inlet analysis has been completed. In Figure 4-7 and 4-8, the oblique shock angles induced by the first and second ramps have been plotted versus the angle of attack and the flight Mach numbers. Each line corresponds to a given flight Mach number between 10 and 15. It is quite clear that the shock angles have a distinct and nearly linear relationship with the angle of attack. The variation due to Mach number is much smaller. In Figure 4-9, the pressure rise across the shock has been plotted against the angle of attack and the Mach number. The pressure variation at the first ramp surface is large and will produce a good signal to noise ratio if a pressure sensor is located there. The relationship is nearly linear with respect to both the angle of attack and the Mach number. However, when the pressure rise at 2nd ramp surface is plotted against angle of attack and Mach number in Figure 4-10, the variation in pressure with respect to angle of attack is very small. Consequently, the second ramp location is not suitable for angle of attack measurements.

Figure 4-11 shows the shock impingement location as a function of the angle of attack variations. For the case of critical operation (Figure 4-6(a)) and condition I (Figure 4-6(c)), an array of pressure sensors can be placed on the lower surface of the engine

combustor and used to locate the shock position as shown in Figure 4-6. Great sensitivity is expected since the shock moves on the order of meters for couple degrees of angle of attack variation.

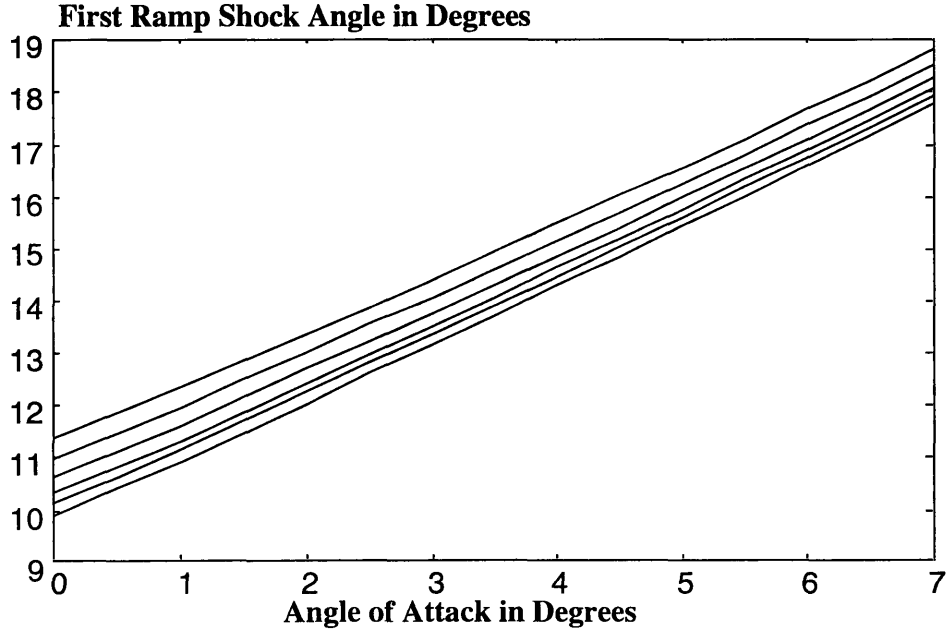

Figure 4-7 Inlet Analysis (1st Ramp Shock Angle vs α and M)

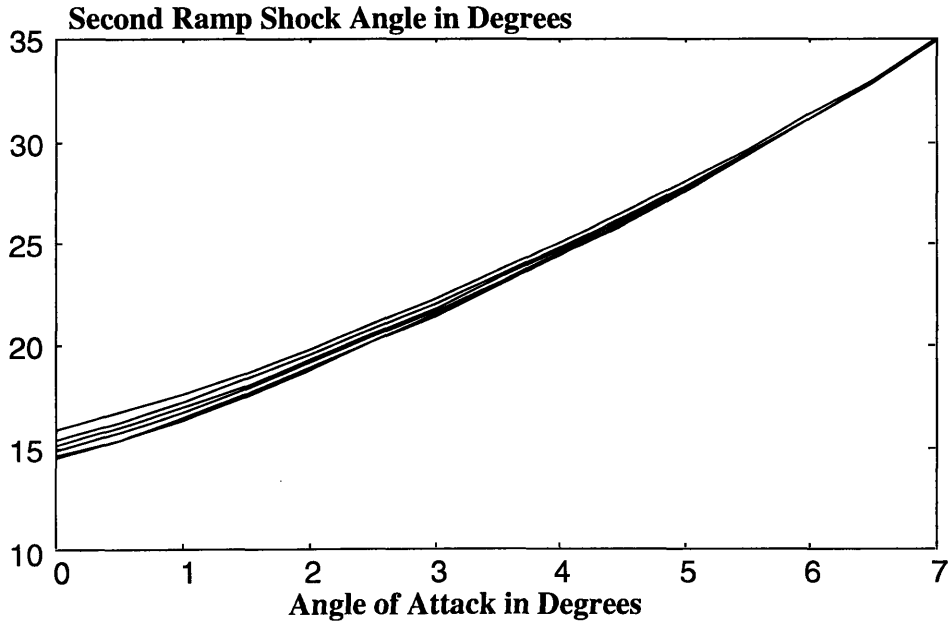

Figure 4-8 Inlet Analysis (2nd Ramp Shock Angle vs α and M)

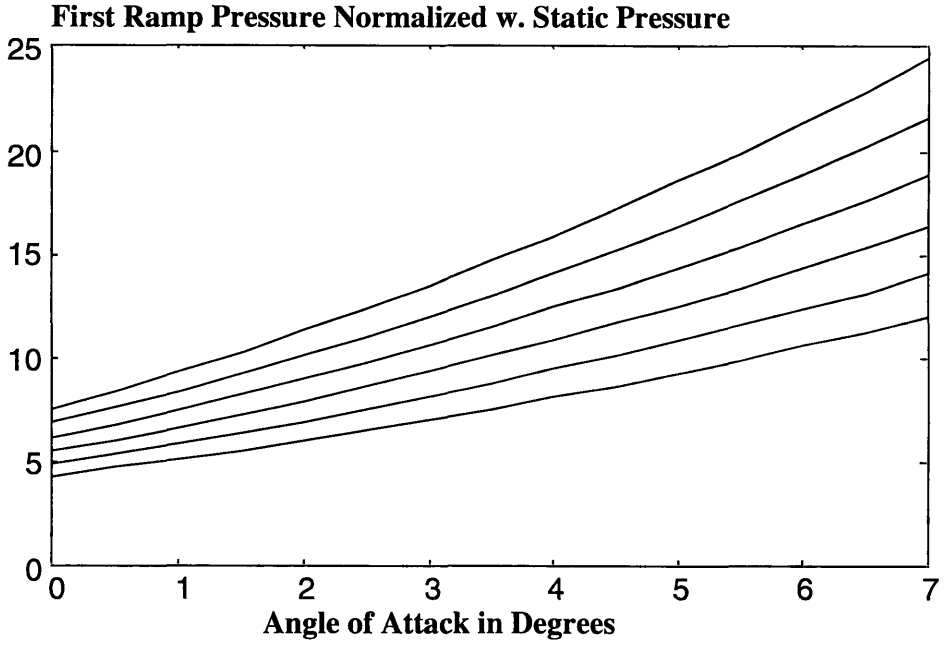

Figure 4-9 Inlet Analysis (1st Ramp Pressure vs α and M)

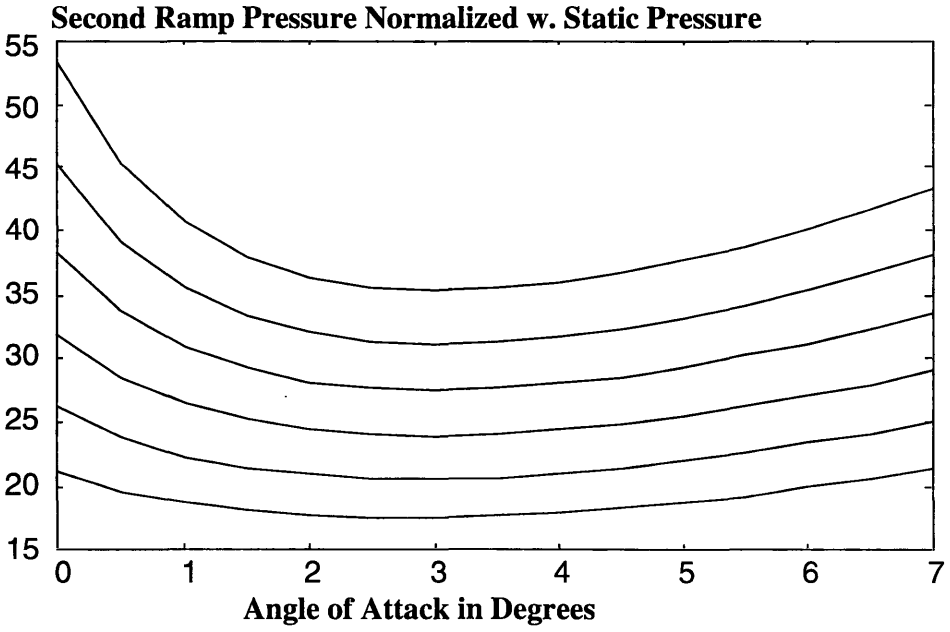

Figure 4-10 Inlet Analysis (2nd Ramp Pressure vs α and M)

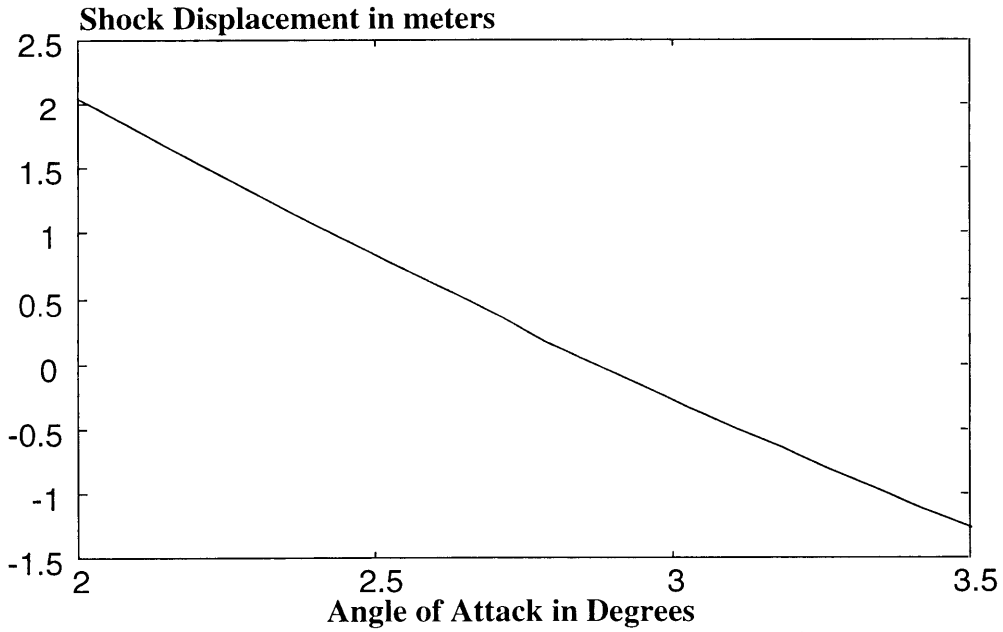

Figure 4-11 Inlet Analysis (Shock Displacement vs α)

Chapter 5

Modeling

5.1 Vehicle Dynamics

Within the context of the AHSV estimation problem, it is desired to use full information about the processes which are to be measured. The source of information can be both, measurements from various sensors and knowledge about the internal processes such as models of vehicle dynamics, aerodynamics, propulsion, environment, and sensors. Under the assumption of a model-based estimation strategy, the appropriate models should be formulated and the accuracy of the models will determine the system stability and precision of the estimates. The flow angle parameters such as angle of attack are considered to be the most important parameter to estimate. Therefore, it is important to include all interactive elements which provide good sensitivity with respect to the angle of attack for the models in the estimator. The models, which are formulated and described in this chapter, will lay out the foundations for AHSV state estimation and will be used extensively in later chapters. Moreover, the nature of the model equations will determine the tractability of the estimation problem.

Some of the desired AHSV states are measured directly and some are obtained implicitly through certain nonlinear functions (called either observation equations or

measurement equations). Regardless of the availability of direct full state measurements, it is desired to augment all available knowledge about the state in order to enhance estimation accuracy. For example, angle of attack measurements may be readily available through air data sensors based on a relationship between angle of attack and vehicle attitude. However, if the achievable accuracy is not acceptable, it is instead possible to use vehicle motion measurements (inertial sensors) to obtain some information regarding angle of attack. Another advantage of incorporating the vehicle motion is to increase the state estimate bandwidth [Kas1] when the sensor system have inherent bandwidth limitations. The drawback to using both sources of information is in the complexity of the computation and the difficulty in obtaining accurate and relevant models for the processes. Therefore it is desirable to obtain accurate models that are also simple for numerical implementation for the vehicle equations of motion. In next few subsections, the vehicle equations of motion are derived with emphasis on air data state estimation.

There are several versions of the equations of motion for AHSVs. The most significant model derivations are done by Chamitoff [Cha1][Cha2] and Schimdt [Bil1][Sch2]. Some related but not clearly attributed empirical aerodynamics and propulsion data are also available from NASA Langley [Sha1]. Bilimora and Schmidt [Bil1] formulated equations of motion based on a Lagrangian approach. The formulated model captures the dynamics of rigid-body motion, elastic structural deformation, fluid flow, rotating machinery, wind, and a spherical rotating Earth. The detailed forcing terms which include aerodynamics, thermodynamics, and propulsion can be found in Chavez and Schmidt [Sch2]. Chavez and Schmidt used 2-D Newtonian theory to analyze hypersonic flow, and coupled it with 1-D aero/thermodynamic analysis of the flow in a Scramjet. Chamitoff's model has higher fidelity in the hypersonic flow and propulsion models by employing panel methods and chemical reaction properties. The model assumed a spherical rotating earth and was formulated in an LVLH frame. Even though this model has more fidelity in the aerodynamics and propulsion representations, it lacks structural deformation and vibration characterizations. In addition to hypersonic vehicle formulations, there exist a vehicle equations of motion applicable to low speed conventional aircraft with special features to treat the wind effects. Most of the formulations are specialized to solve problems of wind shear [Fro1].

For the air data estimation problem here, two different formulations have been selected as applicable. For the lower flight Mach number part of the trajectory, the

equations of motion have been formulated based on generic flight vehicle dynamics equations which include wind effects. The formulations are specialized extensions of the equations derived in the reference [Fro1]. The forcing terms are based on Chamitoff's model (the numerical data from Chamitoff's NASP simulator) [Cha2]. For the higher flight Mach number regime, Chamitoff's controller model has been selected. The formulations here also only address longitudinal motion [Cha2].

5.1.1 Model Selection Criteria

A model-based state estimation scheme is considered the most appropriate technique for estimating flow angles and air-relative velocity in order to enhance the accuracy of given air data sensors. The only previous research where a vehicle dynamics model was incorporated into air data state estimation can be found in the high angle of attack research flight vehicle program.[Kas1] Actual implementation of the concept on a flight vehicle showed improvements in the estimation frequency response and accuracy during transient high angle of attack maneuvers. For simplicity and speed in digital implementation, the zero wind condition was assumed, and acceleration measurements were emulated as input to the vehicle kinematics. Such assumptions may penalize AHSV air-data estimation performance. Since the transfer functions (functional relationships) from aerodynamics, propulsion, and control surfaces contain rich information of the angle of attack and air-speed, it is not desirable to ignore the relationships and use acceleration measurements only. Based on previous experience, if the bandwidths of the air-data sensors are considered too low for the controller, some hybrid algorithms that incorporate inertial data, air-data, and vehicle dynamics, may be used to expand it and also increase accuracy. Consequently, a dynamic model is desired in AHSV applications and the appropriate model should be formulated.

In the process of developing a model for state estimation, the choice of assumptions is critical. Appropriate assumptions can simplify the problem without significant loss of fidelity. The vehicle equations of motion can be written differently depending on three major factors. The first is whether to include models of the external forcing terms. These external forcing terms, excluding gravity effects, are composed of forces induced by propulsion, control, and aerodynamics. These forcing terms can be modeled using either first principles or empirical formulations. The dependence of these forcing terms on the states is implicit while the wind terms are coupled to the states

explicitly. If the modeling uncertainties are relatively large, then applying such a relationship between forcing terms and states does not improve performance and may degrade estimation accuracy. An alternative strategy is to use acceleration measurements to replace the forcing terms within the model as inputs similar to the implementation on the FA-18 high angle of attack research vehicle [Kas1].

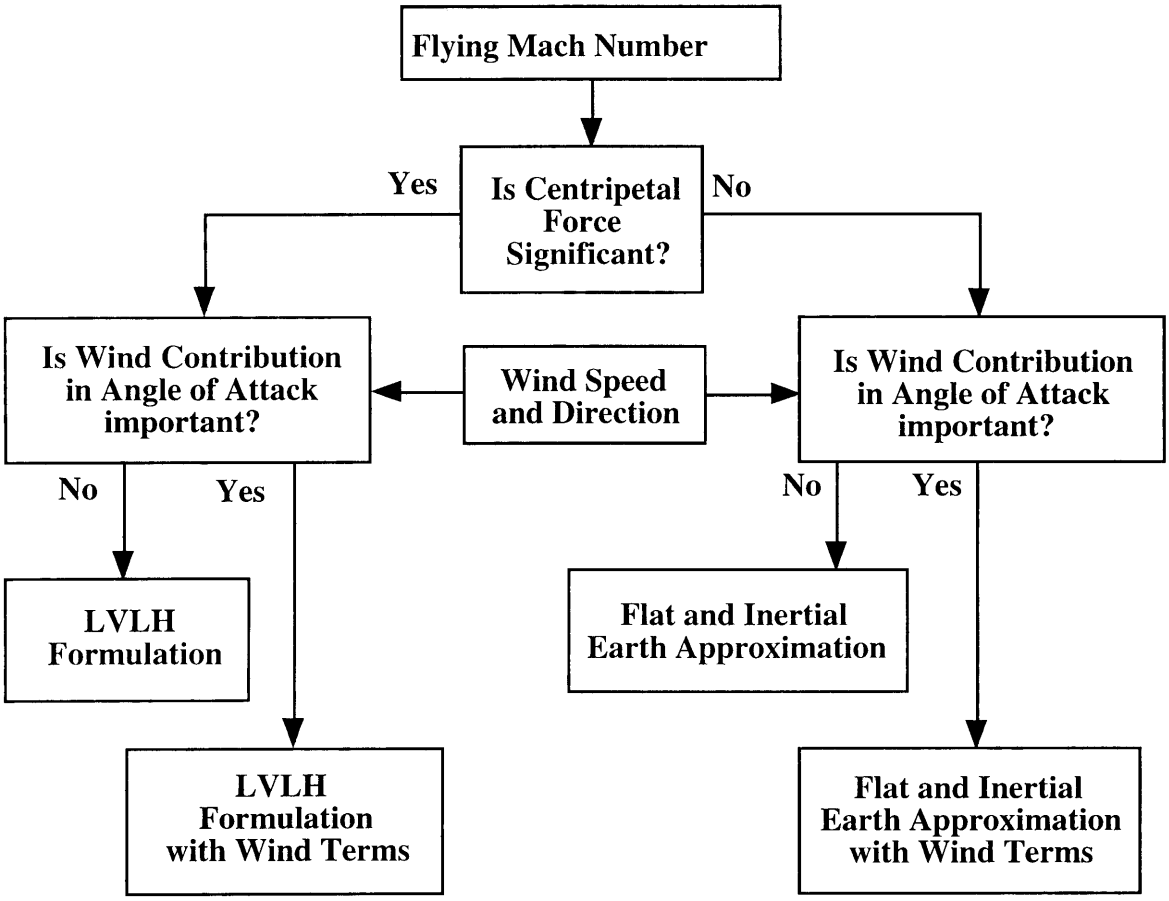

Figure 5-1 Decision Flow Chart for Vehicle Models
(LVLH=Local Vertical Local Horizontal Frame)

Two other major factors are flight speed and wind contributions. As shown in the model selection criteria in Figure 5-1, the magnitude of centripetal acceleration and contributions due to earth rotation must be computed for the given flight speed. If such contributions are large then an Local Vertical Local Horizontal (LVLH) formulation should be used. Otherwise, a flat, inertial earth approximation is adequate. The size of each contributing term is calculated and plotted as a function of the vehicle flight speed in subsection 5.1.3. Once the reference frame and coordinate system is selected, the magnitude of wind contributions should be estimated. If the wind contributions change the flow angle by more than 0.1° (rough estimate of the angle of attack accuracy

requirement at flight Mach number around 10 to 15) then implementation of the wind models can improve performance of the estimator. The criterion for the wind contribution is shown in Figure 5-2.

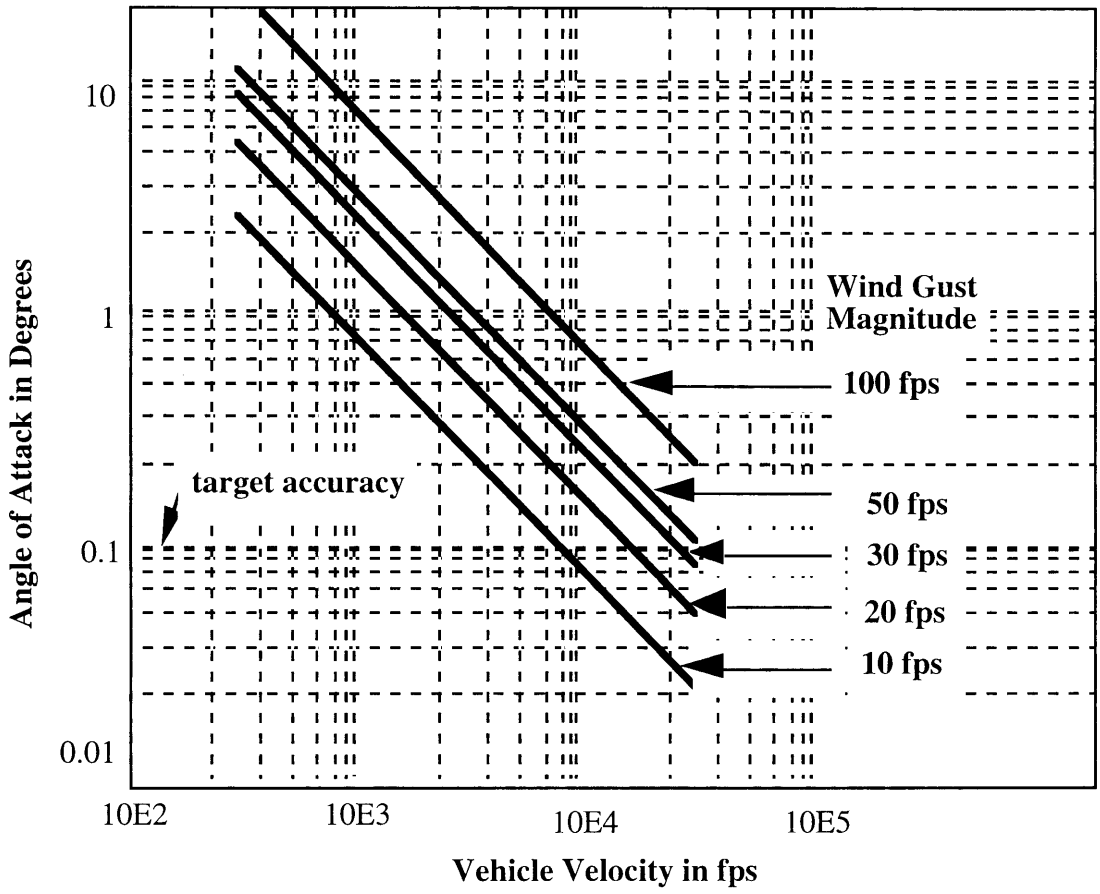

Figure 5-2 Resulting Angle of Attack for Various Vertical Gusts

The wind effects can also be approximated by a simple analysis. If we assume that the lift force and angle of attack is given by

$$L = \frac{\rho}{2} V^2 A_w C_L(\alpha) \qquad \text{and} \qquad \alpha = \alpha_o + \frac{V_w}{V}$$

where V_w is the normal wind gust, and also when we consider the Newtonian flow approximation, then

$$\frac{\partial C_L}{\partial \alpha} \approx \alpha \qquad \text{and} \qquad \delta L \approx \frac{\rho}{2} V^2 A_w \alpha \frac{V_w}{V} = \frac{\rho}{2} V^2 A_w \left(\alpha_o + \frac{V_w}{V} \right) \frac{V_w}{V}$$

If we assume a nearly constant dynamic pressure trajectory,

$$\delta L \approx Q A_w \left(\alpha_o + \frac{V_w}{V} \right) \frac{V_w}{V}$$

It is clear that the vertical gust contribution in angle of attack decreases when Mach number increases. If the nominal angle of attack α_o is much smaller than the gust contribution, then the wind term affects the normal lift force squarely. Otherwise, the wind contribution affects linearly. For the flight speed between Mach 10 to 15, the resulting plot of normal force vs. angle of attack and Mach numbers (Figure 4-3 from a particular design of aerodynamic and propulsion model) suggest that

$$\frac{\partial N}{\partial \alpha} \approx k_o \Delta M \quad \Rightarrow \quad \delta N \approx k_o \frac{\Delta M}{M} V_w$$

Again, the wind gust contribution decreases when the flight speed increases.

For the AHSV applications, two models were selected to represent the complete flight envelope. Based on the analysis of subsection 5.1.3, additional terms including centripetal accelerations and Coriolis terms are found to be small below about Mach 6. Similarly, Figure 5-2 shows the wind contributions to be significant below about Mach 6; therefore, the model with the flat and inertial earth approximation and incorporated wind terms will adequately represent the vehicle during that flight phase. Conversely, since the wind terms are insignificant at higher Mach numbers, the LVLH formulation without wind terms can be applied to represent the vehicle motion during the higher flight Mach number regime.

5.1.2 Flat and Inertial Earth Approximation With Wind Terms

For the lower Mach number flight regime, which is determined by the previously noted criteria, flat and inertial earth approximations are considered adequate for estimation purposes. Moreover, the wind terms can be augmented to improve estimation accuracy. This subsection derives the applicable vehicle equations of motion with incorporated wind effects. The equations of motion are first presented for the full 6 degree of freedom case[Fro1], and then, the equations are specialized to longitudinal motion only. In the end of the subsection, the equations are simplified to be used for estimation. The states to be estimated are air relative velocities and flow angles; therefore, the states are coupled with wind terms to first order.

Incorporation of Wind Contributions Into Vehicle Equations of Motion:

The earth is assumed to be a stationary plane in inertial space. The earth-fixed coordinates define the inertial frame of reference. The body coordinates are fixed at the

center of gravity point as normally applies to the flight vehicle convention. The corresponding force equations projected on body axes are shown in the equation (5.1) below [Fro1].

$$\sum F_x - mg\sin\theta = m\left(\dot{u} + \dot{W}_x\right) + m\left[q(w + W_z) - r(v + W_y)\right] \tag{5.1a}$$

$$\sum F_y + mg\cos\theta\sin\phi = m\left(\dot{v} + \dot{W}_y\right) + m\left[r(u + W_x) - p(w + W_z)\right] \tag{5.1b}$$

$$\sum F_z + mg\cos\theta\cos\phi = m\left(\dot{w} + \dot{W}_z\right) + m\left[p(v + W_y) - q(u + W_x)\right] \tag{5.1c}$$

The wind terms are obtained by using equations (5.2) through (5.4).

$$\begin{bmatrix} W_x \\ W_y \\ W_z \end{bmatrix} = C_{BE}\begin{bmatrix} W_x \\ W_y \\ W_z \end{bmatrix}_E \tag{5.2}$$

$$\begin{bmatrix} \dot{W}_x \\ \dot{W}_y \\ \dot{W}_z \end{bmatrix}_E = \begin{bmatrix} \frac{\partial W_x}{\partial x} & \frac{\partial W_x}{\partial y} & \frac{\partial W_x}{\partial z} \\ \frac{\partial W_y}{\partial x} & \frac{\partial W_y}{\partial y} & \frac{\partial W_y}{\partial z} \\ \frac{\partial W_z}{\partial x} & \frac{\partial W_z}{\partial y} & \frac{\partial W_z}{\partial z} \end{bmatrix}_E \begin{bmatrix} \dot{x} \\ \dot{y} \\ \dot{z} \end{bmatrix}_E + \begin{bmatrix} \frac{\partial W_x}{\partial t} \\ \frac{\partial W_y}{\partial t} \\ \frac{\partial W_z}{\partial t} \end{bmatrix}_E \tag{5.3}$$

$$\begin{bmatrix} \dot{W}_x \\ \dot{W}_y \\ \dot{W}_z \end{bmatrix} = C_{BE}\begin{bmatrix} \dot{W}_x \\ \dot{W}_y \\ \dot{W}_z \end{bmatrix}_E + \dot{C}_{BE}\begin{bmatrix} W_x \\ W_y \\ W_z \end{bmatrix}_E \tag{5.4}$$

If we make the frozen field approximation for the wind then the $\frac{\partial W_i}{\partial t}$ terms are all zeros. Therefore the wind fluctuations are defined purely by the spatial gradient of the wind field. Also notice that the retained forcing terms are dependent on the wind parameters such as angle of attack, side slip angle, and total wind velocity magnitude. For example, the thrust will depend on the flow angles as well as total air relative velocity. The elements of the coordinate transformation matrices and their derivatives are shown in Appendix A.

The moment equations are:

$$\sum M_x = I_x\dot{p} - I_{zx}\left(\dot{r} + pq\right) - (I_y - I_z)qr \tag{5.5a}$$

$$\sum M_y = I_y\dot{q} - I_{zx}\left(r^2 - p^2\right) - (I_z - I_x)rp \tag{5.5b}$$

$$\sum M_z = I_z\dot{r} - I_{zx}(\dot{p} - pr) - (I_x - I_y)pq \tag{5.5c}$$

Notice that none of the wind terms explicitly appear in the moment equations. However, the forcing torque terms do contain wind dependent components. For example, the lift and drag coefficients can be represented as polynomial functions of angle of attack. For the longitudinal motion, these forcing terms are shown in equation (5.14). The rotation angle can be found by the kinematic relations as shown in equation (5.6). These kinematic relations can also be expressed with quaternions if a singularity is expected and must be avoided.

$$\dot{\phi} = p + q\sin\phi\tan\theta + r\cos\phi\tan\theta \tag{5.6a}$$

$$\dot{\theta} = q\cos\phi - r\sin\phi \tag{5.6b}$$

$$\dot{\psi} = (q\sin\phi + r\cos\phi)\sec\theta \tag{5.6c}$$

By definition, the flow angle parameters, angle of attack α, and side slip angle β, are defined as:

$$\tan\alpha = \frac{w}{u} \qquad \text{and} \qquad \sin\beta = \frac{v}{\sqrt{\left|\underset{\sim}{V}\right|^2}} \tag{5.7a,b}$$

where:

$$\left|\underset{\sim}{V}\right|^2 = (\dot{x}_E - W_{xE})^2 + (\dot{y}_E - W_{yE})^2 + (\dot{z}_E - W_{zE})^2 = u^2 + v^2 + w^2 \tag{5.7c}$$

Their derivatives are respectively:

$$\dot{\alpha} = \frac{u\dot{w} - w\dot{u}}{u^2 + w^2} \qquad \text{and} \qquad \dot{\beta} = \frac{\dot{v}(u^2 + w^2) - v(u\dot{u} - w\dot{w})}{\left|\underset{\sim}{V}\right|^2\sqrt{u^2 + w^2}} \tag{5.8a,b}$$

Therefore the velocity vector can be expressed as,

$$\underset{\sim}{V} = \begin{bmatrix} u \\ v \\ w \end{bmatrix} = V_T \begin{bmatrix} \cos\beta\cos\alpha \\ \sin\beta \\ \cos\beta\sin\alpha \end{bmatrix} \tag{5.9}$$

Longitudinal Dynamics: The previously derived equations of motion (5.1 through 5.8) are specialized to longitudinal motion. The lateral dynamics are ignored for convenience (lateral dynamics are not investigated nor well understood at this time). The applicable coordinate system and reference frames are defined in Figure 5-3.

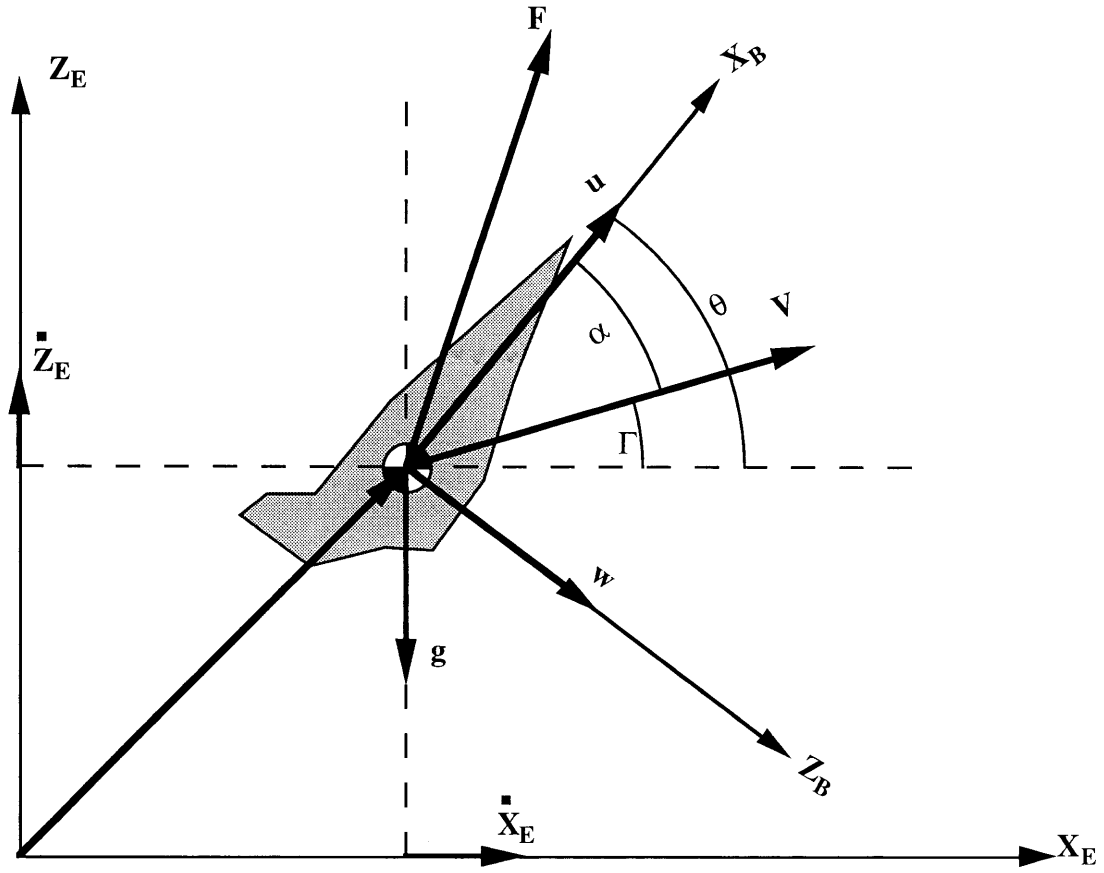

Figure 5-3 Definition of coordinate system and variables

The corresponding longitudinal equations of motion are:

$$\sum F_x - mg\sin\theta = m\left(\dot{u} + \dot{W}_x\right) + mq(w + W_z) \tag{5.10a}$$

$$\sum F_z + mg\cos\theta = m\left(\dot{w} + \dot{W}_z\right) - mq(u + W_x) \tag{5.10b}$$

$$\sum M_y = I_y\dot{q} \tag{5.10c}$$

Where Equations (5.2) and (5.4) reduce to:

$$\begin{bmatrix} W_x \\ W_z \end{bmatrix} = \begin{bmatrix} \cos\theta & -\sin\theta \\ \sin\theta & \cos\theta \end{bmatrix} \begin{bmatrix} W_x \\ W_z \end{bmatrix}_E \tag{5.11}$$

$$\begin{bmatrix} \dot{W}_x \\ \dot{W}_z \end{bmatrix}_E = \begin{bmatrix} \frac{\partial W_x}{\partial x} & \frac{\partial W_x}{\partial z} \\ \frac{\partial W_z}{\partial x} & \frac{\partial W_z}{\partial z} \end{bmatrix}_E \begin{bmatrix} \dot{x} \\ \dot{z} \end{bmatrix}_E \tag{5.12}$$

$$\begin{bmatrix} \dot{W}_x \\ \dot{W}_z \end{bmatrix} = \begin{bmatrix} \cos\theta & -\sin\theta \\ \sin\theta & \cos\theta \end{bmatrix} \begin{bmatrix} \dot{W}_x \\ \dot{W}_z \end{bmatrix}_E + \begin{bmatrix} -\sin\theta\dot{\theta} & -\cos\theta\dot{\theta} \\ \cos\theta\dot{\theta} & -\sin\theta\dot{\theta} \end{bmatrix} \begin{bmatrix} W_x \\ W_z \end{bmatrix}_E \tag{5.13}$$

Equation (5.8) reduces to: $\tan\alpha = \frac{w}{u}$ and $\dot{\alpha} = \frac{u\dot{w} - w\dot{u}}{u^2 + w^2}$. For AHSVs the aerodynamic and propulsion forcing terms can be defined as follows [Cha2]:

$$\begin{aligned} \sum F_{wx} = &\left[C_{Tv}(M,\alpha,R) - C_D(M,\alpha) + C_{x\delta_e}(M,\alpha,\delta_e) + C_{x\delta_T}(M,\alpha,\delta_T)\right] Q(R,V)S \\ &+\left[C_{x\delta_v}(M,\alpha,\delta_v)\left[C_{Tv}(M,\alpha,R) + C_{x\delta_T}(M,\alpha,\delta_T)\right]\right] Q(R,V)S \end{aligned} \tag{5.14a}$$

$$\begin{aligned} \sum F_{wz} = &\left[C_{Tn}(M,\alpha,R) + C_L(M,\alpha) - C_{z\delta_e}(M,\alpha,\delta_e) - C_{z\delta_T}(M,\alpha,\delta_T)\right] Q(R,V)S \\ &-\left[C_{z\delta_v}(M,\alpha,\delta_v)\left[C_{z\delta_T}(M,\alpha,\delta_T) - C_{Tn}(M,\alpha,R)\right]\right] Q(R,V)S \end{aligned} \tag{5.14b}$$

$$\begin{aligned} \sum M_y = &\left[C_{mp}(M,\alpha,R) + C_{ma}(M,\alpha) + C_{m\delta_e}(M,\alpha,\delta_e) + C_{m\delta_T}(M,\alpha,\delta_T)\right] Q(R,V)Sc \\ &+\left[C_{m\delta_v}(M,\alpha,\delta_v)\left[C_{m\delta_T}(M,\alpha,\delta_T) + C_{mp}(M,\alpha,R)\right]\right] Q(R,V)Sc \end{aligned} \tag{5.14c}$$

However, these forcing terms are defined in wind axes, and need to be transformed into body axes by use of a coordinate transformation matrix.

Simplified Representation: Let's start from the longitudinal equations of motion (Equation (5.10), - flat earth approximation). Equations (5.10) through (5.13) can be put together and be simplified. More details on the applied simplifications are in Appendix B. The resulting complete equations of motion are,

$$\begin{bmatrix} \dot{u} \\ \dot{w} \end{bmatrix} = -q\begin{bmatrix} w \\ -u \end{bmatrix} - \begin{bmatrix} \cos\theta & -\sin\theta \\ \sin\theta & \cos\theta \end{bmatrix} \begin{bmatrix} \frac{\partial W_x}{\partial x} & \frac{\partial W_x}{\partial z} \\ \frac{\partial W_z}{\partial x} & \frac{\partial W_z}{\partial z} \end{bmatrix}_E \begin{bmatrix} \dot{x} \\ \dot{z} \end{bmatrix}_E + \begin{bmatrix} a_x \\ a_z \end{bmatrix}_{cg} + g\begin{bmatrix} -\sin\theta \\ \cos\theta \end{bmatrix} \tag{5.15a}$$

with

$$\dot{q} = \frac{1}{I_y}\sum M_y \tag{5.15b}$$

$$\dot{\theta} = q \tag{5.15c}$$

where the states are w and u.

Equation (5.15) can be evaluated with information about pitch angle θ, pitch rate q, inertial velocity $\dot{X}$ and $\dot{Z}$, wind gradient Jacobian, and accelerations. All the inertial quantities, which excludes the wind gradient Jacobian, can be obtained from the inertial

sensor measurements. However, these inertial measurements may also depend on the states.

If equation (5.15) is expressed with state parameters chosen to be angle of attack and total velocity, the equation becomes

$$\begin{bmatrix} \dot{V}_T \\ \dot{\alpha} \end{bmatrix} = \begin{bmatrix} 0 \\ -q \end{bmatrix} + \begin{bmatrix} C_x & C_z \\ -\frac{C_z}{V_T} & \frac{C_x}{V_T} \end{bmatrix} \begin{bmatrix} \cos\alpha \\ \sin\alpha \end{bmatrix} \tag{5.16}$$

where

$$\begin{bmatrix} C_x \\ C_z \end{bmatrix} = \begin{bmatrix} a_{xcg} - g\sin\theta - (\frac{\partial W_x}{\partial x}\dot{x}_E + \frac{\partial W_x}{\partial z}\dot{z}_E)\cos\theta + (\frac{\partial W_z}{\partial x}\dot{x}_E + \frac{\partial W_z}{\partial z}\dot{z}_E)\sin\theta \\ a_{zcg} + g\cos\theta + (\frac{\partial W_x}{\partial x}\dot{x}_E + \frac{\partial W_x}{\partial z}\dot{z}_E)\sin\theta + (\frac{\partial W_z}{\partial x}\dot{x}_E + \frac{\partial W_z}{\partial z}\dot{z}_E)\cos\theta \end{bmatrix} \tag{5.17}$$

More detailed intermediate steps which lead to equations (5.16) and (5.17) are in Appendix B. For better visualization of the above equations, the appropriate block diagram is shown in Figure 5.4.

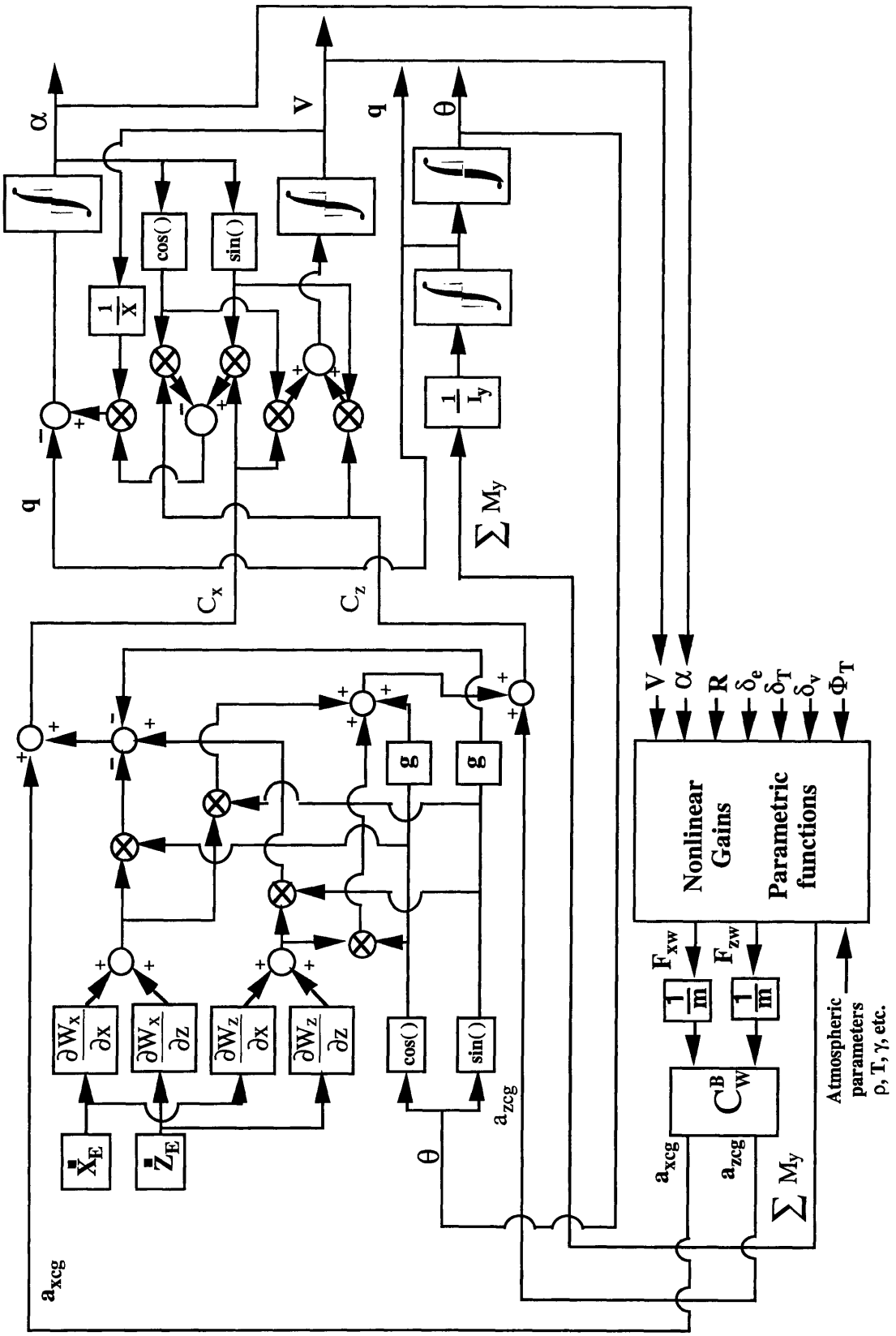

Figure 5.4 Block Diagram of AHSV Equations of Motion (Equations 5.15 - 5.17) (For flight Mach numbers between 3 to 6)

5.1.3 LVLH Formulation of Longitudinal Dynamics

The vehicle equations of Motion in the LVLH frame are based on the formulation given in the reference [Cha2]. This model was derived based on the assumption of rigid body motions through the atmosphere of a rotating spherical Earth. Only the longitudinal motions are considered with an equatorial launch to orbit scenario. Therefore all the lateral variables are omitted. The gravitational acceleration has been modeled with altitude variations. A stationary atmosphere with no wind is assumed. The forcing and control coefficients given by equation (5.14) can be obtained numerically from the simulations which contain sophisticated aerodynamics and propulsion models. For simplicity, the forcing and control coefficients can be further parameterized by polynomial curve fitting the tabulated coefficient data that are generated by the vehicle design program [Cha2]. The resulting equations of motion are,

$$\frac{dV}{dt} = \frac{1}{m}\sum F_{xw} - \left[g(R) - \omega_E^2 R\right]\sin\Gamma \tag{5.18a}$$

$$V\frac{d\Gamma}{dt} = -\frac{1}{m}\sum F_{zw} - \left[g(R) - \omega_E^2 R\right]\cos\Gamma + \frac{V^2}{R}\cos\Gamma + 2\omega_E V \tag{5.18b}$$

$$\frac{dq}{dt} = \frac{1}{I_y}\sum M_y \tag{5.18c}$$

$$\frac{d\theta}{dt} = q \tag{5.18d}$$

$$\frac{dR}{dt} = V\sin\Gamma \tag{5.18e}$$

However it is desirable to express the equations in terms of angle of attack α instead of flight path angle Γ. Since $\Gamma = \theta - \alpha$ and $\dot{\Gamma} = \dot{\theta} - \dot{\alpha}$, equation (5.18 a, b) can be written as:

$$\dot{V} = \frac{1}{m}\sum F_{xw} + \left[-g(R) + \omega_E^2 R\right]\sin(\theta - \alpha) \tag{5.19a}$$

$$V(q - \dot{\alpha}) = -\frac{1}{m}\sum F_{zw} + \left[-g(R) + \omega_E^2 R + \frac{V^2}{R}\right]\cos(\theta - \alpha) + 2\omega_E V \tag{5.19b}$$

Using the trigonometric relations:

$$\sin(x - y) = \sin x\cos y - \cos x\sin y \tag{5.20a}$$

$$\cos(x - y) = \cos x\cos y + \sin x\sin y \tag{5.20b}$$

Then the equations (5.19) turn into:

$$\dot{V} = a_{xw} + \left[\omega_E^2 R - g(R)\right](\sin\theta\cos\alpha - \cos\theta\sin\alpha) \tag{5.21a}$$

$$\dot{\alpha} = \frac{a_{zw}}{V} + \left[\frac{g(R)}{V} - \frac{V}{R} - \frac{\omega_E^2 R}{V}\right](\cos\theta\cos\alpha + \sin\theta\sin\alpha) + q - 2\omega_E \tag{5.21b}$$

with

$$\dot{q} = \frac{1}{I_y}\sum M_y \tag{5.19c}$$

$$\dot{\theta} = q \tag{5.19d}$$

$$\dot{R} = V\sin(\theta - \alpha) = V(\sin\theta\cos\alpha - \cos\theta\sin\alpha) \tag{5.19e}$$

The forcing terms are defined same as equations (5.14a, b, c).

The representative graphs of the forcing coefficients are plotted in Figure 5.5 through 5.13.

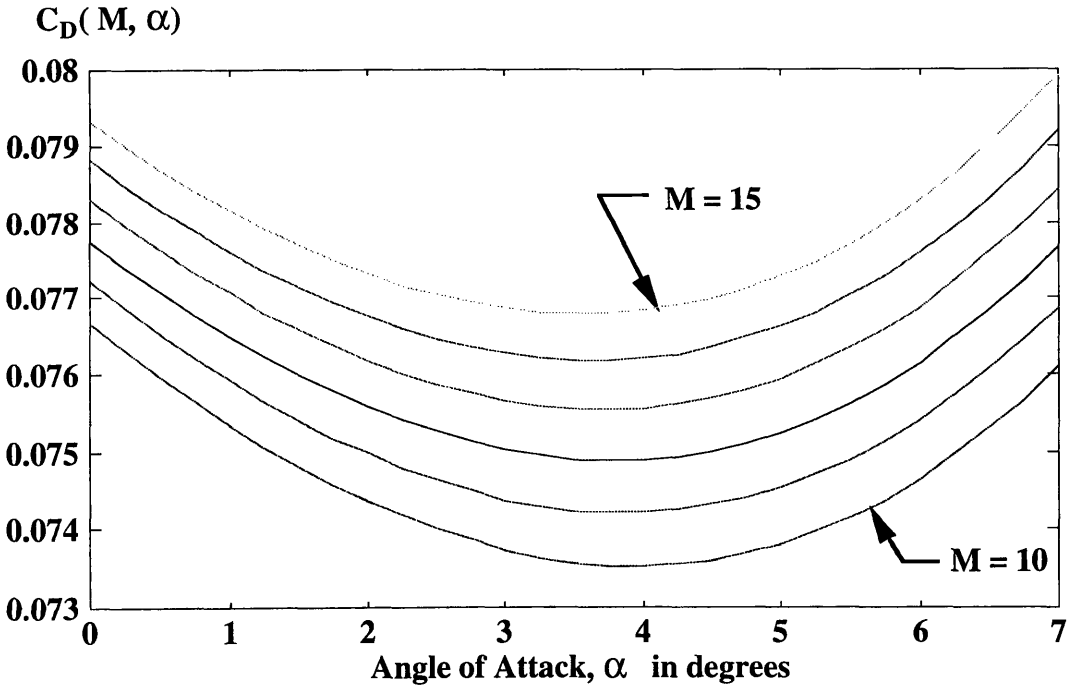

Figure 5.5 Plot of Drag Coefficient

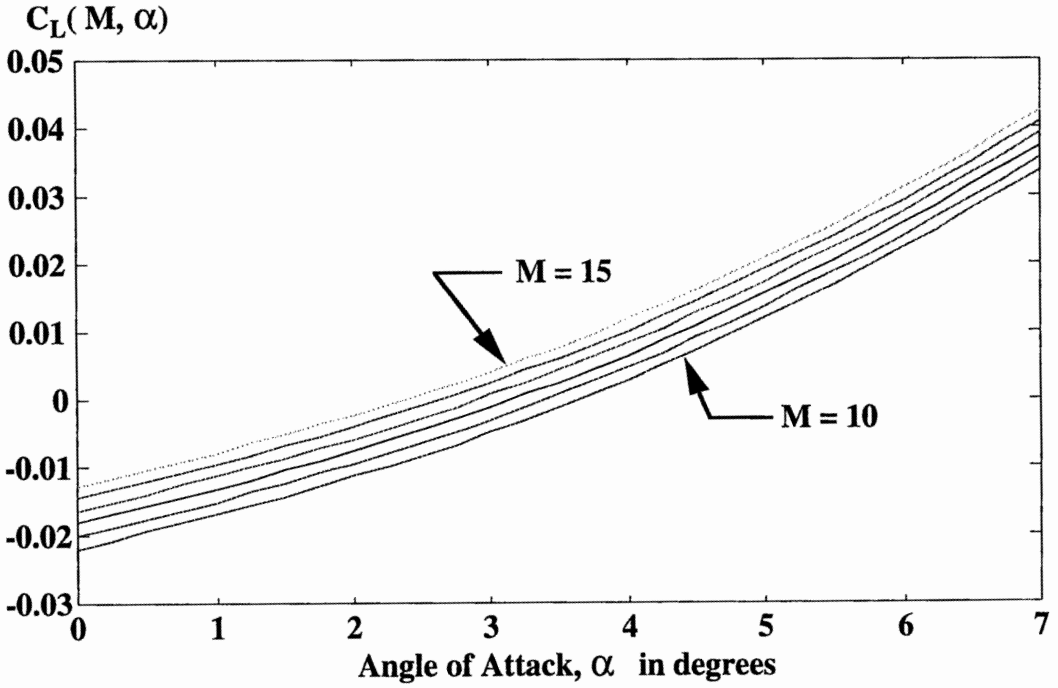

Figure 5.6 Plot of Lift Coefficient

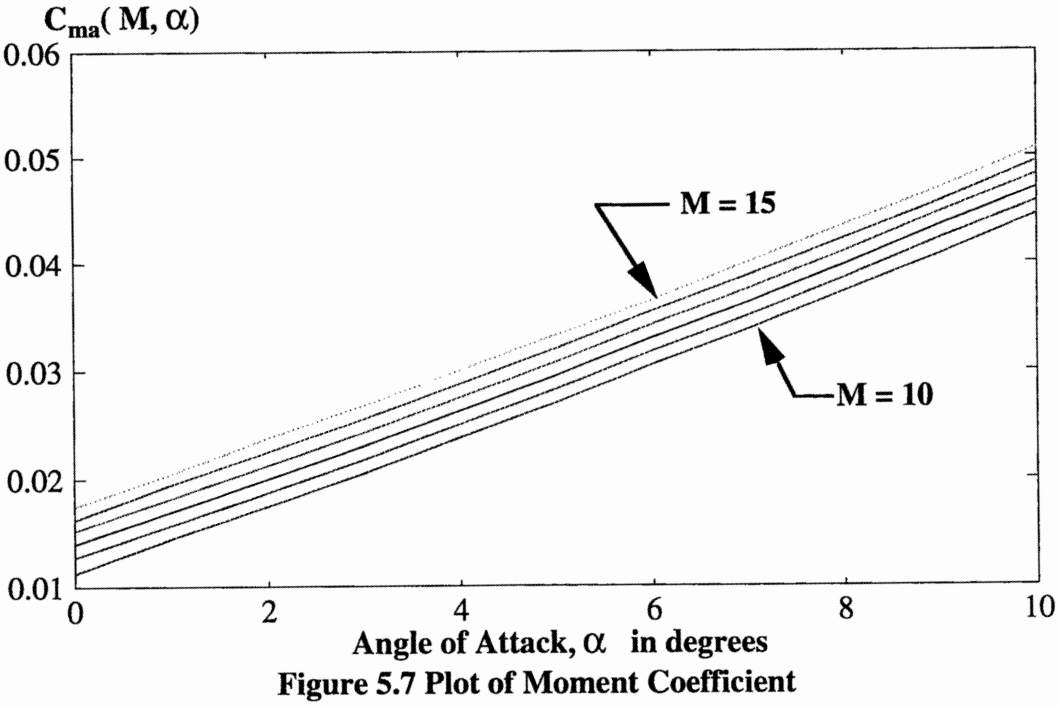

Figure 5.7 Plot of Moment Coefficient

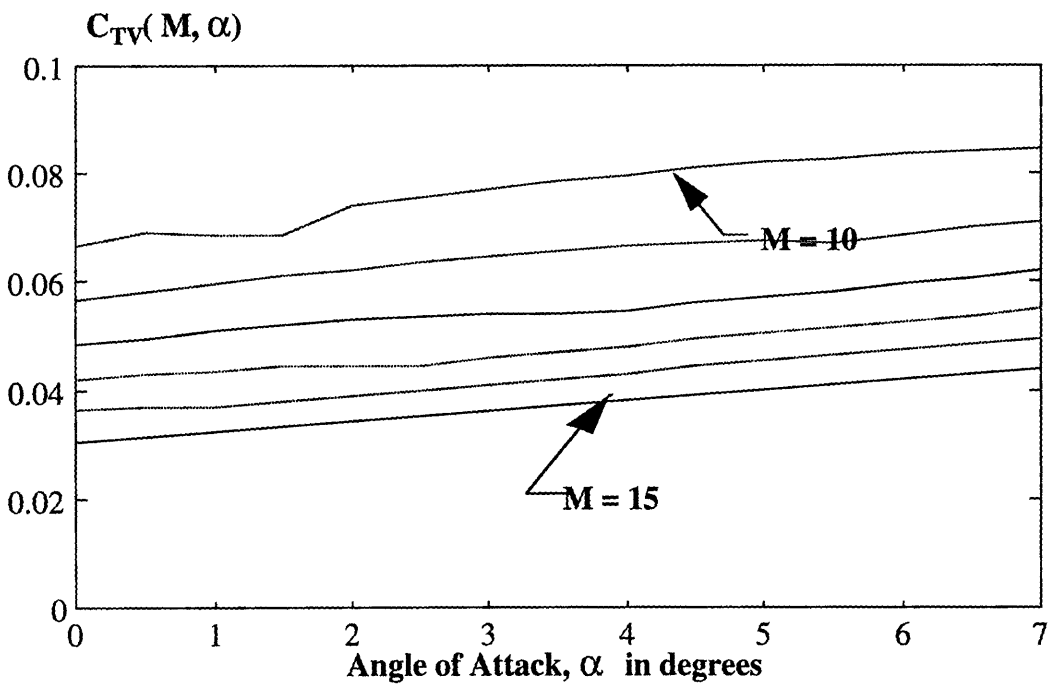

Figure 5.8 Thrust Coefficient - Axial Component

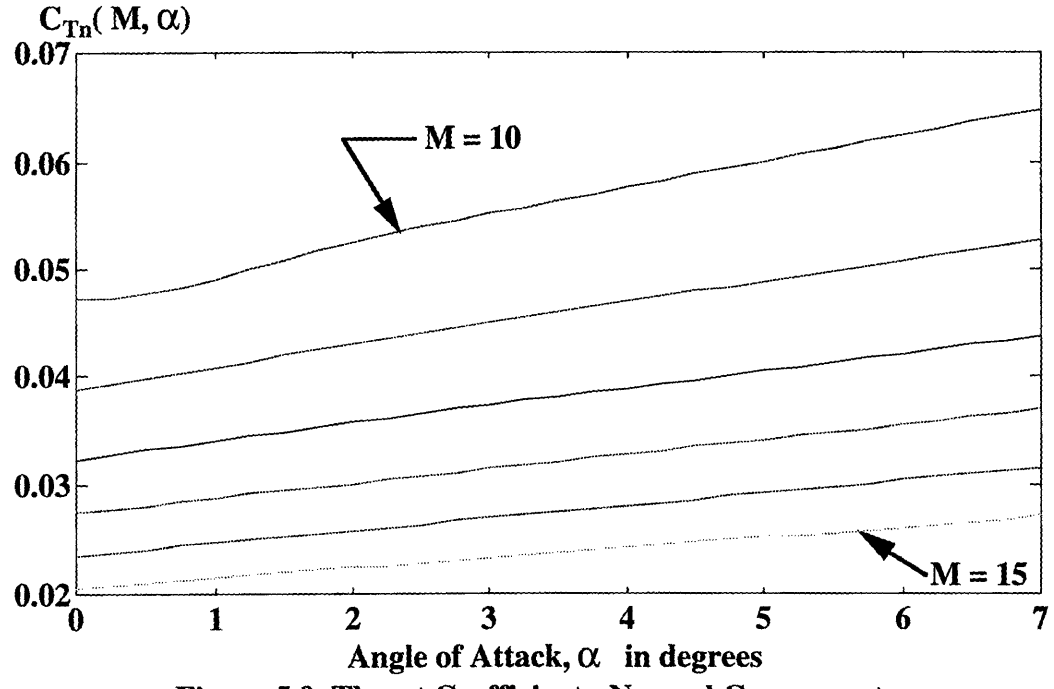

Figure 5.9 Thrust Coefficient - Normal Component

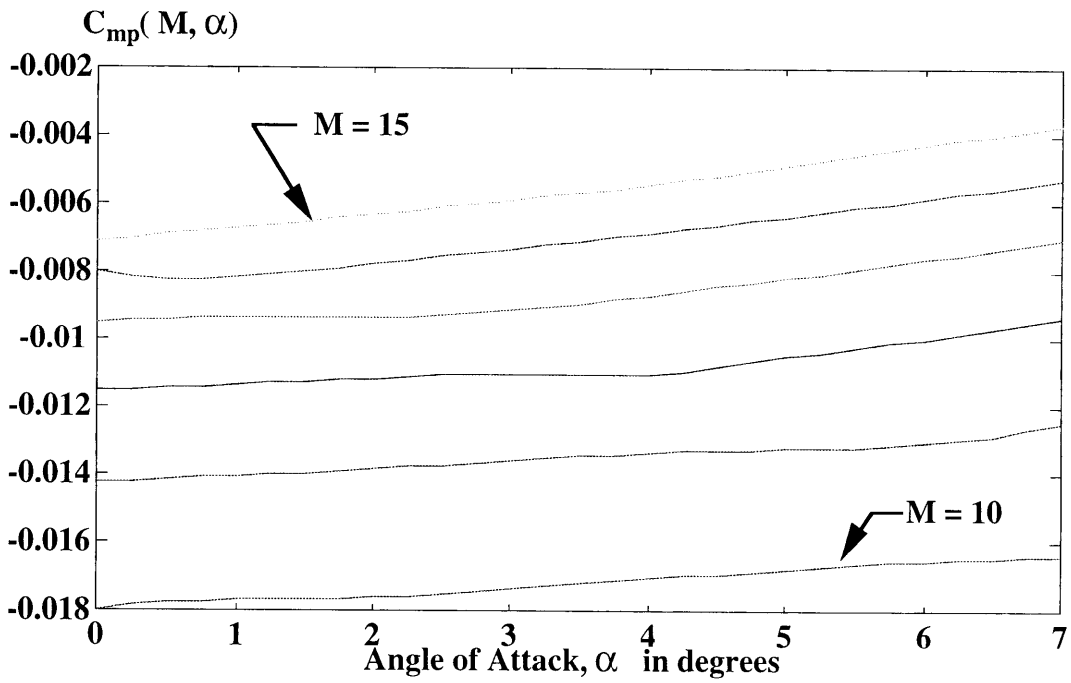

Figure 5.10 Propulsion Moment Coefficient

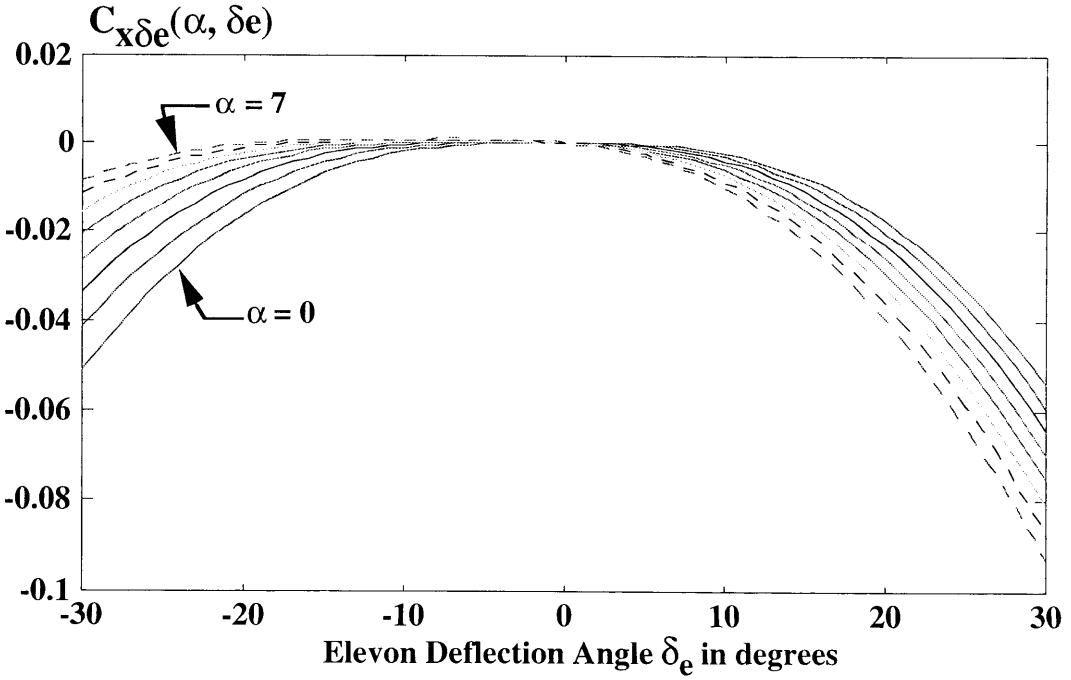

Figure 5.11 Elevon Control Coefficient - X-direction

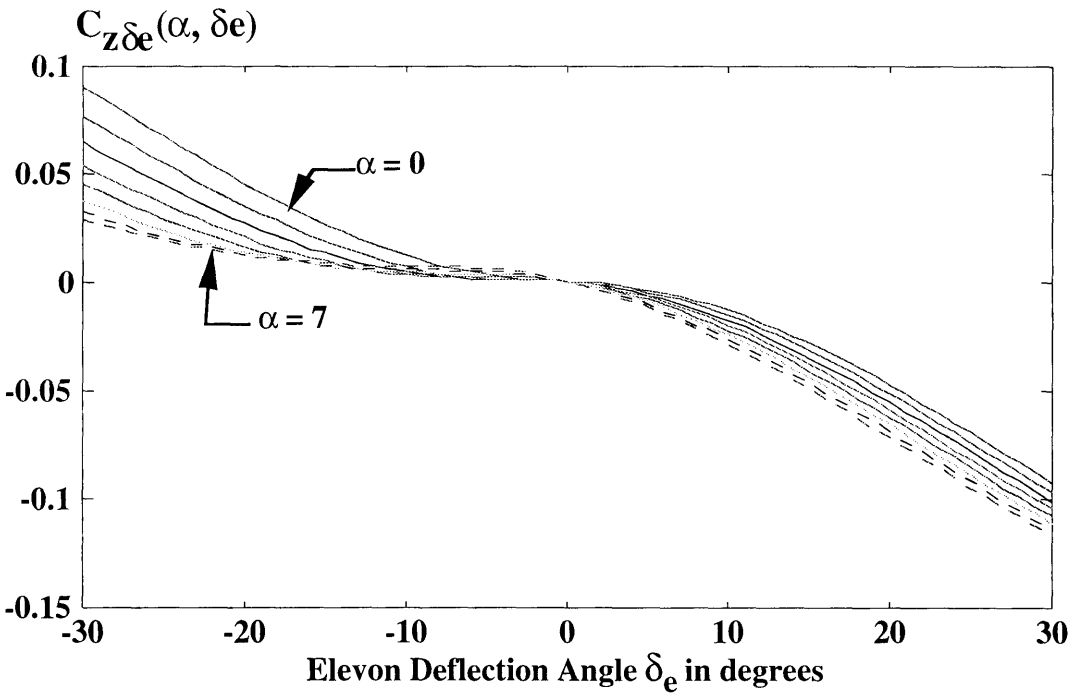

Figure 5.12 Elevon Control Coefficient - Z-direction

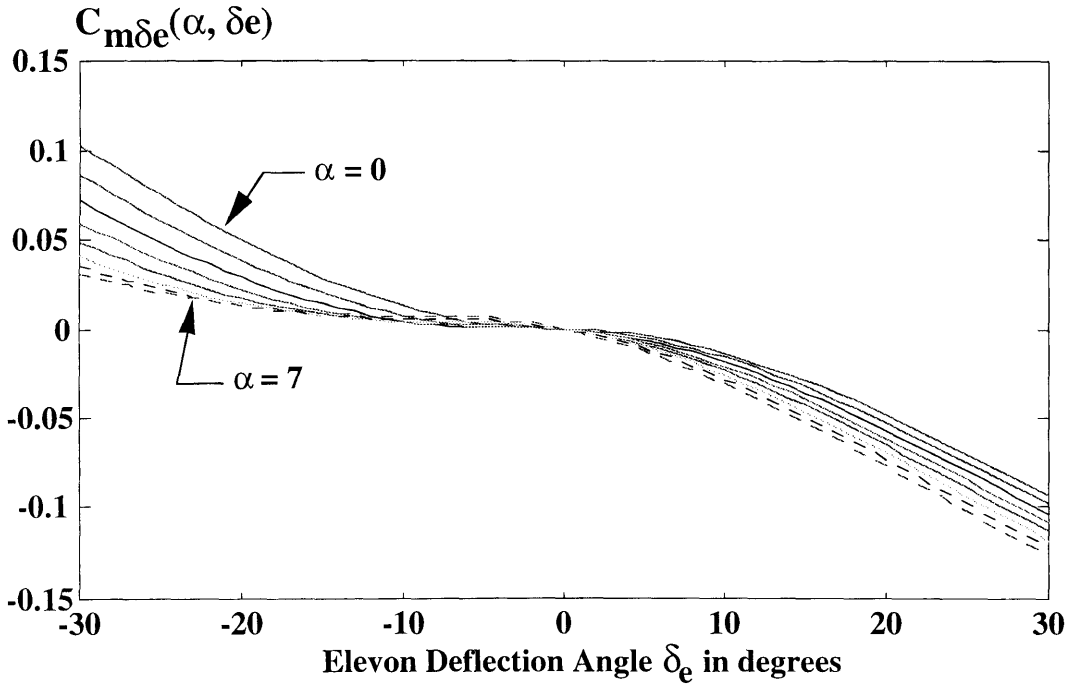

Figure 5.13 Elevon Control Moment Coefficient

The resulting Block diagram of the LVLH formulation (Equation 5.18) is shown in Figure 5.14.

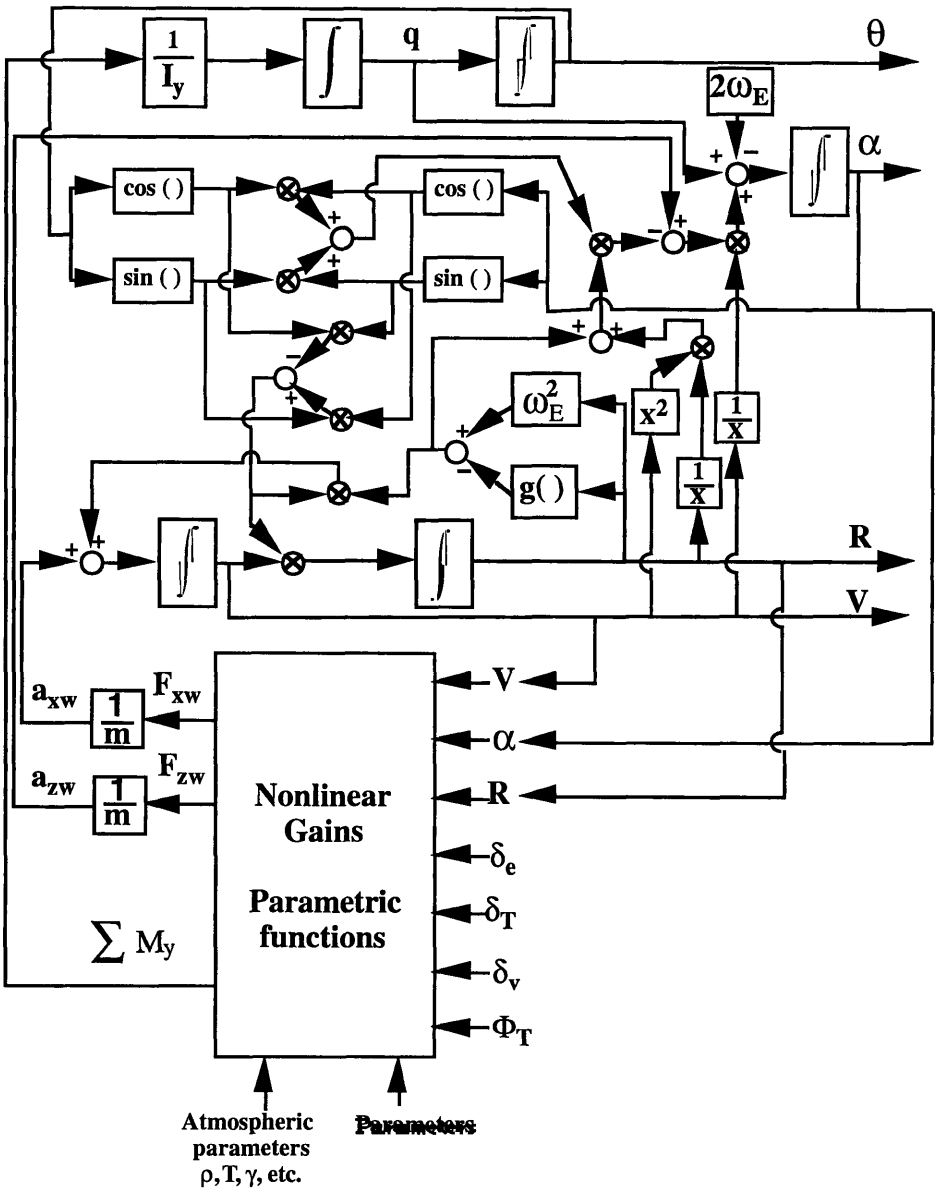

Figure 5.14 Block Diagram of AHSV Equations of Motion in LVLH frame

Term Sizing:

In order to determine the magnitude of centripetal and Coriolis effects imposed on the vehicle equations of motion, each of the additional terms should be calculated. The analysis are based on a rotating spherical earth assumption. It is desirable to compute

each of the centripetal and Coriolis terms as functions of the state variables. From equation (5.18), the terms $\omega_E^2\mathbf{R}$, $\frac{V^2}{\mathbf{R}}$, and $2\omega_E V$ appeared due to a rotating spherical earth assumption. These terms can be calculated and compared with respect to g(**R**), the gravitational acceleration.

The term $\omega_E^2\mathbf{R}$ is only a function of **R**. Since **R** is defined as the earth radius plus flight altitude, the term varies little within the altitude range of an air-breathing corridor. The parameter ω_E is the earth's rotational rate and it's value is 7.3E-5 rad/sec. Since **R** is the earth radius plus altitude, it's value is approximately 6400km. So $\omega_E^2\mathbf{R}$ is about 3.4E-2 m/s^2. In terms of g, it is 3.5E-3 g's . So it is very small compared to gravitation effect. Also it is not dependent on other state variables.

Now compare $\frac{V^2}{\mathbf{R}}$ with respect to g(**R**). This is the centripetal acceleration and it is dependent on V to the second power. Its functional dependence with respect to velocity is plotted in Figure 5-15 below.

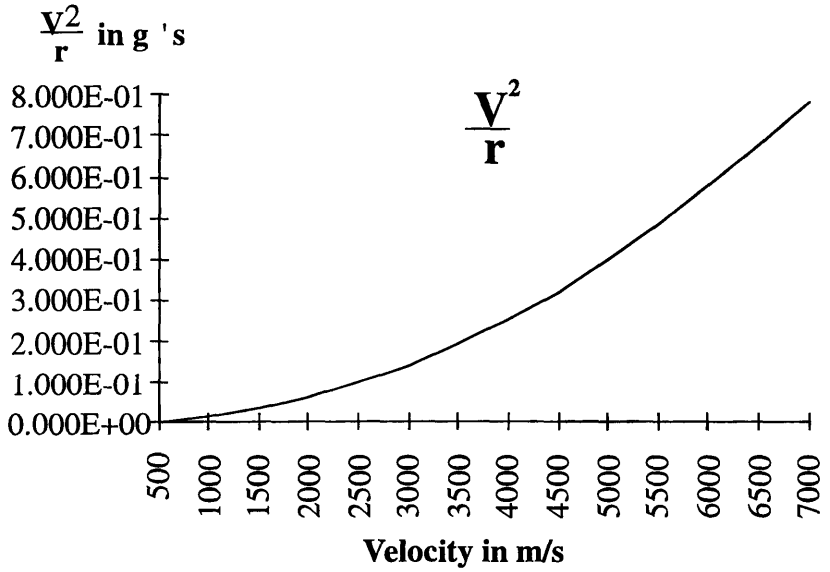

Figure 5-15 Plot of Centripetal Acceleration

Within the low Mach number regime, it stayed under 0.1g. However as Mach number increases, it can approach 1g. The term $2\omega_E V$ (Coriolis acceleration) stayed below 0.1g most of time. It is plotted in Figure 5-16 below.

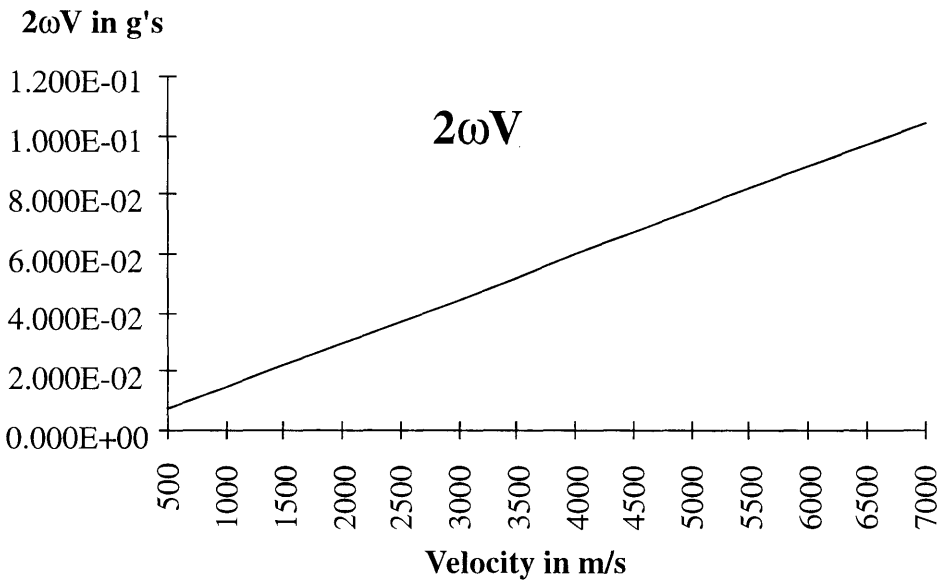

Figure 5-16 Plot of Coriolis Acceleration

5.2 Modeling of Air-Data and Inertial Sensors

Sensor classes, which is needed for proper operation of AHSVs, is presented here for the purpose of setting up observation equations within the scope of the air-data estimation problem. The sensors are analyzed and modeled specifically for use in the air-data estimation problem. Given the objective of obtaining high accuracy air-data information, the air-data estimation problem establishes a guideline for the mathematical representation of the sensors. In order to implement the estimation theory for AHSVs, sensor models are needed in the form of differentiable real-valued functions. Also the Wiener (Brownian motion) process representations for the random components of the sensor noise are highly desirable in order to use readily available and tractable estimation theory. Therefore, the inertial and air-data sensors, which are required and selected for AHSVs, are reviewed and their mathematical models are derived. These mathematical descriptions of the sensors are then combined in a realistic combination to form the observation equations. With realistic numerical values assigned to the models, they are used within the simulation to complete the numerical analysis in later Chapters.

The purpose of the measurements, which provide information on the inertial and air-data state, is to provide necessary information for the operation of propulsion, navigation, guidance and control systems. The measurements will be processed through the estimation algorithms to provide the inertial and air-data states, then the estimated state parameters are distributed to propulsion, navigation, guidance and control systems. If there exists a set of perfect sensors that directly measure the desired states and parameters, then signal processing, including state estimation, is not needed; however, the applicable sensors are far short from being ideal measurement devices. Therefore, accurate modeling of the sensors is important to insure the fidelity of the estimates along with the modeling of the vehicle motion.

Much of the research effort on this project has been devoted to demonstrating the model formulation methodologies and deriving the sensor models. The important aspects of the sensor modeling procedures, include study of the physics involved in the sensing process, derivation of the mathematical models for that physical process, reflection of the estimation problem onto the sensor models, and the formation of the observation equations (i.e. the sensor models). The observation processes are then analyzed based upon the investigation of the physics of the sensor mechanism and the sensing medium. The derived physical law provides the mathematical description of the measurement

process, the observation equations. The resulting mathematical descriptions of the sensors has a major impact on the estimation process. Because the sensor models are combined to determine the estimator observation equations , the formulated mathematical depiction of the sensors can greatly alter the estimation strategy. For example, measurement of the velocity vector defined in rectangular coordinates, with the sensing axis also defined in rectangular coordinates results in a linear set of observation equations while use of polar or spherical coordinates result in nonlinear observation equations.

The nature of the random components of sensor signals must be investigated because the characteristics of the sensor noise, such as its probability densities, influence the estimation algorithm. Most importantly, it is desirable to know whether the noise can be represented as a Wiener (Brownian motion) process since most available and tractable estimation theories rely on the Gaussian assumptions of the process and measurement noise. The sensor noises includes the inherent sensor device noise as well as sensor environment noise. As part of an engineering analysis, it is important to predict how well each sensor can measure as well as its bandwidth.

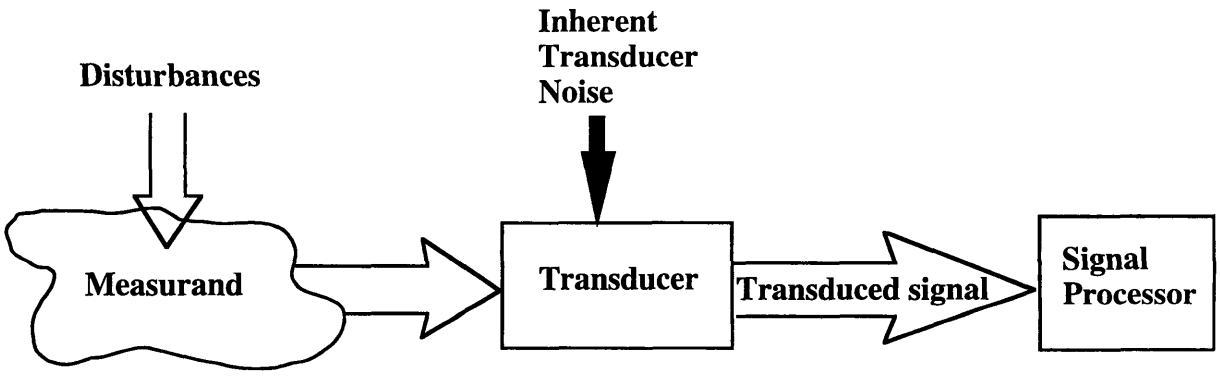

Figure 5-17 Measurement Process

5.2.1 Characterization and Treatment of Sensor Noise

The measurement process can be viewed as shown in Figure 5-17. The noise and error involved with the measurement process can be attributed to three sources: The inherent transducer noise; Errors in the interface between the transducer and the sensing medium (measurand); The disturbances experienced by the sensing medium. For example, the pressure measurement at a vehicle's surface has uncertainties that come from the pressure transducer noise, errors introduced by the orifice and alignment, and

pressure error and fluctuations induced by the flow around the vehicle. During the process of the sensor modeling, the interactions which occur between the measurand and transducer are augmented with transducer dynamics to obtain a sensor system. The inherent errors and noise appear due to the interactions between measurand and transducer combine with transducer noise as the overall sensor system noise.

Due to limitations in existing estimation theory, it is desirable to have the sensor noise in the form of a Wiener (Brownian motion) process. Most sensor noise can be described this way, and in many cases it is justified to assume a fictitious white Gaussian noise. If the noise can be assumed to be in this form and has a finite power spectrum, then it can be modeled using colored dynamics which are driven by white noise. The sensors can also have a non-random components of noise such as temperature induced drifts or integration drifts. A bias should also be modeled if such factor is significant. The states can be augmented to treat the bias as a fictitious additional state to be estimated. The most important part of treating this noise effect is verifying the adequacy of the Wiener process assumption. Using these models of sensors and the associated noise, the estimation problem will be formulated in later chapters.

5.2.2 Inertial Sensors

Most classes of aircraft and spacecraft have some form of inertial sensors for the purpose of flight control, guidance and navigation. The AHSV is no exception. Inertial sensors of a similar to the Space Shuttle IMU (though updated) would likely be employed. The inertial sensors for the AHSVs are assumed to include a GPS receiver and IMUs. IMUs contain three-axis integrating rate gyros to measure attitude and attitude rate. Also inertial platforms update and correct the attitude bias errors. IMUs normally contain three-axes linear accelerometers and integration units. Recently there has been great emphasis on GPS-IMU integration. Since use of the GPS involves slow update rates (about 1Hz) and IMUs have inherent drift problems, GPS and IMU data is combined to take advantage of high IMU bandwidth and using GPS to update and correct position and translational velocity errors every few seconds. It is perfectly justified to treat the combined GPS and IMU system as a single inertial sensor system.

GPS Receivers: GPS measurements are based on telemetry from a constellation of satellites that, when processed, provide extremely accurate inertial

position and translational velocity data. There are no inherent dynamics associated with the GPS positioning process. GPS performance is limited by its update rate and intentional signal corruption if encrypted code is not utilized. The typical update rate is in the order of seconds. Normally a Kalman filter is present within a GPS receiver, and it is typical to have the covariance of the output signal. GPS measurement noise can be modeled in terms of a bias and Gaussian random noise [Tao1]. A representative sensor and noise model are shown in Figure 5-18. Typical GPS performance is tabulated in table 5-1.

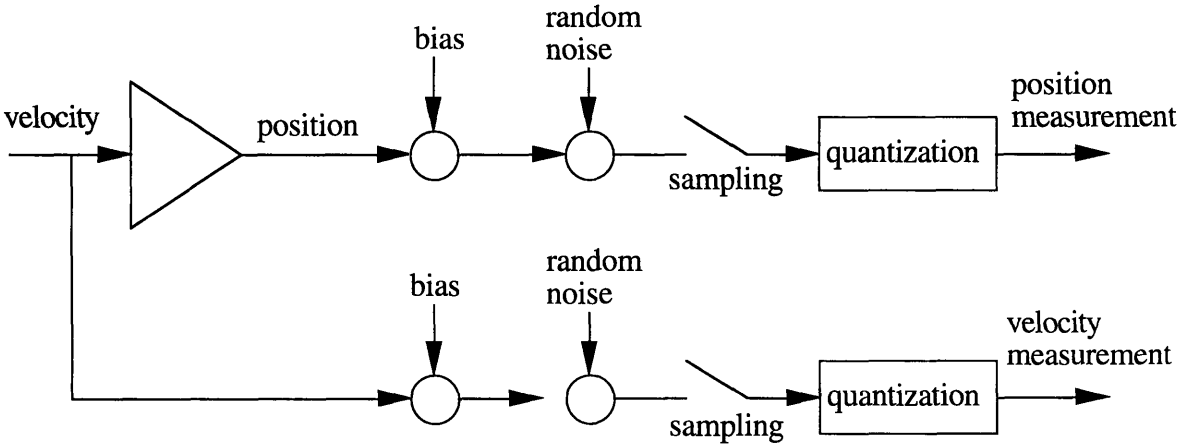

Figure 5-18 System Representation of GPS

Table 5-1 Typical GPS Specification

GPS Pseudo-Range Measurement Specification	
Bias	30 ft/axis
Noise	5 ft/axis
GPS Velocity Measurement Specification	
Bias	1 fps/axis
Noise	0.1 fps/axis

Gyros: Typical IMUs contain either mechanical or optical gyros in all three axes. Mechanical gyros are sometimes still considered because of their superior performance or because of the new trend toward micro-machined devices. The dynamics associated with mechanical gyros can be modeled using either a first or second order low-pass filter. The transfer function of a rate gyro from an angular velocity input to a gimbal angle output is:

$$\frac{\theta_g}{\omega_i} = \frac{H_g \omega_n^2}{k\left(s^2 + 2\zeta\omega_n s + \omega_n^2\right)} \tag{5.22a}$$

where

$$\omega_n = \left(\frac{k}{I_{ga}}\right)^{\frac{1}{2}} \quad \text{and} \quad \zeta = \frac{k_d}{2(kI_{ga})^{1/2}} \tag{5.22b}$$

The transfer function of a rate integrating gyro from an angular velocity input to a gimbal angle output is

$$\frac{\theta_g}{\omega_i} = \frac{H_g}{s\left(I_{ga}s + k_d\right)} \tag{5.23}$$

The gimbal angle derived from a rate gyro is proportional to the rate input. Also the gimbal angle derived from a rate integrating gyro is proportional to the time integral of the rate input. For example, the steady state value of the gimbal angle for a step rate input is given by

rate gyro	rate integrating gyro
$\theta_g = \frac{H_g}{k}\omega_i$	$\theta_g = \frac{H_g}{k_d}\int_0^t \omega_i dt$

(5.24)

Typical roll-off frequency will fall between 12 to 40Hz; however, ring laser gyros are capable of measuring at 500Hz with medium accuracy if the bandwidth becomes a limiting factor (note: fiber optic devices (e.g. IFOG) have even higher bandwidth!). The random components of noise associated with the gyros are assumed to be a Wiener process. The typical gyro error is tabulated in table 5-2 below[Tao1].

Table 5-2. Typical High Performance Gyro errors (1-sigma)

Drift Rate Bias Repeatability	0.02	deg/hr
Scale Factor	200	ppm

On the basis of the dynamics of gyros and gyro errors, a gyro model is formed and shown in Figure 5-19 below.

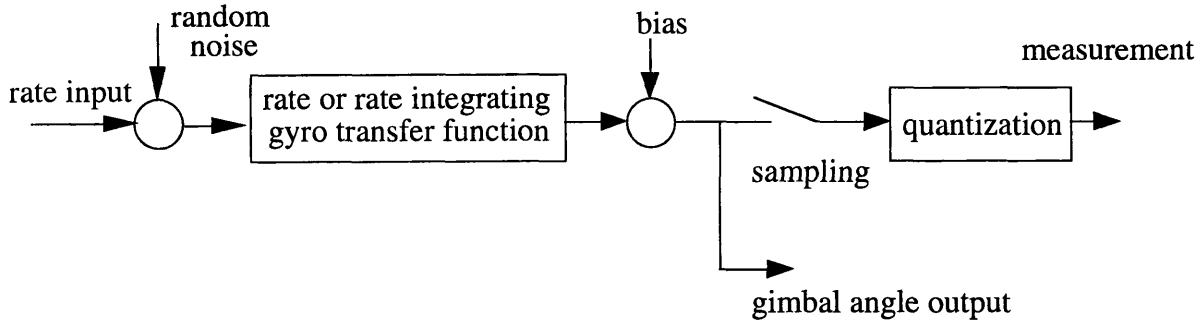

Figure 5-19 System Representation of Gyro

Accelerometers: Similar to the gyro dynamics, accelerometer dynamics can be modeled by either a first or second order low pass filter. The typical mechanical system can be modeled as a mass - spring - damper system. The frequency response of a typical accelerometer can exceed 100Hz. A representative sensor and sensor noise models are shown in Figure 5-20. The typical sensor error[Tao1] is tabulated in table 5-3.

On the basis of previous experiences on integrating these inertial sensors on flight vehicles, the noise characteristics of sensors can be assumed as Wiener processes. If the bandwidth of the vehicle dynamics and/or estimation method is greater than or near the inertial sensor bandwidth, then the dynamics of the sensors need to be augmented at the cost of increasing the dimension of the filter state vector.

Table 5-3. Example Precision Accelerometer Errors

Bias Repeatability	150	μgs
Scale Factor	200	ppm

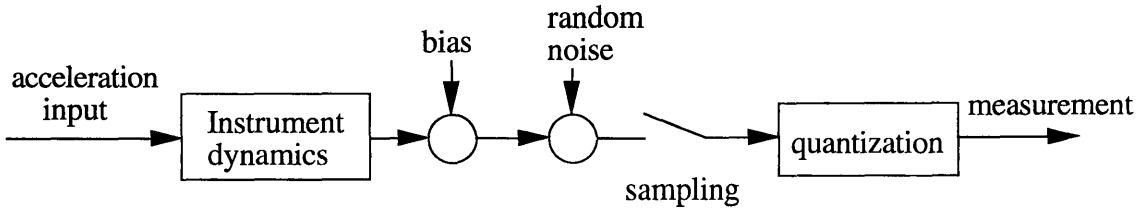

Figure 5-20 System Representation of Accelerometer

5.2.3 Pressure Measurement Based Air Data Sensing Techniques

Pressure measurement based air data systems(ADSs) have been applied to flight vehicles for flight regimes spanning subsonic to hypersonic. Examples include the X-15 and the Shuttle. Heavy thermal load during AHSV cruise prohibits the use of an ideal long nose boom sensor. Therefore the deployable Pitot probe that is similar to the Shuttle ADS is considered a candidate only at speeds below Mach 3.5. A nose pressure field measuring technique similar to the SEADS[Pru1] would also be a good candidate if the AHSV nose permits insertion of pressure ports and the nose cap can be sufficiently cooled to protect the structure and the pressure sensing devices.

The main disadvantages of pressure based air data sensors are flow field - sensor interaction and thermal loads. Since pressure measurements are obtained after flow-vehicle interactions occur, such as shock waves, the function which describes flow-vehicle interactions must be inverted in order to obtain free stream parameters. Therefore extensive knowledge of the flow around the vehicle is needed. In order to minimize the vehicle-flow interaction errors, the pressure sensors must be installed in the vehicle nose region. However, the thermal loads will be maximum at the nearly co-resident stagnation point. Any intrusive technique should be avoided and active cooling is likely to be necessary.

Pitot probes: The Shuttle deploys two Pitot probes, one on either side of the forebody, at Mach numbers less than 3.5.[Hil2] There are upper and lower pressure ports next to the total pressure port to measure the angle of attack. The blunt forebody of the Shuttle causes significant flow field interference, and the sensors have to be calibrated by extensive wind tunnel tests[Hil2]. Even though the operating range is somewhat limited, this technique may be applied to the AHSV directly. By selecting high temperature materials, the operating Mach number may be extended up to 5. Also additional pressure ports at the sides of the total pressure port could measure the side slip angle and the angle of attack. Vehicle-flow interaction can be expected to affect measurements on AHSVs as on the Shuttle with similar empirical calibration requirements.

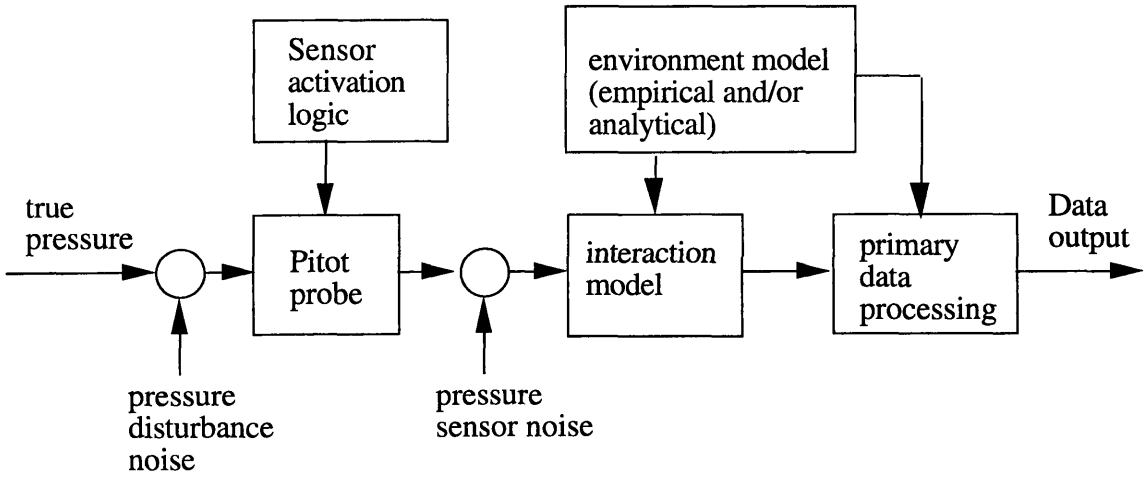

Figure 5-21 System Representation of Pitot Probe

The typical data flow arrangement is shown in Figure 5-21. The sensor deployment logic will keep it active only at Mach numbers less than 3.5 (or maybe up to 5). There are either empirical and/or analytical models to minimize sensor-body

proximity effects. After transforming the pressure data to account for interaction effects, they are processed to provide air data parameters.

The measurement equation can be simplified and written as

$$P_{mi} = P_i \pm P_n \tag{5.25}$$

where the P_i is the true valued pressure at the i-th pressure sensor and the P_n is the corresponding pressure noise including pressure disturbance and sensor noise, and is assumed to be zero-mean Gaussian white noise if the pressure transducers are temperature compensated as well as compensated for other drift sources. Each pressure transducer has its own dynamics such as the maximum structural and electrical bandwidth of the device. The dynamics may be modeled as a first order low pass filter. There are also pressure bias errors, but they are assumed to be small after the temperature effects and built in device compensation. Note that the pressure disturbance noise discussed here includes only the pressure port errors and the errors caused by the boundary layers. Vehicle-flow interaction errors such as sensor position errors and shock wave induced errors are not included. They are treated later through function inversion.

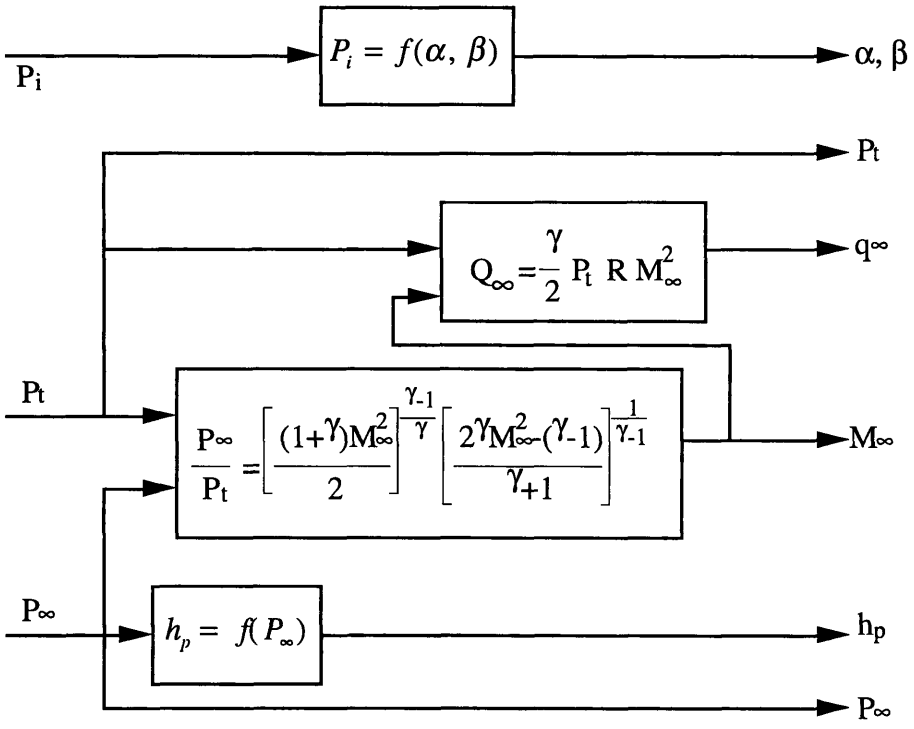

Figure 5-22 Detailed Block Diagram of Functional Relationship Between Surface Pressures to Air-Data States

Once the pressure measurements are corrected for vehicle-flow interaction errors, the total and static pressure measurements can be further processed as shown in Figure 5-22. The Mach number, velocity, and dynamic pressure are computed from the Rayleigh Pitot formula. The errors in the dynamic pressure measurement diminish as the Mach number increases because the measurement becomes mostly dependent on the total pressure, not on the static pressure and Mach number. The extra pressure ports P_i which are located next to the total pressure port, are used to measure the angle of attack and angle of side slip by comparing the pressure differential of two symmetric ports. The environment model can be used to improve the measurement by updating the specific heat, and the pressure altitude function.

SEADS-like system: The fundamental concept behind SEADS-like[Pru1] systems is very similar to the Pitot probe system. Instead of deployable probes, the forebody of the vehicle is used as a probe. Multiple pressure sensors are flush mounted on the nose section of the vehicle. The surface pressure distribution is measured by the array of flush mounted sensors. A mathematical description of the forebody pressure distribution is used to obtain the air data state parameters.

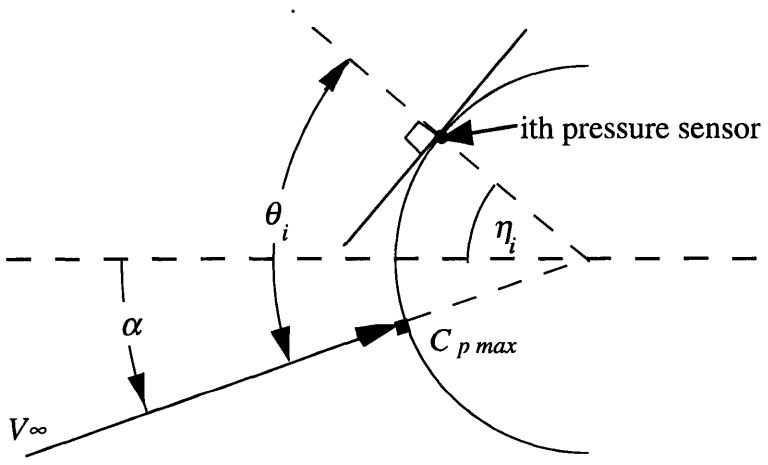

Figure 5-23 Modified Newtonian Approximation of Round Nose

On the basis of the modified Newtonian model, the pressure at the i-th orifice can be written as:

$$P_i = (P_t - P_\infty)\cos^2\theta_i + P_\infty \quad \text{for } M_\infty >> 1 \tag{5.26}$$

where θ_i is the flow incident angle at the i-th orifice (90 deg. incidence, the flow angle to the normal to the surface). The θ_i can be written as:

$$\cos\theta_i = \cos\alpha\cos\beta\cos\eta_i + \sin\beta\sin\eta_i\cos\zeta_i + \sin\alpha\cos\beta\sin\eta_i\sin\zeta_i \tag{5.27}$$

where η_i is the cone angle and ζ_i is the clock angle. If only the longitudinal motion is considered, as shown in Figure 5-23, the equations (5.26) and (5.27) simplify to:

$$P_i = (P_t - P_\infty)\cos^2(\alpha + \eta_i) + P_\infty \quad \text{for } M_\infty >> 1 \tag{5.28}$$

Since the Rayleigh Pitot formula is:

$$R \equiv \frac{P_\infty}{P_t} = \left[\frac{2}{(\gamma+1)M_\infty^2}\right]^{\frac{\gamma}{\gamma-1}} \left[\frac{2\gamma M_\infty^2 - (\gamma-1)}{\gamma+1}\right]^{\frac{1}{\gamma-1}} \quad \text{for } M_\infty > 1 \tag{5.29}$$

the equation (5.28) can be written as:

$$P_i = P_t\left[(1 - R(M_\infty))\cos^2(\alpha + \eta_i) + R(M_\infty)\right] \quad \text{for } M_\infty >> 1 \tag{5.30}$$

Thus the state variables are $[P_t, M_\infty, \alpha]$.

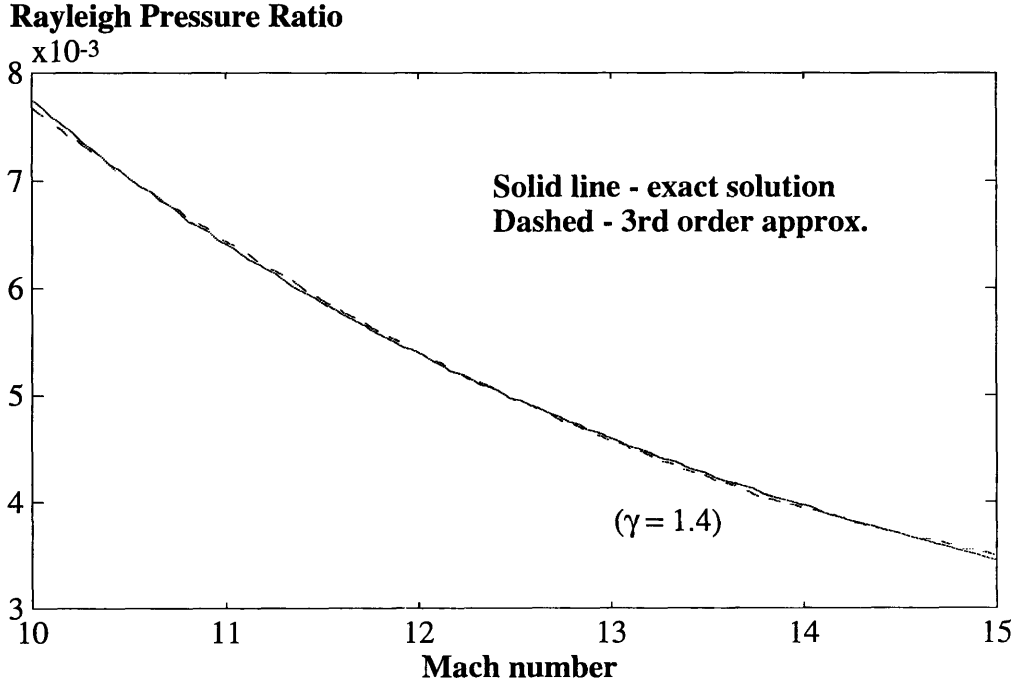

Figure 5-24 Plot of Rayleigh Pitot Formula (γ=1.4)

Equation (5.29) can be approximated with a polynomial function for a small segment of the flight trajectory. For Mach numbers between 10 to 15, where most of the analysis and simulation have been carried out, the Rayleigh pressure ratio has been approximated with a third order polynomial to reduce computation time. The resulting approximation is:

$$R(M) \cong a_3 M^3 + a_2 M^2 + a_1 M + a_0 \tag{5.31}$$

where $[a_3, a_2, a_1, a_0] = [-1.0777e-5,\ \ 5.046e-4,\ \ -8.354e-3,\ \ 5.1584e-2]$

and the Rayleigh pressure ratio is plotted against Mach number in Figure 5-24 along with its approximation.

Each of the pressure sensors and associated noises can be modeled as shown in Figure 5-25, and the noises are augmented as pressure disturbances and assumed to be Wiener processes. The pressure transducer noises are of thermal Johnson type which appears typical of electrical devices and they are Gaussian in nature. The pressure errors are largely non-random due to orifice-surface pressure interactions. Most of the random pressure noise would be of the acoustical (through structure) type.

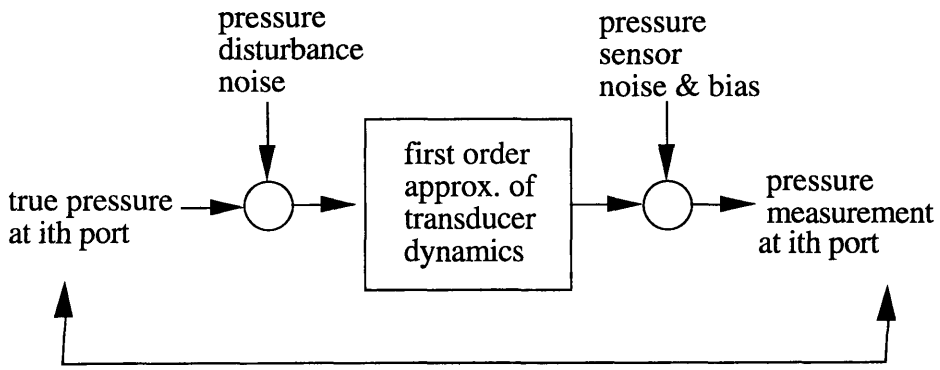

For ith pressure sensor

Figure 5-25 Pressure Port Model for SEADS Like System

For assistance to SEADS-like systems, the stagnation temperature of the flow can be measured with thermocouples located at the stagnation point. The measured total temperature or total enthalpy can be converted into the flow velocity by the equation:

$$H_o - H = \frac{\varepsilon}{2gJ} V^2 \tag{5.32}$$

The uncertainties in free stream temperature penalize the accuracy in low speed measurements. If the free stream temperature can be directly measured, the accuracy will improve. For example, a deviation of 70°R in atmospheric temperature from an assumed 400°R will produce a 100 ft/sec error at Mach 5. As the velocity increases, errors due to uncertainty in free stream temperature would be smaller since the total enthalpy would be much greater than free stream enthalpy; however, at high Mach numbers, the thermal

radiation from the structure would be quite large and will introduce large errors. Therefore, at higher Mach numbers, optical sensors must be used to determine free stream temperature at a distance from the vehicle.

5.2.4 Air Data Sensors, Laser-Optical Techniques

Rayleigh Scattering: Rayleigh scattering is an elastic scattering process where the frequency of the scattered light (electromagnetic wave) is well removed from a resonance in the atom. The scattered light varies from the source frequency due to the Doppler shift resulting from the velocity of the moving gas. The scattered intensity is proportional to the density of scattering molecules. The broadening of the scattered light spectrum is dependent on the temperature of scattering molecules and the Doppler shift is dependent on the mean molecular velocity. On the basis of these first principles, density, temperature, and velocity of the flow can be measured. A Rayleigh scattering sensor may operate in a wide altitude range, up to well over 200k ft. The upper bound is determined by the minimum number density of scattering molecules that can produce a detectable return signal. The lower bound is determined by Mie scattering effects due to high entrained particle concentration at low altitude. A typical Rayleigh sensor model is shown in Figure 5-26.

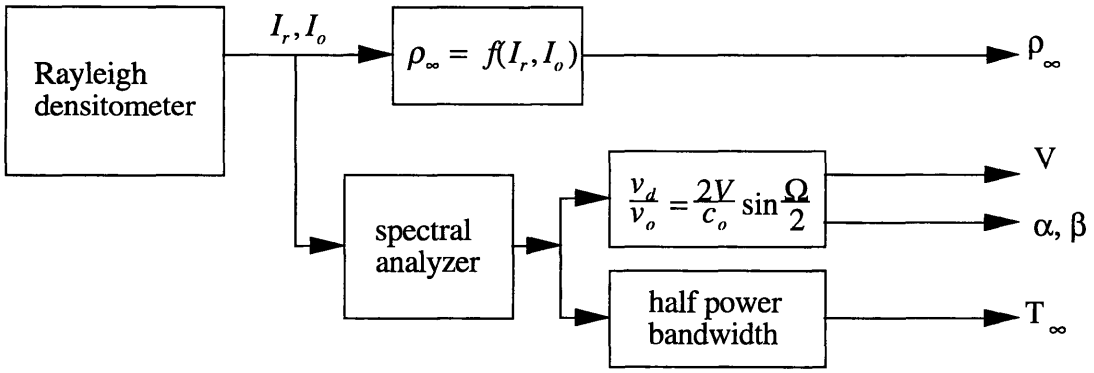

Figure 5-26 Block Diagram of Rayleigh Scattering Sensor

The sensor model for the density measurement can be formed from the first principles. The Rayleigh scattered power is given by;

$$I_r = I_o L \Omega_c \eta_c \eta_d \sum_i N_i Q_i \tag{5.33}$$

Based on the measurement of I_r and other known parameters, the flow density can be estimated. Notice that the Rayleigh cross-section of the species must be known. The major source of measurement process uncertainty is the Rayleigh cross-section estimate. The error due to the variations in ambient gas composition is estimated to be less than 15%.[Mil1] The sensor noise can be modeled as shot noise with standard deviation proportional to the square root of the number of detected Rayleigh photons. The noise intensity can be expressed as follows:

$$|V(k)| = \left| \left(\frac{I_r h\nu}{\Delta t n_p} \right)^{\frac{1}{2}} \right| \tag{5.34}$$

The sensor noise decreases as the pulse duration and the number of pulses during the measurement interval increase; however, the sensor bandwidth decreases. The measurement equation can be written with additive noise as shown below:

$$I_{rm}(k) = I_r(k) \pm V(k) \tag{5.35}$$

Since the noise model contains the square root of the Rayleigh scattered intensity, defining a new state Z_m as the square root of the intensity results in a simpler measurement equation, as shown below:

$$Z_m = \frac{P_{rm}}{\sqrt{P_r}} = \sqrt{P_r} \pm \left| \frac{h\nu}{\Delta t n_p} \right|^{\frac{1}{2}} \tag{5.36}$$

Another source of noise is the Mie scattering from particles. This noise depends on the altitude and the sensor location. The noise increases as altitude decreases since more entrained particles are present at lower altitude.

The Doppler shift in Rayleigh scattered light can be measured by spectroscopic equipment, such as the scanning Fabry-Perot etalon. The Doppler shift frequency and the flow velocity are related by the expression below:

$$\frac{\nu_d}{\nu} = \frac{2V}{c} \sin \frac{\Omega_e}{2} \tag{5.37}$$

where ν_d is the Doppler shift frequency, ν is the laser frequency, c is the speed of light, V is the flow velocity. Three orthogonal sensors are needed to resolve all three velocity components. The major measurement error is in the process of resolving the median

frequency from the broadened spectrum. Another measurement error arises from the spatial resolution and alignment error at the sensing section of the laser beam. The accuracy of this technique is estimated to be about ±2.5%.[Hon1] Also the spatial resolution is ±0.75 deg.[Hon1]

Another performance estimate comes from reference [Tib1]. Based on a specially designed molecular filter to resolve the 50% transmission point (center point of the Doppler broadened return signal), the author concludes that the Rayleigh scattering device can measure the velocity of a sample to about 0.3% at 30km altitude. The performance degrades as altitude increases, because the sensor performance is limited by photoelectron shot noise from the detected signal that increases with altitude. At 60km, the measurement uncertainty is expected to increase to 2%; and will further increase to 19% at 90km altitude. In order to obtain flight velocity and flow angle parameters (angle of attack and side slip angle), the measured velocities of sampled air have to be transformed to body axes as shown in Figure 5-27.

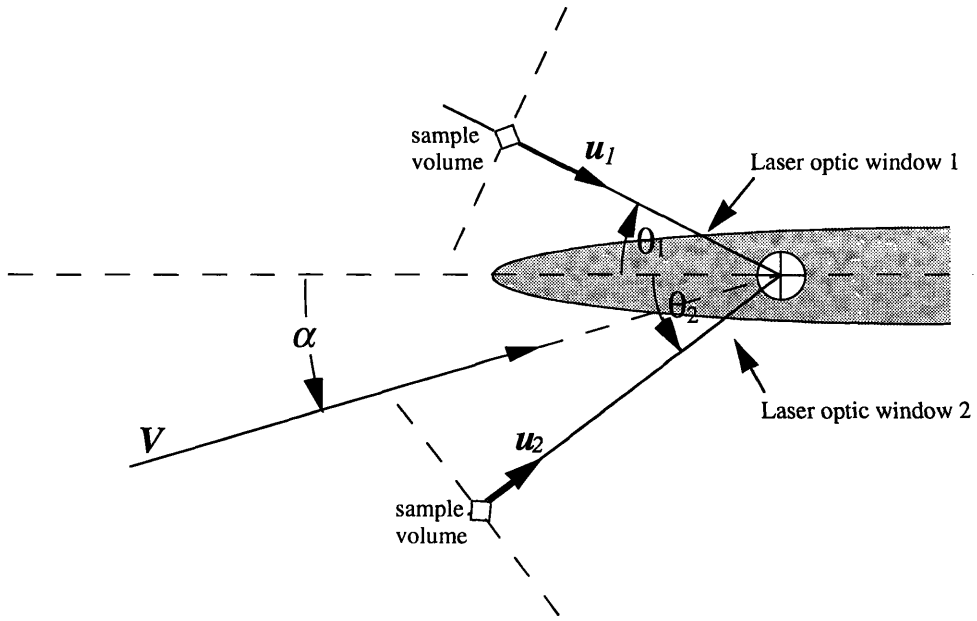

Figure 5-27 Definition of Sensing Coordinate for Rayleigh Scattering Sensors

The measurement equation is

$$\begin{aligned} u_1 &= V\cos(\theta_1 + \alpha) + n_1 \\ u_2 &= V\cos(\theta_2 - \alpha) + n_2 \end{aligned} \tag{5.38}$$

where u_i is the velocity measurement, V is the true velocity and the n(t) is the associated velocity measurement noise.

The broadening of the scattered light spectrum is dependent on the temperature of the scattering medium. By measuring the half power width of the spectrum of the Rayleigh scattered light, the temperature of the flow can be measured. The accuracy of temperature measurement depends on the Q factor of the Fabry-Perot spectrum analyzer's ability to resolve half power width of the broadened spectrum. Also, the intensity of the returned signals plays a key factor in the sensor noise characteristics for this state measurement.

Laser Induced Fluorescence: The laser induced fluorescence technique uses the properties of the electromagnetic wave induced resonance of the scattering particles [Mil1]. When the laser frequency is tuned to the resonant frequency which is a unique signature of the tracing molecules, the particle fluoresces at the resonant frequency and generates stimulated emission. A fluorescence tracking velocimetry uses a laser beam to coherently pump(tag) a small volume of gas upstream to meta-stable level, then another laser which is located downstream elevates the energy of the pre-tagged volume. When the energy level of the molecule reaches a critical point, an electron decays and create fluorescence. Only the pre-tagged volume will respond to the sensing beam since only the energy level of the pre-tagged molecules will be resonant with the sensing beam frequency. The optical detector is used to sense the presence of the fluorescence. The sensor configuration is demonstrated in Figure 5-28.

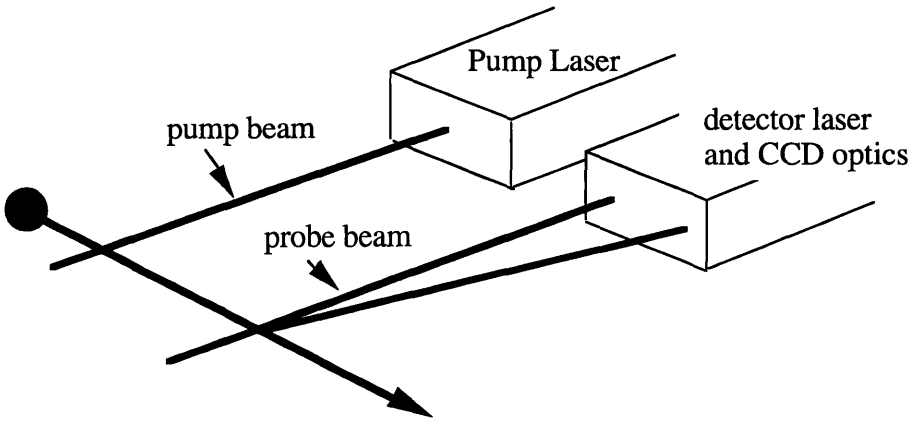

Figure 5-28 LIF Laser And Optical System Configuration

The velocity is determined by

$$V \approx \frac{X_{\text{detector}} - X_{\text{tag}}}{\Delta t} \tag{5.39}$$

which is the difference between the detector position and tagging position divided by the time of travel. The major error source is the spatial misalignment. Both angular position and magnitude error can result from misalignment of the tagging beam and the detector. The measurement noise would be a combination of spatial uncertainties and the false threshold of the fluorescence detection. The threshold of the detectable signal strength is dependent on altitude; and can be expressed as:

$$|S_m(h)| = |S(h)| \pm |S(h)| \exp\left\{6.9\left(h/h_o - 2\right)\right\} \tag{5.40}$$

or the equation can be expressed in terms of signal to noise ratio as:

$$\frac{S}{N} = \exp\left\{-6.9\left(h/h_o - 2\right)\right\} \tag{5.41}$$

where S_m is the measured detector signal, S is the true signal, and h is the altitude in ft., h_o is a constant with value of 300k ft. The noise is dependent on both the signal and the altitude.

The overall sensor placement and configuration are shown in Figure 5-29 below.

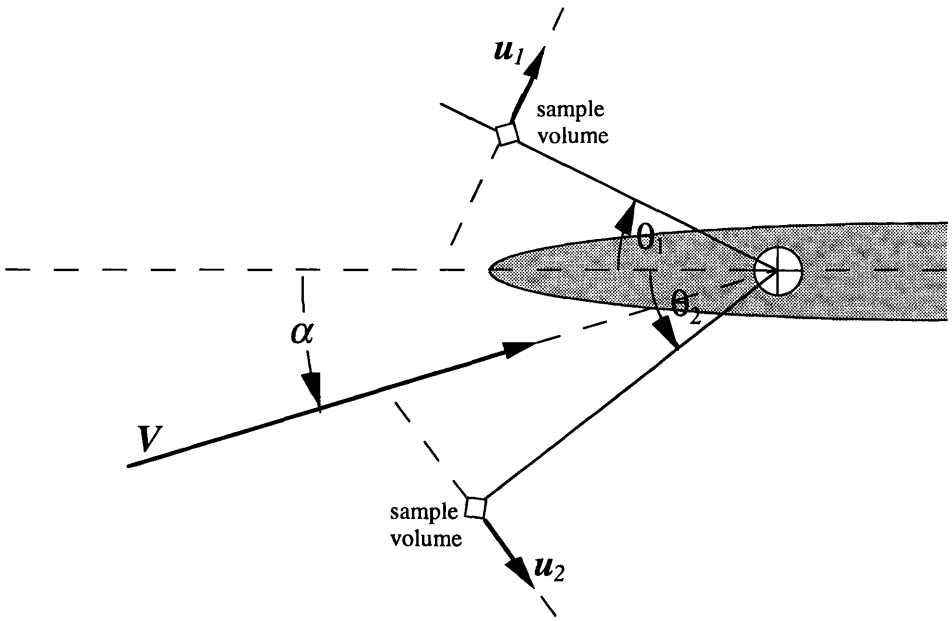

Figure 5-29 Definition of Sensing Coordinate for LIF Sensors

The resulting measurement equation is:

$$u_1 = V\sin(\theta_1 + \alpha) + n_1$$
$$u_2 = V\sin(\theta_2 - \alpha) + n_2 \qquad (5.42)$$

where u_i is the velocity measurement, V is the true velocity and the n(t) is the associated velocity measurement noise.

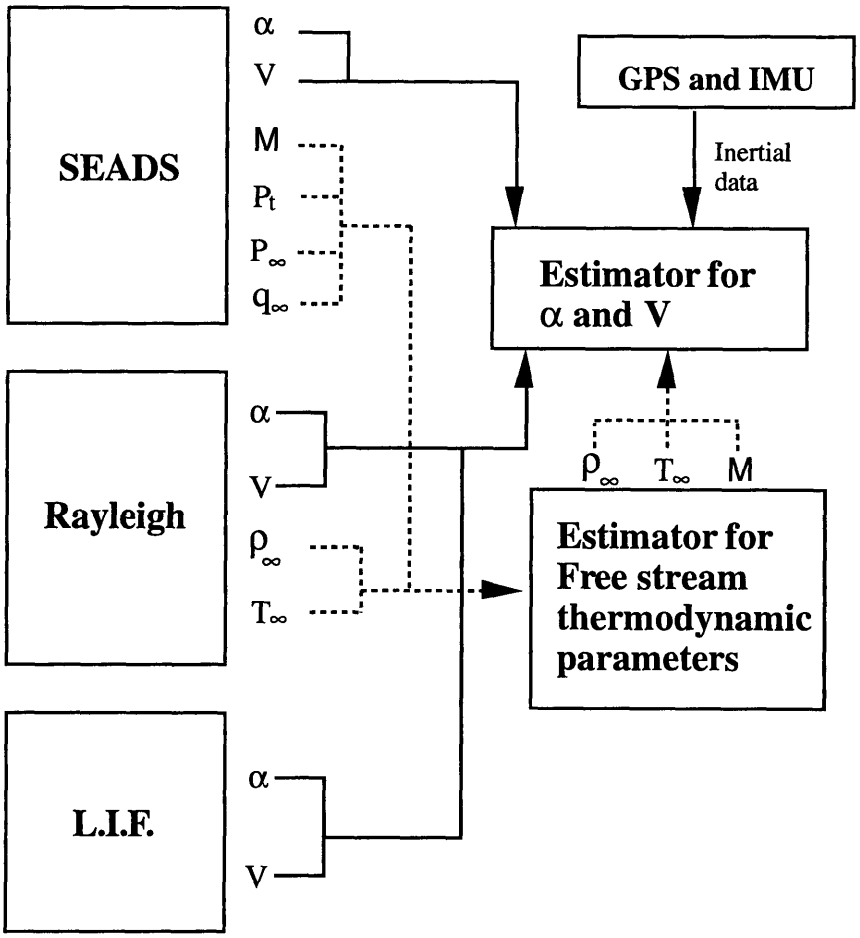

Figure 5-30 Information Route of Air-Data Sensor System

5.2.5 Air-Data Observation Equations

With the sensor models presented in previous subsections, the appropriate observation equations are formed and specialized for flight Mach number segment between 10 and 15. Also only longitudinal motion has been considered for simplicity and that the main findings should be extended to lateral motion for further development of the AHSV. For that Mach regime, SEADS and optical sensors are assumed to operate simultaneously. The sensor models resulted in two sets of observation equations; one for

angle of attack and true air velocity which are needed within the dynamic filtering, and the other for free stream thermodynamic parameters.

A five pressure transducer configuration has been selected for the SEADS-like system. The Shuttle uses an eight pressure sensor configuration for the longitudinal axis, but a configuration with fewer sensors was considered here because of the limitations in reduced computation time required for the numerical analysis. A two-sensor configuration has been selected for both optical sensors. The final design of the sensor information route is shown in Figure 5-30.

For the estimation of angle of attack and true air velocity, the resulting observation equations are:

$$\begin{aligned} P_i &= P_t\left[\left(1-R^*(V)\right)\cos^2\left(\alpha+\eta_i\right)+R^*(V)\right]+n_{p_i} \\ u_1 &= V\cos\left(35^o+\alpha\right)+n_1 \\ u_2 &= V\cos\left(30^o-\alpha\right)+n_2 \\ u_3 &= V\sin\left(35^o+\alpha\right)+n_3 \\ u_4 &= V\sin\left(30^o-\alpha\right)+n_4 \end{aligned} \tag{5-43}$$

where $\eta_i=[30^o,15^o,0^o,-15^o,-30^o]$. and n_i are associated noises.

For the estimation of free stream thermodynamics parameters, the resulting observation equations are:

$$\begin{aligned} P_i &= f\left(P_t,M,q_\infty\right)+n_{p_i} \\ P_{\infty i} &= \left(1-k_p\right)P_\infty+n_{p_\infty} \\ I_m &= {}^{I_r}\!/_{I_o} = k_r\rho_\infty+n_\rho \\ L_F &= k_F T_\infty+n_T \end{aligned} \tag{5-44}$$

5.3 Environment

The important parameters that depict the flight environment are the free stream thermodynamic states such as temperature, density, and pressure as well as the wind effects. This subsection reviews briefly which environment models are available for AHSV applications and the derived simple model for thermodynamics parameters that is used for the estimator design in later chapters. Most of the models that are presently available are numerical-empirical models and are not readily implementable with estimator design. The most serious problem with the available environment models is the excessive computation time required to access necessary information from a large data set. If higher fidelity is required, some segment of these data base models may be specialized (meaning simplified to finite and low dimensional, analytic vector functions) such that they can be implemented for AHSV on board computers. In the next few paragraphs, some methodologies, which seem to be promising for future work, are discussed. Also a simple atmosphere model has been derived such that the model is suitable for estimation.

5.3.1 Available Atmosphere Models

The wind effects can be sub-divided into turbulence and the mean value of wind magnitude and direction. Turbulence can be modeled as a first order Gauss-Markov process. The bias term of wind magnitude and direction can be modeled as a time-invariant vector field along the trajectory with a gradient that is only space dependent. The justification for the frozen field approximation is based on the reference [Hil1]. The wind direction and magnitude vary little within the time scale of interest. The probable wind magnitudes are selected from the reference [Tao1].

Due to the well-known nature of the thermodynamic state parameters at low altitudes (below 100 Kft), a simple model which is based on the perfect gas law and fluid-statics is selected. The density waves and density discontinuities which are commonly experienced at the higher altitudes are excluded in the low Mach model because their effects are small at the altitudes of interest [Rob1].

The Global Reference Atmospheric Model (GRAM-88)[Jus2] and the Four-D model[Jus1] are reviewed. A newer version of GRAM-88 is GRAM-90 with coverage of the altitude range as shown in Figure 5-31 along with the NASP trajectory. The 4-D

model covers altitudes up to 80kft and the Middle Atmosphere Program (MAP) covers from 100kt to up to 300kt. There is also an interpolation method to bridge the two models. Primary use of these models is to simulate the atmosphere, rather than predict the atmosphere. For our purposes, we are more interested in local, but accurate prediction of the atmosphere in order to improve the accuracy of the estimates. The most promising approach in estimation would be first to treat the atmospheric parameters as both random and deterministic, then to generate the most probable value of the atmospheric data and its uncertainties from GRAM and/or other atmospheric data such as balloon measurements prior to the flight. These values and uncertainties should be used as the basis for a first estimate of mean and variance of the atmospheric parameters.

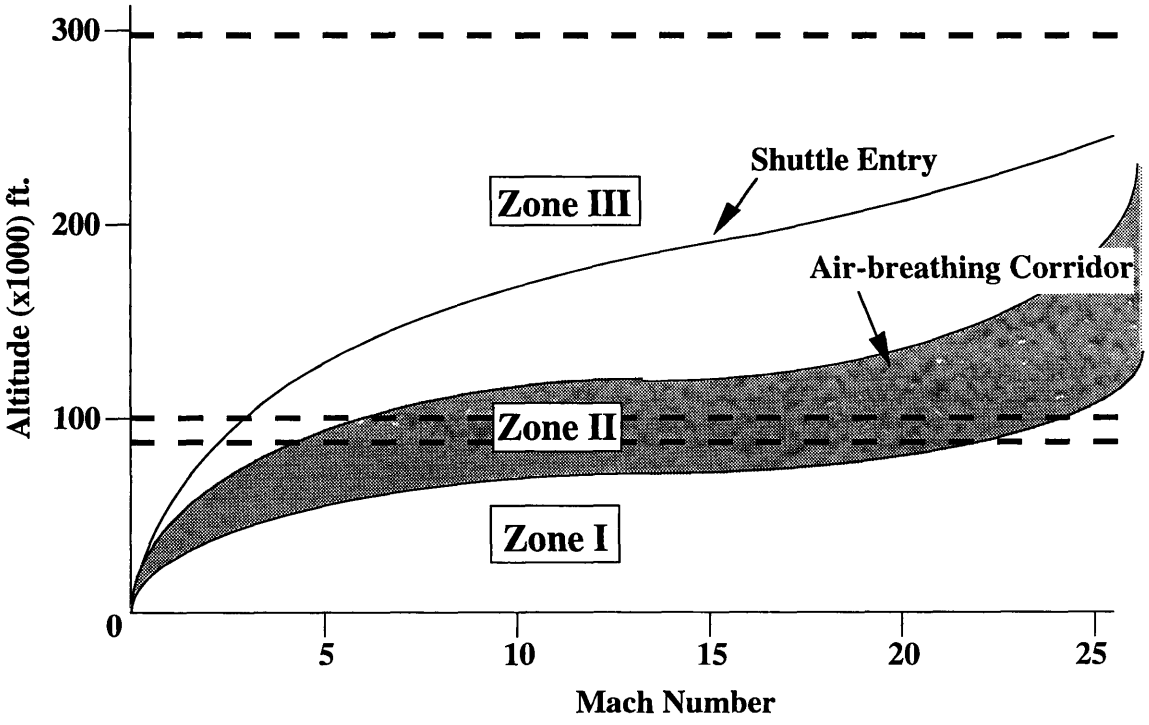

Zone I: **Surface - 25km (83kft)**	**4-D Model (Spiegler and Fowler, 1972)**
Zone II: **25km - 30km (100kft)**	**Interpolation Between The Middle Atmosphere Data and 4-D Values**
Zone III: **30km - 90km (300kft)**	**New Data From the Middle Atmosphere Program (MAP)**

Figure 5-31 Zonal Assignment of Different Atmospheric Models

The free stream thermodynamic parameters such as temperature, density and pressure have distinct profiles which are mainly space-dependent. The deterministic model will be a function of altitude, longitude, and latitude in an Earth-fixed frame. Since the thermodynamic process is a quasi-static compared to the vehicle flight time, the parameters can be assumed to be time-independent. However, when the thermodynamic parameters are viewed in the vehicle frame, they vary with time because of their spatial variation. These spatial variations can be represented as stochastic models with spatial correlation.

Similarly, deterministic and stochastic models can be considered for the wind velocity. The wind velocity model is subdivided into atmospheric turbulence and its mean valued magnitude and direction. The mean values of wind magnitude and direction do not vary very rapidly over short periods of time. Typically nearly 15% change is expected over a 30 minute period. Therefore, the wind magnitude and direction can be modeled as a time-independent velocity vector field along the trajectory. The atmospheric turbulence and spatial variations can be modeled as stochastic processes. Based on spectral analysis, the Von Karman model may provide a more exact description of the processes; however, the model used here, which approximates the process as either a first or second order Markov process, is considered because it is simpler to put into a linear system model.

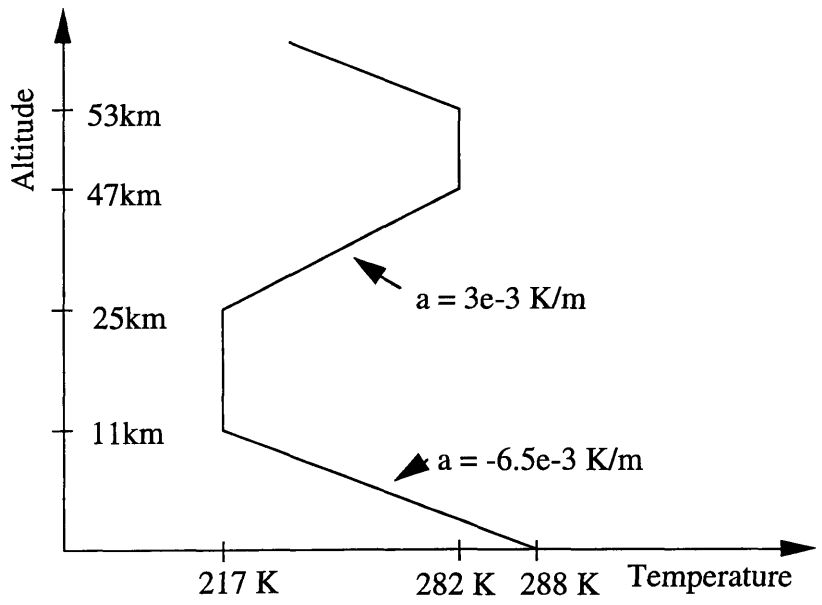

Figure 5-32 Temperature Distribution in the Standard Atmosphere

5.3.2 Simple Model Of Atmosphere

For the lower altitude regime, a piece-wise linear (in temperature) model of atmospheric properties is an adequate representation. Without attempting to compose a sophisticated model of the atmosphere or avoiding a measurement data base, a simple model is presented here. The parameters of interest are temperature, pressure and density. The atmospheric model can be sub-divided into isothermal and gradient layers each corresponding to continuous segment of the atmospheric parameters. The constant temperature regions are the isothermal layers and the constant slope regions are the gradient layers. The isothermal and gradient layers of the atmosphere are shown in Figure 5-32.

For an isothermal region:

$$T = T_r = const. \tag{5.45}$$

$$\ln\left(\frac{P}{P_r}\right) = \ln\left(\frac{\rho}{\rho_r}\right) = -\frac{g}{RT_r}(h - h_r) \tag{5.46}$$

For a gradient layer:

$$T = T_r + a(h - h_r) \tag{5.47}$$

$$\frac{P}{P_r} = \left(\frac{T}{T_r}\right)^{-\frac{g}{aR}} \tag{5.48}$$

$$\frac{\rho}{\rho_r} = \left(\frac{T}{T_r}\right)^{-\left[\frac{g}{aR}+1\right]} \tag{5.49}$$

According to the reference [Duk1], a simple model for the atmosphere estimator can be composed by treating the coefficients of the above relations as the state variables for estimation. According to [Duk1], the first order Taylor expansion of the above equations can be obtained and simplified to:

$$\ln\rho \approx \ln\rho_r - \frac{1}{T_r}(h - h_r)\left(a - \frac{g}{R}\right) \tag{5.50}$$

Let $x_1 = \ln\rho_r$, $x_2 = T_r$, $x_3 = a$ then the temperature and density model for a gradient layer are:

$$T = x_2 + x_3(h - h_r) \tag{5.51}$$

$$\ln\rho = x_1 - \left(1 + \frac{g}{Rx_3}\right)\ln\left(1 + (h - h_r)\frac{x_3}{x_2}\right) \tag{5.52}$$

For an isothermal region, the model becomes:

$$T = x_2 \qquad \text{and} \qquad \ln\rho = x_1 - \frac{g}{x_2 R}(h - h_r) \tag{5.53}$$

Once the coefficients of the model, x_1, x_2, and x_3 are estimated from the sensor output, the thermodynamic states, temperature, density and pressure can be computed using the above relations [Duk1].

Chapter 6

Estimation

6.1 Theoretical Background

The estimation problem for the AHSV air-data system is approached from the fundamental concepts of nonlinear estimation theory. The AHSV estimation problem is derived in the form of the nonlinear filtering of dynamic random processes. The most compact description of the state history (solution) for the estimation of random processes is the A Posteriori conditional probability density of the states. If the equations that depict the time history of the state conditional probability density can be solved, then an appropriate optimal estimation criterion can be defined and the numerical value of the estimate can be obtained [Zak1, Cul1, Lam1].

The differential equations which depict the dynamics of the vehicle tend to increase the uncertainties of state information as time progresses; therefore, this is called diffusion or propagation of the estimation process. When measurements (observations) are available at a given time, the uncertainties on the states decrease since more information has been gained by the observation. The theoretical background which defines the propagation and update of covariance equations in estimation is presented here without rigorous proof. The nonlinear filter equations and the assumptions that are

needed to derive such filters lay out the foundations for filter design procedures discussed in later subsections of this chapter.

The propagation of the state probability density function of nonlinear dynamics that are driven by Gaussian random processes (Brownian motion processes) can be described by the Fokker-Planck equation; and updating of information from measurements is governed by Bayes' rule [Buc1, Buc2]. For continuous measurement cases, the propagation and update cycle can be augmented into a single equation such as Zakai or Kushner equations [Lam1]. The solution to these equations provides the A Posteriori conditional density of the states. Unfortunately, the nature of the solution is infinite-dimensional; and some form of approximation is needed to make the problem tractable [Cul1, Lam1]. Therefore, it is important to recognize the necessary assumptions applied to these general equations since that would provide the limitation of these particular results. One of the most practical and widely used approximate filtering equations is the Extended Kalman Filter (EKF) [Gel1]. The approximations involved in deriving the EKF are shown by presenting its relationship to the general equations.

6.1.1 Nonlinear Filtering Equations

Ito / Langevin Equation for Process and Observation Model: The filtering of continuous parameter processes of nonlinear systems like the AHSV equations of motion, either with continuous or discrete observations, is our main objective. The context for the filtering problem is given by the Ito / Langevin Stochastic Differential Equations(SDEs) and the observation equations for the Markov process, x_t which are:

$$\begin{aligned} \text{Process Law} \quad & dx_t = \mathrm{m}(x_t,t)dt + \mathrm{s}(x_t,t)d\beta \\ \text{Observations} \quad & dy_t = \mathrm{h}(x_t,t)dt + R^{\frac{1}{2}}d\upsilon \end{aligned} \tag{6.1}$$

where $d\beta$ and $d\upsilon$ are unity variance standard Brownian (Wiener) processes and the initial state of the process is a Gaussian random distribution: $x_0 \sim N(X_0, \sigma_0)$.

A Posteriori Filtering Equations for Continuous Observations: The filtering solution is most generally given by the A Posteriori conditional density of the state of the process denoted:

$$\begin{array}{ll} \textit{A Posteriori} & \\ \textit{Conditional Density} & p_{\mathbf{x}}(x_t,t^* / Y) \;\; or \;\; p_{\mathbf{x}}^{+}(x_t,t^*) \\ \textit{where} & Y = \{y_t\}_{t \in [0,t^*]} \end{array} \tag{6.2}$$

The two SDEs which incorporate the continuous update into the Fokker-Planck equation are the Kushner and Zakai equations. The Kushner equation provides the usual A Posteriori conditional density while the Zakai equation provides an un-normalized version (i.e., the density doesn't integrate to one and thus must be normalized), but in a simpler format. Both equations are essentially the Fokker-Planck Equation with added terms due to the continuous update, as shown below [Lam1].

$$\textit{Zakai} \quad \frac{\partial p^{+'}}{\partial t} = Lp^{+'}(x_t,t)dt + h(x_t,t)R^{\frac{1}{2}}p^{+'}(x_t,t)dy_t \tag{6.3}$$

$$\textit{Kushner} \quad \frac{\partial p^{+}}{\partial t} = Lp^{+}(x_t,t)dt + \left(h(x_t,t) - \hat{h}(x_t,t)\right)R^{-1}dI_t \tag{6.4}$$

where dI_t is the innovation process:

$$dI_t = dy_t - \hat{h}(x_t,t)dt \tag{6.5}$$

where the over-hat signifies conditional expectation and where **L** is the Fokker-Planck operator for the system shown below in vector form [Bro1]:

$$L(\bullet) = \sum_i \frac{\partial}{\partial x_i}\left(m_i(x_t,t)\bullet\right) + \frac{1}{2}\sum_{j,k}\frac{\partial}{\partial x_j \partial x_k}\left(s_j(x_t,t)s_k(x_t,t)\bullet\right) \tag{6.6}$$

Note also that because of the observation process, the A Posteriori equations are stochastic, partial differential equations(PDEs) and not deterministic PDE's like the Fokker-Planck equation.

A Posterior Conditional Density and Estimates: At this point it is necessary to recall the following facts concerning obtaining estimates from the A Posteriori conditional density. 1) Extraction of the estimate from the density is a significant problem and this leads to the Loss Function approach for defining optimality. 2) The conditional mean is by definition the minimum variance estimate. 3) A symmetric density implies that all odd higher central moments are zero. 4) For a symmetric, unimodal conditional density, the conditional mean is the optimal estimate regardless of the particular Loss Function.

A Posteriori Conditional Moment Equation: The derivations of the Kushner and Zakai equations are approached based on the use of Bayes' theorem, converting from a measurement history conditioned on a state history to the reverse as in the discrete update equations. The A Posteriori moment equations are derived from the Kushner and Zakai equations similarly to the Fokker-Planck equation.

The A Posteriori equations which describe the dynamics of the conditional expectation of an arbitrary differentiable function $\phi(\mathbf{x}_t)$ are presented.

$$\begin{aligned} &\textit{Arbitrary Function} && \phi(x_t) \\ &\textit{Desired Conditional Expectation} && \hat{\phi}(x_t) = \int_{-\infty}^{\infty} \phi(x) p(x,t \,/\, Y) dx \end{aligned} \tag{6.7}$$

Where Y is the observation history up to and including y_t. The derivation of the A Priori moment equations from the Fokker-Planck equation involved the commutative property of expectation and differentiation and the application of integration by parts. The derivation of the A Posteriori moment equation from the Kushner equation is a little more involved because of the stochastic update term. The final form of the A Posteriori conditional moment equation is:

$$d\hat{\phi}(x_t) = L^* \phi(x_t) dt + \left[\phi(x_t) h(x_t) - \hat{\phi}(x_t) \hat{h}(x_t) \right] R^{-1} dI_t \tag{6.8}$$

where L^* is the formal adjoint of the Fokker-Planck operator shown below in the simplified scalar case:

$$L^*(\bullet) = m(x_t,t) \frac{\partial}{\partial x}(\bullet) + \frac{1}{2} s^2(x_t,t) \frac{\partial^2}{\partial x^2}(\bullet) \tag{6.9}$$

where, as before, the over-hat signifies conditional expectation.

Note that in general the entire conditional density is required to evaluate this differential. Also, in general, moment equations can be expressed in terms of higher order moments which in turn are expressed in even higher order moments, leading to an infinite dimensional set of PDE's. In special cases higher moments may go to zero or are parameterizable which leads to a finite dimensional set of equations. The issue of finite dimensionality is best looked at from a geometric view point. The dimensionality of the filter is related to the dimensionality of the Estimation Lie algebra associated with the

diffusion. If this Algebra is finite dimensional then the resulting filter is also finite dimensional.

In nonlinear filtering, we are typically interested in the conditional mean. The moment equation for this case ($\phi(x_t) = x_t$) becomes :

$$d\hat{x}_t = L^* x_t dt + \left[x_t h(x_t) - \hat{x}_t \hat{h}(x_t)\right] R^{-1} dI_t \tag{6.10}$$

In the linear system case and with sub-optimal filters such as the Extended Kalman Filter, the second moment is also of interest:

$$P_t = E^+\left\{\left[x_t - \hat{x}_t\right]^2\right\} \tag{6.11}$$

The first term can be obtained directly from the moment equation with $\phi(x_t) = x_t^2$. The second term can be simplified by the chain rule for differentiation; however, not the chain rule of ordinary calculus but the chain rule for Ito calculus [Bro2]. By observing from the conditional mean equation, the conditional mean with the observation innovations update term is a stochastic process despite the fact that the expectations produce real numbers. Thus we need to use the Ito differentiation rule for the second term. That is, instead of:

$$d\hat{x}_t^2 = 2\hat{x}_t d\hat{x}_t \quad \text{use} \quad d\hat{x}_t^2 = 2\hat{x}_t d\hat{x}_t + \frac{1}{2}\left[x_s h(x_s) - \hat{x}_s \hat{h}(x_s)\right] R^{-1} dt.$$

Substituting the above expression and the first moment equation into the definition of the second moment and arranging terms gives us the A Posteriori second moment equation:

$$\begin{aligned} dP_t = {} & 2(x_t - \hat{x}_t) m(x_t) dt + s^2(x_t) dt - \left[x_t h(x_t) - \hat{x}_t \hat{h}(x_t)\right]^2 R^{-1} dt \\ & + \left[(x_t - \hat{x}_t)^2 h(x_t) - P_t \hat{h}(x_t)\right] R^{-1} dI_t \end{aligned} \tag{6.12}$$

6.1.2 A Special Case: The Extended Kalman Filter(EKF)

By observing the general first and second moment equations, it is noted that they are full of complicated conditional expectation terms which do not uncouple. Also there exist innovation processes (measurements) in the covariance equations. It would be

beneficial to make some approximations which allow uncoupling and therefore simplify these expectations to get an implementable filter. The first main assumption in deriving the EKF is that the estimation error is small most of the time. Then assuming that the drift, $m(x_t)$, and the observation function, $h(x_t)$, are smooth functions, we can approximate them in a Taylor's expansion:

$$m(x_t) \approx m(\hat{x}_t) + (x_t - \hat{x}_t)\frac{\partial}{\partial x} m(\hat{x}_t) \quad [+Neglected \;\; H.O.T.] \tag{6.13}$$

$$h(x_t) \approx h(\hat{x}_t) + (x_t - \hat{x}_t)\frac{\partial}{\partial x} h(\hat{x}_t) \quad [+Neglected \;\; H.O.T.] \tag{6.14}$$

The conditional expectation of the first central moments is zero and thus:

$$m(x_t) \cong m(\hat{x}_t) \;\text{ and }\; h(x_t) \cong h(\hat{x}_t) \tag{6.15}$$

Similar consideration of the remaining terms gives:

$$\begin{aligned} x_t h(x_t) - \hat{x}_t \hat{h}(x_t) &= (x_t - \hat{x}_t) h(x_t) \\ &\cong (x_t - \hat{x}_t)^2 \frac{\partial}{\partial x} h(\hat{x}_t) = P_t \frac{\partial}{\partial x} h(\hat{x}_t) \end{aligned} \tag{6.16}$$

The resulting expression for the evolution of the conditional mean is:

$$d\hat{x}_t \cong m(\hat{x}_t)dt + P_t \frac{\partial}{\partial x} h(\hat{x}_t) R^{-1}\left[dy_t - h(\hat{x}_t)dt\right] \tag{6.17}$$

Apply these approximations to the second moment equation, and get the evolution equation for the variance:

$$\begin{aligned} dP_t \cong &\left[2P_t \frac{\partial}{\partial x} m(\hat{x}_t) + s^2(x_t) - P_t^2 \left[\frac{\partial}{\partial x} h(\hat{x}_t) \right]^2 R^{-1} \right] dt \\ &+ \; \mathcal{E}\left\{ (x_t - x_t)^3 \right\} \frac{\partial}{\partial x} h(\hat{x}_t) R^{-1}\left[dy_t - h(\hat{x}_t)dt\right] \end{aligned} \tag{6.18}$$

Again, as in the linear case with the Kalman-Bucy filter derivation, the third central moment term couples to the observations allowing the observations to affect the variance of the filter. If we repeat the approximation procedure for the third moment we would find it depending on the fourth moment and so on ... resulting in an infinite dimensional set of equations. Even with a first order approximation, an infinite dimensional filter still results. The second, and crucial assumption associated with the EKF is that the error is symmetrically distributed about its mean value so that the third moment goes to zero with

all other odd central moments. In this case, the first and second moment evolution equations become a closed set known as the Extended Kalman Filter and become innovation independent.

The Extended Kalman Filter

$$\begin{aligned} d\hat{x}_t &\cong m(\hat{x}_t)dt + P_t \frac{\partial}{\partial x} h(\hat{x}_t) R^{-1}\left[dy_t - h(\hat{x}_t)dt\right] \\ dP_t &\cong \left[2P_t \frac{\partial}{\partial x} m(\hat{x}_t) + s^2(x_t) - P_t^2 \left[\frac{\partial}{\partial x} h(\hat{x}_t)\right]^2 R^{-1}\right] dt \end{aligned} \tag{6.19}$$

6.2 Estimation Problem Formulation

6.2.1 Estimation Problem for Velocity and Angle of Attack

The filtering problem can be defined with the models derived in Chapter 5. The equations which describe the diffusion process can be stated as given below.

$$\begin{aligned} \dot{V} = {} & [\omega_E^2 R - g(R)]\sin(\theta - \alpha) + \frac{Q(R,V)S}{m}\left[C_{Tv}(M,\alpha,R) - C_D(M,\alpha)\right] \\ & + \frac{Q(R,V)S}{m}\left[C_{x\delta_e}(M,\alpha,\delta_e) + C_{x\delta_T}(M,\alpha,\delta_T)\right] \\ & + \frac{Q(R,V)S}{m}\left[+C_{x\delta_v}(M,\alpha,\delta_v)\left[C_{Tv}(M,\alpha,R) + C_{x\delta_T}(M,\alpha,\delta_T)\right]\right] \end{aligned} \tag{6.20}$$

$$\begin{aligned} \dot{\alpha} = {} & \left[\frac{g(R)}{V} - \frac{V}{R} - \frac{\omega_E^2 R}{V}\right]\cos(\theta - \alpha) + q - 2\omega_E + \frac{Q(R,V)S}{Vm}\left[C_{Tn}(M,\alpha,R) + C_L(M,\alpha)\right] \\ & - \frac{Q(R,V)S}{Vm}\left[C_{z\delta_e}(M,\alpha,\delta_e) + C_{z\delta_T}(M,\alpha,\delta_T)\right] \\ & - \frac{Q(R,V)S}{Vm}\left[C_{z\delta_v}(M,\alpha,\delta_v)\left[C_{z\delta_T}(M,\alpha,\delta_T) - C_{Tn}(M,\alpha,R)\right]\right] \end{aligned} \tag{6.21}$$

$$\begin{aligned} \dot{q} = {} & \frac{Q(R,V)Sc}{I_y}\left[C_{mp}(M,\alpha,R) + C_{ma}(M,\alpha) + C_{m\delta_e}(M,\alpha,\delta_e) + C_{m\delta_T}(M,\alpha,\delta_T)\right] \\ & + \frac{Q(R,V)Sc}{I_y}\left[C_{m\delta_v}(M,\alpha,\delta_v)\left[C_{m\delta_T}(M,\alpha,\delta_T) + C_{mp}(M,\alpha,R)\right]\right] \end{aligned} \tag{6.22}$$

Several assumptions can be imposed on the equations to simplify the estimation process and also reduce the dimension of the estimator. The first assumption is that the inertial measurements are available with relatively good accuracy. We can assume that the altitude R is available and treated as a known parameter. With GPS and IMU data,

altitude can be measured with accuracy of a few feet (assuming military code). Also it can be assumed that the pitch angle measurement is available with an accuracy of better than 0.01 degrees. It is also presumed that the gravity and earth rotation rate are known exactly. The second assumption is free-stream temperature measurements are available with specific heat ratio such that the Mach number can be converted to air velocity. The final assumption deals with disturbances which occur in the vehicle dynamics. Most of the disturbances are assumed to be caused by density fluctuations. Therefore, the free stream density is assumed to be of the form:

$$\rho(t) = \rho_o(R) + \rho_n(t) \tag{6.23}$$

The density noise is additive to mean density which is a function of altitude only.

If the assumptions are applied onto the equations (6.20) to (6.22), then the resulting equations can be expressed as:

$$\begin{aligned} dV &= f_1(V,\alpha,\delta_e,\delta_T,\delta_v)dt + g_1(V,\alpha,\delta_e,\delta_T,\delta_v)d\rho^* \\ d\alpha &= f_2(V,\alpha,q,\delta_e,\delta_T,\delta_v)dt + g_2(V,\alpha,q,\delta_e,\delta_T,\delta_v)d\rho^* \\ dq &= f_3(V,\alpha,\delta_e,\delta_T,\delta_v)dt + g_3(V,\alpha,\delta_e,\delta_T,\delta_v)d\rho^* \end{aligned} \tag{6.24}$$

Notice that the diffusion processes (6.24) are functions of the control variables $(\delta_e,\delta_T,\delta_v)$, and the solution of the Fokker-Planck equation of (6.24) becomes dependent on the control history. Therefore, a state feedback control law has been assumed and designed. The feedback control law can be written as:

$$u = [\delta_e,\delta_T,\delta_v]^T = K_c(\alpha,V,q,\theta,R) \tag{6.25}$$

Then (6.24) can be written as:

$$\begin{aligned} dV &= f_1^*(V,\alpha,)dt + g_1^*(V,\alpha)d\rho^* \\ d\alpha &= f_2^*(V,\alpha,q)dt + g_2^*(V,\alpha,q)d\rho^* \\ dq &= f_3^*(V,\alpha)dt + g_3^*(V,\alpha)d\rho^* \end{aligned} \tag{6.26}$$

With observation equations from Chapter 5:

$$
\begin{aligned}
dP_1 &= P_t\left[\left(1-R^*(V)\right)\cos^2\left(\alpha+30^o\right)+R^*(V)\right]dt+dn_{p_1}\\
dP_2 &= P_t\left[\left(1-R^*(V)\right)\cos^2\left(\alpha+15^o\right)+R^*(V)\right]dt+dn_{p_2}\\
dP_3 &= P_t\left[\left(1-R^*(V)\right)\cos^2(\alpha)+R^*(V)\right]dt+dn_{p_3}\\
dP_4 &= P_t\left[\left(1-R^*(V)\right)\cos^2\left(\alpha-15^o\right)+R^*(V)\right]dt+dn_{p_4}\\
dP_5 &= P_t\left[\left(1-R^*(V)\right)\cos^2\left(\alpha-30^o\right)+R^*(V)\right]dt+dn_{p_5}\\
du_1 &= V\cos\left(35^o+\alpha\right)dt+dn_1\\
du_2 &= V\cos\left(30^o-\alpha\right)dt+dn_2\\
du_3 &= V\sin\left(35^o+\alpha\right)dt+dn_3\\
du_4 &= V\sin\left(30^o-\alpha\right)dt+dn_4
\end{aligned}
\qquad (6.27)
$$

Objective: Equations (6.26) and (6.27) form the complete filtering equations which are written in the Ito / Langevin Stochastic Differential Equation form as described in subsection 6.1. In simple form:

$$
\begin{aligned}
dx &= f(x,t)dt+g(x,t)dw\\
dz &= h(x,t)dt+dn
\end{aligned}
\qquad (6.28)
$$

with

$$x=[\alpha,V,q] \quad \text{and} \quad z=\left[P_i,u_j\right] \quad i=1....5, \quad j=1....4$$

The filtering problem is to find the conditional mean of state variable x; and the filtering process requires knowledge of:

A Posteriori Conditional Density $p_{\mathbf{x}}(x_t,t^* / Z)$ *or* $p_{\mathbf{x}}^{+}(x_t,t^*)$

where $Z=\{z_t\}_{t\in[0,t^*]}$

6.2.2 Estimation Problem for Atmosphere parameters

The estimation problem for the atmosphere parameters can be posed as a static filtering. From section 5.3.2, the observation equation can be form as:

$$
\begin{aligned}
Z_T &= x_2+x_3\left(h-h_r\right)+n_T\\
\ln Z_\rho &= x_1-\left(1+\frac{g}{Rx_3}\right)\ln\left(1+\left(h-h_r\right)\frac{x_3}{x_2}\right)+n_\rho
\end{aligned}
$$

where $x_1=\ln_\rho$, $x_2=T_r$ and $x_3=a$.

In section 5.2.5, the sensor models for the atmospheric parameters were:

$$P_i = f(P_t, M, q_\infty) + n_{p_i}$$

$$P_{\infty i} = (1 - k_p) P_\infty + n_{p_\infty}$$

$$I_m = {}^{I_r}\!/_{I_o} = k_r \rho_\infty + n_\rho$$

$$L_F = k_F T_\infty + n_T$$

By including the sensor models of above with the atmospheric model of section 5.3.2, a static estimation equation can be formed. Once the coefficients of the model, x_1, x_2, and x_3 are estimated from the sensor output, the thermodynamic states, temperature, density and pressure can be computed using the thermodynamic relations of atmosphere. More related estimation procedures and derivations can be found in [Duk1].

6.3 Estimation Strategy

The estimation problems defined in section 6.2 have been approached from the fundamental estimation equations. The core of the estimation problem involves the propagation and update of the state conditional densities since the conditional densities contain the most compact information on the current states as well as their history. Therefore the estimator design process involves: 1) Estimation problem formulation, where diffusion and observation processes need to be defined. 2) Design of the controller as function of states (state feedback), if the vehicle requires stabilization. 3) Obtain the equations which govern the propagation and update of state conditional probability densities 4) Visualize the behavior of the densities to seek proper approximations 5) Design an estimator which provides a conditional mean of states (minimum variance) 6) Estimator performance verification via simulation.

In order to visualize the estimation problem, the vehicle models and observation equations from sensor models are reviewed. Two major parts of the estimation problem can be formulated. The first part of the estimation problem is to obtain the most accurate estimate of the thermodynamic parameters such as temperature, density, pressure, and Mach number. The appropriate observation equations are in Chapter 5, the sensor modelling section. The filtered thermodynamic parameters are then used to update the vehicle dynamics model coefficients during the estimation of flow magnitude and direction as well as wind effects.

The second part of the estimation problem is to design an estimator for the flow direction parameters (angle of attack and side slip angle), flow magnitude, and wind effects. The most promising strategy is to formulate the problem in a nonlinear dynamic filtering representation. The equations of motion described in Chapter 5 will be used as the propagation (diffusion) process by assuming the controller is in the state feedback form. Appropriate functional representation of the forcing blocks (including aero/propulsion terms) will be dependent on the defined states and thermodynamic parameters. The sensor models discussed in Chapter 5 will be used as the observation equations along with their associated noise and bandwidth characteristics.

6.3.1 Solution Strategy

The flow of ideas in the solution strategy is drawn in Figure 6-1. The first step toward solving this estimation problem is to define proper objectives and appropriate requirements. Based on these objectives and requirements, suitable models are formulated as in Chapter 5. In order to understand the behavior of the processes described as models, mathematical and engineering analysis is applied on these models. The resulting models can be written as a set of differential equations and observation equations as shown in Figure 6-2. The differential equations come from the modelling of the vehicle equations of motion and the observation equations come from the modelling of the sensors.

The existing nonlinear estimation theories suggest that the most compact way of describing the states in the stochastic system is to keep records of the state conditional densities. The estimation process for the discrete measurement case can be described as propagation and update cycles. The propagation can be obtained by solving the Fokker - Planck equation which is a parabolic partial differential equation. The update cycle is operated by using Baye's rule. Similarly, there exist a couple of density equations for the continuous measurement case which contain both the propagation and update cycles. The solution to the Zakai equation provides the conditional density of states in un-normalized form. The solution to the Kushner equation provides the same results but in normalized form at the cost of complexity resulting from operating on expectation.

To solve these probability density equations, appropriate boundary and initial conditions are needed. Unfortunately, the solutions to these PDEs are infinite

dimensional in nature. Very few known solutions exist, such as the linear dynamics case (Gaussian) and Bene's equation. Consequently, numerical approximation is unavoidable. The Extended Kalman Filter is one of the approximations that is widely used because of its simplicity and because its moment equations are innovation independent. As described in section 6.1, the EKF requires several assumptions on its conditional probability densities. The most important one is the density being symmetrical and unimodal such that the all odd moments will vanish. Therefore it is desirable to visualize the behavior of the densities associated with the AHSV air-data estimation problem to validate the usage of EKFs.

If application of an EKF fails, then there are other approaches available. One method is to solve the PDEs directly using finite difference methods. Other methods involve approximating the densities with a finite dimensional series of functions. For example, the simulated densities can be obtained by multiple Monte-Carlo simulation runs, then based on the observed density shapes the appropriate approximating function can be chosen. The orthogonal functions such as Hermite-Gaussian series expansion have advantages over others because the addition of a higher order terms does not affect the previously calculated lower order terms.

This solution strategy is thought to be the most promising way of solving the AHSV estimation problem. The major problems associated in following such a strategy are the convergence problem of the numerical methods and accuracy of the approximation. The solutions to the density equation, and the stochastic partial differential equations, depend on the control history as well as the initial and boundary conditions. Therefore, a reference controller needs to be implemented in order to complete the estimator design. Of course, the obtained solution would only be a particular solution. If a more representative controller and vehicle models are available in the future, then the design process can be repeated to provide correct approximations.

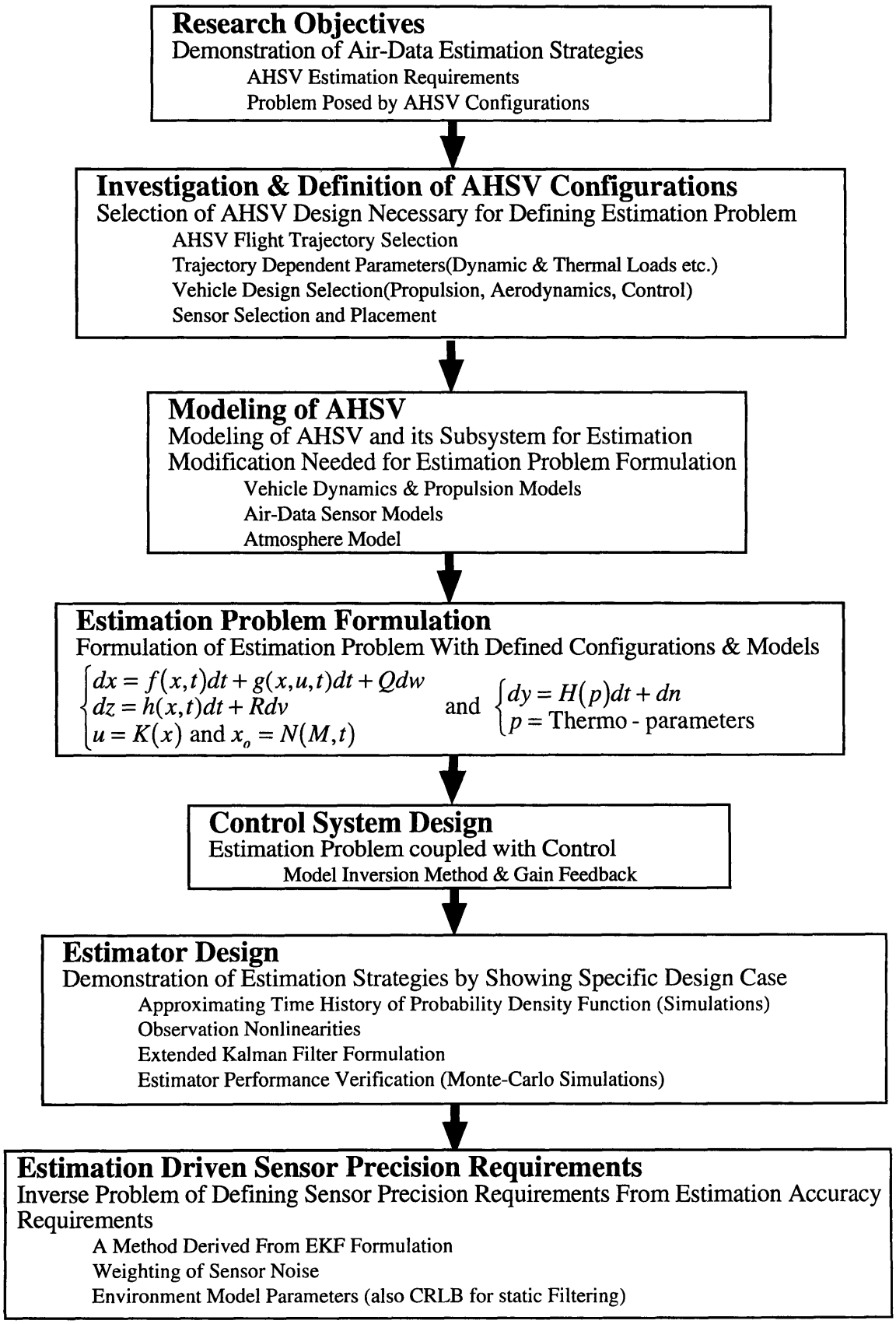

Figure 6-1 Block Diagram of Research Procedure

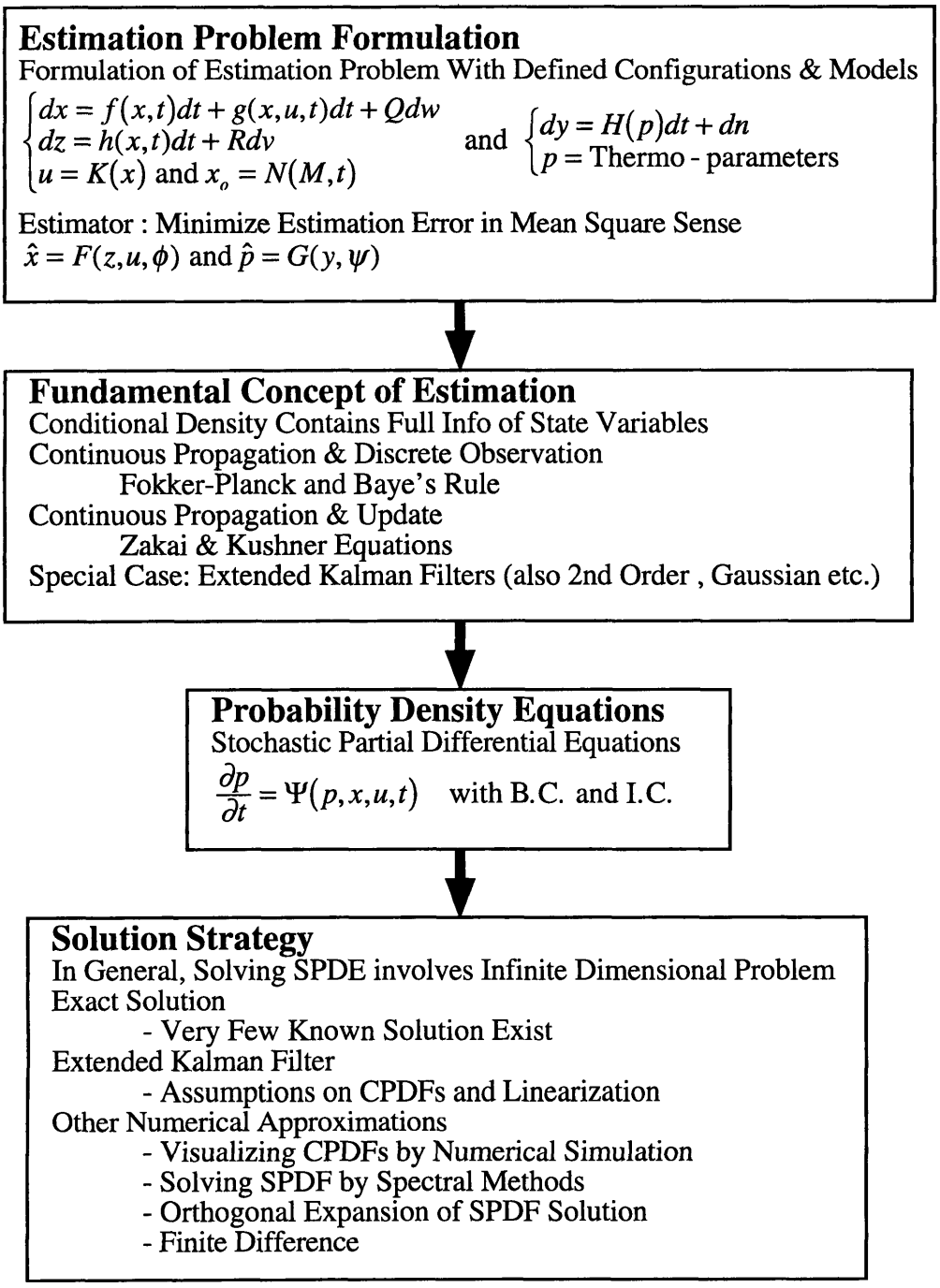

Figure 6-2 Estimator Design Procedure

6.4 Control System Design

6.4.1 Motivation

In general, the desired estimator design in both theory and practice depends upon a specific history of control inputs. The difference in the desired estimator design, especially in nonlinear and/or non-Gaussian noise case, is due to the shape of the state conditional probability density function (PDF); and the equations which depict the evolution of PDF depends upon control variables. Therefore, the main objective of this chapter is to address the design and analysis of a realistic and robust control system that manages the AHSV flight dynamics such that the simulations of the closed loop dynamics can be used to provide the characteristics of the state probability density function.

The vehicle equation of motion and observation can be expressed as shown in equation (6.29). Also, the corresponding Zakai equation is shown below that equation. By observing the Zakai equation, the time rate of change in the conditional densities depend on state variables, time, control variables, and measurements. Even if we assume the feedback control for u, the governing equation for the conditional densities still involves the closed loop behavior (diffusion operator) of the vehicle. Consequently, the time variations in the conditional density function depend on control system design.

$$\begin{aligned} dx &= f(x,t)dt + f_u(x,u,t)dt + g(x,t)dw \\ u &= K_c(x,t) \\ dz &= h(x,t)dt + dn \end{aligned} \tag{6.29}$$

with

$$x = [\alpha, V, q] \quad \text{and} \quad z = [P_i, u_j] \quad i = 1....5, \quad j = 1....4$$

$$Zakai \quad \frac{\partial p^{+}}{\partial t} = Lp^{+}(x_t,t)dt + h(x_t,t)R^{\frac{1}{2}}p^{+}(x_t,t)dz_t$$

$$\text{where} \quad L(\bullet) = \sum_i \frac{\partial}{\partial x_i}\left(f_i(x_t,t)\bullet\right) + \frac{1}{2}\sum_{j,k}\frac{\partial}{\partial x_j \partial x_k}\left(g_j(x_t,t)g_k(x_t,t)\bullet\right)$$

For high Mach number flight, there exists a stable controller design by Chamitoff [Cha2] whose design is based upon Lyapunov stability criterion and an A-star search method applied in a manner similar to that used in nonlinear dynamic programming. However, when considering the estimator design, it is undesirable to have the controller

in a form of numerical search codes; rather, an analytic form, especially a regulatory feedback controller, is highly attractive. For the analysis that has been carried out in this thesis, only a representative control system is needed. Since covering all possible control schemes or an optimal control scheme is beyond the scope of this thesis, only a little effort has been applied to finding an implementable control scheme. The resulting design of the flight control system is derived in this chapter.

6.4.2 Assumptions and Background

To obtain a particular AHSV controller design applicable to high Mach number flight, the LVLH kinematics formulation is used along with the parameterized form of the forcing (aerodynamics and propulsion) terms. The non-dimensionalized forcing coefficients are generated using the Draper developed AHSV design and simulation codes[Cha2] in the form of multi-dimensional numerical tables. The coefficient tables are then polynomial curve-fitted to form an approximate model of the vehicle dynamics. The state vector is defined as in Chapter 5 (vehicle modeling section). Included in the vector are velocity, flight path angle (or angle of attack), pitch rate, pitch angle, and altitude. To simplify the design procedure, it is assumed that all the state variables are available from direct measurement without measurement noise. Finally, the control system design has been customized to the narrow flight envelope spanning flight from Mach 10 to 15.

6.4.3 Control Strategy

The AHSV flight control problem involves stabilization of a highly nonlinear as well as inherently unstable plant(vehicle dynamics). Two different approaches were taken here; the first design is based on a linearization and Linear Quadratic Regulator implementation using the linearized model, and the second design is based on an inversion of the forcing models which provide direct control in terms of the applied forces on the vehicle dynamics. The second approach has not been tested with the numerical examples due to the lengthy computation time it required. The statistical analysis involved with the estimation problem prohibits use of time consuming processes. However, the control system design approach and procedure are discussed and some example designs are included in the Appendix D.

The main objective of the regulator is to command the state x to follow the scheduled state trajectory x_s, while minimizing the defined cost functional C. The constraints are defined by the limitations on the acceleration magnitude which are considered by propulsion, structural dynamics, and human factors.

Let the state error x_e be defined as $x_e = x - x_s$ then the problem is to find the feedback control u such that $\|x_e\|_2$ is minimized while satisfying the input constraints $|\sum F| < M$ by considering $|u| < N$.

In this case, the 2 norm of the error defined by the weighted sum of squares becomes the cost function to be minimized.

The vehicle dynamics have been linearized about the nominal trajectory. With the linearized model, Linear Quadratic Regulator (in the form of constant gain, full state feedback) is designed for operating points at every finite step. The resulting feedback gains were scheduled as a function of angle of attack. More detailed steps in the controller design approach are discussed below:

1) First, the nominal trajectory (the trajectory that vehicle should follow in flight) data has been calculated. With the nominal trajectory value, the perturbation equation is formed from the vehicle dynamics equations.

$$\text{Nominal Trajectory} \quad x_s = x_s(t)$$

Let $x_e = x - x_s$ and $u_e = u - u_s$ then

$$\dot{x}_e = \dot{x} - \dot{x}_s = f(x_s + x_e, t) + f_u(x_s + x_e, u_s + u_e, t) + g(x_s + x_e, t)w \qquad (6.30)$$

2) The next step is to linearize the equation (6.30) about the nominal trajectory x_s, that is taking the Taylor approximations and using only the first order terms.

$$\dot{x}_e \cong f_o(x_o, t) + \left.\frac{\partial f}{\partial x}\right|_{\substack{x=x_o \\ u=u_o}} (x - x_o) + f_{uo}(x_o, t) + \left.\frac{\partial f_u}{\partial x}\right|_{\substack{x=x_o \\ u=u_o}} (x - x_o) + \left.\frac{\partial f_u}{\partial u}\right|_{\substack{x=x_o \\ u=u_o}} (u - u_o) \qquad (6.31)$$

to form a set of equations in the form of

$$\dot{x}_e = Ax_e + Bu_e \qquad (6.32)$$

3) With the linearized dynamics, a set of integrators are included such that the steady state errors will vanish. By including the integrators, the resulting augmented system has twice the dimension of the previous system.

4) With the augmented linearized system dynamics, the Riccati equation is solved numerically. The two weighting matrices are calculated by using the Bryson's rule. The solutions to the Riccati equation provide the feedback controller after augmenting the integrator into the gain structure.

5) The procedure has been repeated from step 1) to 4) for discretely stepped nominal trajectory values such that the feedback gain is curve-fitted with the data as a function of angle of attack, in the form of:

$$u = F(\alpha)x \tag{6.33}$$

This type of control system design is not really recommended for actual implementation for AHSV, because the robustness of the algorithms can not be easily addressed. Because the feedback gain is a function of angle of attack (which is one of the most sensitive parameters to variations in plant dynamics), the feedback control is no longer linear. Also because the feedback gain changes as rapidly as the plant dynamics, the interactions may result in instability. For this thesis, this approach has been taken since the structure of the controller is much simpler than any other and it is much more computationally efficient to use.

6.4.4 Controller Simulation and Performance

By following the steps described in 6.4.3, the control system was designed successfully. Within the narrowly defined operating regions, the controller performed satisfactorily. The break-down point of the controller ranged from 0.5 to 0.7 degrees away from the nominal values of the angle of attack. The controller was much less sensitive to variations in other variables such as Mach number, pitch rate, and pitch angles. Both the initial conditions and disturbance amplitudes were varied to make this determination.

The Figures 6-3 through 6-10 show a sample of the typical transient response of the controller for initial condition errors in the velocity and angle of attack. The response shows good steady state error response, asymptotically going to zero because of the integrators included inside the controller. Most transients died out within a few seconds into the simulation. This design is used throughout the analysis in the later chapters as the main controller.

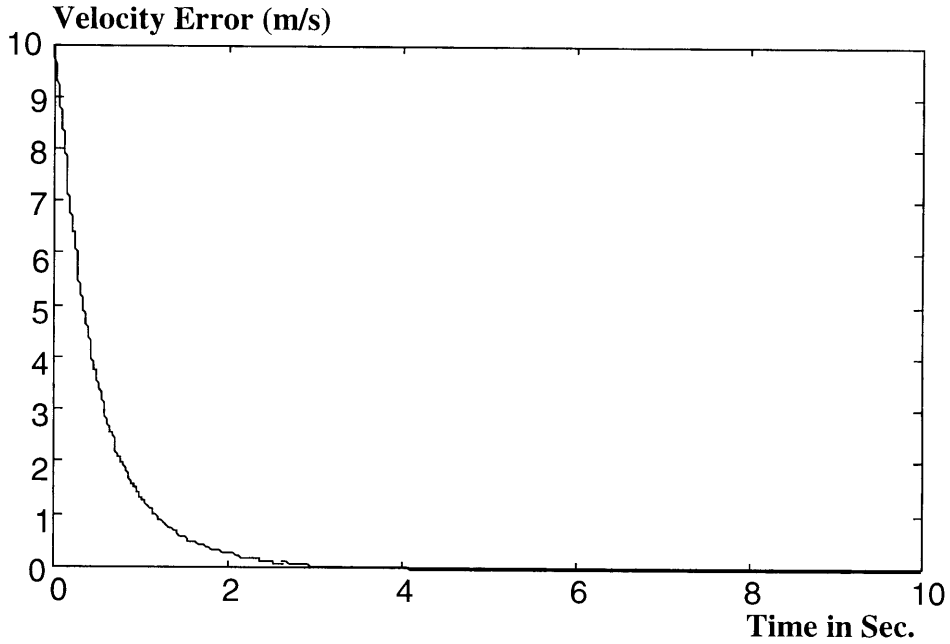

Figure 6-3 Transient Response of Axial Velocity (Velocity Initial Condition Error of 10m/s)

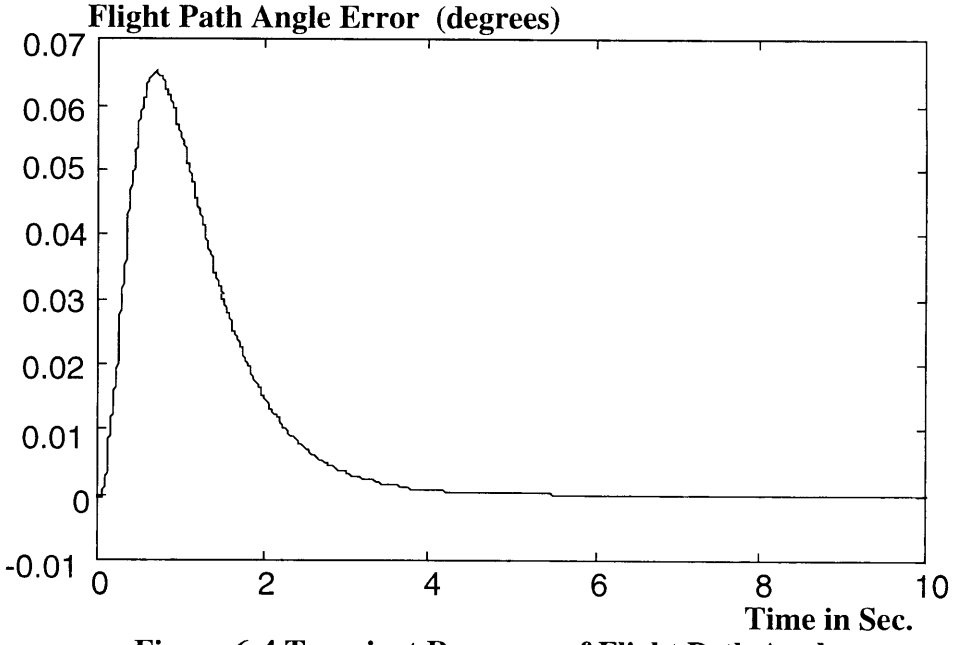

Figure 6-4 Transient Response of Flight Path Angle (Velocity Initial Condition Error of 10m/s)

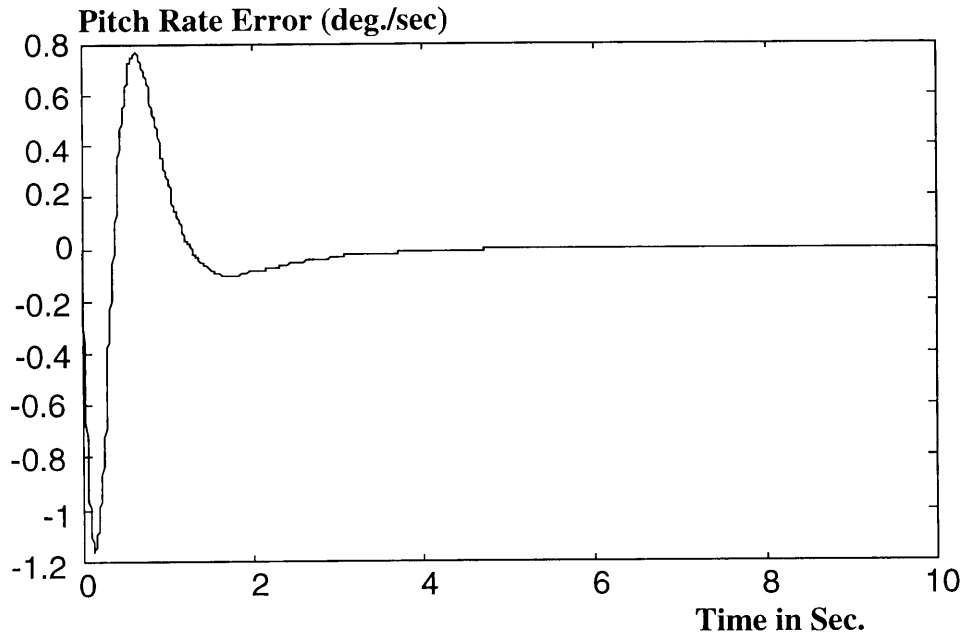

Figure 6-5 Transient Response of Pitch Rate (Velocity Initial Condition Error of 10m/s)

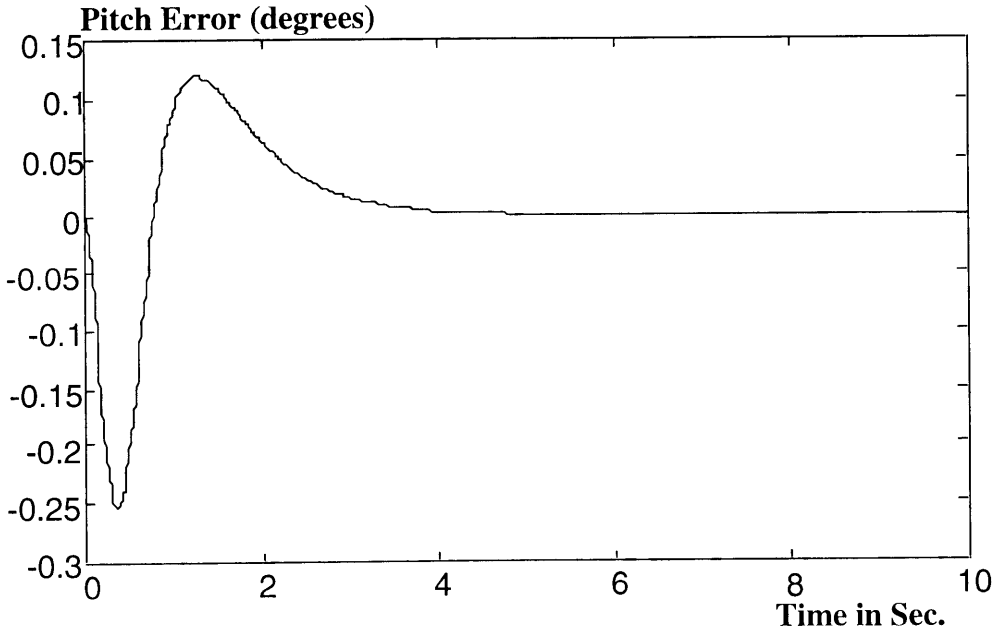

Figure 6-6 Transient Response of Pitch Angle (Velocity Initial Condition Error of 10m/s)

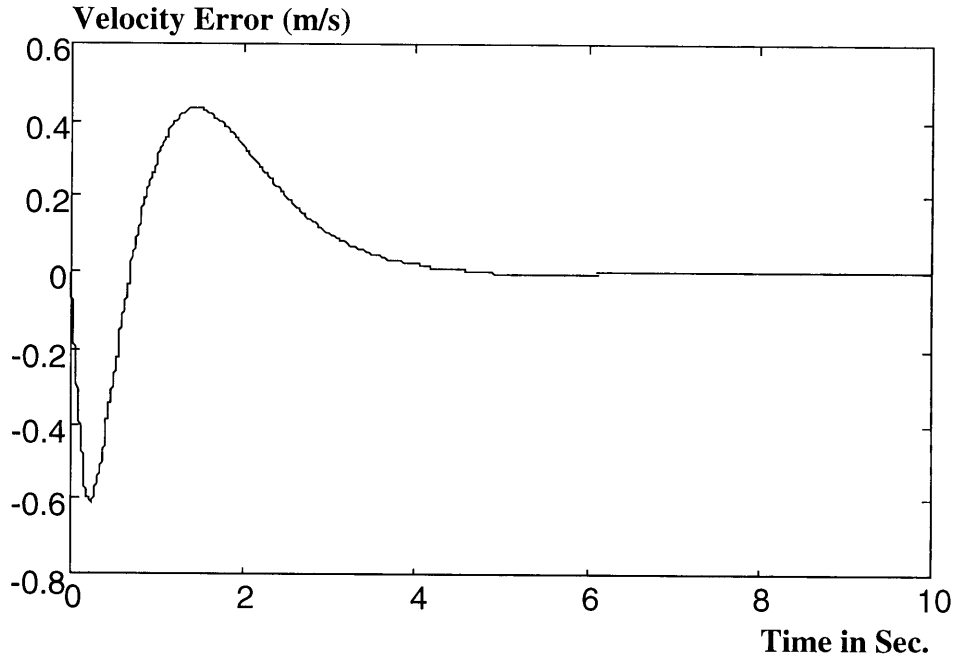

Figure 6-7 Transient Response of Axial Velocity (Flight Path Initial Condition Error of 0.5 deg.)

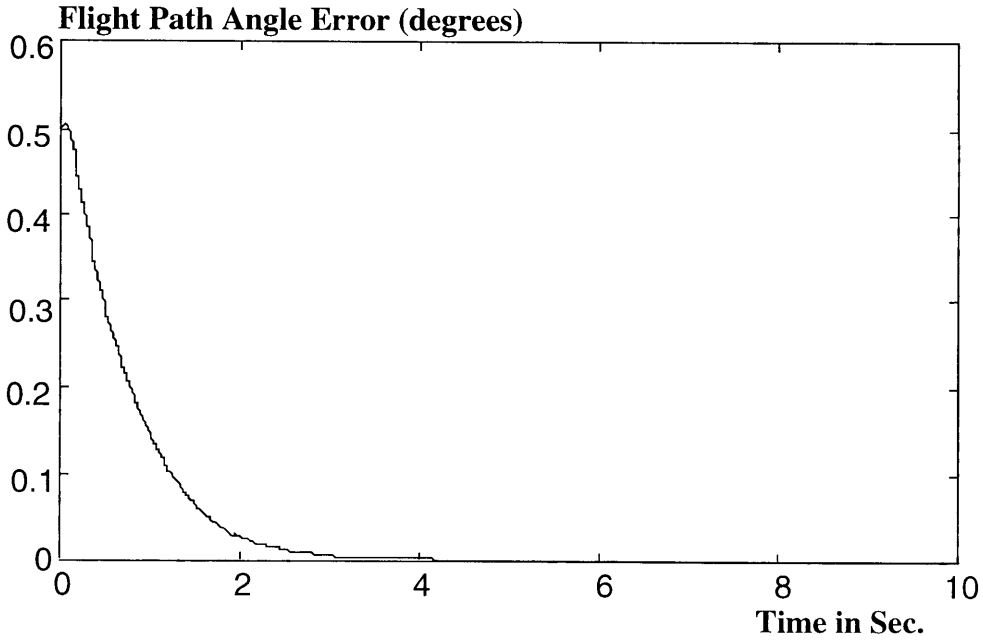

Figure 6-8 Transient Response of Flight Path Angle (Flight Path Initial Condition Error of 0.5 deg.)

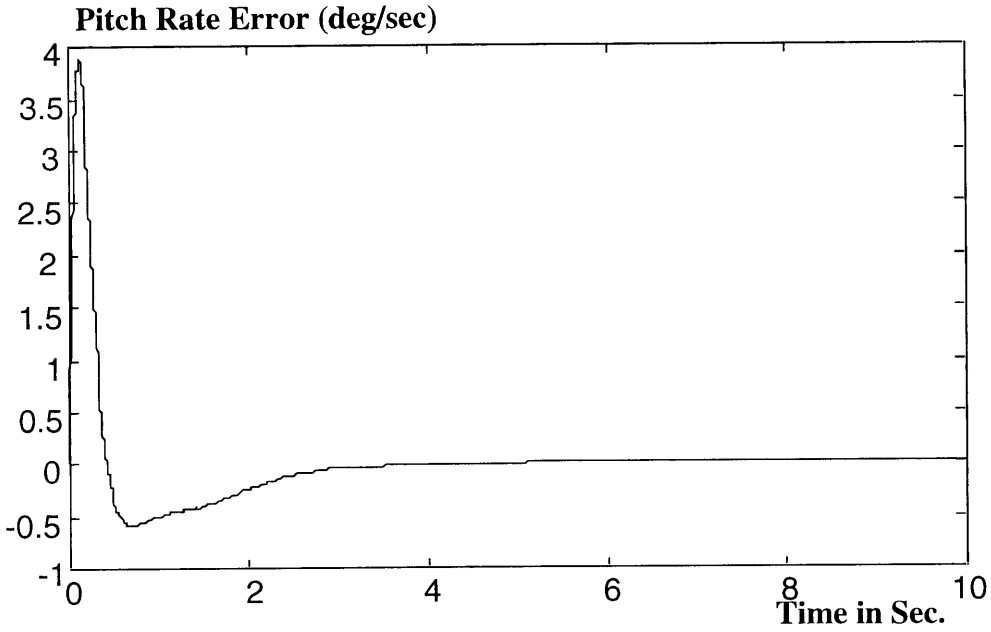

Figure 6-9 Transient Response of Pitch Rate (Flight Path Initial Condition Error of 0.5 deg.)

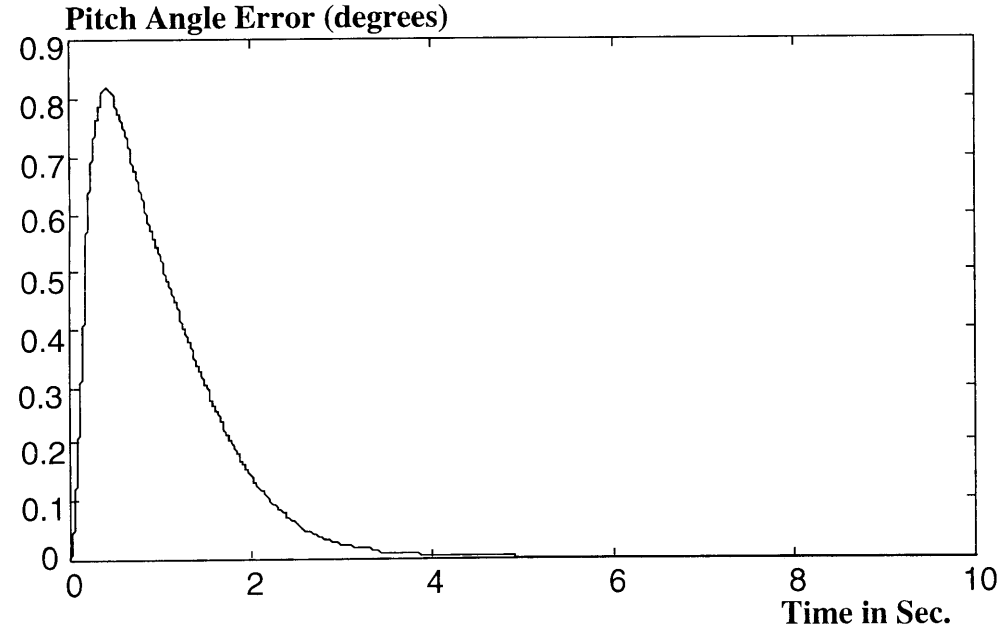

Figure 6-10 Transient Response of Pitch Angle (Flight Path Initial Condition Error of 0.5 deg.)

6.5 Visualization of Conditional Density Propagation

The solution to the estimation problem, which is discussed in section 6.2, is the conditional mean and variance; and the exact solution requires solving the Zakai equation. The solution to this equation provides the A Posteriori conditional density of the states and leads to the conditional mean and variance. The exact solution to the nonlinear filtering problem is not easily attainable since the nature of the solution is infinite-dimensional. Thus, some form of approximation is needed to make the problem tractable. Many different approximation strategies are possible. (For example, Gaussian approximations, Exponential expansion, and orthogonal expansion of Hermite polynomials, etc. [Cul1, Lam1, Buc3]) Performance of the estimator depends on the fidelity of the approximated density functions as compared to the actual densities.

In order to derive finite approximations to the solution, the investigation of the conditional density shape is highly desirable. An engineering method, which visualizes the characteristics of time dependent density functions without solving for the Zakai equation, would be highly desirable in order to seek an appropriate approximation of the densities. The approach taken here is based on the numerical simulation of the vehicle and observations. The AHSV dynamic model has been flown in the simulation for a large number of runs (2000 per flight condition) to obtain the approximate visualization of the Fokker-Planck equations (propagation). With the observation equations, the distortions of density shapes due to the nonlinearities in observation equations are investigated. The results are investigated to substantiate the requirements posed by the Extended Kalman Filter.

6.5.1 Approach And Structure Of Simulation

The purpose of this analysis is the visual inspection of the behavior of the probability densities through use of the vehicle dynamics (propagation) and observations (update). The ultimate goal of the estimation problem is to obtain the conditional mean of the states. The governing equation to solve is the Zakai equation, as shown below. (In return, the solution is the conditional probability density functions of the states with respect to both propagation and update)

$$Zakai \quad \frac{\partial p^{+'}}{\partial t} = Lp^{+'}(x_t,t)dt + h(x_t,t)R^{\frac{1}{2}}p^{+'}(x_t,t)dy_t$$

$$\text{where } L(\bullet) = \sum_i \frac{\partial}{\partial x_i}\left(m_i(x_t,t)\bullet\right) + \frac{1}{2}\sum_{j,k}\frac{\partial}{\partial x_j \partial x_k}\left(s_j(x_t,t)s_k(x_t,t)\bullet\right)$$

The exact solution to the Zakai equation can not be easily found in closed form except for a few special cases (linear and Bene's problem) since the nature of the solution is infinite-dimensional [Lam1].

Due to the tractability problem of the Zakai equation, the solution to the estimation problem has been approached by seeking a finite approximation. There exist many different approaches to obtain a finite approximation of the solutions to the Zakai equation. Most often a finite sum and/or a group of finite known function is used to represent the solution. The only restrictions are the integrability, smooth and compact support assumptions, and positive-real values that are needed to qualify the approximations as a probability density function. There have been several past suggestions to use an exponential Fourier series, power series, Gaussian sum, Gaussian product, Hermite Gaussian polynomials, etc. [Lam1, Cul1, Buc3] If the density looks nearly Gaussian (or at least unimodal and symmetrical), then a Gaussian approximation can be applied. The commonly used Extended Kalman Filter falls into this category.

As an approach to find an appropriate scheme to approximate the functions, a method of visual inspection of the density deformation through use of vehicle dynamics and observation has been taken. The exact procedure requires the following steps: First, multiple simulations of the vehicle flight following the nominal trajectory are made up to one discretizing time step. Secondly, the ensemble cross-section at the end of the time step is taken as the propagated conditional density. Thirdly, the Baye's rule is used to obtain A-Posteriori densities. Lastly, these density shapes are used as the initial condition for the next propagation cycle, and the procedure is repeated over until the desired trajectory has been covered. The exact procedure is difficult to implement and is impractical since the random number generation for arbitrary density shapes is a difficult task. Therefore, the approach taken here is the independent visual investigation of the density evolution process, the propagation and update.

The vehicle dynamic equations, which are shown below, form the stochastic differential equations to simulate the propagation cycle of the filtering. The responses of

the vehicle dynamics to the random air-density disturbances are stored for given initial conditions for the vehicle dynamics (assuming Gaussian density initial condition). These data are used as the statistical basis for creating the estimate of the probability densities during the propagation cycle.

$$\begin{aligned} dV &= f_1(V,\alpha,\delta_e,\delta_T,\delta_v)dt + g_1(V,\alpha,\delta_e,\delta_T,\delta_v)d\rho^* \\ d\alpha &= f_2(V,\alpha,q,\delta_e,\delta_T,\delta_v)dt + g_2(V,\alpha,q,\delta_e,\delta_T,\delta_v)d\rho^* \\ dq &= f_3(V,\alpha,\delta_e,\delta_T,\delta_v)dt + g_3(V,\alpha,\delta_e,\delta_T,\delta_v)d\rho^* \\ d\theta &= qdt \end{aligned} \tag{6.34}$$

With the control variables $(\delta_e,\delta_T,\delta_v)$ defined as: $u=[\delta_e,\delta_T,\delta_v]^T = K_c(\alpha,V,q,\theta,R)$

These dynamic equations form a simulation cell block as shown in Figure 6-11.

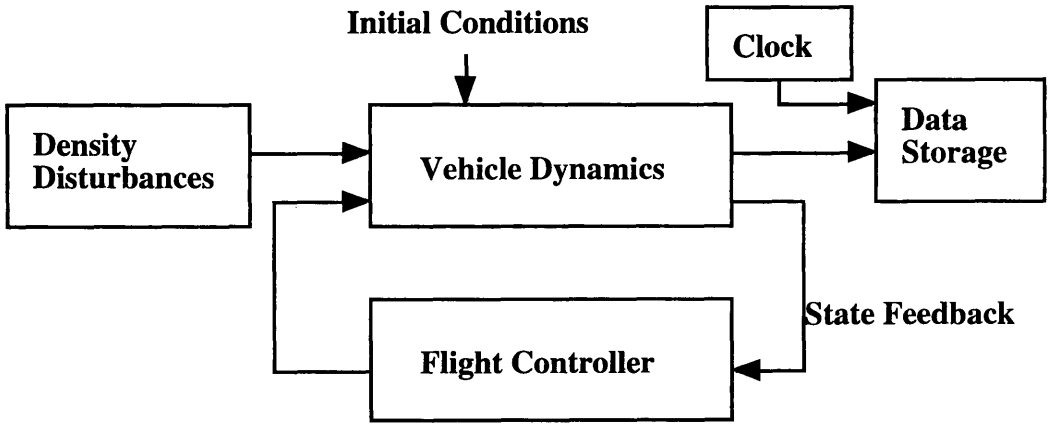

Figure 6-11 Configuration of AHSV Flight Simulation (For Each Cell Block)

The procedure of the simulation is shown in Figure 6-12. First, the simulation starts with set up of the initial condition densities and evaluation of the non-state-dependent parameters. Secondly, the code evaluates the state feedback law and external air-density disturbances, followed by computing the state derivatives. Thirdly, the Runge-Kutta 4/5th order integration routine is used to evaluate the state values at delta t later. Then the output is saved. Once the integration has been achieved up to final time, a flight trajectory data set has been collected. This procedure is repeated for 2000 runs and the collections of trajectory ensembles are presented in a histogram which provides a good visual presentation of the state probability densities. This result is also the solution to the Fokker-Planck equations;

$$\frac{\partial p}{\partial t} = \sum_i \frac{\partial}{\partial x_i}\left(m_i(x_t,t)p\right) + \frac{1}{2}\sum_{j,k}\frac{\partial}{\partial x_j \partial x_k}\left(s_j(x_t,t)s_k(x_t,t)p\right) \tag{6.35}$$

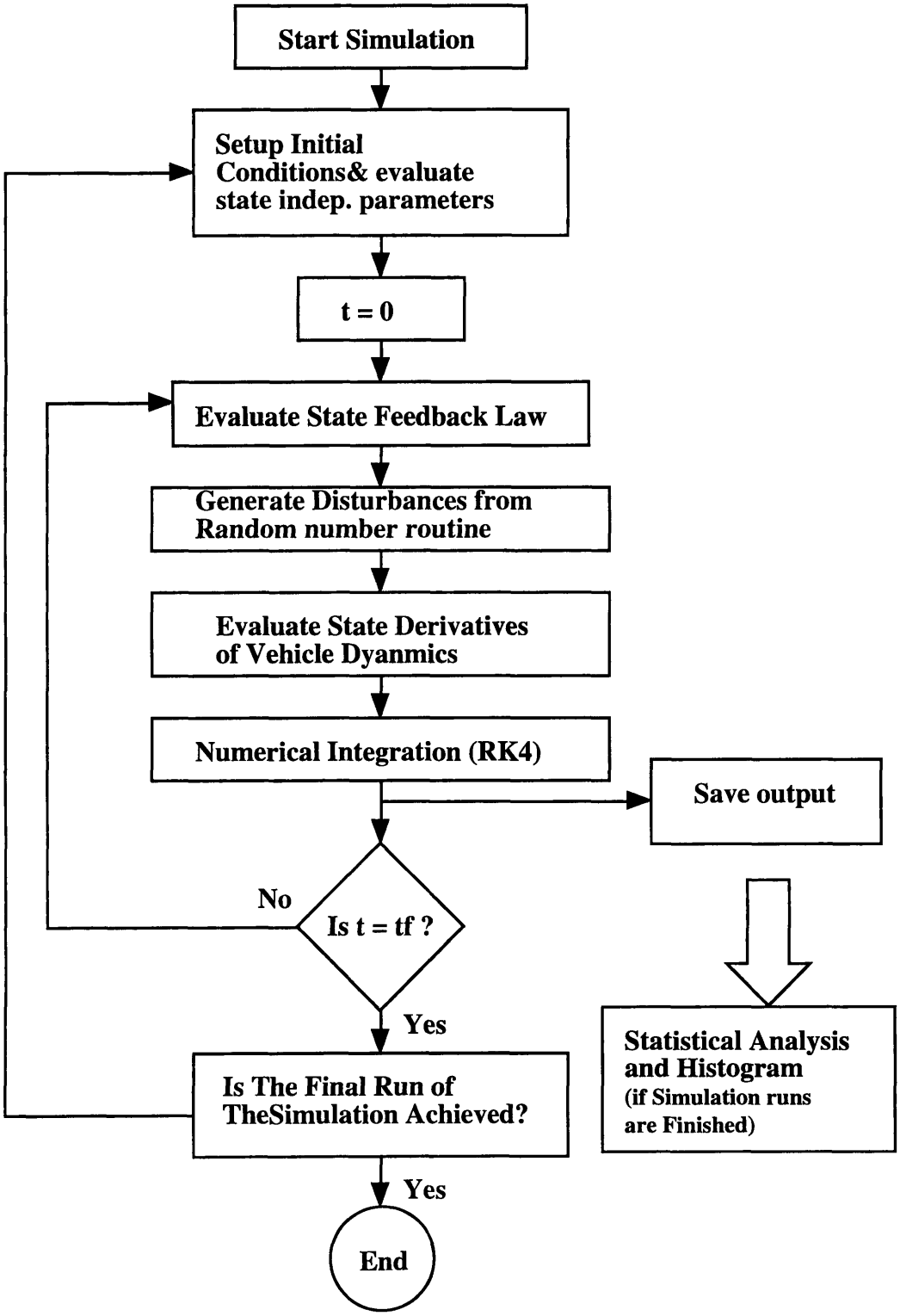

Figure 6-12 Simulation Procedure Block Diagram

The previous step provides the density shape deformation during the propagation cycle. The next step is to observe the deformation of the densities through the

observation nonlinearities. The overall scheme of the simulation is shown in Figure 6-13. First, the state variable ranges of interest (for nominal operation) are selected. At each point along the trajectory, random number generating codes are used to create fictitious state signals. Those signals are then injected into the observation equations (sensor equations) to obtain the measurement outputs. The measurement data (collection of obtained sensor signals) are then transformed into histograms (crude form of probability density construction based on likelihood of each sample).

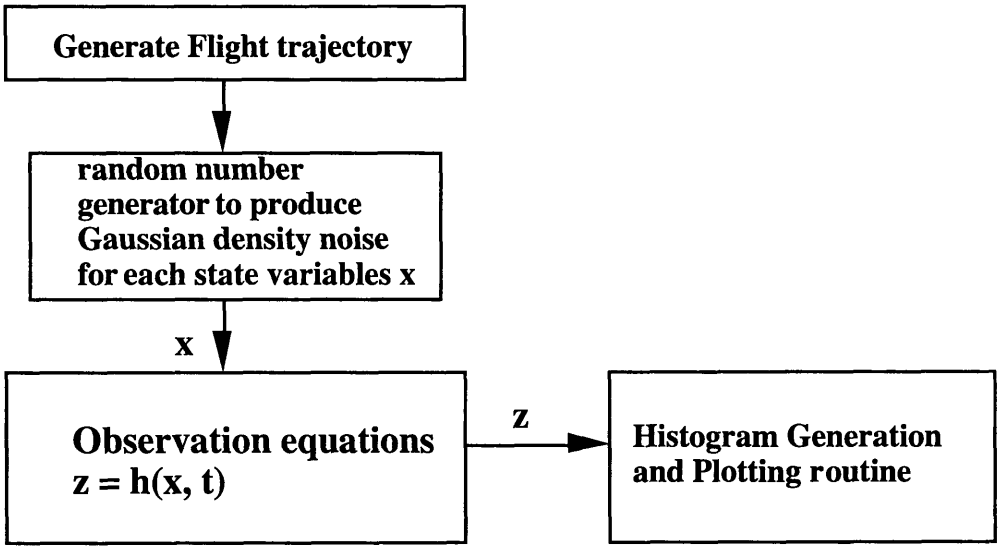

Figure 6-13 Observation Simulation Procedure Block Diagram

6.5.2 Simulation Results

The simulations were completed with 2000 runs per segment of the flight trajectory. The flight conditions corresponding to Mach numbers 10, 13, and 15 are selected. Each flight trajectory consisted of a 10 second flight segment. For the estimation propagation and update process, the statistical behavior of the dynamical system only needs to be verified for the duration of each update time step. Therefore, 10 second duration is considered more than adequate. Most initial transients will die out within a few seconds into the flight as verified in the control system design section. Also, the nominal flight altitude was considered constant throughout the simulation.

The size of fluctuations of the state variables about their nominal values will affect the apparent non-linearities. It is suspected that as the magnitude of the fluctuations increases, the deformation of the densities will increase due to a larger

nonlinear effect. Therefore, the initial conditions and the driving disturbance noises (air-density fluctuations) were set to the maximum allowable values while keeping the flight conditions in a realistic range. The air-density disturbances were increased until the angle of attack response was approximately 0.5 degree r.m.s. at Mach 10, which is the maximum tolerable value for the stable operation of the controller. The value decreased just a little bit (about 0.3 to 0.4 degrees) for higher Mach numbers (Mach 15). Half a degree variation seems small, but if we recall the plot of normal acceleration vs. angle of attack in chapter 4, the figure corresponds to about half a g of normal force fluctuation. That magnitude is certainly not acceptable for a manned vehicle; and may be regarded as an upper bound on normal acceleration variations.

The resulting histograms are shown in Figure 6-14 to 6-19. As can easily be seen from the figures, the densities retained the general shape of the Gaussian initial density. It is hard to conclude that the densities are exactly Gaussian, but it is clear that the density shapes do meet the requirements for the assumptions carried out on deriving the Extended Kalman Filters (symmetric and uni-modal). The results were consistent for all three segments of the nominal flight trajectories. A question also arises to verify the behavior of the dynamics if non-Gaussian densities were to be propagated. To be far away from Gaussian density, (also it is readily available on numerical packages) a uniform density function was used instead as the initial condition to the simulation for the flight segment of Mach 10 only. As shown in Figure 6-20, the diffusion process (vehicle dynamics) still tends to normal (Gaussian) as time progresses. The white Gaussian driving disturbance noises tend to push the state probability toward a Gaussian distribution even though the initial density was uniform. The results suggest that the diffusion process does actually help to preserve normality in this case.

The observation process has been simulated to visualize the deformation of the densities through the nonlinearities in the observation. For each Mach number segment of 10, 13, and 15, angle of attack is varied from 0 to 5 degrees to cover the realistic ranges of the operational regime. At each operating condition, a fictitious state signal is generated (Gaussian noise with a mean equal to the flight condition), then injected into the observation equations. The sensor noises were neglected since we want the deformation solely due to the state signal to measurement transformation. If the sensor noise is included, it will help the probability density of the measurement signal to be more Gaussian-like, based on the Central Limit Theorem. The resulting histogram is shown in Figure 6-22 to 6-30. The nonlinearities in the observation process did not alter

the results significantly. Because the nonlinearities involved in observation are mostly cosines and sines, and due to the small angular ranges of signals considered in this case, the observation process can be considered nearly linear, and the process will not deform the density significantly.

With the results from the propagation of densities, and from the observation process, we can conclude that if the initial condition is nearly Gaussian, then the propagation and update cycle will not destroy the basic characteristics of the initially defined density shapes within the defined operational regime. Therefore, if the control action minimizes the angular perturbation of the vehicle motion, then the overall vehicle system will exhibit at least statistically linear behavior. This evidences suggest that the Extended Kalman Filter should work satisfactorily for the considered range of the flight envelope.

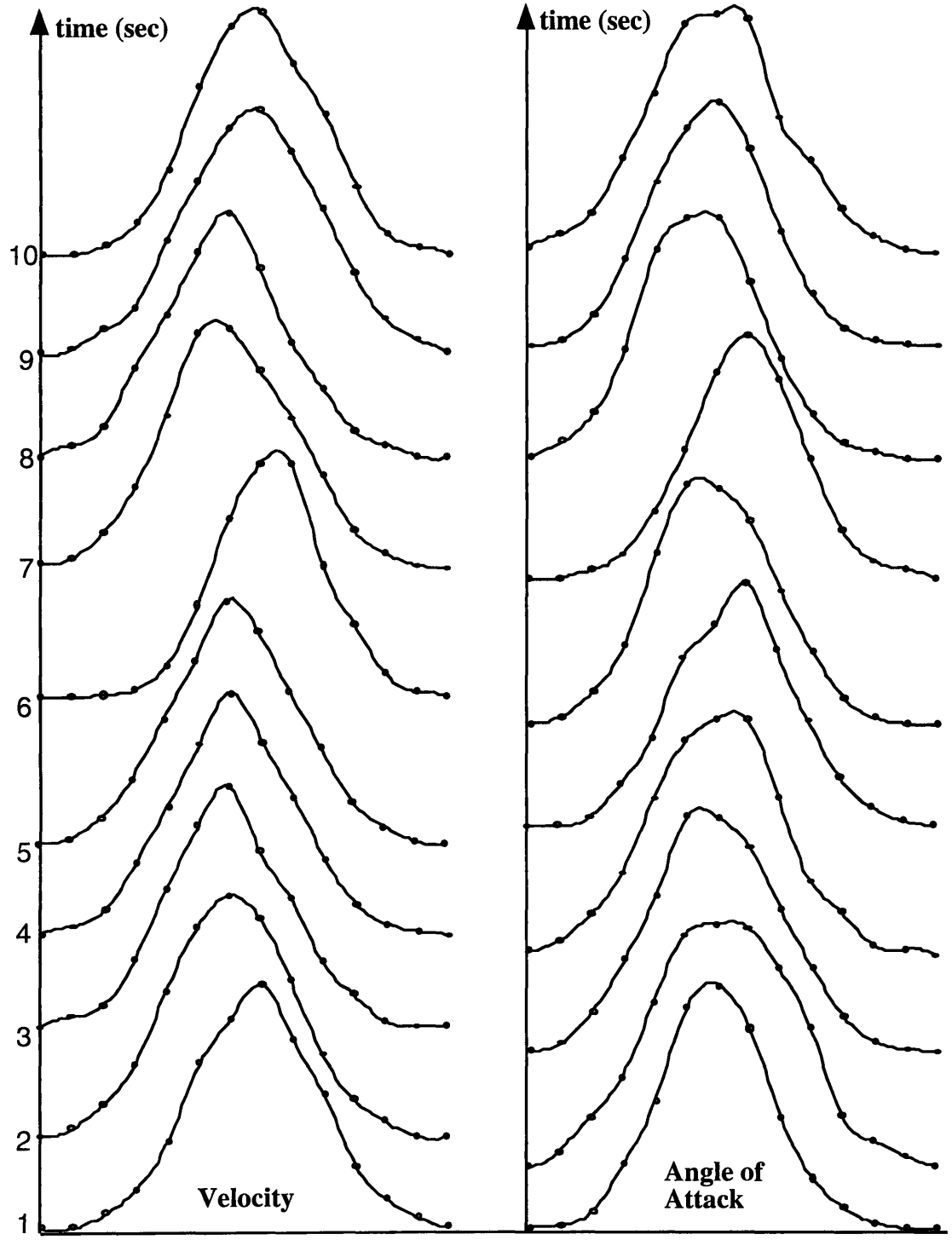

Figure 6-14 Histogram of State Variables - Velocity & Angle of Attack (Mach 10) (Gaussian Density Initial Conditions)

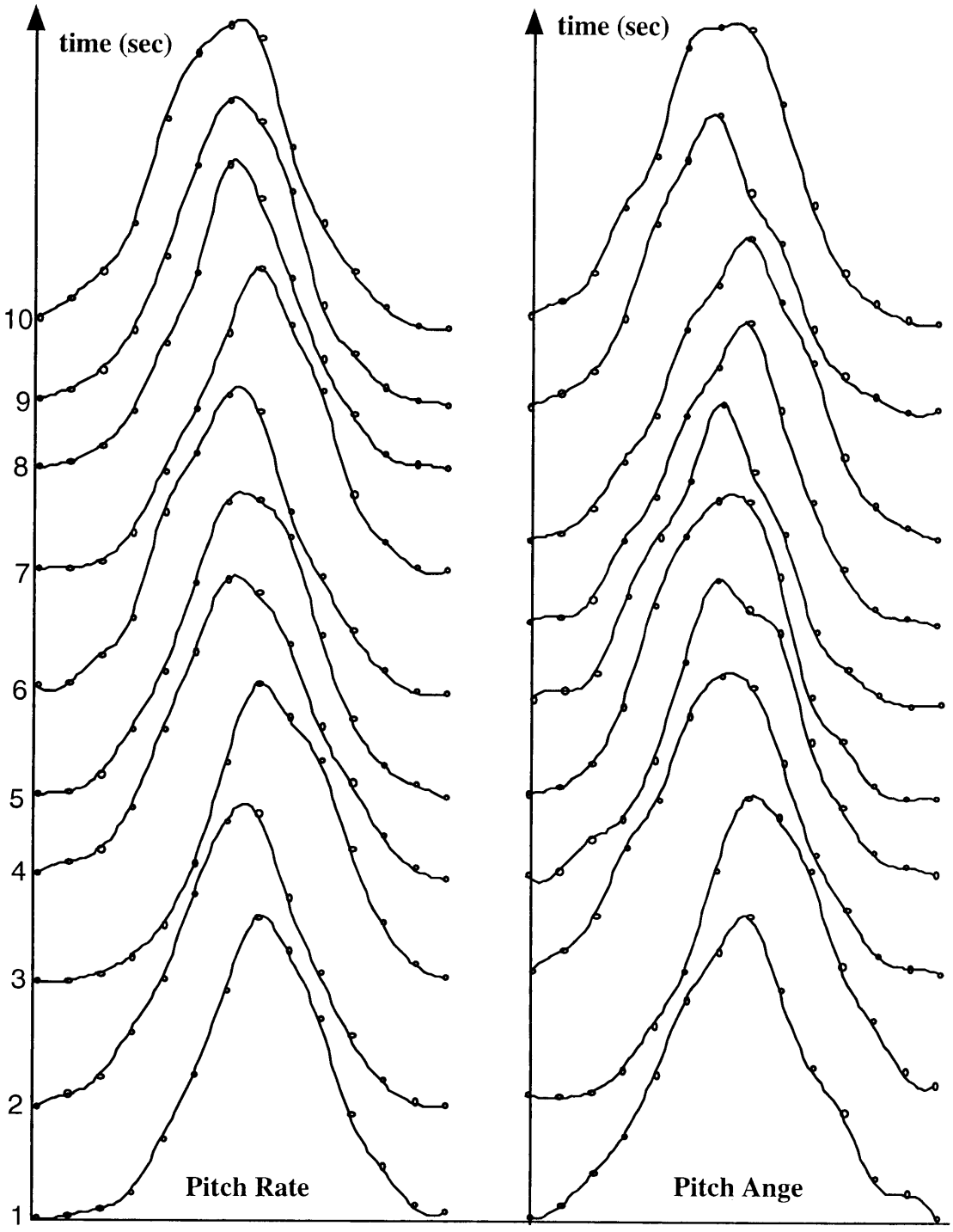

Figure 6-15 Histogram of State Variables - Pitch Rate & Pitch Angle (Mach 10) (Gaussian Density Initial Conditions)

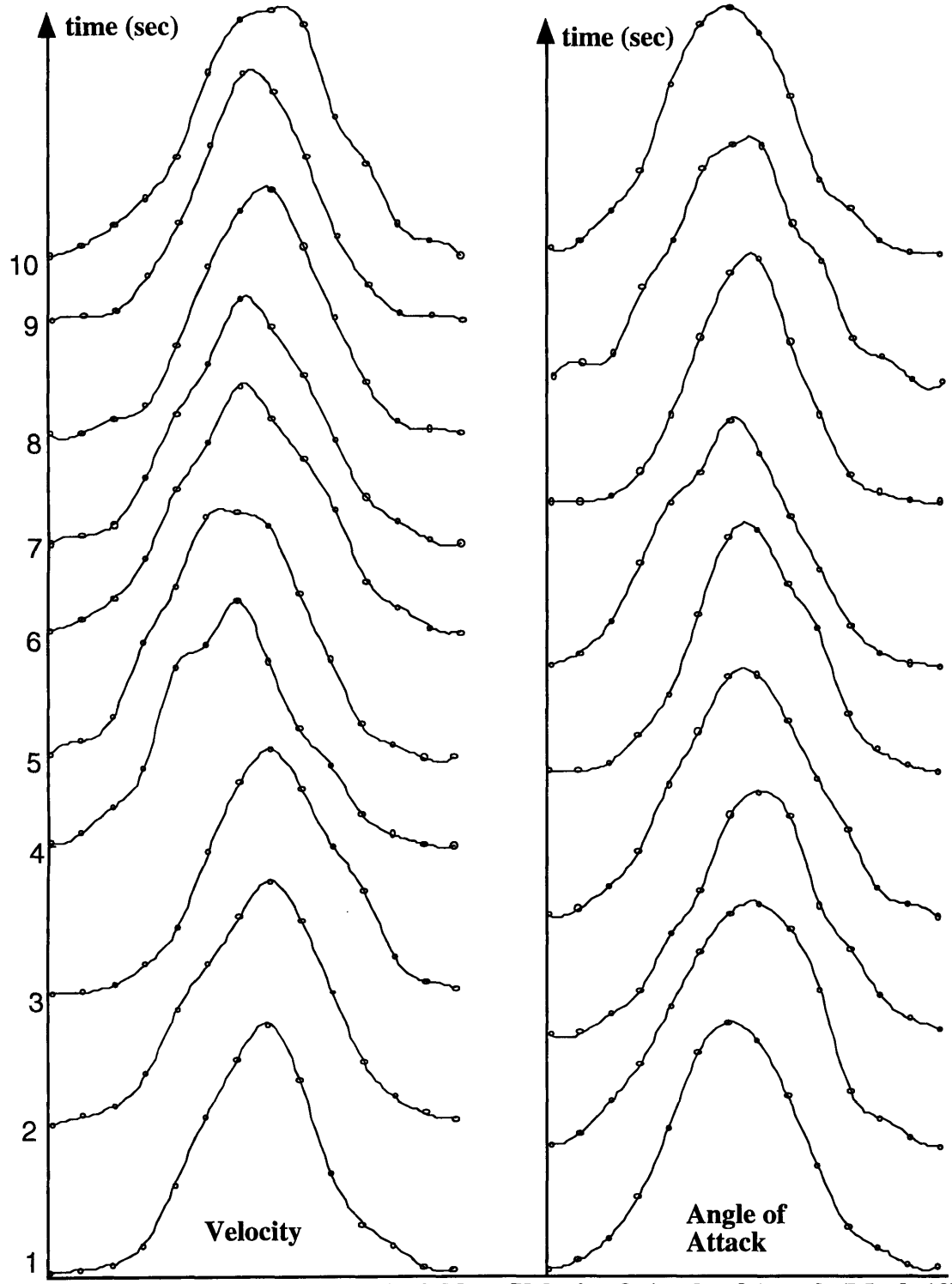

Figure 6-16 Histogram of State Variables - Velocity & Angle of Attack (Mach 13) (Gaussian Density Initial Conditions)

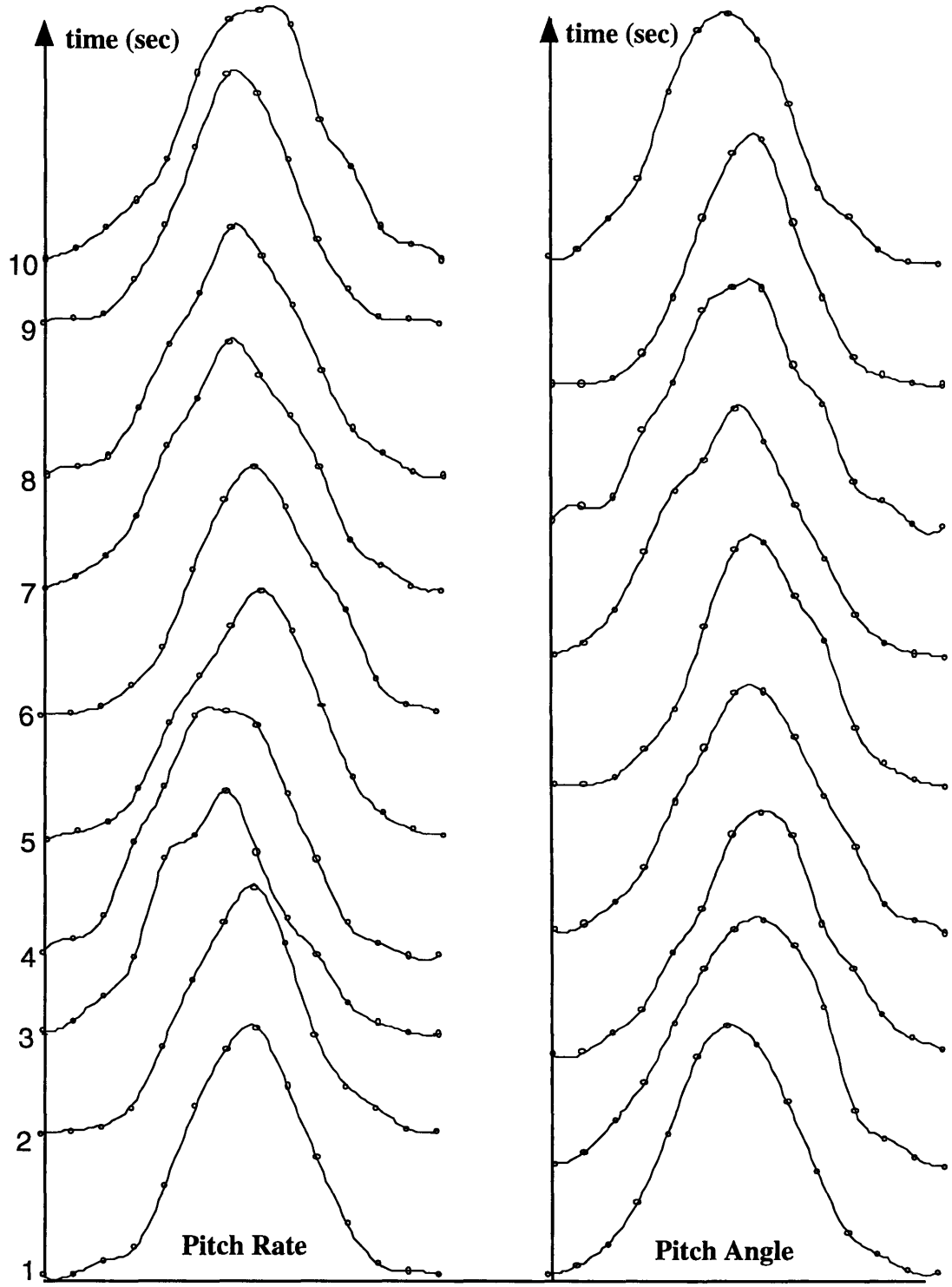

Figure 6-17 Histogram of State Variables - Pitch Rate & Pitch Angle (Mach 13) (Gaussian Density Initial Conditions)

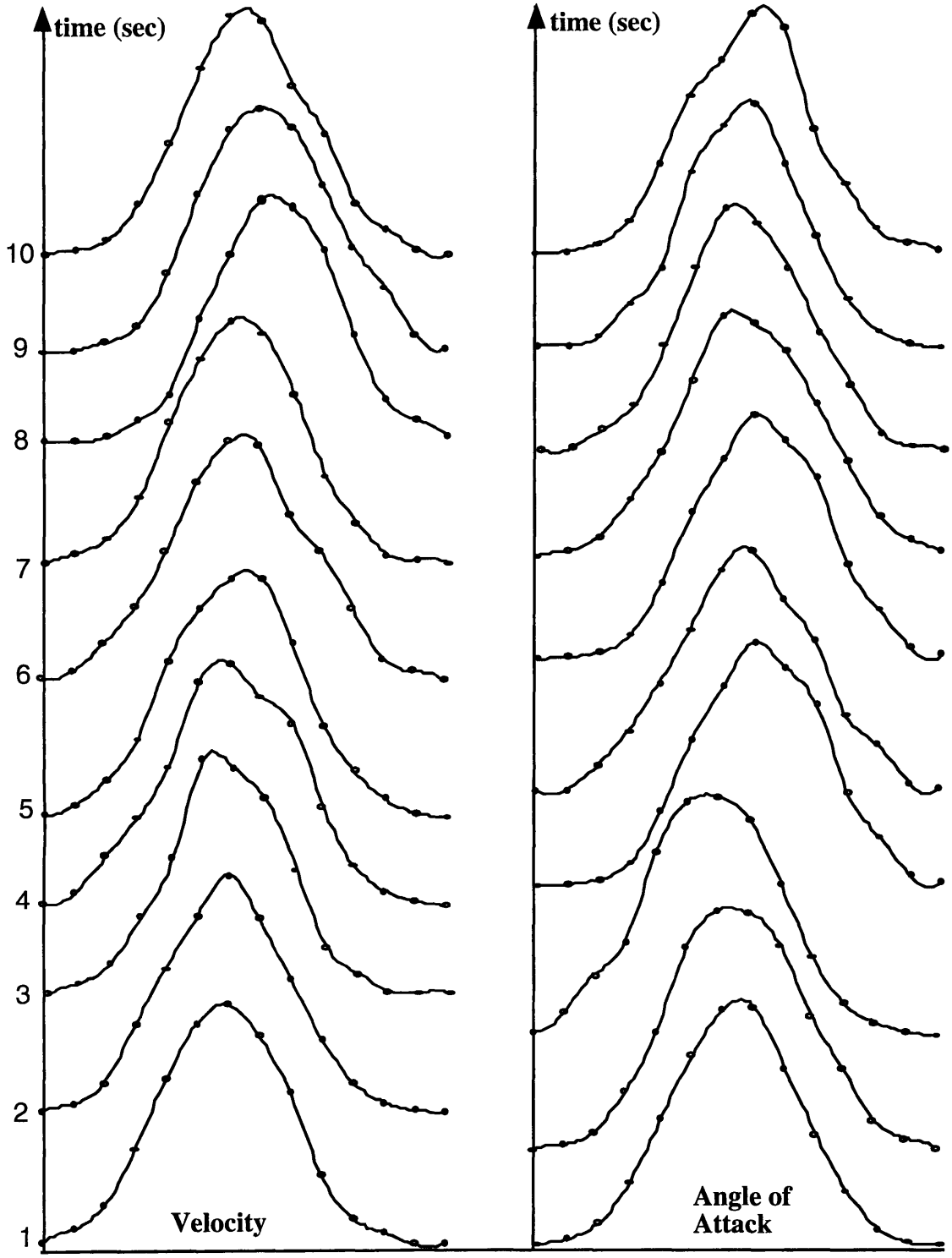

Figure 6-18 Histogram of State Variables - Velocity & Angle of Attack (Mach 15) (Gaussian Density Initial Conditions)

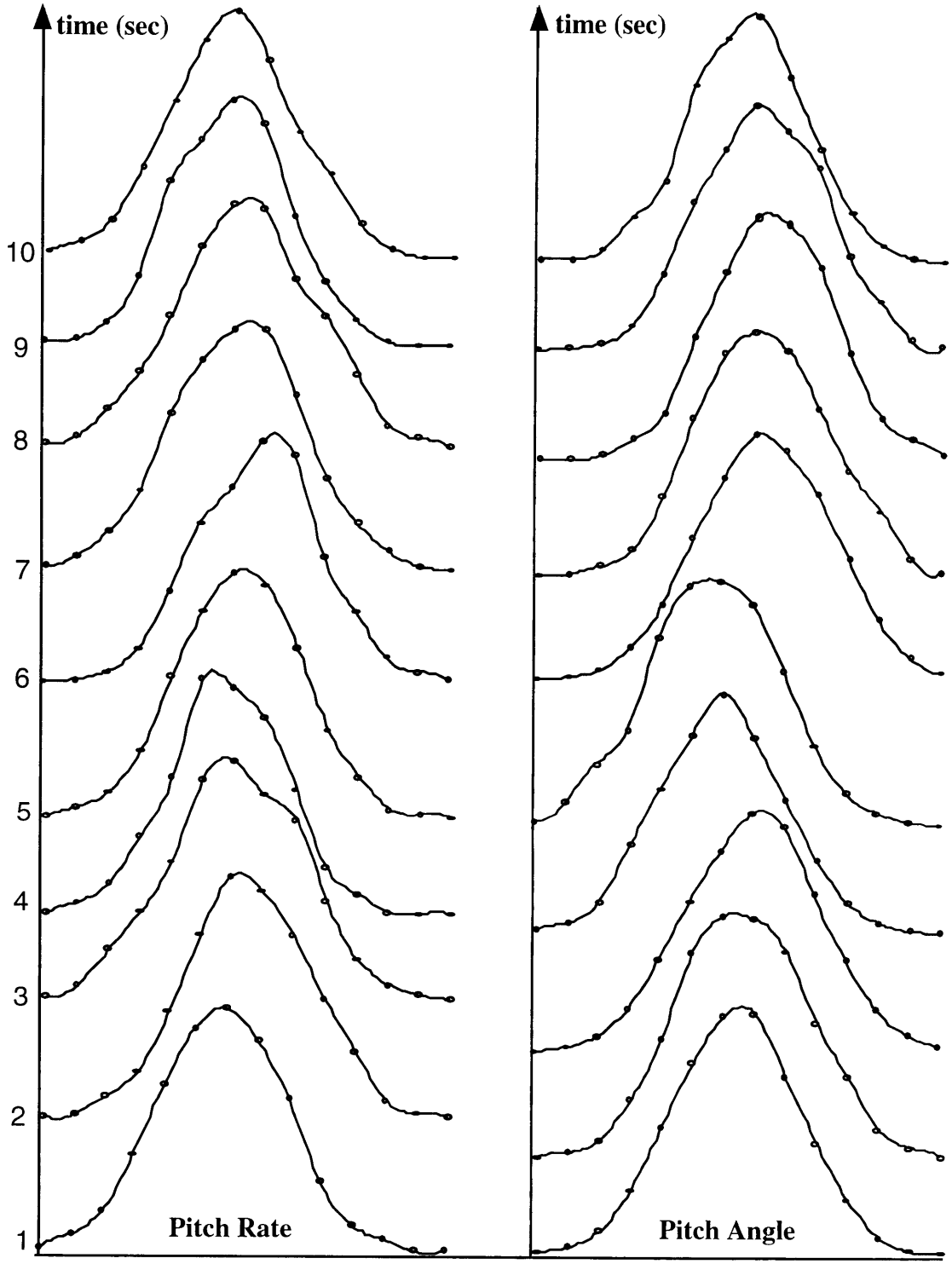

Figure 6-19 Histogram of State Variables - Pitch Rate & Pitch Angle (Mach 15) (Gaussian Density Initial Conditions)

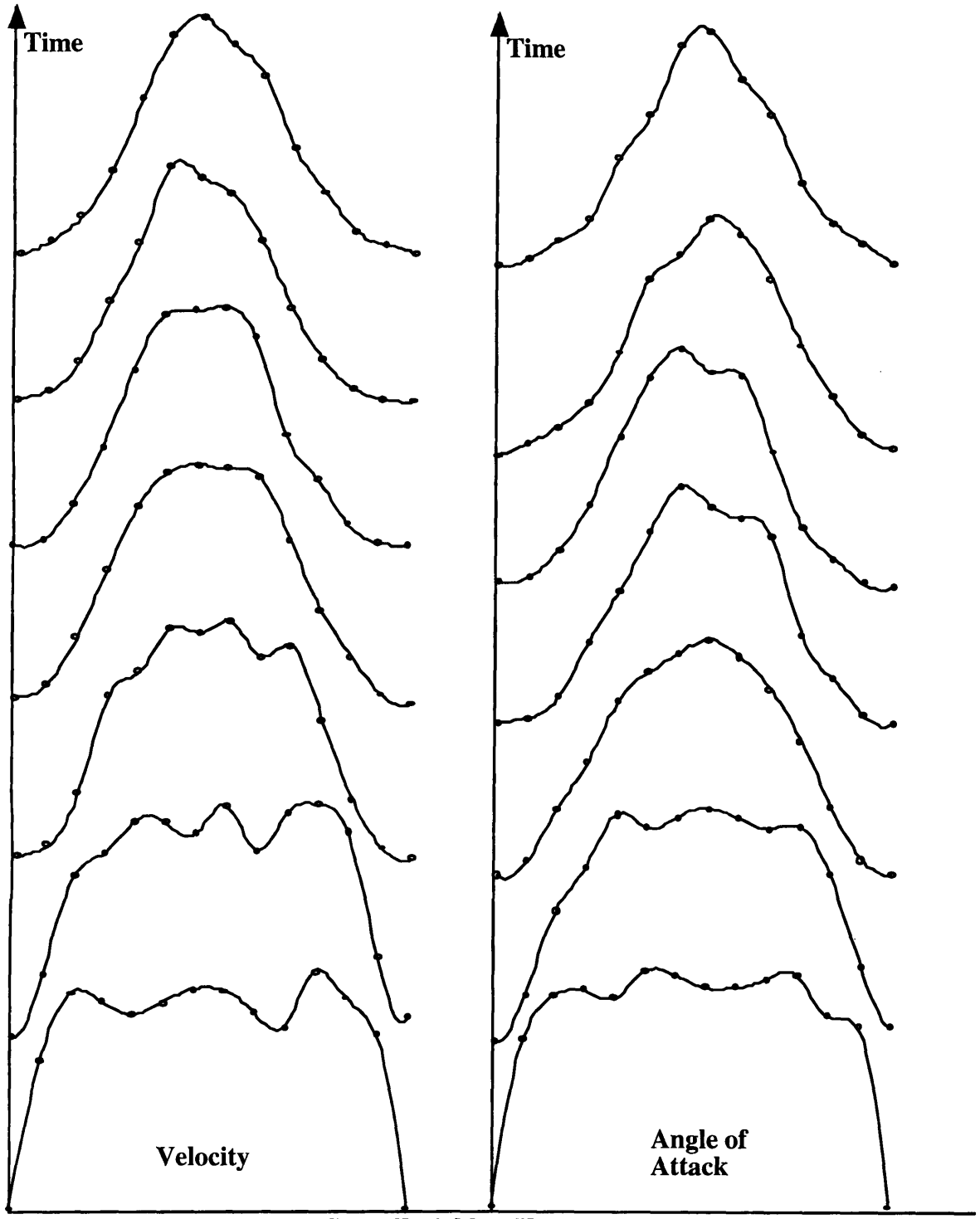

Figure 6-20 Histogram of State Variables -Velocity and Angle of Attack (M=10) (Uniform density Initial Conditions)

Histograms of Pressure Transducer output
(Density Deformation by Transformation of Observation Nonlinearity)

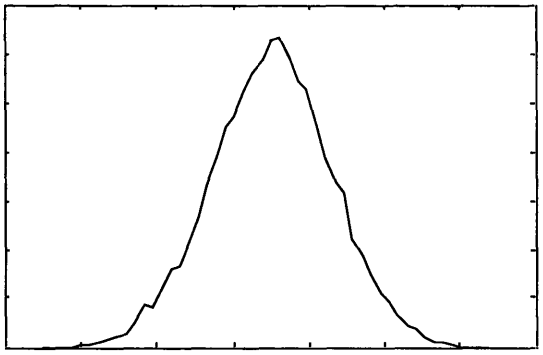

Pressure Transducer #1

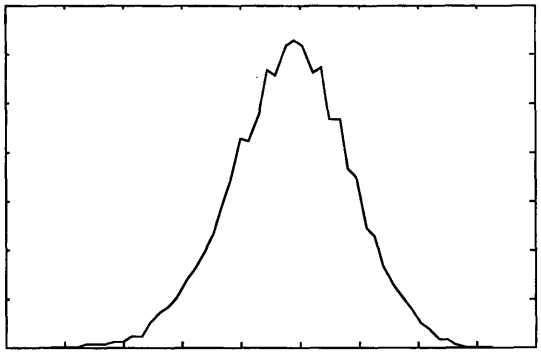

Pressure Transducer #2

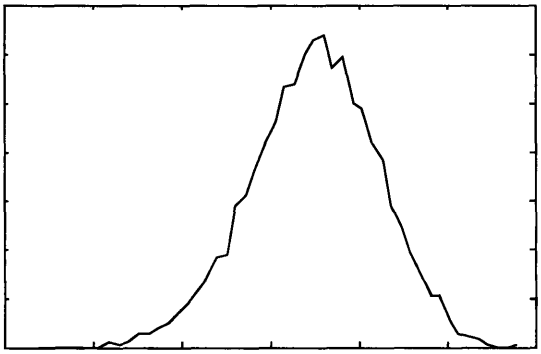

Pressure Transducer #3

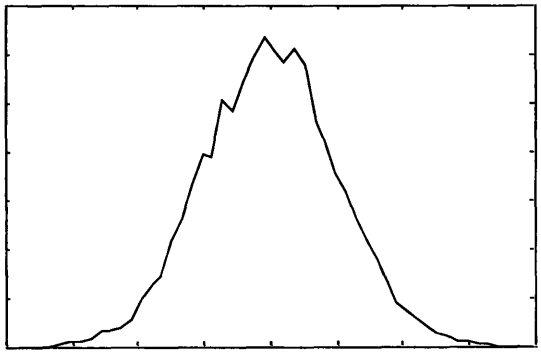

Pressure Transducer #4

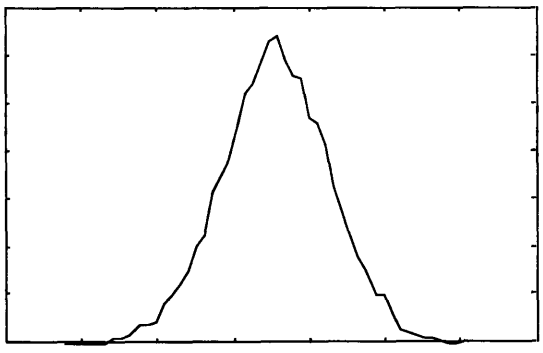

Pressure Transducer #5

Figure 6-21 Histogram of Pressure Sensor Output

Histograms of Rayleigh Scattering Sensor Output

(Density Deformation by Transformation of Observation Nonlinearity)

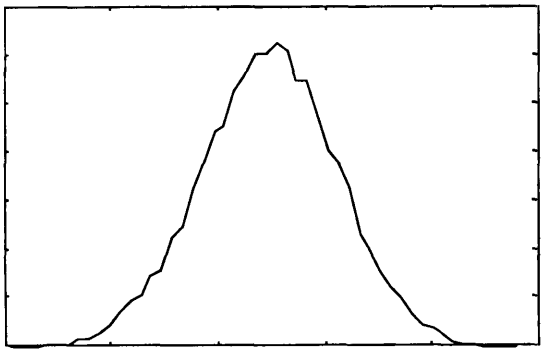

Optical Sensor (R-S) Up

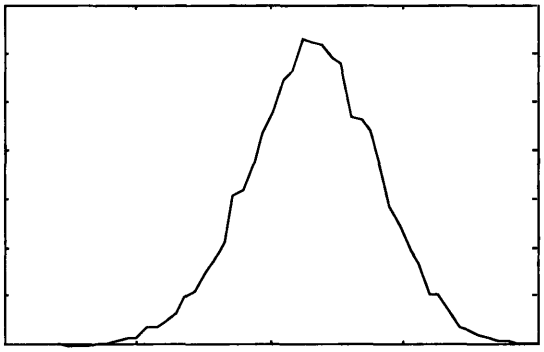

Optical Sensor (R-S) Down

Histograms of L.I.F. Sensor Output

(Density Deformation by Transformation of Observation Nonlinearity)

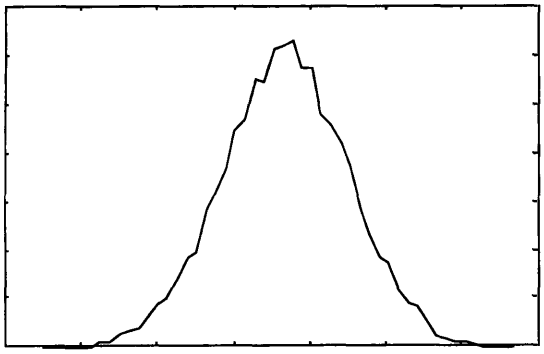

Optical Sensor (LIF) Up

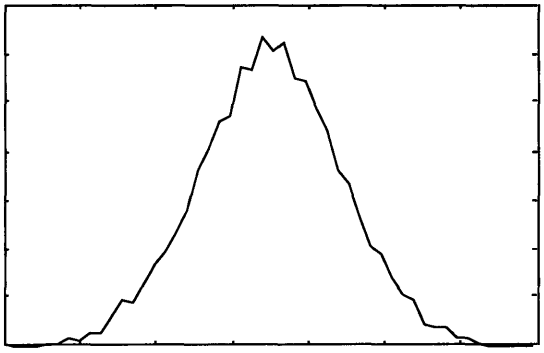

Optical Sensor (LIF) Down

Figure 6-22 Histogram of Optical Sensor Output

6.6 Estimator Development

The evidence shown in the section 6.5, Visualization of Conditional Density Propagation, suggested that the Extended Kalman Filter is applicable for the hypersonic flight condition from Mach 10 to 15. For flight operation within the ball of allowable perturbation, which is defined as a maximum perturbation region centered at the operating trajectory point, the diffusion process (the vehicle dynamics driven by the density disturbances) does not destroy the properties of unimodality and near symmetries about the mean. Also, the observation nonlinearities cause insignificant deformation of densities through the transformation. Consequently, an Extended Kalman Filter is designed for the AHSV air-data estimation problem (defined in section 6.2), and the results are summarized in this section.

The objectives of the design process and results shown in this section are, first, the demonstration of the air-data EKF design methodology, and the verification of the estimator performance. The validity and applicability of the conceptual air-data sensor system were the main emphasis of this thesis. The estimation results were viewed with emphasis on sensor issues such as:

- Can currently available air-data sensors be used with the estimator to obtain the required accuracy?

- How do estimation performance results change if relatively better or worse optical sensors were used (as compared to the SEADS-like pressure system)?

- If we want a certain performance level from the estimator, how accurate must the sensors be?

With an initial guess of flight conditions (the initial conditions and the external disturbances from density fluctuations) and an air-data sensor performance specification, a particular solution of achievable performance of the estimator can be determined. In order to supplement the results of these chapters, Chapter 7 provides an assessment of the sensor requirements which will be approached by a method that does not depend on estimator simulation results.

6.6.1 EKF Design Procedure for AHSV Air-Data Estimation

For the AHSV air-data estimation problem, the EKF formulation is discussed here. As defined in the section 6.2, Estimation Problem Formulation, the diffusion and observation process can be shown as:

Diffusion:

$$\begin{aligned} dV &= f_1^*(V,\alpha,)dt + g_1^*(V,\alpha)d\rho^* \\ d\alpha &= f_2^*(V,\alpha,q)dt + g_2^*(V,\alpha,q)d\rho^* \\ dq &= f_3^*(V,\alpha)dt + g_3^*(V,\alpha)d\rho^* \end{aligned} \tag{6.36}$$

$$\begin{aligned} dP_1 &= P_t\left[\left(1-R^*(V)\right)\cos^2\left(\alpha+30^o\right)+R^*(V)\right]dt + dn_{p_1} \\ dP_2 &= P_t\left[\left(1-R^*(V)\right)\cos^2\left(\alpha+15^o\right)+R^*(V)\right]dt + dn_{p_2} \\ dP_3 &= P_t\left[\left(1-R^*(V)\right)\cos^2(\alpha)+R^*(V)\right]dt + dn_{p_3} \\ dP_4 &= P_t\left[\left(1-R^*(V)\right)\cos^2\left(\alpha-15^o\right)+R^*(V)\right]dt + dn_{p_4} \\ dP_5 &= P_t\left[\left(1-R^*(V)\right)\cos^2\left(\alpha-30^o\right)+R^*(V)\right]dt + dn_{p_5} \end{aligned}$$

Observation:

$$\begin{aligned} du_1 &= V\cos\left(35^o+\alpha\right)dt + dn_1 \\ du_2 &= V\cos\left(30^o-\alpha\right)dt + dn_2 \\ du_3 &= V\sin\left(35^o+\alpha\right)dt + dn_3 \\ du_4 &= V\sin\left(30^o-\alpha\right)dt + dn_4 \end{aligned} \tag{6.37}$$

which include a full state feedback (closed loop dynamics). The density disturbances were modeled as a set of first order linear systems with the 0.3 second time constant. The time constant was estimated by the following arguments. If we assume the frozen field of density distribution along the flight trajectory, then 1km spatial correlation in all directions and the flight speed of 3000 m/s (approx. Mach 10 flight) result in 0.3 second time constant. The associated dynamics and observation equations can be simply stated with discretized measurements as:

$$\begin{aligned} \dot{x}(t) &= m(x,t) + s(x,t)w(t) \\ z(k) &= h\left(x(k),k\right) + n(k) \end{aligned} \tag{6.38}$$

where {w(t)} and {n(t)} are zero-mean, white Gaussian noise processes with:

$$\mathcal{E}\left\{w(t)w(\tau)^T\right\} = Q(t)\delta(t-\tau) \quad \text{and} \quad \mathcal{E}\left\{n(t)n(\tau)^T\right\} = R(t)\delta(t-\tau)$$

and for $t \geq t_o$ and $x\left(t_o\right) \equiv N\left(x_o, P_o\right)$ and $k \equiv t_k$. The problem is specialized by assuming the case of uncorrelated process and sensor noise. Furthermore, the state and noise (process and sensors) are uncorrelated at any given time, as shown below.

$$\mathcal{E}\{w(t)n(\tau)\}=0,\quad \mathcal{E}\{x(t)w(\tau)^T\}=0,\quad \mathcal{E}\{x_i(t)n_j(\tau)\}=0,$$

With the linearization defined as (Results are shown in Appendix C):

$$F(\hat{x},t)\equiv\left.\frac{\partial m(x,t)}{\partial x}\right|_{x=\hat{x}}\qquad\text{and}\qquad H(\hat{x},t)\equiv\left.\frac{\partial h(x,t)}{\partial x}\right|_{x=\hat{x}}$$

the resulting EKF equation is:

Propagation:

$$\dot{\hat{x}}(t)=m(\hat{x}(t),t)$$
$$\dot{P}(t)=F(\hat{x}(t),t)P(t)+P(t)F(\hat{x}(t),t)^T+SQ(t)S^T \tag{6.39}$$

Update:

$$\hat{x}(k+1/k+1)=\hat{x}(k+1/k)+K(k+1)\left[z(k+1)-h(\hat{x}(k+1/k))\right]$$
$$P(k+1/k+1)=\left[I-K(k+1)H(\hat{x}(k+1/k))\right]P(k+1/k)$$
$$K(k+1)=P(k+1/k)H(\hat{x}(k+1/k))^T\left[H(\hat{x}(k+1/k))P(k+1/k)H(\hat{x}(k+1/k))^T+R(k+1)\right]^{-1} \tag{6.40}$$

(note: $\tilde{x}(t)=x(t)-\hat{x}(t)$ is the estimation residual or estimation error and $\hat{x}(k+1/k)$ is the estimate at time k+1 given measurements up to k)

The Extended Kalman Filter for the AHSV air-data system has been implemented by the following numerical computation procedure:

Step 1: Integrate the state and covariance propagation equations (6.39) using a numerical integration routine (Runge-Kutta 4-5 etc.) with initial guess (initial condition) of the state estimate and state covariance. If the filter implementation is for the computer simulation, the vehicle dynamics with disturbances should be integrated altogether. The linearization process within the filter covariance equation should be linearized about the previous update of state estimate.

Step2: Obtain sensor output (measurements). For numerical simulation of the vehicle and the estimator, the observation should be made with the true state values (the propagated state values from integrating the vehicle dynamics).

.

Step3: Compute the filter gain K. With the computed filter gain, update the state estimate and covariance. The linearized matrices are obtained by linearizing the vehicle dynamics and observations about the propagated estimate of state variables.

Step4: Repeat from step 1 to obtain the estimate for next time step.

When the on-line implementation of the EKF is needed, these procedures must be computed by the on board computer. The most serious problem associated with the EKF implementation is its sensitivity with respect to the initial condition of the state and covariance. Since the filter is linearized each step by the current estimate of states, large errors in the initial condition would result in grossly different linearized dynamics.

Different types of estimation strategies are also applicable for the AHSV air-data estimation problem. The extended Kalman filter can be further improved by iterating the update equations with newly linearized functions. Another possibility is the second order Gaussian filter. By taking up to second order terms with Gaussian assumptions, the second order filter can be formulated and can improve the estimate if the second order term is significant. Second order filter imposes about 15% more computational burden compared to EKF. Second order filter performs much better in steady state compared to other nonlinear filters, however it may cause wild transient behavior for high frequency operation. In general, the iterated filter has lower r.m.s. error while the second order filter has lower bias. Regardless of type of filters, these filters require on-line computation and the filter performance is heavily dependent on initial conditions.

6.6.2 Statistical Analysis

Before making an attempt to obtain some measure of the air-data estimator (in general, of any estimator) performance, it is necessary to answer a question regarding the confidence one has in the statistical results. The statistical analysis, via the Monte-Carlo simulation, is achieved by generating large samples of estimation error trajectories. The ensemble of the trajectory cross-section at any given time provides the data for the statistical analysis. The performance of the estimator can be measured by an estimate of mean and a variance of the estimation error. The question that must be answered here is: How many sample trajectories are needed to achieve confidence in the statistics? In other words, if we select a certain number of simulation runs, how good is the estimate of the mean and variance?

In order to estimate the central moments of a random process, a large number of statistically independent samples are generated and the statistic

$$\hat{\mu}_m = \frac{1}{N}\sum_{i=1}^{N}\left(\hat{x}_n^i - x_n^i\right)^m \tag{6.41}$$

is formed. Here μ_m is the mth moment of the difference $\hat{x}_n^i - x_n^i$ for all i. The statistics (6.41) converge quickly and asymptotically to normal by the Central Limit Theorem. With mean and variance given by:

$$\mathrm{E}\{\hat{\mu}_m\} = \mu_m \tag{6.42}$$

$$\mathrm{Var}\{\hat{\mu}_m\} = \frac{\mu_{2m} - \mu_m^2}{N} \tag{6.43}$$

Since the statistics are Normal, we can compute the probability confidence bands for the estimates for large N.

For the purpose of estimating the performance of the estimator, we are only interested in the mean and variance of x, where m=1, and 2. If we assume the asymptotically normal property of the estimate of statistics, and also assume that the samples are statistically independent, the confidence band can be computed. If it is assumed to be normal, then the probability of the estimate of the mean can be stated as:

$$\mathrm{P}\left(\left|\hat{\mu} - \mathrm{E}\{\hat{\mu}\}\right| \le k\sigma_\mu\right) = C \tag{6.44}$$

If the variance is unknown, (in this case a standard deviation), the statistic for unbiased estimate is

$$s^2 = \frac{1}{N-1}\sum_{i=1}^{N}\left(\hat{\mu} - E\{\hat{\mu}\}\right)^2$$

When assuming the fact that μ is normal, the statistic given above has a Student-t distribution (with n-1 degree). For large N (above 30), it can be approximated as normal and use same statistical analysis as for the mean with adjustment factor of $\sqrt{\frac{N}{N-2}}$. Since our simulations' runs are either 1000 or 2000 runs, the adjustment factor can also be approximated to be a unity.

where, as examples for specific k and C are:

k	C
0.674	50%
1.64	90%
1.96	95%
2.58	99%
3 (three sigma)	99.74%

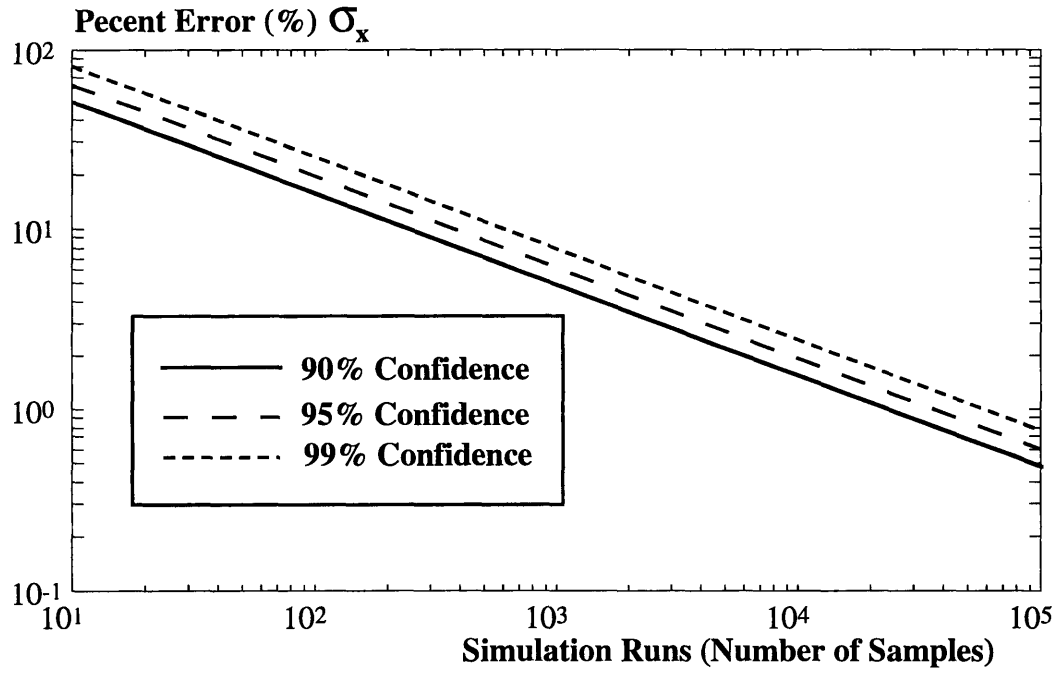

Figure 6-23. Simulation Run Requirements

The resulting error magnitude (as a percentage of one sigma of x) is plotted against the number of simulation runs (number of samples) in Figure 6-23. When considering the fact that the probability (0.9974) that a Gaussian deviate lies within three standard deviations of its mean, any confidence band of fewer than three standard deviations would be at best subject to misinterpretation since the associated probability for plus or minus one standard deviation is only 0.6836 and only 0.9544 for two. It is difficult to compromise for the adequate number of simulation runs because the convergence is extremely slow with N. As shown in Figure 6-23, for 95% confidence, the percent error reduces from 6% to about 2% by increasing the number of runs from one thousand to ten thousands. The increase of the number of simulation runs by an order of magnitude is extremely time consuming while the benefit in the improved confidence seems to be minimal. For the simulation of AHSV air-data estimation, 1000 runs were taken because of computation power and time constraints. This corresponds to about 6% error with 95% confidence. Obviously, a larger number of runs would result in a better estimate of the performance.

6.6.3 Simulation Results

The Monte-Carlo simulation has been performed with the vehicle, sensors and estimator running simultaneously. The initial conditions are the flight velocity of 3000m/s (approximately Mach 10), 2.7 degree angle of attack (design value for steady state), and zero pitch rate. The external disturbances are chosen to match the effective acceleration disturbances, and they are: 0.1m/s^2 (roughly 1/100th of g) axial acceleration, 0.1 deg./sec. angle of attack rate, and 0.01deg./s^2 pitch acceleration. These flight conditions and the effective acceleration are considered to be a mild operating condition.

The air-data sensor configuration consisted of a realistic figure based on available technology. The pressure sensor accuracy of 2% (SEADS) and the Rayleigh Scattering sensor with 0.8% were used for the simulation. A set of typical estimator response is plotted in Figure 6-24 through 6-26. Also a typical estimator performances are plotted in Figure 6-27 through 6-29. As shown in Figure 6-28, the achieved performance of the sensor-estimator combination does not meet the accuracy requirement of 0.1degrees. The achieved angle of attack accuracy was off by factor of 2. Since the estimate of SEADS performance was about 0.5 degree accuracy in angle of attack, the improvements in angle of attack accuracy made by implementing an EKF are limited to a factor of two. This result suggests that the hardware improvements are needed for further accuracy gains, but less than order of magnitude improvements are needed.

The second configuration is based on the balanced design from Chapter 7 analysis, the pressure sensor accuracy of 0.6% and 0.2% for the optical sensor. For this configuration, the estimation result confirmed its required performance. However, when considering the fact that the sensor precision requirements are a function of the external disturbance magnitude and since the precision requirements get tighter as the external disturbances increase, the currently available pressure sensors are not applicable for the AHSV application. Finally, the histograms of the estimation error are plotted in Figure 6-30 and 6-31. These results indeed verfied that the EKF approximation is an adequate application for this vehicle.

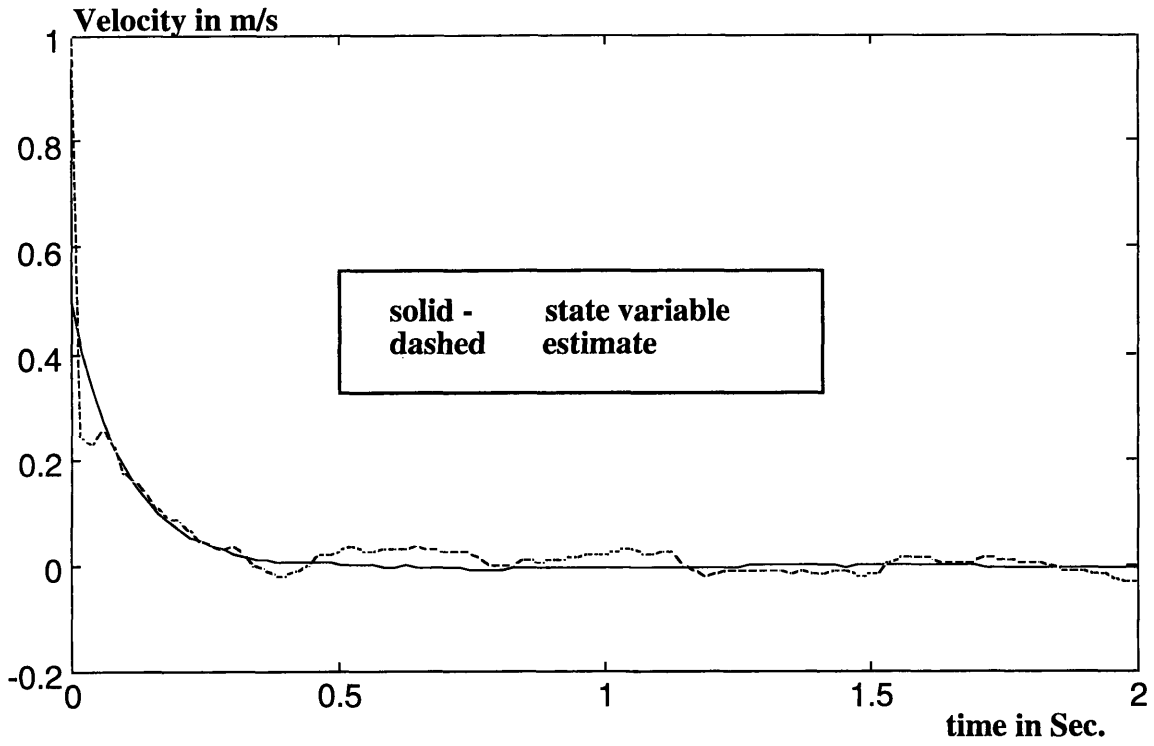

Figure 6-24 Velocity Perturbation Trajectory and Velocity Estimate

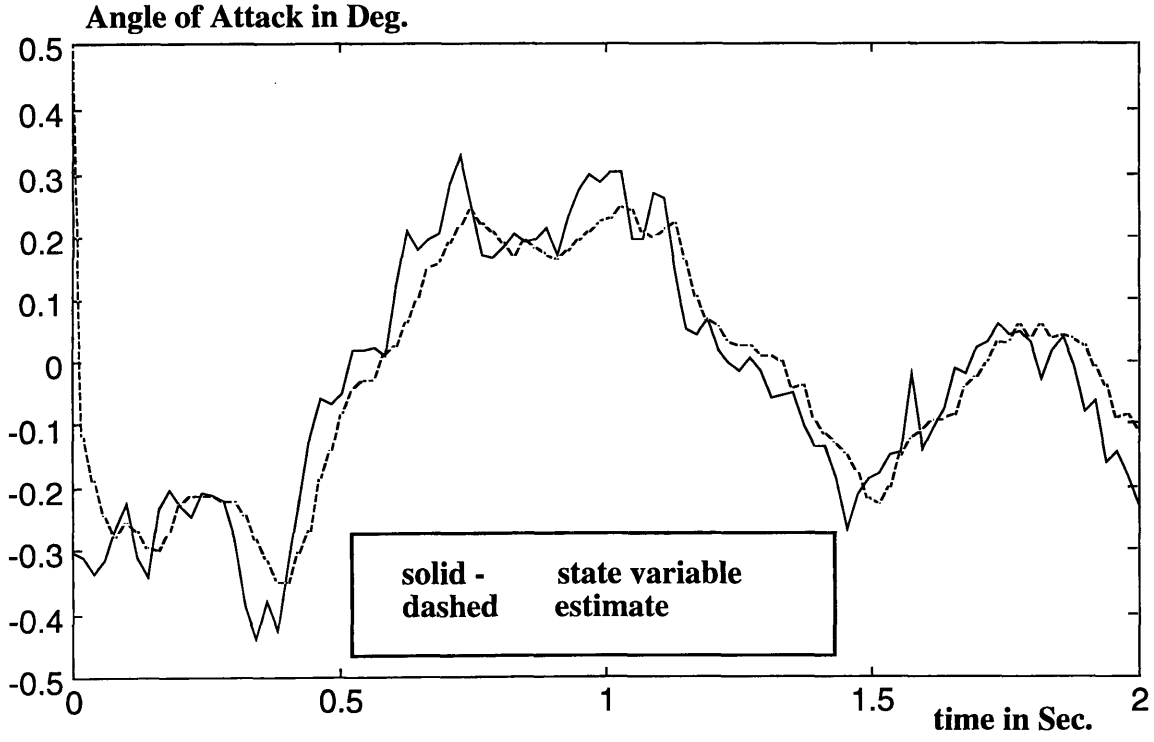

Figure 6-25 Angle of Attack Perturbation Trajectory and Angle of Attack Estimate

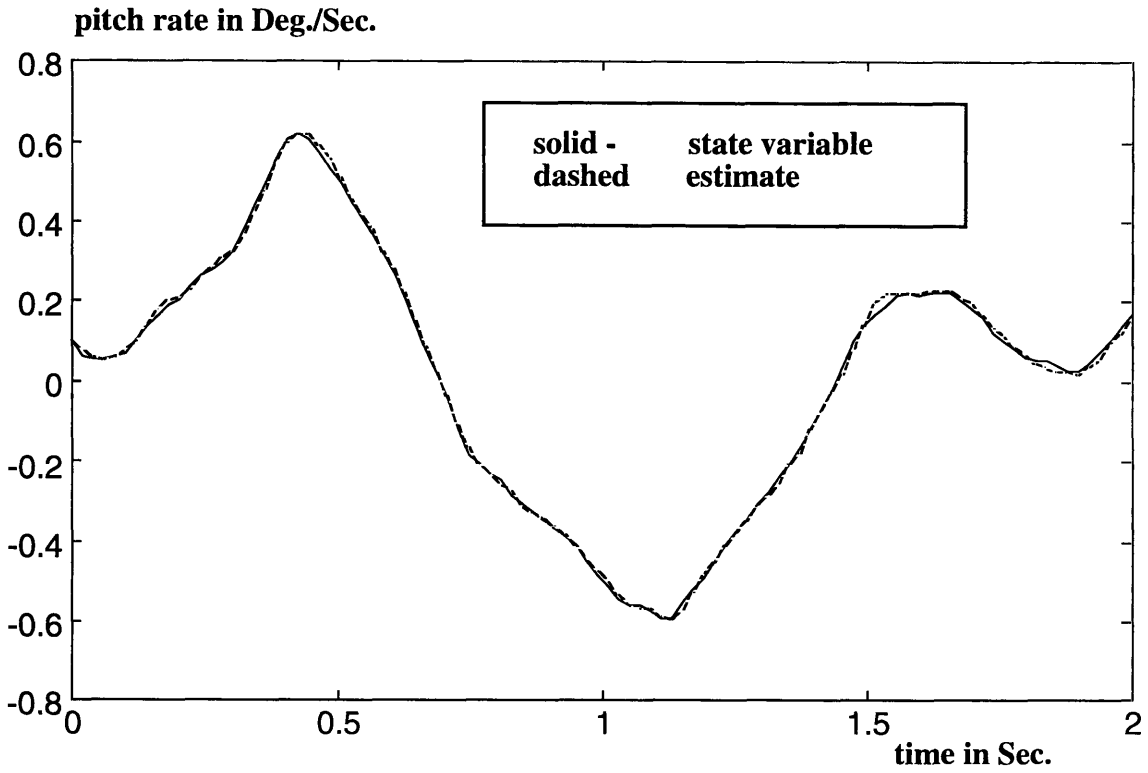

Figure 6-26 Pitch Rate Trajectory and Pitch Rate Estimate

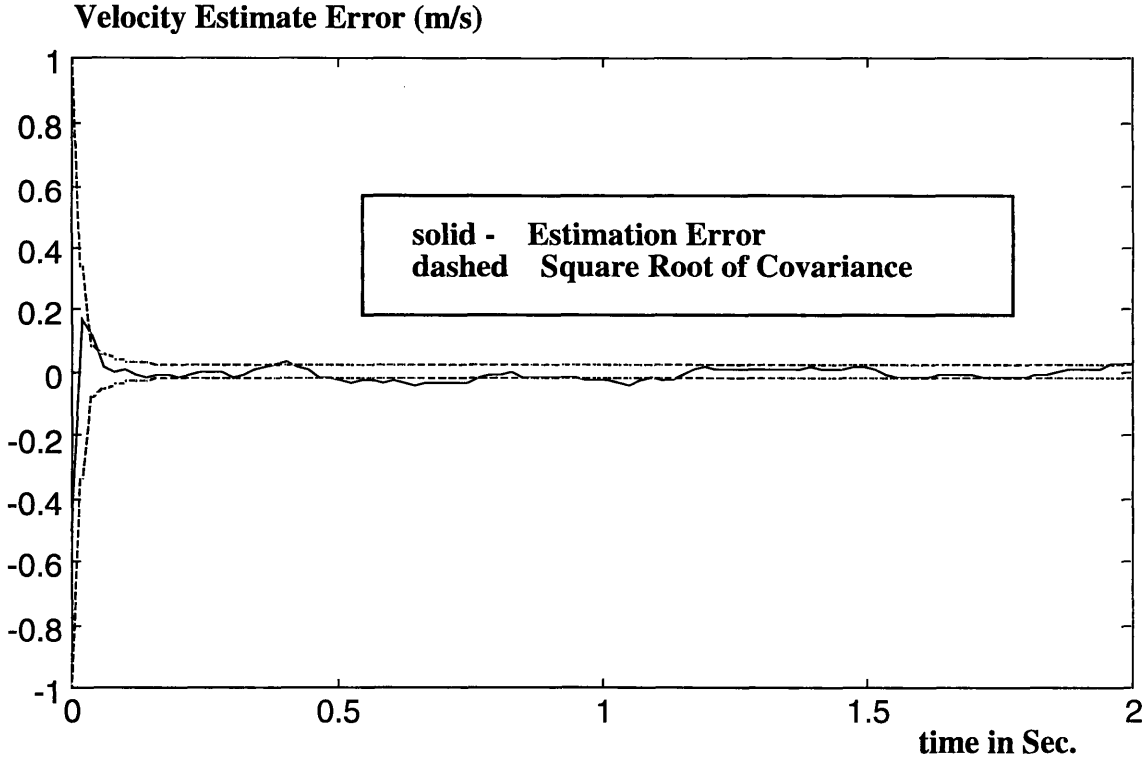

Figure 6-27 Estimator Performance (Velocity Estimation Error)

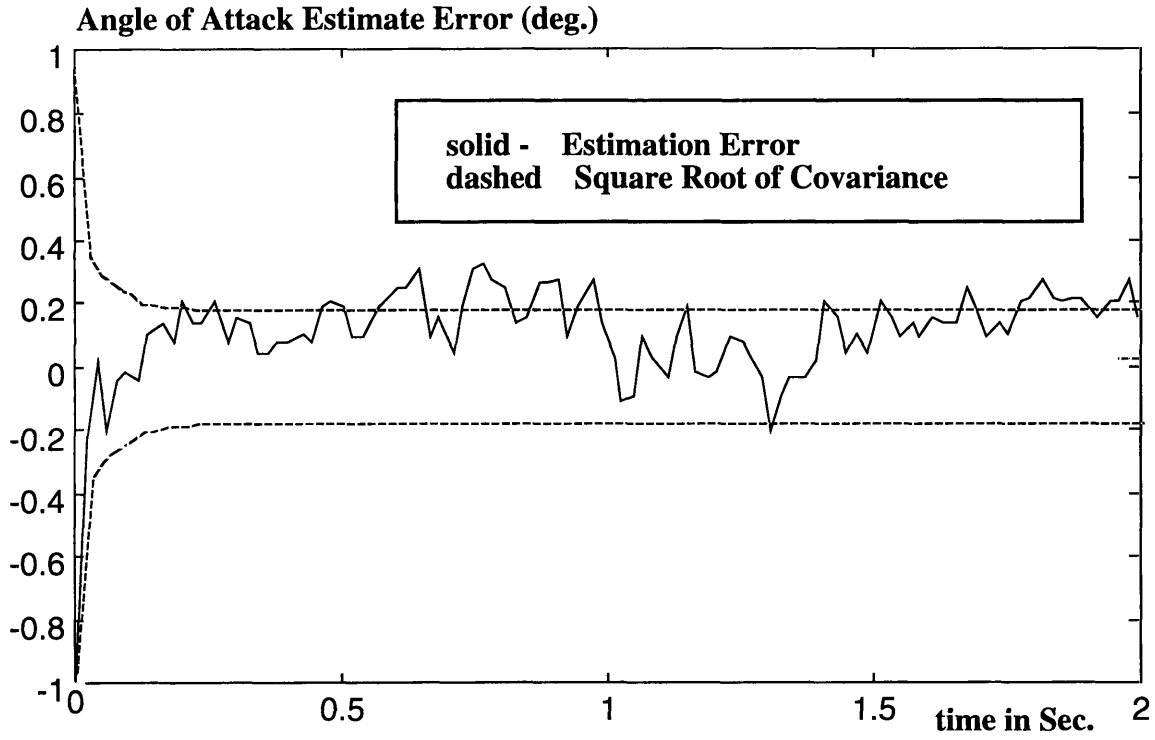

Figure 6-28 Estimator Performance (Angle of Attack Estimation Error)

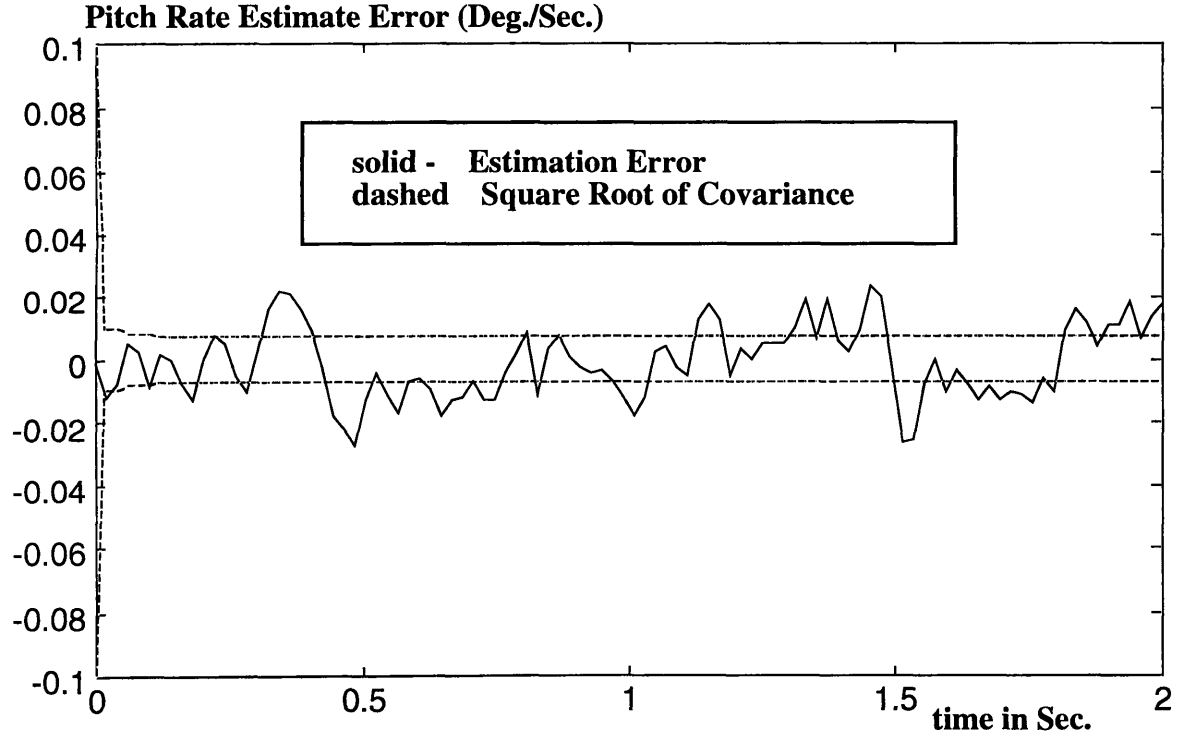

Figure 6-29 Estimator Performance (Pitch Rate Estimation Performance)

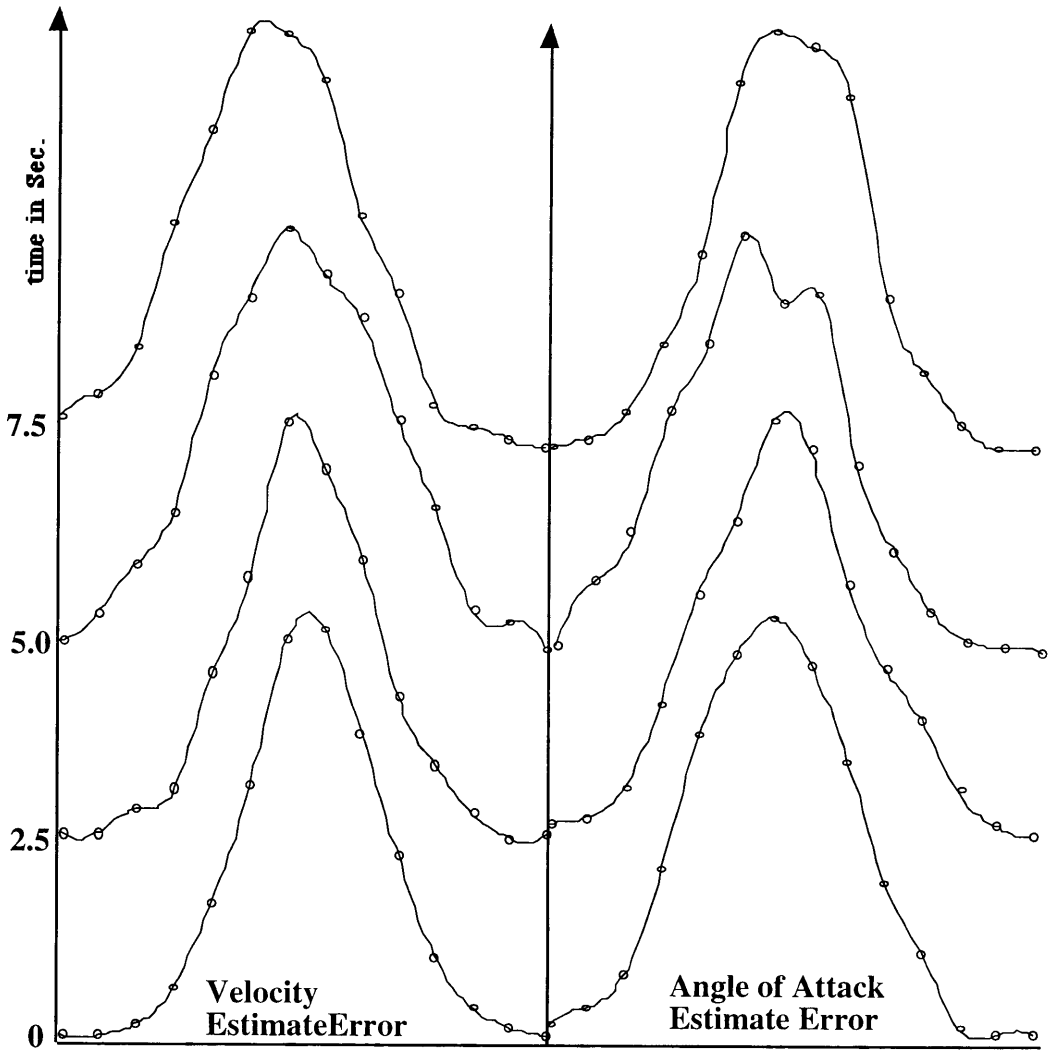

Figure 6-30 Histogram of Estimate Error. Velocity and Angle of Attack

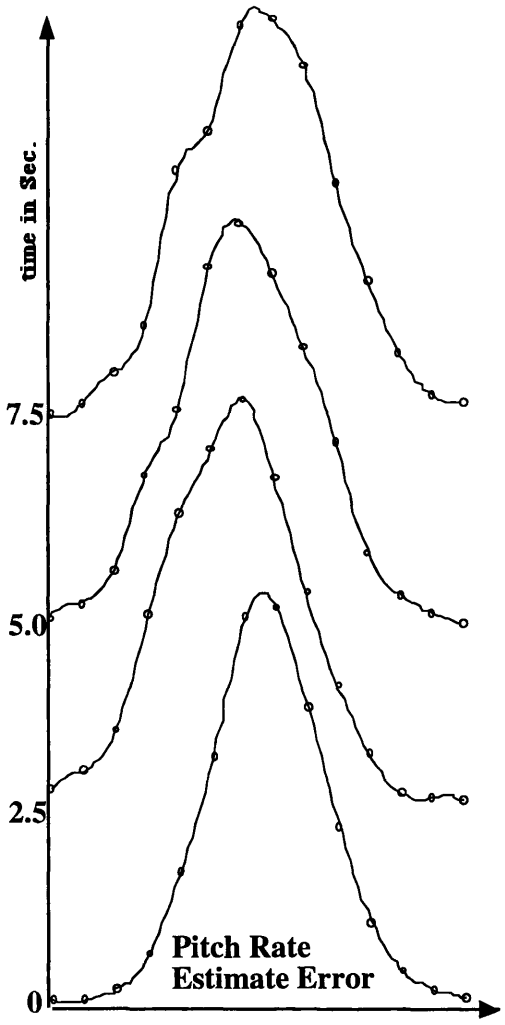

Figure 6-31 Histogram of Estimation Error Pitch Rate

Chapter 7

Estimation Driven Sensor Precision Requirements

7.1 Motivation

For a given estimation problem, it is sometimes desirable to determine upper bounds for sensor noise specifications such that if the sensors have noise specifications below the bounds then the resulting estimator performance would meet the state estimation accuracy requirements. The inverse problem to determining the estimator performance with given models, sensors and initial conditions, is the problem of estimating the minimum quality of the sensor performance. This problem can be defined in context of estimation. A simple example would be a radar system following a flying object. For given requirements from estimation, such as velocity and position accuracy of x meters and y meters per second, the problem can be posed to obtain the performance specifications for the radar parameters (e.g., bounds on signal to noise ratio, angular resolution, pulse width and frequency etc.) that would result in satisfaction of the estimation requirements.

The problem can be approached in several different ways. One not very attractive approach is to design an estimator with specific sensors and the associated sensor noise specifications then perform a statistical analysis such as Monte-Carlo simulations to verify

the estimator performance. If the performance of the estimator is not satisfactory, then the estimator performance verification process can be iterated with different sensor noise specifications. Perhaps, this procedure could result in tighter bounds than other means; however, it requires laborious estimator design and computation-intensive Monte-Carlo simulations of the vehicle and estimator. Consequently, the alternate approach of defining the sensor performance requirements, which are dictated by the estimation accuracy requirements (the upper bounds on the covariance of the state estimation error), is investigated in this chapter.

In the case of the air-breathing hypersonic vehicle (AHSV) estimation problem, it is also desirable to know the upper bounds on sensor noise specifications. Most air-data sensor classes other than the Shuttle Entry Air-Data System (SEADS), are not proven in flight. The optical sensors that are considered for use in future AHSVs, are mostly in-laboratory studies or theoretical conceptions. Therefore the result obtained by this investigation provides a good guideline for the design of these sensors. The work provides a realistic sensor performance specification based on the estimation and control requirements.

The methods that are being considered in this chapter are based on minimum variance estimation criteria. The problem is approached by first defining the filtering equations (propagation and update equations of conditional state probability density function). The most tractable form of the estimator is the one that does not depend on innovation and having the density solution in finite dimensional form. The second moment equation of Extended Kalman Filter (EKF) does meet those criteria. Secondly, a given required covariance measure, which is based on the state estimation requirements described in the previous chapter, is used in the propagation and update of covariance equations (second moment equations) to obtain the sensor noise bounds.

7.2 Problem Formulation And Approach

The main objective of this analysis is to obtain an inequality relationship between the state conditional covariance and the sensor noise covariance matrix. The resulting relationship is then used to provide a guideline for sensor selection criteria. For a particular operating condition regime of the estimator, the problem can be defined as:

$$\text{Find } U \text{ s.t. } R \le U(P_R, x, t) \text{ for given } x_o$$

where R is the sensor noise covariance and P_R is the desired upper bound of state conditional covariance.

The relationship between the state conditional covariance and sensor noise covariance can be extracted from the equation of evolution of second moments. For the dynamic system, which is driven by the Wiener processes, as shown in equation (7.1) below:

$$\begin{aligned} &\text{Process Law} \quad dx_t = \mathrm{m}(x_t,t)dt + \mathrm{s}(x_t,t)d\beta \\ &\text{Observations} \quad dz_t = \mathrm{h}(x_t,t)dt + R^{\frac{1}{2}}d\upsilon \end{aligned} \tag{7.1}$$

the associated equation for the second moment evolution is:

$$\begin{aligned} dP_{ij} = &[\left(\mathcal{E}\{x_i\,\mathrm{m}_j\} - \hat{x}_i\,\hat{\mathrm{m}}_j\right) + \left(\mathcal{E}\{\mathrm{m}_i\,x_j\} - \hat{\mathrm{m}}_i\,\hat{x}_j\right) + \left(sQs^T\right)_{ij} \\ &-\left(\mathcal{E}\{x_i\,\mathrm{h}\} - \hat{x}_i\,\hat{\mathrm{h}}\right)^T R^{-1}\left(\mathcal{E}\{\mathrm{h}\,x_j\} - \hat{\mathrm{h}}\,\hat{x}_j\right)]dt \\ &+\left(\mathcal{E}\{x_i x_j\,\mathrm{h}\} - \mathcal{E}\{x_i x_j\}\hat{\mathrm{h}} - \hat{x}_i\mathcal{E}\{x_j\,\mathrm{h}\} - \hat{x}_j\mathcal{E}\{x_i\,\mathrm{h}\} + 2\hat{x}_i\hat{x}_j\,\hat{\mathrm{h}}\right)^T R^{-1}\left(dz_t - \hat{\mathrm{h}}\,dt\right) \end{aligned} \tag{7.2}$$

The resulting equation (7.2) is difficult to solve because the equation is a stochastic differential equation (SDE) and the equation involves the innovation process at current time. For practicality, an innovation independent equation is highly desirable. In order to have an innovation independent equation for evolution of second moments, first order approximations of dynamics and observation equations are used and an assumption of symmetry for the conditional densities is made. Such an equation is, as previously shown in 6.1, the Extended Kalman Filter formulation. The results from the visualization of conditional densities in chapter 6 substantiate the assumptions of the EKF.

From the EKF formulation, covariance equations that are innovation independent can be obtained. The necessary assumptions are:

- The estimation error is small most of the time.
- The drift, $\mathrm{m}(x_t)$, and the observation function, $\mathrm{h}(x_t)$, are smooth functions.
- The error is symmetrically distributed about its mean value so that the third moment goes to zero with all other odd central moments.

For the AHSV air-data estimation problem, the EKF covariance equation with continuous process and discrete measurements is used. The associated dynamics and observation equations can be written as:

$$\dot{x}(t) = m(x,t) + s(x,t)w(t)$$
$$z(k) = h(x(k),k) + n(k) \tag{7.3}$$

with the assumptions applied identical to Chapter 6. The EKF covariance equation was:

$$\textbf{Propagation:}\quad \dot{P}(t) = F(\hat{x}(t),t)P(t) + P(t)F(\hat{x}(t),t)^T + SQ(t)S^T$$
$$\textbf{Update:}\quad P(k+1/k+1) = \left[I - K(k+1)H(\hat{x}(k+1/k))\right]P(k+1/k)$$
$$K(k+1) = P(k+1/k)H(\hat{x}(k+1/k))^T\left[H(\hat{x}(k+1/k))P(k+1/k)H(\hat{x}(k+1/k))^T + R(k+1)\right]^{-1} \tag{7.4}$$

With the above propagation and update equations, we have an equation relating the sensor noise intensity R with the required covariance of state P. The above equations are not easy to implement into numerical algorithms because the propagation requires time integration for each step. For simplicity of manipulation, the propagation equation is discretized with same interval as the measurement update rate. Then the resulting equations are a set of difference equations, as shown below:

$$\textbf{Propagation:}\quad P(k+1/k) = \phi^*(\hat{x}(k),k)P(k/k)\phi^*(\hat{x}(k),k)^T + SQ(k)S^T$$
$$\textbf{Update:}\quad P(k+1/k+1) = \left[I - K(k+1)H(\hat{x}(k+1/k))\right]P(k+1/k)$$
$$K(k+1) = P(k+1/k)H(\hat{x}(k+1/k))^T\left[H(\hat{x}(k+1/k))P(k+1/k)H(\hat{x}(k+1/k))^T + R(k+1)\right]^{-1} \tag{7.5}$$

With the difference equations (7.5), one more important assumption is needed to obtain a set of algebraic equations. The necessary assumption is the statistical steady state of the estimation process. The covariance of state variables at k-th time step is assumed to be reciprocating at (k+1)th time step. The assumption of a statistical steady state is a less stringent requirement than a dynamical steady state. If such an assumption is applied, then the equation (7.5) turns into:

$$\textbf{Propagation:}\quad P(k^+) = \phi^*(\hat{x}(k),k)P(k)\phi^*(\hat{x}(k),k)^T + SQ(k)S^T$$
$$\textbf{Update:}\quad P(k) = \left[I - K(k^+)H(\hat{x}(k^+))\right]P(k^+)$$
$$K(k^+) = P(k^+)H(\hat{x}(k^+))^T\left[H(\hat{x}(k^+))P(k^+)H(\hat{x}(k^+))^T + R(k+1)\right]^{-1} \tag{7.6}$$

By replacing the covariance at the k^+ propagation step into the update equation, the final form of the equation is obtained which relates the covariance of state P to the sensor noise covariance R, as shown below:

$$P = \left[I - \left[\left[\phi^* P \phi^{*T} + SQS^T \right] H^T \left[H \left[\phi^* P \phi^{*T} + SQS^T \right] H^T + R \right]^{-1} \right] H \right] \left[\phi^* P \phi^{*T} + SQS^T \right] \quad (7.7)$$

The final objective of manipulating the equation (7.7) is to obtain an inequality bound on R for a given bound on P. The problem associated with the solution process is the convergence of the numerical algorithm. First, the objective is to obtain the initial condition (or performance bound) of P such that the solution of R becomes a diagonal matrix. If next, the solution process is set up as an iteration routine, then the problem contains more unknowns than the number of equations. However, if the sensors can be scheduled, meaning that the sensor noise covariance is assigned by a reference sensor specification, then an easier solution process can be achieved. By setting up an initial guess of R, which can be assigned by just picking the reference value, an iteration routine is formed by taking advantage of the nonlinear equations solver.

7.3 Procedure and Numerical Implementation

Step 1) Form the sensor noise covariance matrix into a diagonal matrix with reference to a scalar variable R_o, as shown below:

$$\begin{bmatrix} R_{11} & 0 & \bullet & \bullet & 0 \\ 0 & \bullet & & & \bullet \\ \bullet & & \bullet & & \bullet \\ \bullet & & & \bullet & 0 \\ 0 & \bullet & \bullet & 0 & R_{mm} \end{bmatrix} \Rightarrow \begin{bmatrix} k_1 R_o & 0 & \bullet & \bullet & 0 \\ 0 & k_2 R_o & & & \bullet \\ \bullet & & \bullet & & \bullet \\ \bullet & & & \bullet & 0 \\ 0 & \bullet & \bullet & 0 & k_m R_o \end{bmatrix}$$

Also, prepare the linearization routine of the vehicle dynamics and observation. Generate the nominal trajectory and the required bounds on P.

Step 2) The iteration starts here. First, compute the linearized matrix of the nonlinear estimation problem (Vehicle dynamics and observation) for a reference point on the nominal trajectory. Pick an initial value for R_o, and Q matrix.

Step 3) With the linearized problem of Step 2), solve the system of nonlinear equation and obtain P for that particular condition.

Step 4) Observe the diagonal elements of P and form an inequality comparison with the bounds on P. If the obtained solution is greater than the defined bounds, decrease

the R_o and repeat the process from step 2). If the obtained solution is within the defined bounds and within the zone of acceptability, then stop the iteration. The value of R_o at the end of iteration is the final solution. Other sensor noise covariance can be recovered by extrapolation. Otherwise, repeat from step 2) with a slight increase in the value of R_o.

7.4 Numerical Results

The problem of finding an AHSV air-data sensor precision requirement is demonstrated by executing a few numerical examples from a realistic flight condition at Mach 10. The nominal operating condition was Mach 10 flight speed with zero acceleration and angle of attack of 2.7 degrees. The results are a function of the random disturbance magnitude, operating conditions, and sensor configurations. Therefore, three different cases of effective density disturbances were considered. The density fluctuations were translated into effective acceleration random disturbances and are shown below.

	Effective Disturbances
Case 1	$\dot{V}_{de} \approx 1 {}^{m}/_{s^2}$, $\dot{\alpha}_{de} \approx 0.5 {}^{\deg}/_{s}$, $\dot{q}_{de} \approx 0.1 {}^{\deg}/_{s^2}$
Case 2	$\dot{V}_{de} \approx 0.1 {}^{m}/_{s^2}$, $\dot{\alpha}_{de} \approx 0.1 {}^{\deg}/_{s}$, $\dot{q}_{de} \approx 0.01 {}^{\deg}/_{s^2}$
Case 3	$\dot{V}_{de} \approx 0.1 {}^{m}/_{s^2}$, $\dot{\alpha}_{de} \approx 0.01 {}^{\deg}/_{s}$, $\dot{q}_{de} \approx 0.01 {}^{\deg}/_{s^2}$

Since the sensor noise covariance matrix must be scheduled with a reference parameter, five different configurations of sensor arrangements that were considered to explore the possible sensor combination. They are shown below.

BAL:	Balanced Design between Optical and Pressure Sensors
POS:	Poor Optical Sensor Case, Corresponds to 30m/s (one sigma) optical sensor noise and 0.2PSF (one sigma) pressure sensor noise when normalized with schedule coefficient of one.
GOS:	Good Optical Sensor Case, Corresponds to 3m/s (one sigma) optical sensor noise and 10PSF (one sigma) pressure sensor noise when normalized with schedule coefficient of one.

NOS:	No Optical Sensor Case
NPS:	No Pressure Sensor Case

The results are shown in Table 7-1 to 7-3 for three cases of external disturbances. The sensor precision requirement results showed large sensitivity with respect to the weighting factor between the pressure and optical sensors. If the balance between two classes of sensor systems is shifted to one side by small fraction, then the algorithm tends to rely on one type of sensor (the better quality sensor in relative terms) more heavily than the other. For example, in Table 7-1, when the pressure sensors have an accuracy greater than about 0.2%, only minor degradation is seen in the requirements on the optical system even when we vary the pressure sensor precision from 0.2% to non-pressure-sensor operation case. Similarly, a change of the precision of optical system from 0.1% to 4% and to the extreme of the non-optical-sensor operation case has only a small impact on the requirements for the pressure system. The results are consistent with other two disturbance cases.

The results suggest that if one class of sensor is better than the other, then the resulting improvement in the estimation accuracy by installing poor sensors is minimal unless a large number of sensors are installed. However, for an AHSV air-data system, the pressure sensor system does provide other air-data parameters (total pressure, static pressure, etc.) that no optical sensor can provide. Also the Rayleigh scattering sensor has the advantage of providing accurate density measurements. Therefore, the combinatory use of an optical and pressure sensor system seems to be unavoidable.

The results of this analysis depend heavily on the magnitude of external disturbances. As shown by comparing three different disturbance cases, the sensor precision requirements can be relaxed if the external disturbances are decreased. By going from case 1 to case 3, the precision requirements on the sensor system can be relaxed by a factor of 4 to 5. Also the results are dependent on the operating condition of the AHSV. The procedure can be repeated to cover all possible envelopes of the flight trajectory if overall sensor precision requirements are needed.

The pressure sensors on the Shuttle Entry Air-Data System (SEADS) have a precision of 2%. [Hon1] Clearly the SEADS system can not meet the 0.1 degree angle of

attack accuracy requirement with the current configurations. The reconstruction of data from a Shuttle trajectory [Hon1] confirms that the one-sigma angle of attack error ranged from 0.3 to 0.7 degrees for Mach 10 to 15 depending on the external disturbance level. The reference [Hon1] suggested that the SEADS performance can be improved by using more accurate pressure data (0.02% one-sigma) available from recent transducer advances and with the incorporation of actual flight data into the vehicle characterization data. The results from this analysis show that the SEADS system can be used for AHSV application if such an improvement is made on the air-data system.

Table 7-1 Sensor Precision Requirements for Case 1

	Pressure Sensor Requirements	Optical Sensor Requirements
BAL	0.2% (1.6 PSF, 1-sigma at M=10)	0.07% (2m/s, 1-sigma at M=10)
POS	0.1% (0.8 PSF, 1-sigma at M=10)	4% (120m/s, 1-sigma at M=10)
GOS	0.5% (6 PSF, 1-sigma at M=10)	0.05% (1.6m/s, 1-sigma at M=10)
NOS	0.07% (0.7PSF, 1-sigma at M=10)	
NPS		0.05% (1.5m/s, 1-sigma at M=10)

Table 7-2 Sensor Precision Requirements for Case 2

	Pressure Sensor Requirements	Optical Sensor Requirements
BAL	0.6% (4.7 PSF, 1-sigma at M=10)	0.2% (6m/s, 1-sigma at M=10)
POS	0.35% (2.8 PSF, 1-sigma at M=10)	14% (400m/s, 1-sigma at M=10)
GOS	2.4% (19 PSF, 1-sigma at M=10)	0.2% (5.7m/s, 1-sigma at M=10)
NOS	0.35% (2.8 PSF, 1-sigma at M=10)	
NPS		0.2% (5.5m/s, 1-sigma at M=10)

Table 7-3 Sensor Precision Requirements for Case 3

	Pressure Sensor Requirements	Optical Sensor Requirements
BAL	0.85% (6.8 PSF, 1-sigma at M=10)	0.3% (8.5m/s, 1-sigma at M=10)
POS	0.5% (3.8 PSF, 1-sigma at M=10)	19% (570m/s, 1-sigma at M=10)
GOS	3.2% (25 PSF, 1-sigma at M=10)	0.24% (7.5m/s, 1-sigma at M=10)
NOS	0.5% (3.7 PSF, 1-sigma at M=10)	
NPS		0.24% (7.4m/s, 1-sigma at M=10)

Chapter 8

Summary and Conclusions

8.1 Summary of Results

The main objective of this thesis has been to develop an air-data sensing and estimation methodologies for generic air-breathing hypersonic vehicles (AHSVs). This thesis presented a systematic approach to address an air-data estimation problem motivated by the interaction between the vehicle attitude and the air-breathing propulsion system that is a unique characteristic of the AHSVs. The design and analysis tools, that are acquired by following the presented analysis and demonstrated solutions, will be directly applicable for future development of the AHSV technology. The methodologies covers steps from the problem formulation and modeling through the resulting nonlinear estimator design. The core emphasis of the AHSV air-data estimation strategy was to improve the accuracy of the angle of attack estimate to meet the goal that are necessitated by the stringent operational requirements of the air-breathing propulsion and flight stabilization systems.

On the basis of the preliminary analysis of the vehicle dynamics and the associated propulsion sensitivity as discussed in Chapter 4 and 5, the flow angle parameters such as angle of attack and side-slip angle were considered to be the most

critical parameters to control, measure, and estimate. The criteria of performance and stability of the air-breathing engines can not be addressed without prescribing the angle of attack condition. Largely, the observation requirements on the angle of attack were posed by the propulsion performance and control constraints. In order to formulate an appropriate estimation problem for this particular case, several preparatory research efforts were needed. A vehicle configuration was selected and designed based on the Draper Laboratory developed design and simulation code for the Mach 10 to 15 flight envelope. [Cha1] Resulting equations for the vehicle dynamics and plots of the vehicle model parameters were shown in Chapter 5. State of the art hypersonic air-data instrumentation techniques were reviewed in Chapter 4 and modeled in Chapter 5 for the estimation purpose.

With the defined foundations of the conceptual AHSV design, an estimation problem was formulated to improve the estimate accuracy of angle of attack. The chapter 6 was devoted to describe the development of the air-data estimation. This chapter begins with the theoretical backgrounds, estimation problem formulation and estimator design procedures. By observing the nonlinearities within the AHSV dynamics and the air-data sensor models, it was highly suspected that the problem might require a more sophisticated and difficult nonlinear filtering technique that accommodates for the deformation (spatial deformation and temporal variations) of the state conditional probability density functions. However, the resulting statistical behavior of both the vehicle and the flight control was uncertain and that combined dynamics were needed to address the estimation problem. The advantage of the flight control was considered to be in its stabilizing and linearizing efforts via feedback. The stringent regulatory control of angle of attack and physical constraints that can be imposed on the AHSV motion may result in a locally linear behaving estimation problem.

In order to select an appropriate nonlinear filtering technique, an analysis that visualizes the statistical behavior of the closed loop system (dynamics of the combined vehicle and control) was needed and developed. In section 6.5, a visualization method that is based on the Monte-Carlo simulations and statistical analysis is presented. Based on two thousand runs of the flight simulations at Mach 10, 13 and 15 and along with the statistical analysis on the observation nonlinearities, the visualization showed that the state conditional probability density would be nearly Gaussian (at least nearly symmetric and unimodal). This evidence substantiated the initial hypothesis on the behavior of the closed loop dynamics. In later part of Chapter 6, a statistical analysis was performed on

the estimation error trajectories that are generated by the simulation of the vehicle and estimator. Histograms of the estimation error confirmed the prediction of the visualization results by exhibiting nearly symmetric and unimodal behavior. The results can be extended to any differently configured air-breathing hypersonic vehicles as long as the stringent restrictions are imposed on the regulation of angle of attack and vehicle motion.

In order to complete the analysis and design described in previous paragraphs, a flight control system was needed and designed. In section 6.4, the controller design procedure is described and the simulation results are presented. Also an alternative control strategy is formulated and discussed in Appendix D. The motivation of the control system design was based on the estimation strategy. In nonlinear estimation problem, the control action affects the deformation of state conditional probability density.

The visualization results suggested applicability of the Extended Kalman Filter technique. The design and results from implementation of the EKF were shown in section 6.6. When realistic values were assigned for the sensor noise, the angle of attack estimation accuracy improved by a factor of two. The assumptions on the sensor specifications were based on the SEADS pressure transducer performance and the laboratory demonstrated performance of the optical system. The accuracy enhancement by the EKF with a set of realsitic sensor suite was not significant enough to meet the initial goal of 0.1 degrees in angle of attack accuracy (at Mach 10). The result suggests that hardware improvements are needed for further accuracy gains with the current estimator. When considering the fact that the simulation did not include the source of performance degrading effects such as modeling errors and the sensor precision requirements get tighter as the external disturbances increase, even better sensors are recommended to achieve the desired performance goal.

In Chapter 7, the sensor precision requirements were derived based on the assumptions of the EKF implementation. The problem was posed to find an inequality relationship between the state estimate error covariance and the sensor noise covariance to bound the maximum allowable sensor noise when given a performance bound on the EKF. A digital implementable numerical algorithm has been developed based on the EKF covariance equations with the assumption of statistical steady state and a sensor scheduling technique. For the case with larger external disturbances, at least a factor of

10 improvements for the pressure transducers and a factor of 4 improvements for the optical sensors are suggested. The results from this analysis concluded with same answer as the EKF performance verification results. Better hardware is needed if the EKF is the only source of improving the estimate of angle of attack.

The configurations and design of the future developmental vehicle may be different from the one analyzed here. However, the general constraints imposed by the air-breathing engines on the AHSV system will result in the vehicle closed loop dynamics with the similar statistical behaviors. The estimator design methodologies described in this thesis may be used as a guideline for a future development of the AHSV air-data estimator and the air-data sensor technology.

8.2 Suggestions for Further Research

The analysis and demonstrated solutions provided in this thesis has been limited to the longitudinal motion. The lateral motion is predicted to be as sensitive to the flow angle (side-slip angle for this case) as the longitudinal case. The analysis and design for lateral direction require an accurate propulsion model and a vehicle lateral dynamic model. If such data are available, then the methodologies presented in this thesis may be used to acquire insights of lateral effects. Also another estimator formulation is needed to cover the supersonic and lower Mach number (M<6) hypersonic flight phase. For this formulation, the derivation of the vehicle equations of motion presented in Chapter 5 can be used as the vehicle model and the ramjet propulsion system should be modeled. Since the wind disturbance is the dominant factor for this part of flight trajectory, the atmosphere model should be emphasized for the wind contributions. Fortunately, more information on external disturbances and the propulsion sensitivity is available for this segment of flight.

The estimator problem formulation presented in this thesis is not a unique way of approaching this problem. Different designs, different models can be formulated. For example, this problem could have been approached similar to the air-data estimator of the high angle of attack research vehicle [Kas1]. This formulation would result in much simpler estimation problem; however, the formulation presented in the thesis is considered more applicable for the AHSV application since the propulsion and

aerodynamic models contain rich information on angle of attack. Also the differences are the AHSV flight control is always in regulatory mode and the resulting AHSV motion is limited. As long as we can compose very accurate models for the propulsion and flight system, the technique described in this thesis should be a better formulation. Therefore, it is recommended to look into the effect of modeling uncertainties on the estimation. It is suspected that the usefulness of these models fades as the modeling uncertainties increase.

A formulation of parameter identification algorithm would be useful for further improving the accuracy of the air-data estimator by updating the model coefficients. The acceleration measurements can be used to obtain the more precise mapping between the control action to the resulting forces. The problem associated with the parameter identification is the identifiability of the parameters with given small set of measurements.

Based on the results shown in this thesis, the estimation and sensing of angle of attack variable is a very difficult problem. Further improvements of air-data sensors seem to be a very challenging problem. The pressure measurement sensors have inherent error sources such as alignment error, flow field modelling error, orifice and flow error. The optical sensors have problems of alignment and the optical window. May be the problem should be approached from the engine performance alone. Since the stringent accuracy requirement of angle of attack is mainly due to the propulsion performance, a different instrumentation strategy can be approached. As suggested in Chapter 4, several inlet and nozzle sensors may be installed to detect the propulsion process aft of the oblique shocks. In principle, the angle of attack can be extracted from the propulsion processes. If we can have accurate models or relationships between the inlet and nozzle parameters and the flight control actuators, then we can take advantage of direct control of the propulsion parameters with the flight control actuators. This approach seems to be more promising since we don't have to measure the angle of attack directly. For example, if we can detect the pressure jump inside the cowl lip (as discussed in Chapter 4),. then the resulting sensitivity increases. However, it is difficult to obtain an accurate model of the propulsion processes. The pressure jump inside the inlet is a very complex process including the shock-boundary layer interactions. Therefore further research is recommended to model the inlet processes and to obtain a functional relationship between the inlet parameters to the control actuators.

Appendix A
Coordinate Transformation Matrices

$$C_{BE} = \begin{bmatrix} \cos\theta\cos\psi & \cos\theta\sin\psi & -\sin\theta \\ \sin\phi\sin\theta\cos\psi - \cos\phi\sin\psi & \sin\phi\sin\theta\sin\psi + \cos\phi\cos\psi & \sin\phi\cos\theta \\ \cos\phi\sin\theta\cos\psi + \sin\phi\sin\psi & \cos\phi\sin\theta\sin\psi - \sin\phi\cos\psi & \cos\phi\cos\theta \end{bmatrix}$$

$$\dot{C}_{BE} = \begin{bmatrix} -(\sin\theta\cos\psi)\dot{\theta} - (\cos\theta\sin\psi)\dot{\psi} & -(\sin\theta\sin\psi)\dot{\theta} + (\cos\theta\cos\psi)\dot{\psi} & -\cos\theta\dot{\theta} \\ (\cos\phi\sin\theta\cos\psi + \sin\phi\sin\psi)\dot{\phi} + (\sin\phi\cos\theta\cos\psi)\dot{\theta} + (-\sin\phi\sin\theta\sin\psi + \cos\phi\cos\psi)\dot{\psi} & (\cos\phi\sin\theta\sin\psi - \sin\phi\cos\psi)\dot{\phi} + (\sin\phi\cos\theta\sin\psi)\dot{\theta} + (\sin\phi\sin\theta\cos\psi - \cos\phi\sin\psi)\dot{\psi} & (\cos\phi\cos\theta)\dot{\phi} - (\sin\phi\sin\theta)\dot{\theta} \\ (-\sin\phi\sin\theta\cos\psi + \cos\phi\sin\psi)\dot{\phi} + (\cos\phi\cos\theta\cos\psi)\dot{\theta} + (-\cos\phi\sin\theta\sin\psi + \sin\phi\cos\psi)\dot{\psi} & -(\sin\phi\sin\theta\sin\psi + \cos\phi\cos\psi)\dot{\phi} + (\cos\phi\cos\theta\sin\psi)\dot{\theta} + (\cos\phi\sin\theta\cos\psi + \sin\phi\sin\psi)\dot{\psi} & -(\sin\phi\cos\theta)\dot{\phi} - (\cos\phi\sin\theta)\dot{\theta} \end{bmatrix}$$

$$C_{BW} = \begin{bmatrix} \cos\alpha\cos\beta & -\cos\alpha\sin\beta & -\sin\alpha \\ \sin\beta & \cos\beta & 0 \\ \sin\alpha\cos\beta & -\sin\alpha\sin\beta & \cos\alpha \end{bmatrix}$$

$$C_{WE} = \begin{bmatrix} \cos\theta\cos\psi & \cos\theta\sin\psi & -\sin\theta \\ \sin\phi\sin\theta\cos\psi - \cos\phi\sin\psi & \sin\phi\sin\theta\sin\psi + \cos\phi\cos\psi & \sin\phi\cos\theta \\ \cos\phi\sin\theta\cos\psi + \sin\phi\sin\psi & \cos\phi\sin\theta\sin\psi - \sin\phi\cos\psi & \cos\phi\cos\theta \end{bmatrix}_{\substack{\phi = \phi_w \\ \theta = \theta_w \\ \psi = \psi_w}}$$

Appendix B
Further Simplifications

Starting from the longitudinal equation of motion (Equation (5.10), flat earth approximation). The Equations (5.10) through (5.13) can be put together and be simplified to one equation. The equations (5.10) through (5.13) are

$$\begin{aligned} \sum F_x - mg\sin\theta &= m(\dot{u} + \dot{W}_x) + mq(w + W_z) \\ \sum F_z + mg\cos\theta &= m(\dot{w} + \dot{W}_z) - mq(u + W_x) \\ \sum M_y &= I_y\dot{q} \end{aligned} \tag{5.10}$$

$$\begin{bmatrix} W_x \\ W_z \end{bmatrix} = C_E^B \begin{bmatrix} W_x \\ W_z \end{bmatrix}_E \tag{5.11}$$

where

$$C_E^B = \begin{bmatrix} \cos\theta & -\sin\theta \\ \sin\theta & \cos\theta \end{bmatrix}$$

And from the previous results on incorporation of wind, the time change of wind velocity is

$$\begin{bmatrix} \dot{W}_x \\ \dot{W}_z \end{bmatrix}_E = \begin{bmatrix} \frac{\partial W_x}{\partial x} & \frac{\partial W_x}{\partial z} \\ \frac{\partial W_z}{\partial x} & \frac{\partial W_z}{\partial z} \end{bmatrix}_E \begin{bmatrix} \dot{X}_E \\ \dot{Z}_E \end{bmatrix} + \begin{bmatrix} \frac{\partial W_x}{\partial t} \\ \frac{\partial W_z}{\partial t} \end{bmatrix}_E \tag{5.12}$$

where the last $\frac{\partial W_i}{\partial t}$ terms can be neglected due to the frozen field approximation. If time derivatives of wind terms are derived and expressed in an Earth attached frame, then the resulting equation is,

$$\begin{bmatrix} \dot{W}_x \\ \dot{W}_z \end{bmatrix} = C_E^B \begin{bmatrix} \dot{W}_x \\ \dot{W}_z \end{bmatrix}_E + \dot{C}_E^B \begin{bmatrix} W_x \\ W_z \end{bmatrix}_E \tag{5.13}$$

where

$$\dot{C}_E^B = q \begin{bmatrix} -\sin\theta & -\cos\theta \\ \cos\theta & -\sin\theta \end{bmatrix}$$

The coordinate system suggests that

$$\begin{bmatrix} \dot{X} \\ \dot{Z} \end{bmatrix}_E = C_B^E \begin{bmatrix} \mathbf{u} \\ \mathbf{w} \end{bmatrix} + \begin{bmatrix} W_x \\ W_z \end{bmatrix}_E \quad \text{and} \quad C_B^E = C_E^{BT} \tag{B-1}$$

$$\begin{bmatrix} \mathbf{u} \\ \mathbf{w} \end{bmatrix} = V_T \begin{bmatrix} \cos\alpha \\ \sin\alpha \end{bmatrix} \tag{B-2}$$

$$\begin{bmatrix} \dot{V}_T \\ -V_T\dot{\alpha} \end{bmatrix} = \begin{bmatrix} \cos\alpha & \sin\alpha \\ -\sin\alpha & \cos\alpha \end{bmatrix} \begin{bmatrix} \dot{\mathbf{u}} \\ \dot{\mathbf{w}} \end{bmatrix} = C_B^W \begin{bmatrix} \dot{\mathbf{u}} \\ \dot{\mathbf{w}} \end{bmatrix} \tag{B-3}$$

The objective of this simplification is to obtain one equation that combines equations (6.10) through (6.13). It is desirable to have an equation which can be described with parameters which are measurable. The chosen states are u and w. All the inertial parameters are assumed to be measured using inertial sensors. Equation (6.10) can be rewritten in terms of accelerations as shown in Equation (B-4).

$$\begin{bmatrix} a_x \\ a_z \end{bmatrix}_{cg} + g \begin{bmatrix} -\sin\theta \\ \cos\theta \end{bmatrix} - \begin{bmatrix} \dot{\mathbf{u}} \\ \dot{\mathbf{w}} \end{bmatrix} = \begin{bmatrix} \dot{W}_x \\ \dot{W}_z \end{bmatrix} + \mathbf{q} \begin{bmatrix} \mathbf{w} \\ -\mathbf{u} \end{bmatrix} + \mathbf{q} \begin{bmatrix} W_z \\ -W_x \end{bmatrix} \tag{B-4}$$

Applying wind terms as defined in inertial coordinates and using equations (6.13) and (B-1),

$$\begin{bmatrix} a_x \\ a_z \end{bmatrix}_{cg} + g \begin{bmatrix} -\sin\theta \\ \cos\theta \end{bmatrix} - \begin{bmatrix} \dot{\mathbf{u}} \\ \dot{\mathbf{w}} \end{bmatrix} = C_E^B \begin{bmatrix} \dot{W}_x \\ \dot{W}_z \end{bmatrix}_E + \dot{C}_E^B \begin{bmatrix} W_x \\ W_z \end{bmatrix}_E + \mathbf{q} \begin{bmatrix} \mathbf{w} \\ -\mathbf{u} \end{bmatrix} + \mathbf{q} C_E^B \begin{bmatrix} W_z \\ -W_x \end{bmatrix}_E \tag{B-5}$$

$$= C_E^B \begin{bmatrix} \frac{\partial W_x}{\partial x} & \frac{\partial W_x}{\partial z} \\ \frac{\partial W_z}{\partial x} & \frac{\partial W_z}{\partial z} \end{bmatrix}_E \begin{bmatrix} \dot{X} \\ \dot{Z} \end{bmatrix}_E + \dot{C}_E^B \left\{ \begin{bmatrix} \dot{X} \\ \dot{Z} \end{bmatrix}_E - C_E^{BT} \begin{bmatrix} \mathbf{u} \\ \mathbf{w} \end{bmatrix} \right\} + \mathbf{q} \begin{bmatrix} \mathbf{w} \\ -\mathbf{u} \end{bmatrix} + \mathbf{q} C_E^B \left\{ \begin{bmatrix} \dot{Z} \\ -\dot{X} \end{bmatrix}_E - C_E^{BT} \begin{bmatrix} \mathbf{w} \\ -\mathbf{u} \end{bmatrix} \right\}$$

Since

$$\mathbf{q} C_E^B \left\{ \begin{bmatrix} \dot{Z} \\ -\dot{X} \end{bmatrix}_E - C_E^{BT} \begin{bmatrix} \mathbf{w} \\ -\mathbf{u} \end{bmatrix} \right\} = \mathbf{q} C_E^B \begin{bmatrix} \dot{Z} \\ -\dot{X} \end{bmatrix}_E - \mathbf{q} C_E^B C_E^{BT} \begin{bmatrix} \mathbf{w} \\ -\mathbf{u} \end{bmatrix} = \mathbf{q} C_E^B \begin{bmatrix} \dot{Z} \\ -\dot{X} \end{bmatrix}_E - \mathbf{q} \begin{bmatrix} \mathbf{w} \\ -\mathbf{u} \end{bmatrix}$$

Equation (B-5) becomes

$$= C_E^B \begin{bmatrix} \frac{\partial W_x}{\partial x} & \frac{\partial W_x}{\partial z} \\ \frac{\partial W_z}{\partial x} & \frac{\partial W_z}{\partial z} \end{bmatrix}_E \begin{bmatrix} \dot{X} \\ \dot{Z} \end{bmatrix}_E + \dot{C}_E^B \left\{ \begin{bmatrix} \dot{X} \\ \dot{Z} \end{bmatrix}_E - C_E^{BT} \begin{bmatrix} \mathbf{u} \\ \mathbf{w} \end{bmatrix} \right\} + \mathbf{q} C_E^B \begin{bmatrix} \dot{Z} \\ -\dot{X} \end{bmatrix}_E \tag{B-6}$$

Since

$$\dot{C}_E^B\left\{\begin{bmatrix}\dot{X}\\ \dot{Z}\end{bmatrix}_E - C_E^B T\begin{bmatrix}u\\ w\end{bmatrix}\right\} = qC_E^B\begin{bmatrix}-\dot{Z}\\ \dot{X}\end{bmatrix} + q\begin{bmatrix}w\\ -u\end{bmatrix}$$

Equation (B-6) becomes,

$$\begin{bmatrix}a_x\\ a_z\end{bmatrix}_{cg} + g\begin{bmatrix}-\sin\theta\\ \cos\theta\end{bmatrix} - \begin{bmatrix}\dot{u}\\ \dot{w}\end{bmatrix} = C_E^B\begin{bmatrix}\frac{\partial W_x}{\partial x} & \frac{\partial W_x}{\partial z}\\ \frac{\partial W_z}{\partial x} & \frac{\partial W_z}{\partial z}\end{bmatrix}_E\begin{bmatrix}\dot{X}\\ \dot{Z}\end{bmatrix}_E + q\begin{bmatrix}w\\ -u\end{bmatrix} \qquad \text{(B-7)}$$

If the terms are rearranged then Equation (B-7) becomes,

$$\begin{bmatrix}\dot{u}\\ \dot{w}\end{bmatrix} = -q\begin{bmatrix}w\\ -u\end{bmatrix} - C_E^B\begin{bmatrix}\frac{\partial W_x}{\partial x} & \frac{\partial W_x}{\partial z}\\ \frac{\partial W_z}{\partial x} & \frac{\partial W_z}{\partial z}\end{bmatrix}_E\begin{bmatrix}\dot{X}\\ \dot{Z}\end{bmatrix}_E + \begin{bmatrix}a_x\\ a_z\end{bmatrix}_{cg} + g\begin{bmatrix}-\sin\theta\\ \cos\theta\end{bmatrix} \qquad \text{(B-8)}$$

The resulting complete equation of motion is,

$$\begin{bmatrix}\dot{u}\\ \dot{w}\end{bmatrix} = -q\begin{bmatrix}w\\ -u\end{bmatrix} - \begin{bmatrix}\cos\theta & -\sin\theta\\ \sin\theta & \cos\theta\end{bmatrix}\begin{bmatrix}\frac{\partial W_x}{\partial x} & \frac{\partial W_x}{\partial z}\\ \frac{\partial W_z}{\partial x} & \frac{\partial W_z}{\partial z}\end{bmatrix}_E\begin{bmatrix}\dot{X}\\ \dot{Z}\end{bmatrix}_E + \begin{bmatrix}a_x\\ a_z\end{bmatrix}_{cg} + g\begin{bmatrix}-\sin\theta\\ \cos\theta\end{bmatrix} \qquad \text{(B-9)}$$

The states are w and u. Equation (B-9) can be evaluated with information on pitch angle θ, pitch rate q, inertial velocity $\dot{X}$ and $\dot{Z}$, the wind gradient Jacobian, and accelerations. All the inertial quantities, which excludes the wind gradient Jacobian, can be obtained from the inertial sensor measurements. Note that these inertial measurements may depend on the states.

If the states are chosen as α and V_T, start from equation (B-8) which is

$$\begin{bmatrix}\dot{u}\\ \dot{w}\end{bmatrix} = -q\begin{bmatrix}w\\ -u\end{bmatrix} - C_E^B\begin{bmatrix}\frac{\partial W_x}{\partial x} & \frac{\partial W_x}{\partial z}\\ \frac{\partial W_z}{\partial x} & \frac{\partial W_z}{\partial z}\end{bmatrix}_E\begin{bmatrix}\dot{X}\\ \dot{Z}\end{bmatrix}_E + \begin{bmatrix}a_x\\ a_z\end{bmatrix}_{cg} + g\begin{bmatrix}-\sin\theta\\ \cos\theta\end{bmatrix} \qquad \text{(B-8)}$$

and let

$$\tilde{C}_1 = C_E^B\begin{bmatrix}\frac{\partial W_x}{\partial x} & \frac{\partial W_x}{\partial z}\\ \frac{\partial W_z}{\partial x} & \frac{\partial W_z}{\partial z}\end{bmatrix}_E\begin{bmatrix}\dot{X}\\ \dot{Z}\end{bmatrix}_E \text{ and } \vec{a} = \begin{bmatrix}a_x\\ a_z\end{bmatrix}_{cg} \qquad \text{(B-10)}$$

Also use the relation

$$\begin{bmatrix}\dot{V}_T\\ -V_T\dot{\alpha}\end{bmatrix} = \begin{bmatrix}\cos\alpha & \sin\alpha\\ -\sin\alpha & \cos\alpha\end{bmatrix}\begin{bmatrix}\dot{u}\\ \dot{w}\end{bmatrix} = C_B^W\begin{bmatrix}\dot{u}\\ \dot{w}\end{bmatrix}$$

Then equation (B-8) becomes,

$$C_W^B \begin{bmatrix} \dot{V}_T \\ -V_T\dot{\alpha} \end{bmatrix} = -\mathbf{q}\begin{bmatrix} \mathbf{w} \\ -\mathbf{u} \end{bmatrix} - \tilde{C}_1 + \vec{a} + g\begin{bmatrix} -\sin\theta \\ \cos\theta \end{bmatrix} \tag{B-11}$$

Since

$$\begin{bmatrix} \mathbf{u} \\ \mathbf{w} \end{bmatrix} = V_T\begin{bmatrix} \cos\alpha \\ \sin\alpha \end{bmatrix}$$

$$C_W^B \begin{bmatrix} \dot{V}_T \\ -V_T\dot{\alpha} \end{bmatrix} = -\mathbf{q}V_T\begin{bmatrix} \sin\alpha \\ -\cos\alpha \end{bmatrix} - \tilde{C}_1 + \vec{a} + g\begin{bmatrix} -\sin\theta \\ \cos\theta \end{bmatrix} \tag{B-12}$$

Carry out the transform to the right hand side,

$$\begin{bmatrix} \dot{V}_T \\ -V_T\dot{\alpha} \end{bmatrix} = -\mathbf{q}V_T C_B^W \begin{bmatrix} \sin\alpha \\ -\cos\alpha \end{bmatrix} - C_B^W\tilde{C}_1 + C_B^W\vec{a} + gC_B^W\begin{bmatrix} -\sin\theta \\ \cos\theta \end{bmatrix} \tag{B-13}$$

Since

$$-\mathbf{q}V_T C_B^W \begin{bmatrix} \sin\alpha \\ -\cos\alpha \end{bmatrix} = -\mathbf{q}V_T\begin{bmatrix} \cos\alpha & \sin\alpha \\ -\sin\alpha & \cos\alpha \end{bmatrix}\begin{bmatrix} \sin\alpha \\ -\cos\alpha \end{bmatrix}$$

$$= -\mathbf{q}V_T\begin{bmatrix} \sin\alpha\cos\alpha - \sin\alpha\cos\alpha \\ -\sin\alpha\sin\alpha - \cos\alpha\cos\alpha \end{bmatrix} = \mathbf{q}V_T\begin{bmatrix} 0 \\ 1 \end{bmatrix}$$

The equation (B-13) can then be written as

$$\begin{bmatrix} \dot{V}_T \\ -V_T\dot{\alpha} \end{bmatrix} = \begin{bmatrix} 0 \\ \mathbf{q}V_T \end{bmatrix} - C_B^W\tilde{C}_1 + C_B^W\begin{bmatrix} a_{xcg} - g\sin\theta \\ a_{zcg} + g\cos\theta \end{bmatrix} \tag{B-14}$$

Let

$$\tilde{C}_1 = \begin{bmatrix} c_1 \\ c_2 \end{bmatrix}$$

Then

$$\begin{bmatrix} \dot{V}_T \\ -V_T\dot{\alpha} \end{bmatrix} = \begin{bmatrix} 0 \\ \mathbf{q}V_T \end{bmatrix} + C_B^W\begin{bmatrix} a_{xcg} - g\sin\theta - c_1 \\ a_{zcg} + g\cos\theta - c_2 \end{bmatrix} \tag{B-15}$$

Let

$$\begin{bmatrix} C_x \\ C_z \end{bmatrix} = \begin{bmatrix} a_{xcg} - g\sin\theta - c_1 \\ a_{zcg} + g\cos\theta - c_2 \end{bmatrix}$$

then

$$\begin{bmatrix} \dot{V}_T \\ -V_T\dot{\alpha} \end{bmatrix} = \begin{bmatrix} 0 \\ \mathbf{q}V_T \end{bmatrix} + \begin{bmatrix} C_x\cos\alpha + C_z\sin\alpha \\ C_z\cos\alpha - C_x\sin\alpha \end{bmatrix}$$

Since

$$- C_B^W \tilde{C}_1 = -\begin{bmatrix} \cos\alpha & \sin\alpha \\ -\sin\alpha & \cos\alpha \end{bmatrix} \begin{bmatrix} \cos\theta & -\sin\theta \\ \sin\theta & \cos\theta \end{bmatrix} \begin{bmatrix} \frac{\partial W_x}{\partial x} & \frac{\partial W_x}{\partial z} \\ \frac{\partial W_z}{\partial x} & \frac{\partial W_z}{\partial z} \end{bmatrix}_E \begin{bmatrix} \dot{X} \\ \dot{Z} \end{bmatrix}_E$$

The final expression is

$$\begin{bmatrix} \dot{V}_T \\ \dot{\alpha} \end{bmatrix} = \begin{bmatrix} 0 \\ -\mathbf{q} \end{bmatrix} + \begin{bmatrix} C_x & C_z \\ -\frac{C_z}{V_T} & \frac{C_x}{V_T} \end{bmatrix} \begin{bmatrix} \cos\alpha \\ \sin\alpha \end{bmatrix} \tag{B-16}$$

where

$$\begin{bmatrix} C_x \\ C_z \end{bmatrix} = \begin{bmatrix} a_{xcg} - g\sin\theta - \left(\frac{\partial W_x}{\partial x}\dot{X}_E + \frac{\partial W_x}{\partial z}\dot{Z}_E\right)\cos\theta + \left(\frac{\partial W_z}{\partial x}\dot{X}_E + \frac{\partial W_z}{\partial z}\dot{Z}_E\right)\sin\theta \\ a_{zcg} + g\cos\theta + \left(\frac{\partial W_x}{\partial x}\dot{X}_E + \frac{\partial W_x}{\partial z}\dot{Z}_E\right)\sin\theta + \left(\frac{\partial W_z}{\partial x}\dot{X}_E + \frac{\partial W_z}{\partial z}\dot{Z}_E\right)\cos\theta \end{bmatrix} \tag{B-17}$$

Appendix C
Linearization of LVLH Model of AHSV

Linearization is sometimes required for analyzing linearized behavior of vehicle dynamics, constructing a control system or formulating an Extended Kalman Filter (EKF). In some cases, linearization can help understanding the vehicle characteristics in a localized region around some nominal state trajectory. The vehicle model in LVLH frame described in Chapter 5 is used for the linearization. Two linearization results are presented here. First linearization is for the flight control system in section 6.4 and second linearization is for the EKF design in section 6.6.

C.1 Linearization Results for Control

The vehicle equations of motion in LVLH frame are:

$$\frac{dV}{dt} = -K_R \sin\Gamma + \frac{1}{m}\sum F_{xw}(M,\alpha,\delta_e,\delta_T,\delta_v) \tag{C-1a}$$

$$V\frac{d\Gamma}{dt} = \left(\frac{V^2}{R} - K_R\right)\cos\Gamma + 2\omega_E V - \frac{1}{m}\sum F_{zw}(M,\alpha,\delta_e,\delta_T,\delta_v) \tag{C-1b}$$

$$\frac{dq}{dt} = \frac{1}{I_y}\sum M_y(M,\alpha,\delta_e,\delta_T,\delta_v) \tag{C-1c}$$

$$\frac{d\theta}{dt} = q \tag{C-1d}$$

where $K_R = g(R) - \omega_E^2 R$

The vehicle dynamic Equations (C-1) used here assume vehicle motion over a spherical earth. The vehicle motion in an inertial Newtonian frame is described in Local Vertical Local Horizontal (LVLH) coordinates. The equations are transformed into body axis coordinates. The equations describe only longitudinal dynamics and include all the forcing terms found in the equations that describe aerodynamics, propulsion, and control. If we assume nearly constant dynamic pressure trajectory and also assume that the variations in aerodynamics and propulsion coefficients with respect to altitude are small during a selected flight trajectory segment (Mach 10 to 15 for our case), then we can obtain a simpler functions for the linearization. These equations can be described as a

system of nonlinear differential equations with four state variables and three control variables. The state variables contain the vehicle inertial velocity, flight path angle, pitch rate and pitch angle. The control input vector contains elevon deflection angle, throttle setting, and thrust vectoring. The Equations (C-1) can be written as below.

$$\dot{X} = f(X,t) + g(X,U,t)$$

$$X \in R^4 \mathrm{X} R^1 \text{ and where } X = [V, G, q, \theta]$$
$$U \in R^3 \mathrm{X} R^1 \text{ and where } U = [\delta_e, \delta_T, \delta_v]$$

The linearization results are obtained by

$$\dot{X} = f_o(X_o,t) + \left.\frac{\partial f}{\partial X}\right|_{X_o} (X - X_o) + g_o(X_o,U_o,t) + \left.\frac{\partial g}{\partial X}\right|_{X_o,U_o} (X - X_o) + \left.\frac{\partial g}{\partial U}\right|_{X_o,U_o} (U - U_o)$$

and forms a linear system of the form:

$$\delta\dot{X} = (F + G_x)\delta X + G_u \delta U$$

Linearization Results:

The partial derivatives of the nonlinear functions of the system variables form the linearized matrices F, G_x, and G_u. The results of linearization are shown below.

Elements of F Matrix:

$$\frac{\partial f_1}{\partial V} = \frac{QS}{m}\left(\frac{\partial C_{Tv}}{\partial M} - \frac{\partial C_D}{\partial M}\right)\frac{\partial M}{\partial V}$$

$$\frac{\partial f_2}{\partial V} = \left(\frac{1}{R} + \frac{K_R}{V^2}\right)\cos\Gamma - \frac{QS}{mV}\left(\frac{\partial C_{Tn}}{\partial M} + \frac{\partial C_L}{\partial M}\right)\frac{\partial M}{\partial V} + \frac{QS}{mV^2}(C_{Tn} + C_L)$$

$$\frac{\partial f_3}{\partial V} = \frac{QSc}{I_y}\left(\frac{\partial C_{mp}}{\partial M} + \frac{\partial C_{ma}}{\partial M}\right)\frac{\partial M}{\partial V} \qquad \frac{\partial f_4}{\partial V} = 0$$

$$\frac{\partial f_1}{\partial \Gamma} = -K_R \cos\Gamma + \frac{QS}{m}\left(\frac{\partial C_{Tv}}{\partial \alpha} - \frac{\partial C_D}{\partial \alpha}\right)\frac{\partial \alpha}{\partial V}$$

$$\frac{\partial f_2}{\partial \Gamma} = -\left(\frac{V}{R} + \frac{K_R}{V}\right)\sin\Gamma - \frac{QS}{mV}\left(\frac{\partial C_{Tn}}{\partial \alpha} + \frac{\partial C_L}{\partial \alpha}\right)\frac{\partial \alpha}{\partial \Gamma}$$

$$\frac{\partial f_3}{\partial \Gamma} = \frac{QSc}{I_y}\left(\frac{\partial C_{mp}}{\partial \alpha} + \frac{\partial C_{ma}}{\partial \alpha}\right)\frac{\partial \alpha}{\partial \Gamma} \qquad \frac{\partial f_4}{\partial \Gamma} = 0$$

$$\frac{\partial f_1}{\partial q} = 0 \qquad \frac{\partial f_2}{\partial q} = 0$$

$$\frac{\partial f_3}{\partial q} = 0 \qquad \frac{\partial f_4}{\partial q} = 1$$

$$\frac{\partial f_1}{\partial \theta} = \frac{QS}{m}\left(\frac{\partial C_{Tv}}{\partial \alpha} - \frac{\partial C_D}{\partial \alpha}\right)\frac{\partial \alpha}{\partial \theta} \qquad \frac{\partial f_2}{\partial \theta} = -\frac{QS}{mV}\left(\frac{\partial C_{Tn}}{\partial \alpha} + \frac{\partial C_L}{\partial \alpha}\right)\frac{\partial \alpha}{\partial \theta}$$

$$\frac{\partial f_3}{\partial \theta} = \frac{QSc}{I_y}\left(\frac{\partial C_{mp}}{\partial \alpha} + \frac{\partial C_{ma}}{\partial \alpha}\right)\frac{\partial \alpha}{\partial \theta} \qquad \frac{\partial f_4}{\partial \theta} = 0$$

Elements of G_x Matrix:

$$\frac{\partial g_1}{\partial V} = \frac{QS}{m}\left(\frac{\partial C_{x\delta e}}{\partial M} + \frac{\partial C_{x\delta T}}{\partial M} + \frac{\partial C_{x\delta v}}{\partial M}\left(C_{Tv} + C_{x\delta T}\right) + C_{x\delta v}\left(\frac{\partial C_{Tv}}{\partial M} + \frac{\partial C_{x\delta T}}{\partial M}\right)\right)\frac{\partial M}{\partial V}$$

$$\frac{\partial g_2}{\partial V} = \frac{QS}{mV^2}\left(C_{z\delta e} + C_{z\delta T} + C_{z\delta v}\left(C_{z\delta T} - C_{Tn}\right)\right)$$
$$-\frac{QS}{mV}\left(\frac{\partial C_{z\delta e}}{\partial M} + \frac{\partial C_{z\delta T}}{\partial M} + \frac{\partial C_{z\delta v}}{\partial M}\left(C_{z\delta T} - C_{Tn}\right) + C_{z\delta v}\left(\frac{\partial C_{z\delta T}}{\partial M} - \frac{\partial C_{Tn}}{\partial M}\right)\right)\frac{\partial M}{\partial V}$$

$$\frac{\partial g_3}{\partial V} = \frac{QSc}{I_y}\left(\frac{\partial C_{m\delta e}}{\partial M} + \frac{\partial C_{m\delta T}}{\partial M} + \frac{\partial C_{m\delta v}}{\partial M}\left(C_{mp} + C_{m\delta T}\right) + C_{m\delta v}\left(\frac{\partial C_{mp}}{\partial M} + \frac{\partial C_{m\delta T}}{\partial M}\right)\right)\frac{\partial M}{\partial V}$$

$$\frac{\partial g_4}{\partial V} = 0$$

$$\frac{\partial g_1}{\partial \Gamma} = \frac{QS}{m}\left(\frac{\partial C_{x\delta e}}{\partial \alpha} + \frac{\partial C_{x\delta T}}{\partial \alpha} + \frac{\partial C_{x\delta v}}{\partial \alpha}\left(C_{Tv} + C_{x\delta T}\right) + C_{x\delta v}\left(\frac{\partial C_{Tv}}{\partial \alpha} + \frac{\partial C_{x\delta T}}{\partial \alpha}\right)\right)\frac{\partial \alpha}{\partial \Gamma}$$

$$\frac{\partial g_2}{\partial \Gamma} = -\frac{QS}{mV}\left(\frac{\partial C_{z\delta e}}{\partial \alpha} + \frac{\partial C_{z\delta T}}{\partial \alpha} + \frac{\partial C_{z\delta v}}{\partial \alpha}\left(C_{z\delta T} - C_{Tn}\right) + C_{z\delta v}\left(\frac{\partial C_{z\delta T}}{\partial \alpha} - \frac{\partial C_{Tn}}{\partial \alpha}\right)\right)\frac{\partial \alpha}{\partial \Gamma}$$

$$\frac{\partial g_3}{\partial \Gamma} = \frac{QSc}{I_y}\left(\frac{\partial C_{m\delta e}}{\partial \alpha} + \frac{\partial C_{m\delta T}}{\partial \alpha} + \frac{\partial C_{m\delta v}}{\partial \alpha}\left(C_{m\delta T} + C_{mp}\right) + C_{m\delta v}\left(\frac{\partial C_{m\delta T}}{\partial \alpha} + \frac{\partial C_{mp}}{\partial \alpha}\right)\right)\frac{\partial \alpha}{\partial \Gamma}$$

$$\frac{\partial g_4}{\partial \Gamma} = 0$$

$$\frac{\partial g_1}{\partial q} = 0 \qquad \frac{\partial g_2}{\partial q} = 0 \qquad \frac{\partial g_3}{\partial q} = 0 \qquad \frac{\partial g_4}{\partial q} = 0$$

$$\frac{\partial g_1}{\partial \theta} = \frac{QS}{m}\left(\frac{\partial C_{x\delta e}}{\partial \alpha} + \frac{\partial C_{x\delta T}}{\partial \alpha} + \frac{\partial C_{x\delta v}}{\partial \alpha}\left(C_{Tv} + C_{x\delta T}\right) + C_{x\delta v}\left(\frac{\partial C_{Tv}}{\partial \alpha} + \frac{\partial C_{x\delta T}}{\partial \alpha}\right)\right)\frac{\partial \alpha}{\partial \theta}$$

$$\frac{\partial g_2}{\partial \theta} = -\frac{QS}{mV}\left(\frac{\partial C_{z\delta e}}{\partial \alpha} + \frac{\partial C_{z\delta T}}{\partial \alpha} + \frac{\partial C_{z\delta v}}{\partial \alpha}\left(C_{z\delta T} - C_{Tn}\right) + C_{z\delta v}\left(\frac{\partial C_{z\delta T}}{\partial \alpha} - \frac{\partial C_{Tn}}{\partial \alpha}\right)\right)\frac{\partial \alpha}{\partial \theta}$$

$$\frac{\partial g_3}{\partial \theta} = \frac{QSc}{I_y}\left(\frac{\partial C_{m\delta e}}{\partial \alpha} + \frac{\partial C_{m\delta T}}{\partial \alpha} + \frac{\partial C_{m\delta v}}{\partial \alpha}\left(C_{m\delta T} + C_{mp}\right) + C_{m\delta v}\left(\frac{\partial C_{m\delta T}}{\partial \alpha} + \frac{\partial C_{mp}}{\partial \alpha}\right)\right)\frac{\partial \alpha}{\partial \theta}$$

$$\frac{\partial g_4}{\partial \theta} = 0$$

Elements of G_u Matrix:

$$\frac{\partial g_1}{\partial \delta_e} = \frac{QS}{m}\frac{\partial C_{x\delta e}}{\partial \delta_e} \qquad \frac{\partial g_2}{\partial \delta_e} = -\frac{QS}{mV}\frac{\partial C_{z\delta e}}{\partial \delta_e}$$

$$\frac{\partial g_3}{\partial \delta_e} = \frac{QSc}{I_y}\frac{\partial C_{m\delta e}}{\partial \delta_e} \qquad \frac{\partial g_4}{\partial \delta_e} = 0$$

$$\frac{\partial g_1}{\partial \delta_T} = \frac{QS}{m}\left(1 + C_{x\delta v}\right)\frac{\partial C_{x\delta T}}{\partial \delta_T} \qquad \frac{\partial g_2}{\partial \delta_T} = -\frac{QS}{mV}\left(1 + C_{z\delta v}\right)\frac{\partial C_{z\delta T}}{\partial \delta_T}$$

$$\frac{\partial g_3}{\partial \delta_T} = \frac{QSc}{I_y}\left(1 + C_{m\delta v}\right)\frac{\partial C_{m\delta T}}{\partial \delta_T} \qquad \frac{\partial g_4}{\partial \delta_T} = 0$$

$$\frac{\partial g_1}{\partial \delta_v} = \frac{QS}{m}\left(C_{Tv} + C_{x\delta T}\right)\frac{\partial C_{x\delta v}}{\partial \delta_v} \qquad \frac{\partial g_2}{\partial \delta_v} = -\frac{QS}{mV}\left(C_{z\delta T} - C_{Tn}\right)\frac{\partial C_{z\delta v}}{\partial \delta_v}$$

$$\frac{\partial g_3}{\partial \delta_v} = \frac{QSc}{I_y}\left(C_{m\delta T} + C_{mp}\right)\frac{\partial C_{m\delta v}}{\partial \delta_v} \qquad \frac{\partial g_4}{\partial \delta_v} = 0$$

C.2 Linearization Results for Estimation

For the Extended Kalman Filter algorithms, the control variables are now functions of state variables (by assuming full state feedback). Therefore, the control variables can be defined as:

$$\delta_e = \delta_e(V,\alpha,q,\theta) \qquad \delta_T = \delta_T(V,\alpha,q,\theta) \qquad \delta_v = \delta_v(V,\alpha,q,\theta)$$

With the vehicle dynamic equations of:

$$\begin{aligned}\dot{V} = {} & [\omega_E^2 R - g(R)]\sin(\theta-\alpha) + \frac{Q(R,V)S}{m}\left[C_{Tv}(M,\alpha,R) - C_D(M,\alpha)\right] \\ & + \frac{Q(R,V)S}{m}\left[C_{x\delta_e}(M,\alpha,\delta_e) + C_{x\delta_T}(M,\alpha,\delta_T)\right] \\ & + \frac{Q(R,V)S}{m}\left[+C_{x\delta_v}(M,\alpha,\delta_v)\left[C_{Tv}(M,\alpha,R) + C_{x\delta_T}(M,\alpha,\delta_T)\right]\right]\end{aligned}$$

$$\begin{aligned}\dot{\alpha} = {} & \left[\frac{g(R)}{V} - \frac{V}{R} - \frac{\omega_E^2 R}{V}\right]\cos(\theta-\alpha) + q - 2\omega_E + \frac{Q(R,V)S}{Vm}\left[C_{Tn}(M,\alpha,R) + C_L(M,\alpha)\right] \\ & - \frac{Q(R,V)S}{Vm}\left[C_{z\delta_e}(M,\alpha,\delta_e) + C_{z\delta_T}(M,\alpha,\delta_T)\right] \\ & - \frac{Q(R,V)S}{Vm}\left[C_{z\delta_v}(M,\alpha,\delta_v)\left[C_{z\delta_T}(M,\alpha,\delta_T) - C_{Tn}(M,\alpha,R)\right]\right]\end{aligned}$$

$$\begin{aligned}\dot{q} = {} & \frac{Q(R,V)Sc}{I_y}\left[C_{mp}(M,\alpha,R) + C_{ma}(M,\alpha) + C_{m\delta_e}(M,\alpha,\delta_e) + C_{m\delta_T}(M,\alpha,\delta_T)\right] \\ & + \frac{Q(R,V)Sc}{I_y}\left[C_{m\delta_v}(M,\alpha,\delta_v)\left[C_{m\delta_T}(M,\alpha,\delta_T) + C_{mp}(M,\alpha,R)\right]\right]\end{aligned}$$

and with polynomial representation of each coefficients, a set of appropriate linearization matrices can be obtained. Each elements of linearized matrices are shown below.

Elements of F matrix:

$$\frac{\partial f_1}{\partial V} = 0 \qquad \frac{\partial f_2}{\partial V} = \left[\frac{1}{R} + \frac{K_R}{V^2}\right]\cos(\theta-\alpha) \qquad \frac{\partial f_3}{\partial V} = 0$$

$$\frac{\partial f_1}{\partial \alpha} = -K_R\cos(\theta-\alpha) \qquad \frac{\partial f_2}{\partial \alpha} = \left[\frac{V}{R} - \frac{K_R}{V}\right]\sin(\theta-\alpha) \qquad \frac{\partial f_3}{\partial \alpha} = 0$$

$$\frac{\partial f_1}{\partial q} = 0 \qquad \frac{\partial f_2}{\partial q} = 1 \qquad \frac{\partial f_3}{\partial q} = 0$$

Elements of G matrix:

$$\frac{\partial g_1}{\partial V} = \frac{VS}{m}\left[C_{Tv} - C_D + C_{x\delta e} + C_{x\delta T} + C_{x\delta v}\left(C_{Tv} + C_{x\delta T}\right)\right]$$
$$+\frac{V^2 S}{2m}\left(\frac{\partial C_{x\delta e}}{\partial M} + \frac{\partial C_{x\delta T}}{\partial M} + \frac{\partial C_{x\delta v}}{\partial M}\left(C_{Tv} + C_{x\delta T}\right) + C_{x\delta v}\left(\frac{\partial C_{Tv}}{\partial M} + \frac{\partial C_{x\delta T}}{\partial M}\right)\right)\frac{\partial M}{\partial V}$$

$$\frac{\partial g_2}{\partial V} = \frac{S}{2m}\left[C_{Tn} + C_L + C_{z\delta e} + C_{z\delta T} + C_{z\delta v}\left(C_{z\delta T} - C_{Tn}\right)\right]$$
$$-\frac{VS}{2m}\left(\frac{\partial C_{z\delta e}}{\partial M} + \frac{\partial C_{z\delta T}}{\partial M} + \frac{\partial C_{z\delta v}}{\partial M}\left(C_{z\delta T} - C_{Tn}\right) + C_{z\delta v}\left(\frac{\partial C_{z\delta T}}{\partial M} - \frac{\partial C_{Tn}}{\partial M}\right)\right)\frac{\partial M}{\partial V}$$

$$\frac{\partial g_3}{\partial V} = \frac{VSc}{I_y}\left[C_{mp} + C_{ma} + C_{m\delta e} + C_{m\delta T} + C_{m\delta v}\left(C_{m\delta T} + C_{mp}\right)\right]$$
$$+\frac{V^2 Sc}{2I_y}\left(\frac{\partial C_{m\delta e}}{\partial M} + \frac{\partial C_{m\delta T}}{\partial M} + \frac{\partial C_{m\delta v}}{\partial M}\left(C_{m\delta T} + C_{mp}\right) + C_{m\delta v}\left(\frac{\partial C_{m\delta T}}{\partial M} + \frac{\partial C_{mp}}{\partial M}\right)\right)\frac{\partial M}{\partial V}$$

$$\frac{\partial g_1}{\partial \alpha} = \frac{QS}{m}\left(\frac{\partial C_{x\delta e}}{\partial \alpha} + \frac{\partial C_{x\delta T}}{\partial \alpha} + \frac{\partial C_{x\delta v}}{\partial \alpha}\left(C_{Tv} + C_{x\delta T}\right) + C_{x\delta v}\left(\frac{\partial C_{Tv}}{\partial \alpha} + \frac{\partial C_{x\delta T}}{\partial \alpha}\right)\right)$$

$$\frac{\partial g_2}{\partial \alpha} = -\frac{QS}{mV}\left(\frac{\partial C_{z\delta e}}{\partial \alpha} + \frac{\partial C_{z\delta T}}{\partial \alpha} + \frac{\partial C_{z\delta v}}{\partial \alpha}\left(C_{z\delta T} - C_{Tn}\right) + C_{z\delta v}\left(\frac{\partial C_{z\delta T}}{\partial \alpha} - \frac{\partial C_{Tn}}{\partial \alpha}\right)\right)$$

$$\frac{\partial g_3}{\partial \alpha} = \frac{QSc}{I_y}\left(\frac{\partial C_{m\delta e}}{\partial \alpha} + \frac{\partial C_{m\delta T}}{\partial \alpha} + \frac{\partial C_{m\delta v}}{\partial \alpha}\left(C_{m\delta T} + C_{mp}\right) + C_{m\delta v}\left(\frac{\partial C_{m\delta T}}{\partial \alpha} + \frac{\partial C_{mp}}{\partial \alpha}\right)\right)$$

$$\frac{\partial g_1}{\partial q} = 0 \qquad \frac{\partial g_2}{\partial q} = 0 \qquad \frac{\partial g_3}{\partial q} = 0$$

Linear Model of Density Disturbances:

$$\frac{d\rho}{dt} = M\rho + Bw$$

The above linearization results and the linear system representation of density models can be augmented to form a full set of the linearization results.

Appendix D
Alternative Control System Design Methodology

D.1 Motivation

In general, the desired estimator design in both theory and practice depends upon a specific history of control inputs. The difference in the desired estimator design, especially in the case of nonlinear and/or non-Gaussian noise, is due to the shape of the state conditional probability density function (PDF); and the equations which depict the evolution of PDF depend upon control variables. Therefore, the main objective of this chapter is to address the design and analysis of a realistic and robust control system that manages the AHSV flight dynamics such that the simulations of the closed loop dynamics can be used to provide the characteristics of the state probability density function.

For high Mach number flight, there exists a stable controller design by Chamitoff [Cha2] whose design is based upon Lyapunov stability criterion and an A-star search method applied in a manner similar to that used in nonlinear dynamic programming. However, when considering the estimator design, it is undesirable to have the controller in the form of numerical search codes; rather, an analytic form, especially a regulatory feedback controller, is highly attractive. In addition to the control system design provided in section 6.4, another control system design approach is derived in this Appendix.

D.2 Assumptions and Background

To obtain a particular AHSV controller design applicable to high Mach number flight, the LVLH kinematics formulation is used along with the parameterized form of the forcing (aerodynamics and propulsion) terms. The non-dimensionalized forcing coefficients are generated by the Draper developed AHSV design and simulation codes[Cha2] in the form of multi-dimensional numerical tables. Then the coefficient tables are curve-fitted with polynomials to form an approximate model of the vehicle

dynamics. The state vector is defined as in Chapter 5 (vehicle modelling section). Included in the vector are velocity, flight path angle (or angle of attack), pitch rate, pitch angle, and altitude.

D.3 Control Strategy

The major control problem involves stabilization of a highly nonlinear as well as inherently unstable plant(vehicle dynamics). For this particular control problem, the solution of the feedback control is approached by finding the control input trajectory which results in the particular trajectory of applied forces on the system. If the forces applied on the vehicle can be controlled precisely, then the states can be regulated to certain accuracies since the kinematics of the vehicle are relatively well known. In order to visualize the controller design procedure, it is best to view the AHSV vehicle dynamics as two functional segments as shown in Figure D-1.

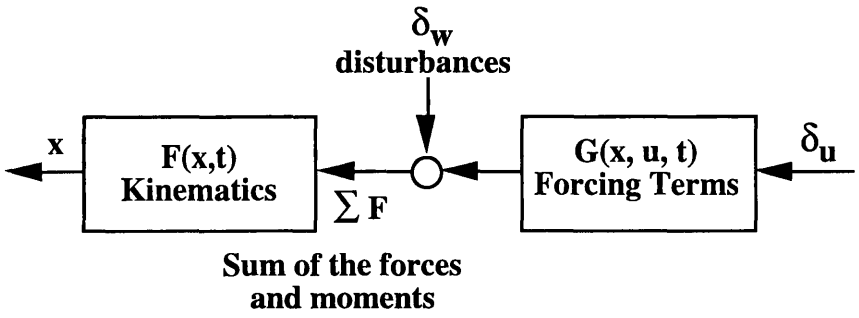

Figure D-1 Block Diagram of AHSV Vehicle Dynamics

The Kinematic block is separated from the forcing terms by distinct differences in available information on its coefficients. If the vehicle structure is assumed to be rigid, the kinematics of the AHSV are well defined with relatively well known gains such as the vehicle inertia matrix. On the other hand, the forcing terms, which include aerodynamics and propulsion interactions with the vehicle, are difficult to know or measure accurately. As a consequence of the differences, it is a much easier task to control from the forces to states instead of from control actuators to states.

Three assumptions are needed to control via forces. The first assumption that is required for this particular control approach is that all components of applied forces are observable with good accuracy and linearity. This assumption is needed since the control

system requires an inner feedback loop which causes the actual forces to follow the command forces. Observability is required for the forces. Linearity and good measurements are not necessary conditions, but they are highly desirable since they simplify the control design and make it easier to deal with modelling uncertainties. The second assumption regards the sensitivity and smoothness of the forcing terms. Within a reasonable bound of control inputs and forces, it is justifiable to assume that the forcing terms are infinitely differentiable upon consideration of the physics of flight and actuators. Also if the inner loop (from forces to command forces) is much faster than the time variations of kinematic state variables, then the variations of the forcing functions from the scheduled nominal condition would be small and the forcing functions would then just be dependent on the control input signal. This third assumption is necessary in order to segment the problem into two blocks. The physics of air-breathing hypersonic flight confirm the validity of this assumption.

The procedure of the AHSV control system design can be visualized as follows. The control problem is segmented into two by considering the inner feedback loop from the force command to actual applied forces as one element and the outer loop of control system which stabilizes the kinematics as the other.

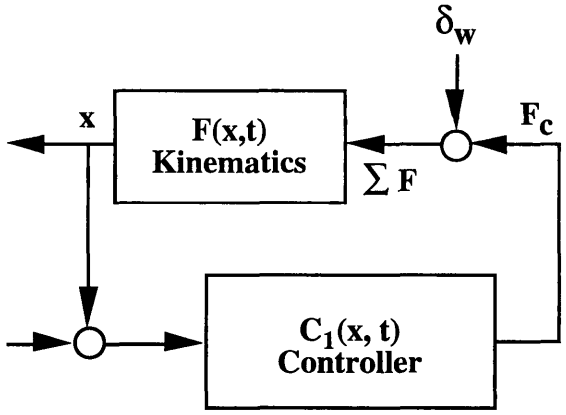

Figure D-2 Controller Design for Vehicle Kinematics Stabilization

For the outer loop, the controller is designed assuming that the control action occurs at the point of application of forces and moments as shown in Figure D-2. The feedback controller is designed to stabilize and to regulate the states near the desired steady state values while rejecting the disturbances. An appropriate cost functional for this control system is defined and the control problem becomes an effort to find a optimal and robust solution. The optimal control is sought since the coefficients to the kinematics

are well known and the perturbation of angle of attack will directly influence the total fuel consumption.

A subsequent task is to obtain the control actuator trajectories which will emulate the applied force on the vehicle to the force command output of the designed controller. The task of obtaining the control actuator signal from the desired force command is to invert the mapping defined by the forcing terms as shown in Figure D-3. In other words, the identity or linear relationship is needed, via linearization, from the force command to the actual force applied on the vehicle.

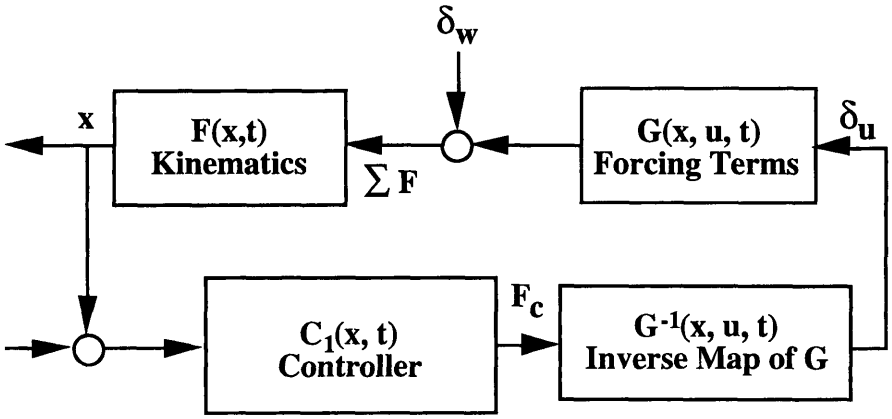

Figure D-3 Controller Configuration When Inverse Map of G is Available

There exist several possible problems to consider in obtaining the inverse mapping of the forcing block. First, the forcing block must be analyzed to verify that the mapping between the control actuators and the applied forces is one to one and onto at least locally within the operating region if not globally. Even a smooth forcing function may not have a unique inverse map, or the map may be asymptotically ill-behaved. The saturation regions of the forcing block must be defined. An elevon control as would be used for AHSV longitudinal rotation management has a limited range of motion which produces the desired torque to the vehicle due to the shadowing effects as well as the shock - aero-surface interactions. The throttle control has limited thrust variation due to the stringent combustion constraints. Because scramjet propulsion does not fully burn Hydrogen fuel, and added Hydrogen fuel lowers the exhaust molecular weight, often the optimal stoichiometric ratio which causes best Isp can be found somewhat higher than 1.0 (fuel rich). Consequently, for the best fuel efficiency, thrust variation outside the optimum propulsion performance regime should be minimized. Also the thrust vectoring, which is produced by varying nozzle lip length, is bounded by limited motion of nozzle

lip actuators. Consequently, the required force control trajectories must satisfy these constraints.

For the case when the inverse map is difficult to obtain or difficult to put in analytic form, even though it is one to one and onto (at least in a piecewise manner), the inversion can be obtained by simple feedback strategy as shown in Figure D-4. If the model of the forcing terms is available, then the local feedback can be designed to match the output of the forcing model with the force command. However, the local feedback loop should be much faster than the overall feedback loop to insure the separation of controller interactions.

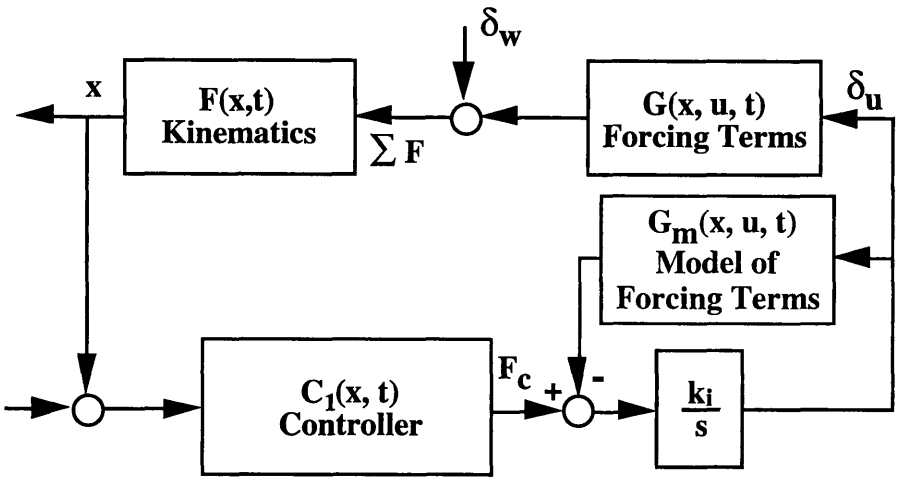

Figure D-4 The Inverse Map Obtained by Local Feedback

The performance of the control system design in Figures D-3 and D-4 strongly depend on the accuracy of the forcing models or its inverse. In reality, these terms can not be known exactly. The gains (coefficients) of the model can not be obtained exactly, even though extensive tests and in-flight tests maybe performed; moreover, the structure of the model may not be certain either. In order to overcome the inaccuracy of the model, a couple of additional control strategies can be added to those discussed above.

If the acceleration (torque and forces) measurements are available, then the slow adaptation rule can be used to tune the model of the forcing terms by taking advantage of the differential between the measurements and the force command as shown in Figure D-5. In this adaptive scheme, stability is the most significant problem. The problem is not trivial since there is a hidden information route (feedback) from the states to each of the functional blocks in this controller design; furthermore, the controller design results in a

local feedback route from the differential force error to the main control loop. The stability and performance analysis strategy for this highly nonlinear feedback structure is unknown.

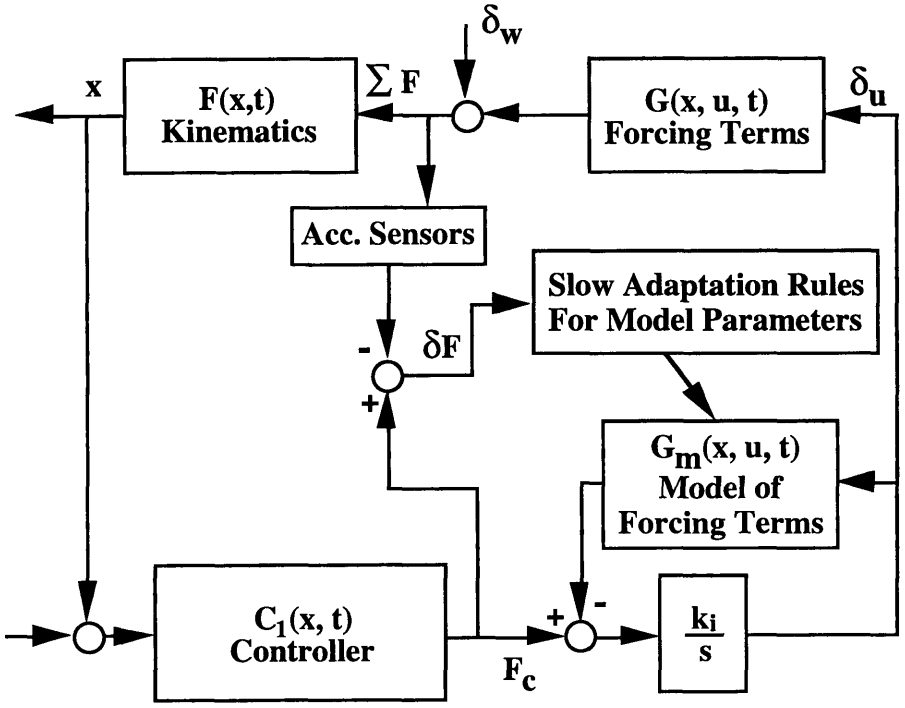

Figure D-5 Slow Adaptation of Model Parameters via Acceleration Measurements

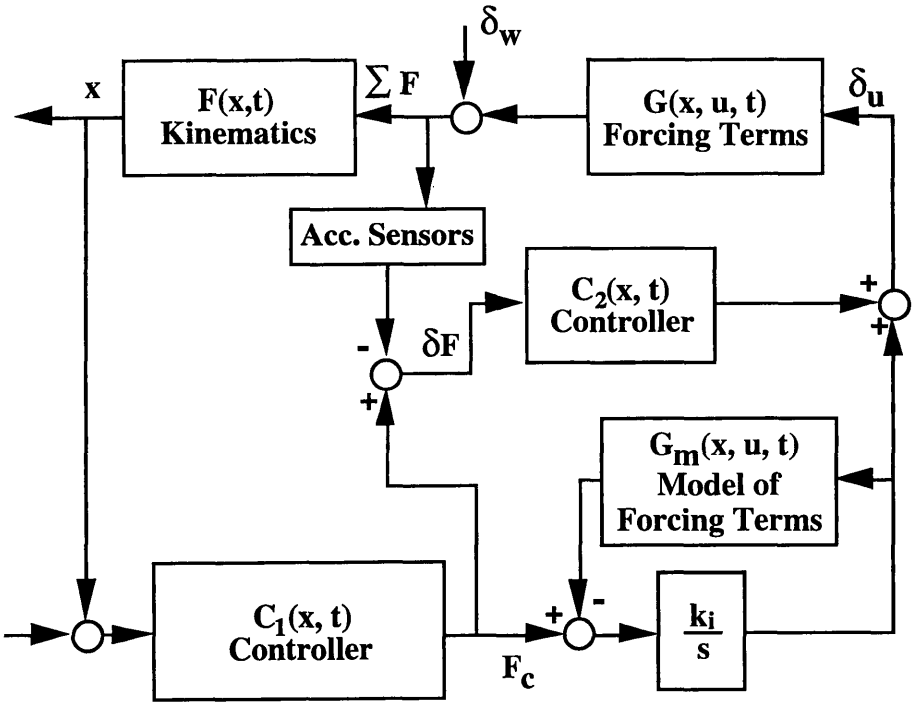

Figure D-6 Final Configuration of AHSV Controller

Similarly, if the acceleration measurements are available, then another controller can be designed and augmented to the existing control structure as shown in Figure D-6. The local feedback loop, which includes the model of forcing block, attempts to linearize or invert the complicated nonlinear forcing equations while the secondary controller compensates for the errors accumulated by the inexact modelling. This secondary controller will have higher bandwidth than the primary control loop and will null out the differences between the measured forces and the commanded forces.

D.4 Design Procedure

The final design of the control system is structured as shown in Figure D-6. The design procedure is outlined below:

1) Find the necessary conditions for the existence and uniqueness of the inverse map. Define the bounds on input and output images of the forcing function $G(\cdot)$ such that the inverse map exists within that bound.

2) Design the controller C_2 such that the inner loop is stable and provides good tracking performance from the force command to actual force applied on the vehicle. The design block diagram for C_2 is shown in Figure D-7. The first order linear dynamics have been included into $G(\cdot)$ in order to accommodate the actuator lag. The poles for the dynamics are assumed to be much faster than the fastest eigenvalues of the vehicle dynamics. For this approach, the actual state variables of the vehicle do not contribute directly to the states of the local feedback loop. The state variables will change the gains G and G_i. However, assuming that the state variables do not change greatly within the time frame of the local feedback loop, the control problem can be viewed as a linear control system with varying gains.

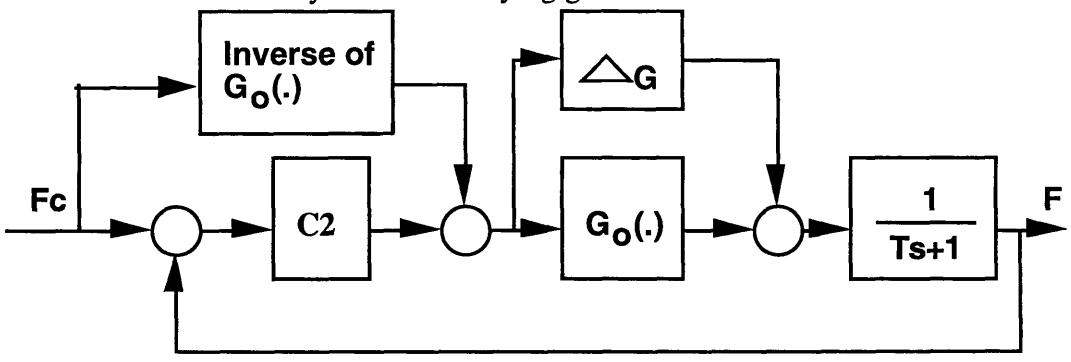

Figure D-7 Force Control Block Diagram

3) Obtain the closed loop dynamics structure of the local feedback loop with uncertainty. As shown in Figure D-8, the closed loop dynamics are represented as the nominal part which tries best to create an identity matrix, and the uncertainty part which augments all the modelling uncertainties after the loop has been closed.

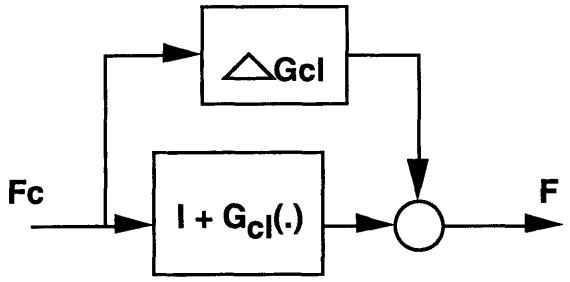

Figure D-8 Simplified Closed Loop of Control System

4) Linearize the kinematic equations around the nominal trajectory. Based on feedback linearization, the kinematic equations are linearized such that both gain scheduling and linear theory can be implemented. The control inputs for this case would be the forces and moments.

5) Based on linearized kinematic equations and uncertainty structure of the procedure step **2)**, design the C_1 controller with the cost functional associated with physical state variables. The structure for this control system design is shown in Figure D-9.

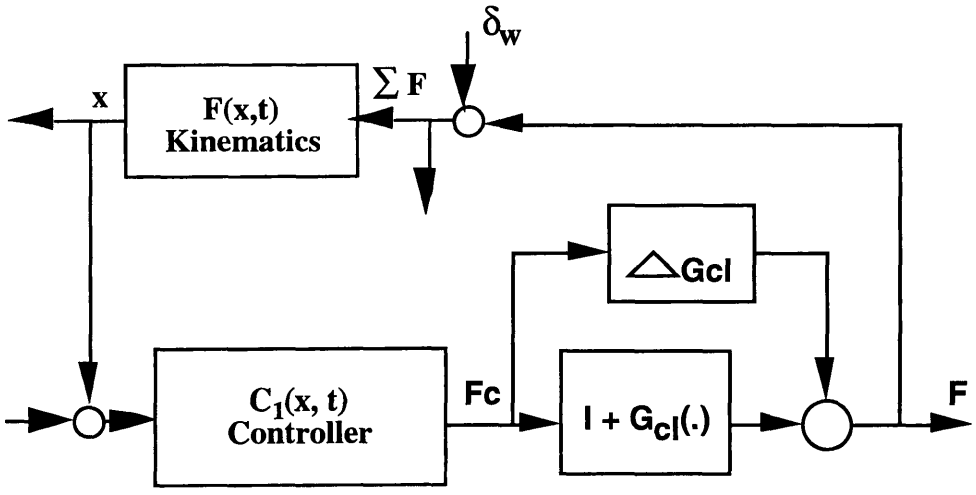

Figure D-9 Closed Loop Block Diagram with Modeling Uncertainties

D.5 Uniqueness Conditions

Definition 1) Let A be an open set $A \subset R^n$, and let $f: A \to R$ be a function. The value of f at $x = (x_1, ..., x_n)$ is denoted $f(x) = f(x_1, ..., x_n)$. Let f be C^∞. A function f is analytic if it is C^∞ and for each point $x^o \in A$, $\exists$ Neighborhood U of x^o s.t. the Taylor series expansion of f at x^o converges to $f(x)$ for $\forall x \in U$.

Definition 2) Let $U \in R^n$ and $V \in R^n$ be open sets. A mapping $F: U \to V$ is a diffeomorphism if it is bijective (i.e. one to one and onto) and both F and F^{-1} are of class C^∞.

Theorem 1) Inverse Function Theorem: Let A be an open set $A \subset R^n$, and let $F: A \to R^n$ a C^∞ mapping. If the Jacobian $\frac{\partial f}{\partial x}\Big|_{x^o}$ is nonsingular at some point $x^o \in A$, then there exists an open neighborhood U of x^o in A such that $V = F(U)$ is open in R^n and the restriction of F to U is a diffeomorphism onto V.

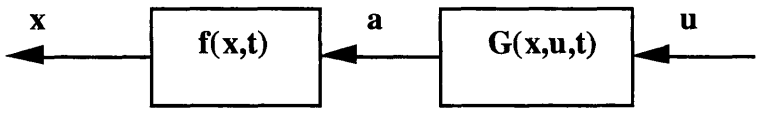

Condition for Existence of Inverse Mapping:

Assume that the vehicle is completely controllable from $u \to x$. Which implies that there exists at least a control trajectory u^* such that $x \to x^o$ in finite time. In addition assume that u^* is unique for each trajectory of $x \to x^o$. In such case, the mapping G is implicitly said to be one to one, and there is a unique a^* for given u. For a unique u^*, in a sense of controllability, there exists a^* such that $x \to x^o$ in finite time. The important issue here is to show bijectivity of mapping G (one to one and onto).

Let G to be C^∞ mapping and $u^* \in L_2[0,T]$. Define

$$\bar{a} = \sup_{t \le T} u^*(t) \quad \text{and} \quad \underline{a} = \inf_{t \le T} u^*(t)$$

Let $I = [\underline{a}, \bar{a}]$

If $\det \frac{\partial G}{\partial u}\Big|_I \neq 0$ then $\exists \supset$ I such that $\det \frac{\partial G}{\partial u}\Big|_J \neq 0$. By the inverse function theorem, if such conditions are met, then the restriction of G to U ($u \in U$) is a diffeomorphism onto A ($a \in A$). By definition 2, the function G is bijective (i.e. one to one and onto) and both G and G^{-1} are of class C^∞.

D.6 C_1 Controller Design

Objective: The main objective of this regulator is to command the state x to follow the scheduled state trajectory x_s, while minimizing the defined cost functional C. The constraints are defined by the limitations on the available and survivable acceleration magnitude.

Problem Statement: Let the state error e_x be defined as $e_x = x - x_s$ then the problem is to find force control Fu (acceleration in this case) such that

$$\min \|e_x\|_2$$

while satisfying the input constraints

$$\left|\sum F\right| < M \quad \text{by considering } |u| < N.$$

In this case, the 2 norm of error defined by the weighted sum of squares becomes the cost functional to be minimized.

Controller Implementation:

The controller design strategy of previous section will be implemented using the LVLH formulation of the AHSV dynamics. First, the controller for the kinematic block will be derived for the high Mach number flight regime. During this flight regime, several assumptions can be made to simplify the equations without loss of fidelity. The full AHSV equations of motion in LVLH frame are,

$$\frac{dV}{dt} = \frac{1}{m}\sum F_{xw} - \left(g(R) - \omega_E^2 R\right)\sin\Gamma$$

$$V\frac{d\Gamma}{dt} = -\frac{1}{m}\sum F_{zw} - \left(g(R) - \omega_E^2 R - \frac{V^2}{R}\right)\cos\Gamma + 2\omega_E V$$

$$\frac{dq}{dt} = \frac{1}{I_y}\sum M_y$$

$$\frac{d\theta}{dt} = q$$

$$\frac{dR}{dt} = V\sin\Gamma$$

Apply small angle approximations on flight path angle. Which implies:

$$\Gamma \approx \text{small} \quad \Rightarrow \quad \sin\Gamma \approx \Gamma \quad \Rightarrow \quad \cos\Gamma \approx 1$$

Also assume that the variations in **R** are small such that any function which depends on **R** (which is earth radius plus altitude) will be considered constant during short time period. Define new variables $C_0(\mathbf{R})$ and u as:

$$C_o \equiv C_o(R) = \omega_E^2 R - g(R)$$

and

$$u_1 \equiv \frac{1}{m}\sum F_{xw}, \quad u_2 \equiv \frac{1}{m}\sum F_{zw}, \quad u_3 \equiv \frac{1}{m}\sum M_y$$

Then, the equations can be written as:

$$\frac{dV}{dt} = C_o\Gamma + u_1$$
$$\frac{d\Gamma}{dt} = \frac{C_o}{V} + \frac{V}{R} + 2\omega_E - \frac{1}{V}u_2$$
$$\frac{dq}{dt} = u_3$$
$$\frac{d\theta}{dt} = q$$
$$\frac{dR}{dt} = V\Gamma$$

By inspecting the equations above, it is clear that the pitch dynamics are decoupled from other equations and can be controlled separately. Also the pitch dynamics are linear second order, a double integrator; therefore, a simple proportional-integral-differential (PID) controller can be implemented. However, the forcing function which represents the u_3 has to be analyzed assuming that the applied torque is within the saturation limit of the actuators.

The velocity equation can be also be decoupled from other equations by assuming that the $C_o\Gamma$ term is very small during level flight. We can also apply nonlinear feedback on the u_1 to eliminate that term. Before designing the nonlinear feedback law, it is desirable to understand the three equations from above,

$$\frac{dV}{dt} = C_o\Gamma + u_1$$
$$\frac{d\Gamma}{dt} = \frac{C_o}{V} + \frac{V}{R} + 2\omega_E - \frac{1}{V}u_2$$
$$\frac{dR}{dt} = V\Gamma$$

The $C_o\Gamma$ term consists mainly of the gravity contribution on the tangential velocity axis. Therefore, most of the changes in the tangential velocity would come from the aerodynamic drag and propulsion terms in u_1 during level flight. The major effector of

the altitude derivative term is the flight path angle Γ, since the flight path angle is the only variable which can change its sign. Simply, the direction of the velocity vector is moved around the horizon in order to gain or lose altitude. The second equation, which represents the acceleration normal to the velocity axis, consists of gravity, centripetal, and Coriolis terms.

For simplicity, the nonlinear feedback is applied on the first equation to decouple it from the rest of the equations. Let,

$$u_1 = -C_o\Gamma_m + u_1^*$$

where Γ_m is the measured flight path angle. Then a simple PID feedback controller is applied to u_1^* to control and improve the command following characteristics of the velocity. Then the nonlinear feedback is applied on the second equation to control both the flight path angle and the altitude. Let,

$$u_2 = C_o + \frac{V_m^2}{R_m} + 2\omega_E V_m + V_m u_2^*$$

The resulting control strategy is shown in Figure D-10 and D-11.

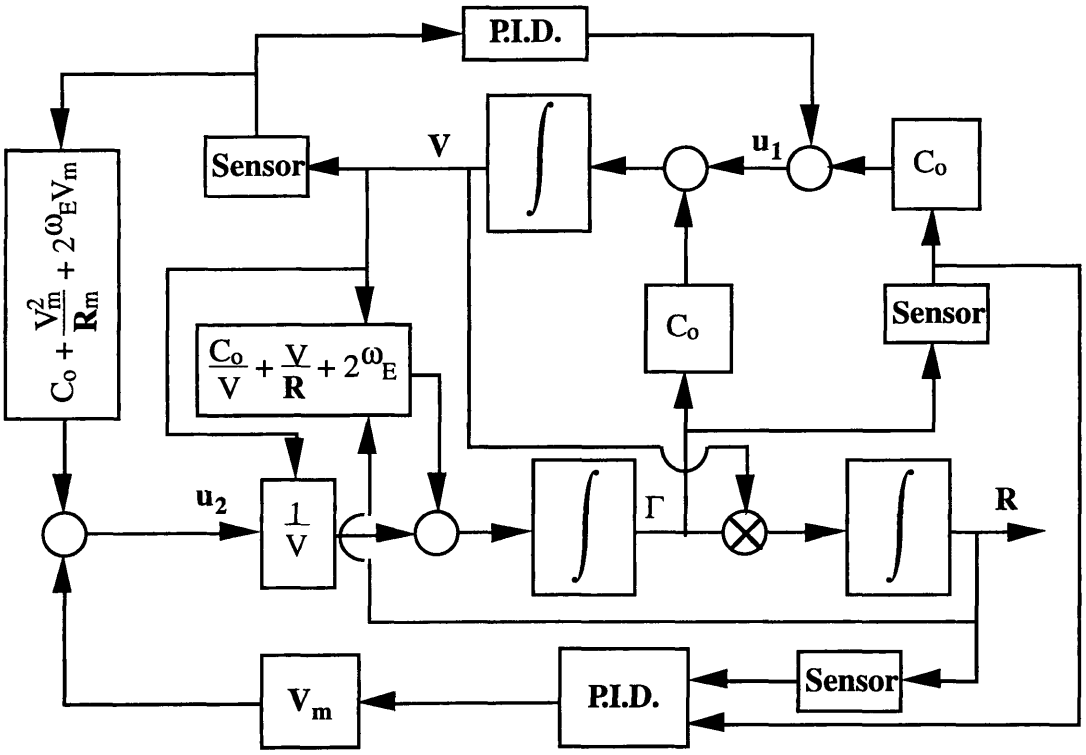

Figure D-10 Block Diagram of Kinematic Controller C1

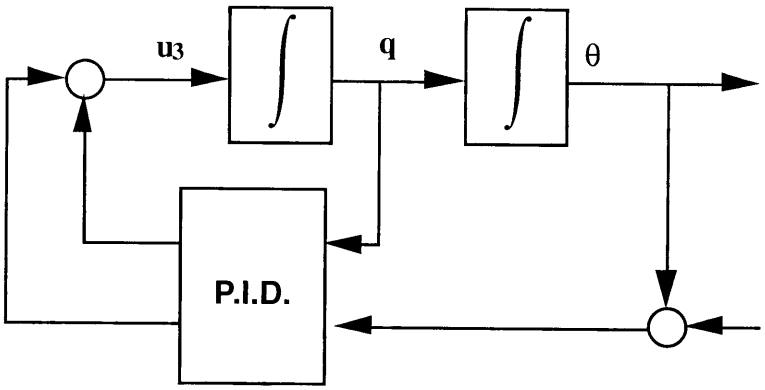

Figure D-11 Pitch Controller

References

[Ada1] Adamson, T.C.; Messiter, ***"Analysis of 2-D Interactions between Shocks and Boundary Layers"***, Annual Review of Fluid Mechanics, 12: pp. 103-138, 1980

[And1] Anderson, J. D. Jr., ***"Introduction to Flight"***, McGraw-Hill Inc., 1978

[Avi1] Stanley, W.K., ***"NASP Cancelled, Program Redirected"***, Aviation Week & Space Technology, June 14, 1993, pp.33-34

[Bil1] Bilimoria, K. D.; Schmidt, D. K., ***"An Integrated Development of the Equations of Motion For Elastic Hypersonic Flight Vehicles"***, AIAA paper, 92-4605-CP

[Bro1] Brockett, R., ***"Nonlinear Systems and Nonlinear Estimation Theory"***, NASA Technical Notes, N82-21986

[Bro2] Brockett, R., ***"Stochastic Control"*** , Harvard Univ. Lecture Notes ES203, spring 1992

[Buc1] Bucy, R. S., ***"Linear And Nonlinear Filtering."***, Univ. of Southern California, Los Angeles, Proceedings IEEE v 58 n 6 June 1970 p 854-64

[Buc2] Bucy, R. S., ***"Bayes Theorem And Digital Realizations For Non-Linear Filters."***, Univ. of Southern California, Los Angeles, J Astronautical Sciences v 17 n 2 Sept.-Oct. 1969 p 80-94

[Buc3] Bucy, R. S.; Youssef, Hussein M., ***"Nonlinear Filter Representation via Spline Functions"***, University of Southern California Los Angeles Dept. of Aerospace Engineering, Sponsor: Air Force Office of Scientific Research, Arlington, Va., Report No.: AFOSR-TR-75-0621, Journal Announcement: GRAI7515, Contract No.: AF-AFOSR-2141-71; AF-9769; 976901

[Cha1] Chamitoff, G. E., ***"Unofficial Memo On AHSV Dynamics"*** Draper Lab, June 1990

[Cha2] Chamitoff, G. E., ***"Robust Intelligent Flight Control for Hypersonic Vehicles"***, CSDL-T-1106, Draper Report, Also in MIT Ph.D. Thesis, Department of Aeronautics & Astronautics, February 1992.

[Cul1] Culver, C. O., ***"Optimal Estimation for Nonlinear Stochastic Systems"***, Ph.D. Thesis, 1969, instrumentation lab, MIT

[Duk1] Duke, J.C., Shen, C.N., ***"On-Line Estimate of Nonlinear Atmosphere Above Earth"***, Pub. in the Proceedings Symposium on Non-Linear Estimation (2nd), La Jolla, Calif., 114-126 Sept. 71.

[Fro1] Frost, W., ***"Incorporation Of Wind Shear Terms Into the Governing Equations of Aircraft Motion"***, AIAA-84-0275, AIAA 22nd Aerospace Sciences Meeting, January 9-12, 1984, Reno Nevada

[Gel1] Gelb, editor***"Applied Optimal Estimation"***, MIT press, 1974

[Hat1] Hattis, P. D., ***"Hypersonic Vehicle Air Data Collection: Assessing the Relationship Between the Sensor and Guidance and Control System Requirements"*** , American Automatic Control Conference, May 23 - 25, 1990, San Diego, CA.

[Hat2] Hattis, P. D., ***"Propulsion and Thermal Inputs to HSV Air Data Sensor Design Requirements"***, CDSL Intralab Memorandum EGD-90-019, February 1, 1990

[Hat3] Hattis, P. D., ***"A Look at Data Integration Studies and Issues Relevant to the Hypersonic Vehicle Air Data Problem"***, CDSL Intralab Memorandum EGD-89-087, November 14, 1989

[Hat4] Hattis, P. D., ***"A Look at Air Data Sensor Candidates for Hypersonic Vehicles"***, CDSL Intralab Memorandum ESC-92-052, February 7, 1992

[Hat5] Hattis, P. D., ***"Optimal Air-Breathing Launch Vehicle Design"***, Journal of Guidance and Control, September-October 1981, pp. 543-550

[Hat6] Hattis, P. D.; Smolskis, R.K., ***"Optimal Trajectory Generation and Design Trades for Hypersonic Vehicles"***, Proceedings for the 1989 American Control Conference, June 21-23, 1989, pp.1125-1130

[Hil1] Hill, K., ***"Idealized Wind Direction and Speed Changes for Shuttle Design Studies"***, S&E-AERO-YA-19-72, April 11,1972

[Hil2] Hillje, E. R.; Tymms, D. E., ***"Wind Tunnel and Flight Calibration of the Shuttle Orbiter Air Data System"***, AIAA Paper 78-792, April 1978.

[Hil3] Hillje, E., ***"The Orbiter Air Data System"***, AIAA Paper, 1983

[Hon1] Benser, E.T., Honeywell Systems and Research Center (Minn.), ***"Proposed System Functional Requirements for a NASP type Vehicle Air Data System"***, NASP Contractor Report 1044, June 1989

[Kas1] Kasich, D. C.; Cheng, P. Y., ***"Flush Port /Inertially Blended Air Data Estimator"***, AIAA Paper 91-0670, Jan. 7, 1991

[Jus1] Justus, C. G.; Woodrum, A. W.; Roper, R. G.; Smith, O. E., ***"NASA Global Reference Atmosphere: Four-D User Manual"***, NASA technical memo, TMX-64871 and TMX-64872, 1974

[Jus2] Justus, C. G.; Alyea, F. N.; Cunnold, D. M.; Blocker, R. S.; Johnson, D. L., ***"GRAM 88: Improvements to the Perturbation Simulation of the Global Reference Atmospheric Model"***, NASA-Marshall Space Flight Center Memo ES-44-11-9-88, 1988

[Kan1] Kang B. H., ***"Integrated Data Processing System for Air-Breathing Hypersonic Vehicles"***, CSDL Memo EGD-91-030, June 13, 1991

[Kan2] Kang, B.H.; Hansman Jr., R.J., ***"Preliminary Definition of Pressure Sensing Requirements for Hypersonic Vehicles"***, AIAA Paper 88-4652-CP, September 7, 1988

[Kop1] Koppenwallner, G., ***"Hypersonic Aerothermodynamics"***, Von Karmann Institute for Fluid Dynamics, Lecture Series 1984-01, February 1984

[Lam1] Lamb, Jr. R. H., ***"Parametric Nonlinear Filtering"***, LIDS- TH- 1723, Lab. for Information and Decision Systems, thesis MIT, Department of Electrical Engineering & Computer Science, May 1987

[Leh1] Lehtinen, B.; Zeller, J.; Geyser, L., ***"Optimal Control of Supersonic Inlets to Minimize Unstarts"***, NASA TND-6408, July 1971.

[Lew1] Lewis, M. J., ***"The Prediction of Inlet Flow Stratification and Its Influence on the Performance of Air-Breathing Hypersonic Propulsion System"***, Ph.D. Thesis, MIT, Department of Aeronautics and Astronautics, June 1988.

[McR1] McRuer, D., ***"Design and Modeling Issues for Integrated Airframe/Propulsion Control of Hypersonic Flight Vehicles"***, Proceedings of the American Control Conference, Boston, MA., June, 1991, pp 729 -735

[Mil1] Miles, R. B.; Santavicca, D. A.; Zimmermann, M., ***"Evaluation Of Non-Intrusive Flow Measurement Techniques for a Re-entry Flight Experiment"***, NASA Contractor Report 172142, November 1983.

[Mil2] Miles, R. B.; Lempert, W. R.; Forkey, J., ***"Imaging Turbulent Structure In High-Speed Air By Filtered Rayleigh Scattering."***, Twelfth Turbulence Symposium, Preprints for the Symposium on Turbulence. Publ by Univ of Missouri, Extension Division, Rolla, MO, USA. p A28.1-A28.8, 1990 Sep 24-26

[Mil3] Miles, R. B.; Connors, J. J.; Markovitz, E. C.; Howard, P. J.; Roth, G. J., ***"Instantaneous Profiles And Turbulence Statistics Of Supersonicfree Shear Layers By Raman Excitation Plus Laser-Induced Electronic Fluorescence (Relief) Velocity Tagging Of Oxygen"***, Experiments in fluids v 8 n 1-2 1989 p 17-24

[Mil4] Miles, R. B, ***"Oxygen Flow Tagging By Raman Excitation And Laser-Induced Electronic Fluorescence"***, Proceedings of the conference on lasers and electro-optics p 344, OSA/IEEE conference on lasers and electro-optics (CLEO 86), 9 June 1986

[Nas1] ***NASA Conference on Supersonic Missile Propulsion***, March 1952.

[Neu1] Neumann, R. D., ***"Instrumentation Concepts for X Series Aircraft "***, AIAA Paper no. 88-4650-CP, AIAA/NASA/AFWAL Conference on Sensors and Measurement Techniques for Aeronautical Applications, Sept. 1988

[Peg1] Pegg, R. J., ***"National Aero-space Plane"***, NASA Briefing to the Congressional Aeronautical Advisory Committee, March 1988.

[Pet1] Peterson, C.R.; Hill, P.G., ***"Mechanics and Thermodynamics of Propulsion"***, 3rd Edition. Addison-Wesley Pub. November 1970.

[Pru1] Pruett, C. D.; Wolf, H.; Simers, P. M.; Heck, M. L., ***"An Innovative Air Data System for the Space Shuttle Orbiter: Data Analysis Technique"***, AIAA Paper 81-2455, November 1981.

[Rob1] Robertson, W., ***"Short Time and Spatial Density Variations in the Upper Atmosphere (Description and Models)"***, CSDL-P-1956, September, 1984

[Sch1] Schmidt, D. K.; Mamich, H.; Chavez, F., ***"Dynamics and Control of Hypersonic Vehicles - The Integration Challenge for the 1990's"***, AIAA paper 91-5057, Dec. 1991

[Sch2] Schmidt, D. K.; Chavez, F.,***"An Integrated Analytical Aeropropulsive/Aeroelastic Model for the Dynamic Analysis of Hypersonic Vehicles"***, AIAA paper 92-4567, Presented at the Atmospheric Flight Mechanics Conference, August 1992

[Sch3] Schmidt, D. K.; Schierman, J.; Garg, S., ***"Analysis of Airframe/Engine Interactions - An Integrated Control Perspective"***, Proceedings of the Joint Propulsion Conference, Paper no. 90-1918 (Also to appear in the Journal of Guidance, Control and dynamics)

[Sch4] Schmidt, D. K., ***"Dynamics and Control of Hypersonic Aeropropulsive/Aeroelastic Vehicles"***, AIAA paper 92-4326-CP

[Sha1] Shaughnessy, J. D.; Pinckney, S. Z.; McMinn, J. D.; Cruz, C. I.; Kelly, M.L., ***"Hypersonic Vehicle Simulation Model: Winged-Cone Configuration"***, NASA Langley Report, June 1990

[Sha2] Shapiro, R., ***"An Adaptive Finite Element Solution Algorithm for the Euler Equations"***, Ph.D. Thesis, MIT, Department of Aeronautics and Astronautics, May 1988.

[Tib1] Tibbetts, B.R.; Lempert, W.R.; Miles, R.B.; Kenefick,P.D.Jr., ***"Optically-Based Air-Data System"***, 10th National Aero-Space Plane Technology Symposium, Paper # 185, April 23-26, 1991

[Tao1] Tao, Y. C., ***"Navigation System Design for Air-Breathing Hypersonic Vehicle"***, Draper memo EGB-90-216, June 29, 1990

[Wal1] Waldman, B.; Harsha, P., ***"The First Year of Teaming: A Progress Report"***, NASP National Program Office, AIAA Paper, AIAA-91-5008, AIAA Third International Aerospace Planes Conference, December 1991

[Wal2] Waltrup. P. J.; Billig, F. S.; Stockbridge, R. D., ***"A Procedure for Optimizing the Design of Scramjet Engines"***, Journal of Spacecraft and Rockets, Vol. 16, No.3, May-June 1979

[Web1] Webb, L., ***"Characteristic and Use of X-15 Air Data Sensors"***, NASA TND-4597, November 1967

[Wol1] Wolowicz, C.; Gossett, T., ***"Operational and Performance Characteristic of the X-15 Spherical Hypersonic Flow Direction Sensor"*** , NASA TND-3070, August 1965.

[YF12] ***YF-12 Experiments Symposium***, Vol. 1, NASA Conference Publication 2054, September 1978.

[Zak1] Zakai, M., ***"On the Optimal Filtering of Diffusion Processes "***, *Z. Wahr. Verw. Gebiete*, 11, 1969, pp230-243